

## Abstract

# Progress Toward Observation of Radiation Pressure Shot Noise

Benjamin Michael Zwickl

2011

It has been over 100 years since the first conclusive demonstration of radiation pressure by Lebedev [1] and Nichols and Hull [2, 3]. Cavity optomechanical systems—high finesse optical cavities coupled to mechanical resonators—are good testing grounds for the mechanical properties of light. The system described in this dissertation is a 7 mm long cavity coupled to a 1 mm square, 50 nm thick silicon nitride membrane. Like many similar optomechanical systems, ranging from the Laser Interferometer Gravitational Wave Observatory to microtoroids, this work has moved beyond detecting the steady state force of light on a mirror to a rich array of dynamical effects. Classical effects include shifts in the mechanical resonant frequency and optical damping, both of which are demonstrated in this thesis.

The (relatively) strong coupling between the light and mechanical resonator can, in principle, demonstrate effects beyond classical mechanics and classical light. This thesis represents an attempt to directly measure random quantum fluctuations in the force of light reflecting from a surface, an effect we call the radiation pressure shot noise.

A correlation measurement scheme developed theoretically by Børkje et al. [4] was implemented. This measurement scheme is capable of distinguishing the effects of the random thermal force from the random radiation pressure shot noise. Successful suppression of thermal effects was demonstrated, though unfortunately not to the level required to measure the radiation pressure shot noise. In spite of not accomplishing this major physics goal, much was learned about this measurement scheme and its potential for future measurements of the radiation pressure shot noise.

The dissertation begins with an overview of a variety of physical manifestations of the radiation pressure shot noise. The relevant theoretical formalism is then developed, and the correlation scheme is explained. Our technical accomplishments in developing the correlation measurement scheme are

presented. The correlation measurement scheme is then used to accomplish successful suppression of thermal effects consistent with the theory developed by Børkje et al. The paper concludes with a brief look at proposed optomechanical systems that may offer a better opportunity to observe the radiation pressure shot noise.

# Progress Toward Observation of Radiation Pressure Shot Noise

A Dissertation  
Presented to the Faculty of the Graduate School  
of  
Yale University  
in Candidacy for the Degree of  
Doctor of Philosophy

by  
Benjamin Michael Zwickl

Dissertation Director: Jack Harris

06/03/11

Copyright © 2011 by Benjamin Michael Zwickl  
All rights reserved.

# Contents

<b>Contents</b>	<b>iii</b>
<b>List of Figures</b>	<b>viii</b>
<b>List of Symbols</b>	<b>xvi</b>
<b>Acknowledgments</b>	<b>xviii</b>
<b>1 Introduction to radiation pressure shot noise and quantum limited measurement</b>	<b>1</b>
1.1 History . . . . .	1
1.2 Quantum limited measurement . . . . .	9
1.3 Examples of quantum limited measurements . . . . .	11
1.4 Standard quantum limits . . . . .	15
1.5 Physical manifestations of the radiation pressure shot noise . . . . .	17
1.6 This dissertation in relation to previous work . . . . .	21
<b>2 Basic theory of cavity optomechanics</b>	<b>27</b>
2.1 Overview of cavity optomechanics . . . . .	28
2.2 The most basic model: A cavity with one harmonically bound end mirror. . . . .	30
2.3 Derivation of the cavity equation of motion from the steady-state solution . . . . .	30
2.3.1 Derivation of the steady-state field amplitudes . . . . .	30
2.3.2 From steady-state fields to an equation of motion . . . . .	37
2.3.3 Applying the cavity equation of motion to other optomechanical systems . . . . .	39

2.3.4	Note: Why a single time varying number is sufficient to describe the intracavity field . . . . .	40
2.4	Differences between the movable end mirror and the membrane-in-the-middle geometries . . . . .	40
2.4.1	Advantages of the membrane-in-the-middle geometry . . . . .	41
2.4.2	Membrane-in-the-middle: Calculation of the steady-state intracavity fields and optomechanical coupling . . . . .	41
2.4.3	Other interesting attributes of the membrane-in-the-middle geometry . . . . .	46
2.5	Mechanical resonator's equation of motion in the high- $Q$ limit . . . . .	47
2.6	Derivation of the quantum equations of motion for a coupled optical cavity and mechanical resonator . . . . .	48
2.6.1	Linearized cavity equations of motion in the rotating frame . . . . .	50
2.6.2	Linearized mechanical equation of motion in the rotating (optical) frame . . . . .	53
2.6.3	Solution to cavity linearized equation of motion in the Fourier domain . . . . .	54
2.6.4	Solution to the mechanical equation of motion in the Fourier domain . . . . .	54
2.7	Optical resonant frequency shift and optical damping . . . . .	58
2.7.1	Effective susceptibility of the resonator . . . . .	58
2.7.2	Longer expressions for the frequency shift and optical damping . . . . .	60
2.8	Derivation of the position power spectral density $S_z[\omega]$ . . . . .	62
2.9	Radiation pressure shot noise as a limit to laser cooling . . . . .	65
2.10	Ratio of the radiation pressure shot noise and thermal force . . . . .	67
2.10.1	Special case of on resonance $\Delta = 0$ and slow fluctuations $\omega \ll \kappa$ . . . . .	67
2.10.2	Special case of $\omega \approx \omega_M$ . . . . .	68
2.10.3	Power spectral densities in SI units . . . . .	71
2.11	Useful formulas for the noise terms $\eta[\omega]$ and $\xi_i[\omega]$ . . . . .	72
<b>3</b>	<b>Correlation scheme to measure the radiation pressure shot noise</b>	<b>73</b>
3.1	Introduction . . . . .	73

3.2	Correlation scheme on resonance . . . . .	75
3.2.1	The basic idea for classical amplitude noise input on the cavity . . . . .	75
3.2.2	Expected form for the RPSN-induced correlation . . . . .	75
3.2.3	Definition of arbitrary quadratures of transmitted and reflected beams . . . . .	76
3.2.4	Transmitted intensity quadrature on resonance using the quantum formulation . . . . .	78
3.2.5	Reflected phase quadrature on resonance using the quantum formulation . . . . .	80
3.3	Non-zero detuning correlation scheme . . . . .	81
3.3.1	Derivation of the critical angle $\theta_C$ . . . . .	81
3.4	A full expression for the correlation between $\delta\hat{X}_\phi[\omega]$ and $\delta\hat{Y}_{\theta_L}[\omega]$ . . . . .	84
3.5	Key results from Børkje et al. . . . .	85
3.6	Plots near zero detuning . . . . .	87
3.6.1	Figure of merit near zero detuning . . . . .	87
3.7	Plots at large, finite detuning ( $\Delta = -3.1\kappa$ ) . . . . .	89
3.8	Plots at half-linewidth detuning . . . . .	90
3.9	Effect of finite measurement time . . . . .	92
3.9.1	Averaging time on resonance . . . . .	92
<b>4</b>	<b>Experimental Design</b>	<b>95</b>
4.1	Mechanical resonator: Silicon nitride membrane . . . . .	95
4.1.1	Mechanical loss in silicon nitride membranes . . . . .	97
4.1.2	Optical loss in silicon nitride membranes . . . . .	100
4.2	The cavity and optical mount . . . . .	101
4.3	Optics Setup . . . . .	103
4.3.1	Stage 1 . . . . .	103
4.3.2	Stage 2 . . . . .	104
4.3.3	Stage 3 . . . . .	106
4.3.4	Stage 4 . . . . .	108
4.3.5	Stage 5 . . . . .	108

4.4	Vacuum systems . . . . .	108
4.5	Electronic signal processing and data acquisition . . . . .	108
4.6	Using a heterodyne measurement to detect an arbitrary quadrature . . . . .	109
4.7	Converting the ZI-HF2 demodulator into the correlation signal . . . . .	113
4.8	Reconstructing the transmitted intensity fluctuations $\delta X_\phi[\omega]$ . . . . .	114
4.9	Reconstructing the reflected fluctuations in an arbitrary quadrature $\delta Y_{\theta_L}[\omega]$ (Ideal measurement) . . . . .	115
4.10	Reconstructing the reflected fluctuations in an arbitrary quadrature $\delta Y_{\theta_L}[\omega]$ (Actual measurement) . . . . .	118
4.10.1	Correction #1 - Phase changes between the local oscillator and signal beams	118
4.10.2	Correction #2 - A constant phase offset in the heterodyne phase $\theta_{\text{offset}}$ . . . .	120
4.10.3	Correction #3 - A variation in amplifier gain over the 2 MHz bandwidth between the upper and lower mechanical sidebands . . . . .	121
4.10.4	Correction #4 - An overall phase shift to reflected heterodyne quadrature $Y_{\theta_L}[\omega] \rightarrow e^{i\theta_g} Y_{\theta_L}[\omega]$ . . . . .	121
<b>5</b>	<b>Preliminary Results and Discussion</b>	<b>123</b>
5.1	Calibrating the measurement scheme . . . . .	123
5.1.1	Calibration of $\theta_{\text{offset}}$ . . . . .	124
5.1.2	Calibration of $\beta$ . . . . .	124
5.1.2.1	Method 1: Laser far-detuned from cavity resonance . . . . .	124
5.1.2.2	Method 2: Ratio of sidebands at zero detuning . . . . .	126
5.1.3	Calibration of $\theta_g$ . . . . .	128
5.2	Determining cavity decay rates $\kappa$ and $\kappa_L$ . . . . .	129
5.3	Measurement of detuning . . . . .	130
5.3.1	Method 1: Phase shift of the reflected heterodyne carrier . . . . .	133
5.3.2	Method 2: Phase shift of the reflected phase modulation sidebands . . . . .	134
5.3.3	Method 3: Ratio of the mechanical motion-induced sidebands . . . . .	134

5.3.4	Agreement of Methods 1 and 3 . . . . .	135
5.4	Optomechanics . . . . .	136
5.5	Measurement of the critical quadrature . . . . .	140
5.6	Suppression of the thermal contribution to the correlation . . . . .	143
<b>6</b>	<b>Future directions and conclusions</b>	<b>147</b>
6.1	Optimization of optomechanical parameters . . . . .	147
6.1.1	Relevance of the static radiation pressure bistability to the experiments in this dissertation . . . . .	149
6.2	Conclusion . . . . .	150
<b>A</b>	<b>Calculations of stressed membrane properties</b>	<b>154</b>
A.1	Calculation of spring constant . . . . .	154
A.2	Calculation of Kinetic Energy, Effective Mass, and Resonant Frequency . . . . .	156
<b>B</b>	<b>Derivation of thermo-elastic dissipation limited <math>Q</math></b>	<b>157</b>
B.1	Introduction . . . . .	157
B.2	Derivation . . . . .	158
B.2.1	Modifications of argument in Norris and Photiadis . . . . .	158
B.2.2	Setting up the basic equations to solve . . . . .	158
B.2.3	Calculating the temperature field $\theta(\vec{x}, t)$ (part 1) . . . . .	160
B.2.4	Calculating $\alpha \cdot \sigma$ . . . . .	161
B.2.5	Calculating the temperature field $\theta(\vec{x}, t)$ (Part 2) . . . . .	162
B.2.6	Computing the mean loss rate during an oscillation . . . . .	164
B.3	Calculation of $Q$ . . . . .	166
B.4	Discrepancy with other calculations of $Q_{\text{TED}}$ . . . . .	168
	<b>Bibliography</b>	<b>169</b>

# List of Figures

1.1	A comet's trajectory as drawn by Kepler in <i>De Cometis Libelli Tres</i> (1619). Note the comet tail is always facing away from the Sun. (Used with permission from UCL Library Services, Special Collections) . . . . .	2
1.2	Heisenberg's Microscope offers an intuitive origin for the uncertainty relationship. A photon scatters off of an electron and is focused by a lens onto a CCD camera. The aperture of the lens limits the position resolution $\Delta x$ , while the uncertain direction of the photon recoil causes an uncertainty in the photon's momentum $\Delta p_x$ , satisfying $\Delta x \Delta p_x \sim h$ . . . . .	12
1.3	Optical cavity with a movable end mirror. . . . .	15
1.4	Phonon number as a function of the optical damping. For small optical damping (e.g. low laser powers) the phonon number was chosen to be 1000. A classical theory of laser cooling would predict the mean energy of the oscillator would decrease indefinitely, but the radiation pressure shot noise drives a small amount of motion limiting the lowest achievable phonon number. The solid curve is a theoretical plot of Eq. 1.31 with $\bar{n}_{\text{th}} = 1000$ and $\bar{n}_{\text{m}}^O = 0.1$ . . . . .	19
1.5	Membrane-in-the-middle cavity geometry used in this dissertation. . . . .	22

2.1	Cavity with a harmonically bound end mirror. This is the canonical system in cavity optomechanics. The $P_i$ refer to the input, reflected, circulating and transmitted laser power. The $(r_i, t_i)$ pair refers to the amplitude reflection and transmission coefficients for the end mirrors. The mass $m$ , resonant frequency $\omega_M$ , and damping constant $\gamma$ are given for the harmonically bound end mirror. . . . .	31
2.2	Cavity with a movable end mirror. The six electric fields are shown which are used in the steady state derivation for the cavity equations of motion. . . . .	33
2.3	Membrane-in-the-middle cavity geometry. A membrane of thickness $d$ has amplitude reflection and transmission coefficients of $r_d$ and $t_d$ , respectively. (A) represents the intracavity field as a standing wave field, showing that the membrane's interaction with the intracavity field will be periodic. (B) represents all the left- and right-going waves needed to describe the system in one dimension. . . . .	42
2.4	(A) A plot of the theoretical variation in cavity resonance frequency $\omega_C(x)$ as a function of membrane position. The different curves represent different membrane reflectivities. (B) A plot of the cavity transmission for a scan of laser frequency and membrane position. Darker colors correspond to a higher transmission. The darkest line represents the lowest order Gaussian cross-section cavity mode. The dashed lines correspond to the empty cavity modes (i.e. a membrane with zero reflectivity). . .	45
2.5	A phasor diagram of the classical input field $a_{\text{in}}(t) = \bar{a}_0 + \delta x(t) + i\delta y(t)$ which is written in in the rotating frame. Note that $\bar{a}_0$ , $\delta x(t)$ , and $\delta y(t)$ are always assumed to be real valued. The fluctuations $\delta x(t)$ have the same phasor orientation as the mean amplitude $\bar{a}_0$ , which implies they are amplitude fluctuations. Similarly the fluctuations $i\delta y(t)$ have a phasor orientation orthogonal to the mean amplitude $\bar{a}_0$ , which implies they are phase fluctuations. . . . .	52

2.6	Plots of the radiation pressure induced changes to the mechanical resonant frequency $\delta\omega_M$ (in subplots A and C) and damping $\gamma_{\text{opt}}$ (in subplots B and D). The 3D subplots in C and D show the transition from the resolved sideband regime $\kappa/\omega_M = 0.1$ to the non-resolved sideband regime $\kappa/\omega_M = 3.0$ . Only the cavity damping rate $\kappa$ and the detuning $\Delta$ are varied. All other parameters are held constant. The magnitude of the optomechanical coupling which can be varied by changing the incident power $P_{\text{in}}$ and the slope $\partial\omega_{\text{csv}}/\partial z$ acts as a vertical scaling factor for the curves, but otherwise does not change the shape. . . . .	61
2.7	Ratio of RPSN to thermal force noise. The series of plots show that as $\kappa$ decreases (finesse increases) there is no increase in the ratio beyond $\kappa = \omega_M$ . . . . .	71
3.1	Radiation pressure shot noise measurement scheme developed by Børkje et al. [4]. The scheme involves a single beam incident upon the cavity. The correlation will be calculated between an arbitrary quadrature of the reflected field $Y_{\theta_L}[\omega]$ and the transmitted amplitude quadrature $X_\phi[\omega]$ . . . . .	74
3.2	Plot of the correlation between the transmitted intensity fluctuations and reflected phase given in Eq. 3.1. The laser is assumed to be on resonance ( $\Delta = 0$ ) and only noise considered is classical amplitude noise on the laser. The vertical axis scale is normalized to have a maximum correlation of one. . . . .	77
3.3	Theoretical plots of the various contributions to the correlation $R[\omega]$ . The detuning is $\Delta = \Delta_0 + \delta\Delta$ where $\Delta_0 \approx 0$ , and $\delta\Delta = -2\pi \times 0.1$ Hz for the blue curve, and $\delta\Delta = -2\pi \times 1.0$ Hz for the red curve. The reflected heterodyne quadrature is $\theta = \pi/2$ . The frequency axis is centered about the bare resonant frequency $\omega_M = 2\pi \times 788$ kHz and scaled by the bare mechanical linewidth $\gamma = 2\pi \times 1.1$ Hz. The incident power is $P_{\text{in}} = 10 \mu\text{W}$ . $\kappa = 4.45 \times 10^6 \text{ s}^{-1}$ and $\kappa_L = 0.155\kappa$ . $T = 295$ K. The membrane is positioned about 10 nm from a node of the intracavity field. The classical amplitude and phase noise have the same magnitude as the quantum noise ( $C_X = C_Y = 1$ , where $C_X$ and $C_Y$ are defined in Eqs. 3.56 and 3.57). . . . .	88

3.4	<p>Theoretical plots of the various contributions to the correlation <math>R[\omega]</math>. The detuning is <math>\Delta = \Delta_0 + \delta\Delta</math> where <math>\Delta_0 \approx -3.1\kappa</math>, and <math>\delta\Delta = 0.1 \times 2\pi</math> Hz for the blue curve, and <math>\delta\Delta = 1.0 \times 2\pi</math> Hz for the red curve. The reflected heterodyne quadrature was <math>\theta = \theta_C(\Delta_0)</math>. The frequency axis is centered about the bare resonant frequency <math>\omega_M = 2\pi \times 788</math> kHz and scaled by the bare mechanical linewidth <math>\gamma = 2\pi \times 1.1</math> Hz. The incident power is <math>P_{\text{in}} = 10 \mu\text{W}</math>. <math>\kappa = 4.45 \times 10^6 \text{ s}^{-1}</math> and <math>\kappa_L = 0.155\kappa</math>. <math>T = 295 \text{ K}</math>. The membrane is positioned about 10 nm from a node of the intracavity field. The classical amplitude and phase noise is the same magnitude as the quantum noise (<math>C_X = C_Y = 1</math>). . . . .</p>	91
3.5	<p>Theoretical plots of the various contributions to the correlation <math>R[\omega]</math>. The detuning is <math>\Delta = \Delta_0 + \delta\Delta</math> where <math>\Delta_0 = -0.5\kappa</math>, and <math>\delta\Delta = 0.1 \times 2\pi</math> Hz for the blue curve, and <math>\delta\Delta = 1.0 \times 2\pi</math> Hz for the red curve. The reflected heterodyne quadrature was <math>\theta = \theta_C(\Delta_0)</math>. The frequency axis is centered about the bare resonant frequency <math>\omega_M = 2\pi \times 788</math> kHz and scaled by the bare mechanical linewidth <math>\gamma = 2\pi \times 1.1</math> Hz. The incident power is <math>P_{\text{in}} = 10 \mu\text{W}</math>. <math>\kappa = 4.45 \times 10^6 \text{ s}^{-1}</math> and <math>\kappa_L = 0.155\kappa</math>. <math>T = 295 \text{ K}</math>. The membrane is positioned about 10 nm from a node of the intracavity field. The classical amplitude and phase noise is the same magnitude as the quantum noise (<math>C_X = C_Y = 1</math>). . . . .</p>	92
4.1	<p>Ring-down of the fundamental mechanical mode of silicon nitride membranes at room temperature (green) and cryogenic temperatures (red). The membranes were 1 mm square, 50 nm-thick Norcada low-stress silicon nitride membranes with a fundamental resonant frequency of about 130 kHz. . . . .</p>	98

4.2	Measured quality factor for different mechanical modes of four 1 mm square, 50 nm-thick, high-stress stoichiometric membranes used over the period of a month. The mountings all used epoxy, but amount and location of the epoxy joint differed between membranes. The measurements were made by driving the membrane and sweeping the drive across the mechanical resonant frequency and measuring the width of the resonance peak. The estimates are relatively crude when compared to the ring-down measurements in Fig. 4.1. The most significant point is that higher frequency mechanical modes tend to have higher quality factors. . . . .	99
4.3	Position dependence of cavity finesse for a high-stress stoichiometric membrane inside the $L = 7$ mm cavity. Each of the points is measured by taking an optical ring-down similar to Fig. 4.4. The variation in finesse from node to antinode is used to determine an upper limit on membrane absorption of $\text{Im}(n) \lesssim 9 \times 10^{-5}$ using Eq. 4.10. Table 4.2 compares this result with previous estimates of membrane absorption. . . . .	102
4.4	Cavity ring-downs at the node and antinode. . . . .	102
4.5	Diagram of the cavity spacer, membrane mount, and associated positioning optomechanics. . . . .	104
4.6	Schematic of the optics from laser to cavity to photodiodes. . . . .	105
4.7	Diagram of the main optical signals. The local oscillator beam (purple), the signal beam (green), and the phase modulation sidebands of the signal beam (blue) are all incident upon the cavity (gray, dashed line). The reflected beam has the additional $\pm 800$ kHz modulation of the signal beam (shown in red), which results from the membrane's Brownian motion modulating the intracavity field. . . . .	106
4.8	Electronic Detection Scheme. The portion inside the dashed rectangle in the Zurich Instruments HF2. The diagram tracks the signals from the various photodiodes (also shown in the optical schematic Fig. 4.6) to the final mixed down quadratures from the ZI-HF2. Omitted from the diagram are a number of attenuators and amplifiers needed for adjusting the signal strengths to appropriate levels for mixers and the ZI-HF2 inputs. . . . .	110

4.9	A plot of the reference heterodyne phase and the reflected heterodyne phase as a function of time. The reflected phase appears noisier because it is measuring low frequency $< 3$ kHz position fluctuations of the membrane which are driven by acoustic noise. . . . .	120
5.1	(A) The power in the upper and lower sidebands. The frequency is the deviation from the sideband frequency, so that the USB and LSB overlap for easy comparison. In this case the integrated power is the same to about 0.4 percent, meaning $\beta = 1.002$ . (B) Integrated power (at the modulation frequency) in a quadrature of the reflected field as the quadrature angle is varied. The USB and LSB data whose PSDs are shown in (A) have been used to reconstruct an arbitrary quadrature of the reflected field. . . . .	125
5.2	Plot showing the variation of the integrated Brownian motion signal in transmission, for a series of data sets taken at different detunings. The data sets closest to zero detuning should correspond to the smallest Brownian motion signal. . . . .	127
5.3	Ratio of real and imaginary parts of the correlation integrated over frequencies near the mechanical resonant frequency. The data set is near zero detuning ( $\Delta = -0.03\kappa$ ). When the detuning is not exactly zero, the ratio depends on the heterodyne angle. The optimal fit gives a calibration of $\theta_g = 5.566$ . A value of $\theta_g = 5.55$ , determined from an earlier analysis, is used in all subsequent analysis of correlation data for all detunings. Both estimates of $\theta_g$ are consistent with a 2% uncertainty in $\kappa$ . . . . .	129
5.4	Plot of the cavity's complex-valued reflection coefficient as a function of laser frequency, $r[\omega_{\text{laser}}]$ . The data is shown for just one sweep of the carrier laser frequency through the cavity's resonance. The three colors represent the carrier (blue) and two phase modulation sidebands (red and green). The theoretical reflection coefficient for the case of a lossless, symmetric cavity is shown for comparison (black solid line). . . . .	131

5.5	Reflected phase and amplitude vs laser detuning. Fits are solid lines, dots are data. Blue shows the carrier, which is the largest signal with best signal-to-noise ratio. Red and green are the phase modulation sidebands at $\pm 1$ MHz from the carrier. . . . .	132
5.6	Plot of the phase shift of the reflected signal beam measured using the heterodyne detection. The measured data (blue dots) agrees best with the red theory curve using parameters $\kappa = 4.45 \times 10^6 \text{ s}^{-1}$ and $\kappa_L = 0.132\kappa$ . The green theory curve uses $\kappa = 4.45 \times 10^6 \text{ s}^{-1}$ and $\kappa_L = 0.155\kappa$ , which were determined from the data shown in Figs. 5.4 and 5.5. . . . .	134
5.7	Comparison of the detuning as estimated by the ratio of the power in the upper and lower mechanical motion-induced sidebands ( $x$ -axis) and as estimated by the carrier heterodyne phase shift $\alpha_{\text{carrier}}$ ( $y$ -axis). . . . .	136
5.8	Power spectral densities of the Brownian motion of the membrane for three detunings. As the detuning becomes increasingly negative, the linewidth increases and the resonant frequency shifts due to optical damping and the optical frequency shift. . .	138
5.9	Resonant frequency drift of the membrane over an hour of measurements. Two data sets near zero detuning (meaning the optomechanical frequency shift was also zero) were chosen as the two points to define the uniform drift estimate (green dashed line). The laser became unlocked from the cavity at times labeled “Lost Lock.” . . .	139
5.10	Measured optical damping and frequency shift as a function detuning. The theory curve has one free parameter, the distance of the membrane from a node of the intracavity field, which was difficult to determined experimentally. This parameter essentially sets the strength of the optomechanical coupling, and the best fit value was 12 nm. A value between 5 and 15 nm was expected. There was a drift in the resonant frequency during the measurement. The green frequency drift data has had a uniform drift subtracted, as is detailed in Fig. 5.9. . . . .	139

5.11	Measured real part of the correlation $R[\omega] = \text{Re}S[\omega]$ for different heterodyne quadratures. When the heterodyne quadrature angle is chosen to be the critical quadrature, the real part of the correlation is substantially reduced. The resonant frequency $f_m = 783.723$ kHz. . . . .	141
5.12	Plot of the measured critical quadrature as a function of detuning. The theoretical prediction that $\theta_C = \arctan(2\Delta/\kappa)$ is plotted as the blue dashed line. The blue circle data points represent the heterodyne quadratures which minimized the real part of the correlation $R[\omega]$ . A similar relationship can be measured for the imaginary part of the correlation, and the theory (dashed line) and data (circles) is plotted in red. . . . .	142
5.13	(A) The theoretically expected profile of the real part of the correlation $R[\omega]$ at the critical quadrature for a detuning of $\Delta \approx -0.037\kappa$ . (B) The dashed line is a plot of the theoretical expectation for the real part of the correlation at $\theta_C + \pi/2$ in the limit of an infinite measurement time. This is the quadrature that maximizes the correlation due to Brownian motion, and is used to calibrate the scale of the measured correlation data (shown in red). (C) Measured real part of the correlation $R[\omega]$ at critical quadrature $\theta_C$ . The vertical axis is in the same units as the top plot, showing that there are still fluctuations about $10^4$ times larger than the desired quantum signal. . . . .	145
5.14	Plot of the Brownian motion in transmission. The dark noise of the transmitted detector is a factor of $5 \times 10^4$ larger than the estimated shot noise for a power of 800 nW incident upon the detector. The dark noise was measured using an unlocked and far-detuned data set with no transmission. The specified photodiode dark noise is $4 \times 10^{-15} \text{ V}^2/\text{Hz}$ . The total dark noise in the transmission detection scheme was a factor of 30 larger than the specified dark noise of the photodiode indicating additional noise was added after the photodiode. The detuning for the locked near-resonance transmission data (blue and dashed green) was $\Delta = -0.037\kappa$ . . . . .	146

# List of Symbols

$c$	speed of light
$F$	finesse of cavity
$I$	intensity, energy flux of light
$k$	spring constant
$k$	wave number $k = \omega/c$ . Usually shows up in exponents like $e^{ikz}$
$k_B$	Boltzmann's constant
$m$	mass
$n_m$	phonon number of mechanical resonator
$\bar{n}_m^O$	minimum phonon number reachable by optomechanical cooling
$\bar{n}_{th}$	thermal phonon number (before any optical damping)
$p$	momentum
$P$	optical power
$P_{in}$	optical power incident on a cavity
$Q$	mechanical quality factor of a mechanical resonator
$r_i$	amplitude reflection coefficient for mirror $i$ .

$R_i$	power reflection coefficient for mirror $i$ . $R_i =  r_i ^2$
$S_F^{\text{th}}[\omega]$	Force power spectral density of the Langevin force [force <sup>2</sup> /Hz]
$S_F^{\text{sn}}[\omega]$	Force power spectral density of the RPSN [force <sup>2</sup> /Hz]
$S_x^{\text{imp}}[\omega]$	Position imprecision power spectral density (does not include measureback action)
$S_x^{\text{sn}}[\omega]$	Power spectral density of the position error due to radiation pressure shot noise (i.e. back action)
$S_x^{\text{th}}[\omega]$	Power spectral density of the thermal (Brownian) motion
$S_x^{\text{tot}}[\omega]$	Power spectral density of the total position error $S_x^{\text{tot}} = S_x^{\text{imp}} + S_x^{\text{sn}} + S_x^{\text{th}}$
$t_i$	amplitude transmission coefficient for mirror $i$ .
$T_i$	power transmission coefficient for mirror $i$ . $T_i =  t_i ^2$
$\gamma$	energy decay rate (damping constant) of a mechanical harmonic oscillator in units of angular frequency[s <sup>-1</sup> ]
$\gamma_{\text{opt}}$	optomechanical damping
$\eta^{\text{th}}(t)$	Langevin force [force]
$\kappa$	Full cavity linewidth. Same as energy decay rate from cavity.
$\lambda$	wavelength of light
$\omega_m$	mechanical resonant frequency

# Acknowledgments

When I arrived at Yale as a beginning graduate student, I was eager to discover the secrets of the quantum world. Lucky for me, Jack Harris joined the faculty and already had plans for how to discover these secrets. Thank you, Jack, for taking me on as a graduate student. I owe 98 percent of my training as an experimental physicist to Jack and to the various post-docs, graduate students, and undergrads with whom I have worked. It was a pleasure and honor to work in the lab with such good people. I especially want to extend a hearty “thank you” to Andrew Jayich, Cheng Yang, Nathan Flowers-Jacobs, Jack Sankey, and Jeff Thompson, with whom I have worked closely during various phases of our research in cavity optomechanics. I am excited to follow their future progress in optomechanics, continuing and/or finishing projects which keep pushing cavity optomechanics closer to the quantum regime of light and mechanics. Although our overlap was shorter I wish the best to Scott Hoch and Israel Kositsky. I also want to thank those fine folks in SPL 16 who convinced me electrons really can keep on moving in a normal metal without slowing down: Will Shanks, Ania Bleszynski Jayich, Manuel Castellanos-Beltran, and Dustin Ngo. I owe much to Will’s organizational prowess, including the LyX dissertation template and the many seasons he served as local commissioner of fantasy college football.

Kjetil Børkje, Andreas Nunnenkamp, and Steve Girvin were great theoretical collaborators, and their ideas gave a lot of direction to this project. Børkje et al. is by far the most cited paper in this dissertation. Also, thanks to my dissertation committee: Jack Harris, Steve Girvin, Dave DeMille, Sean Barrett, and Nergis Mavalvala. You are the last line of defense protecting the world from Dr. Benjamin Zwickl.

Also, I owe a lot to the patience of my current employer, Heather Lewandowski at the University

of Colorado Boulder, who hired me without a PhD. I love working in science education, so thank you, Jack, for mentioning to Heather that I was looking for post-docs in science education.

The only people more patient than Heather are my wife Jill (soon to be a PhD in Chemistry) and our kids Henry and Violet. We have yet to spend a weekend in the mountains as I have worked on this dissertation for at least part of every weekend for many, many months. It is time to take a hike. Also, I must thank Jill for being my primary editor. She made the dissertation much more readable, though I take full credit for any remaining mistakes. Thank you so much, Jill, for your support and encouragement. I love you guys.

Finally, thanks to all the other friends and family who supported, prayed, and encouraged me that yes, one day, I would probably finish this thing...

*Great are the works of the Lord, studied by all who delight in them. Psalm 111:2*

# Chapter 1

## Introduction to radiation pressure shot noise and quantum limited measurement

### 1.1 History

The story of radiation pressure, the mechanical force that light exerts when it is reflected or absorbed by an object, spans almost 400 years, starting with Johannes Kepler's guess that it causes particles around a comet to be pushed into a tail pointing away from the sun. Today, astronomers attempting to observe gravitational waves understand that radiation pressure sets limits on the sensitivity of their kilometer-long gravitational wave antennae. In fact, the quantum nature of the radiation pressure is required to explain both comet tails and quantum-limited gravitational wave interferometers. The research described in this dissertation is an experimentalist's attempt to observe quantum fluctuations in the radiation pressure, which we call radiation pressure shot noise. I will begin by tracing the development of these ideas from Kepler to the present day.

#### **Classical radiation pressure**

The warmth of sunlight on the skin is sufficient evidence that light carries energy, but does this mean it also has momentum? It seemed reasonable that upon absorption or reflection it may impart some force, called radiation pressure. The question was, how large should this force be?

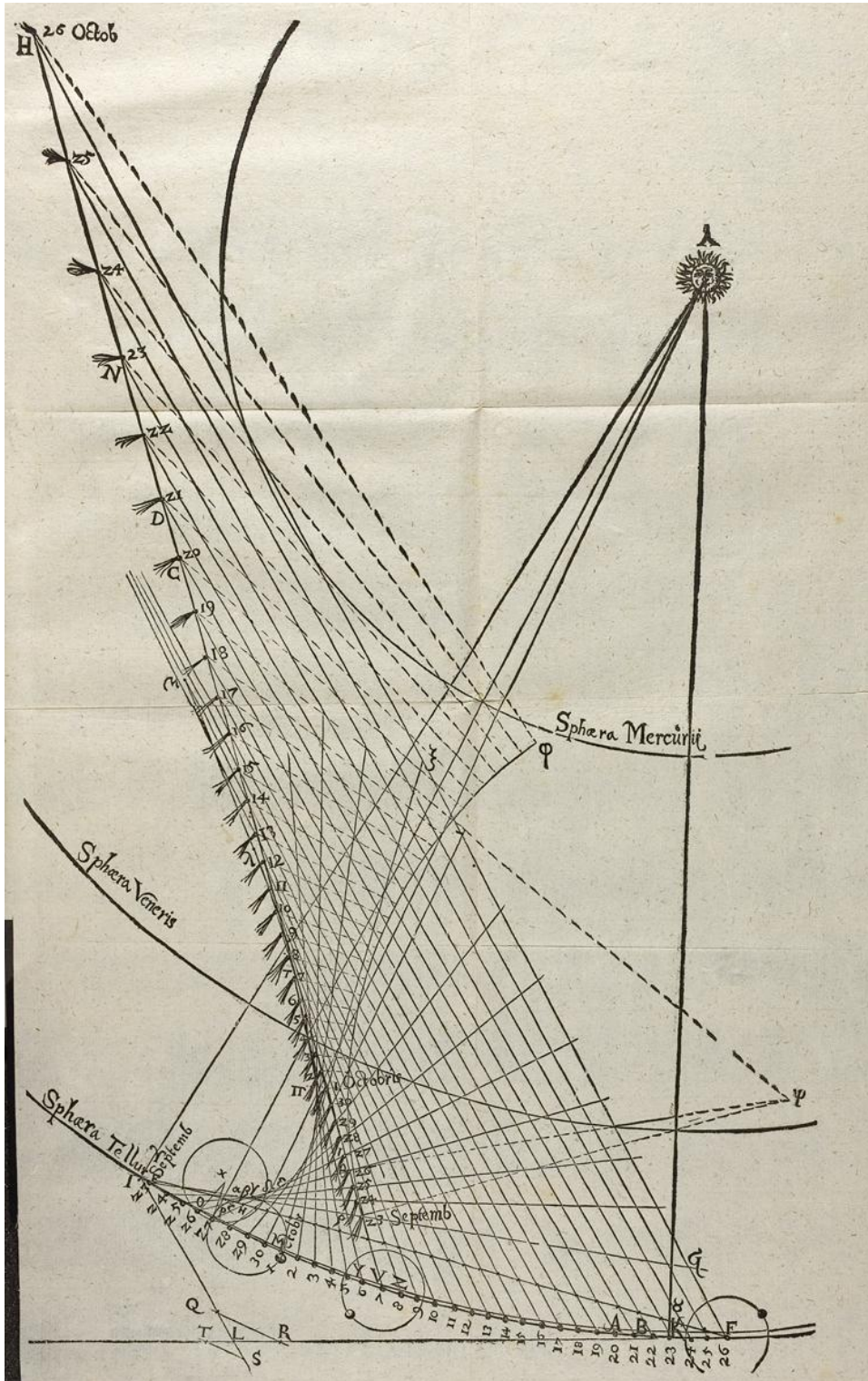


Figure 1.1: A comet's trajectory as drawn by Kepler in *De Cometis Libelli Tres* (1619). Note the comet tail is always facing away from the Sun. (Used with permission from UCL Library Services, Special Collections)

Certainly the force of light is smaller than a person can feel under normal circumstances. The first observation of radiation pressure was described by Kepler in 1619 [5]. He noted that comets have tails which point directly away from the sun, as shown in Fig. 1.1, and proposed that radiation pressure was the cause.

What did theory suggest for the magnitude of the radiation pressure? Euler showed in 1746 that a longitudinal wave could impart momentum on an object in its path [6], and by 1803 the wave theory of light seemed well established by Young's double slit experiment [7]. So it seemed plausible that light waves could exert forces on objects. However, there was still no hint at the magnitude of this force. It was not until 1873 that Maxwell demonstrated that radiation pressure was a direct consequence of his equations of electricity and magnetism, and gave a precise theoretical prediction for its magnitude [8].

Maxwell's relationship between the momentum flux (i.e. the momentum per unit time per unit area)  $\vec{P}_{\text{rad}}$  of the electromagnetic field and the energy flux  $\vec{S}$  can be written as

$$\vec{P}_{\text{rad}} = \frac{1}{c} \vec{S} \quad (1.1)$$

where  $\vec{S} = \frac{1}{\mu_0} (\vec{E} \times \vec{B})$  and  $\vec{E}$  and  $\vec{B}$  are the electric and magnetic fields,  $c$  is the speed of light, and  $\mu_0$  is the permeability of free space. The energy flux  $\vec{S}$  is also called the Poynting vector, and its magnitude is equal to the intensity  $I = |\vec{S}|$ .

Einstein derived Maxwell's relationship between the intensity of light and radiation pressure (Eq. 1.1) in his 1905 article about special relativity *On the electrodynamics of moving bodies* [9]. Einstein compared the flux of electromagnetic energy in a light beam before and after it reflects off a moving mirror. The difference in energies is attributed to work done by a radiation pressure on the mirror.

Another simple relativistic derivation of Eq. 1.1 is illustrated by noting that for all massless particles which travel at the speed of light, we can relate the momentum  $p$  and energy  $E$  by

$$p = \frac{1}{c} E \quad (1.2)$$

If instead of a single particle we have a flux of particles, the momentum  $p$  turns into a momentum flux  $P_{\text{rad}}$ , and the energy  $E$  turns into an energy flux (intensity)  $I$ , and we get the same result as Eq. 1.1. A third derivation, given by Bartoli in 1876, derived Maxwell’s radiation pressure result without any detailed assumptions about the electromagnetic field, but rather as a thermodynamic process where radiant energy is transferred from a warm body to a cold body by moving mirrors [10].

The momentum of light as described by Maxwell (Eq. 1.1) or Einstein (Eq. 1.2) becomes radiation pressure when the light is absorbed or reflected by a surface. For a perfectly absorbing surface the reflectivity  $R$  is zero, and all the momentum of the light is transferred to the object. For a perfectly reflective surface  $R = 1$ , twice the momentum of light is transferred to the object. In general, for a reflectivity  $0 \leq R \leq 1$

$$F = \frac{1 + R}{c} P \tag{1.3}$$

where  $F$  is the force on the surface and  $P$  is the power of light incident on the surface.

For a perfect reflector  $R = 1$ , the proportionality constant has a numerical value of  $6.67 \times 10^{-9}$  W/m. To put this number in perspective, consider the optical force that could be produced by an ordinary 150 Watt household light bulb. Typical incandescent light bulbs have an efficiency of 3% or less, meaning there is at most 5 W of visible light. If this light could be collected and collimated, it could produce a force upon reflection of  $F = 2P/c = 2 \times 5 \text{ W} / 3 \times 10^8 \text{ m/s} \approx 3 \times 10^{-8}$  N. If this force was directed in opposition to gravity it could suspend a maximum mass of about  $3 \times 10^{-9}$  kg, which is the mass of a water droplet of about 100  $\mu\text{m}$  diameter. Maxwell, in his *Treatise on Electricity and Magnetism* [8], also endeavored to put this in everyday terms, writing, “the mean pressure [of strong sunlight] on a square foot is 0.0000000882 of a pound.” Because radiation pressure is an extremely small effect, it played no role in everyday experience, and was even difficult to observe in early laboratories.

Both before and after Maxwell’s prediction, many experimental attempts were made to measure the radiation pressure. Until 1901 all were inconclusive. Large systematic errors were commonplace due to interactions with gas surrounding the force detectors [11, 12]. This was the case for the

famous Crookes radiometer (a.k.a. a light mill) [13–18], which is available for sale at most scientific curiosity stores.

The first convincing measurement of radiation pressure used a torsion pendulum suspended in a partial vacuum. The measurements, first published in 1901 by Lebedev [1] and Nichols and Hull [19], did not offer sufficient accuracy to verify Maxwell’s theoretical result (Eq. 1.1). However, by 1903 Nichols and Hull had sufficiently improved their setup to achieve a result within about twenty percent of the theoretical prediction and within their expected error [2]. The 1901 and 1903 papers by Nichols and Hull are very readable and offer a more detailed history of radiation pressure for the interested reader. Lebedev later went on to study the effect of radiation pressure on gases, putting Kepler’s theory of comet tails on a firmer foundation [20].

## **Radiation pressure and early quantum mechanics**

So far we have not considered the role of quantum mechanics in radiation pressure. In the early 1900s two important papers were published concerning the quantization of energy in light. In 1901 Planck published his work on quantization of radiation to account for the spectrum of black body radiation [21], and in 1905 Einstein published his explanation of the photoelectric effect using quantized packets of light [22]. Campbell, in 1909, realized that quantization of light implies any source of light should have random power fluctuations [23, 24]. He assumed that quanta of light were emitted independently by different atoms at random times, like a Poisson process. When the light is detected, there should be fluctuations about the mean power, which in modern physics parlance is called shot noise. He estimated the magnitude of these quantum fluctuations and devised a scheme to measure them. Unfortunately the noise in his measurement was larger than the fluctuations due to shot noise, but he published his null result anyway [23].

One of the first papers clearly linking radiation pressure and quantum mechanics was published in 1919 by Megh Nad Saha. In *On Radiation-Pressure and the Quantum Theory* [25], Saha argues that a classical picture of light waves scattering off gaseous molecules is inadequate to explain Lebedev’s observations of radiation pressure on gases. He claims classical theory would result in a negligible momentum transferred to all the gas molecules, whereas Lebedev’s data show the

gas molecules receive a measurable push from the light. He then claims only a theory of light where momentum comes in discrete chunks equal to  $h\nu/c$  would be consistent with experimental and astronomical observations of comet tails. Saha's argument sounds like the momentum analog of Einstein's explanation of the photoelectric effect. A classical prediction for the photoelectric effect suggests for modest intensities it would take a very long time for light to transmit sufficient energy to an atom to liberate an electron. In reality even the weakest beams of sufficiently short wavelength will immediately liberate electrons from the surface. Saha claims a similar calculation of the radiation pressure on gas molecules predicts Lebedev's observations should have required far greater intensities than were actually used. One effect Saha seems to neglect is that while the geometric cross-section for an atom is roughly the square of its diameter or  $\sigma_{\text{geo}} \simeq 10^{-19}$ , the cross-section to radiation can be much higher. For example, the cross-section of an atom to radiation resonant with the transition is  $\sigma(\omega_0) \simeq (\lambda/2)^2 \simeq 10^{-13}\text{m}$ , or roughly a million time larger than the geometric cross-section. What is clear is that Saha recognized that quantum mechanics would change the nature of radiation pressure, and he was looking for evidence of the quantization of momentum.

The quantized momentum of light was convincingly verified in 1923 by Compton in his experiments scattering gamma rays off lightweight gas atoms and molecules [26]. Now both radiation pressure and quantum theory had firm experimental footing.

## Radiation pressure after the laser

The laser ushered in a new era of optics. Compared to earlier light sources, the laser offered a very narrow linewidth, which enabled long-distance interferometry, more than one quantum in a mode, which is essential for quantum optics, and extremely high intensities needed for nonlinear optics. Furthermore, the theoretical description of a laser and its coherent interaction with matter required a quantum picture that advanced the field of quantum optics .

With the advent of the laser, and the surprising correlations found in Hanbury Brown and Twiss interferometry [27], noise turned from a nuisance to a property of light that could uncover quantum features of radiation. The role of noise and statistics in understanding light is significant enough

that Roy Glauber was awarded the 2005 Nobel Prize in Physics for its theoretical description.

Radiation pressure also entered a new era. The same high intensities and narrow linewidths which made nonlinear optics possible also enabled the observation of radiation pressure effects in optical cavities [28]. In addition, the well-defined mode shapes imposed by laser cavities enabled intense diffraction-limited focusing patterns useful for the manipulation and trapping of particles through radiation pressure, a technique known as optical tweezers [29]. The laser became an enabling device in many fields, including the study of shot noise and radiation pressure, and in the near future will enable the measurement of radiation pressure shot noise (RPSN).

## Simple derivation of shot noise

When light of power  $P$  is incident on a photodiode, the average number of photons of frequency  $\omega$  which hit the detector in a short time  $dt$  is

$$N = \frac{P}{\hbar\omega} dt \quad (1.4)$$

However, these photons arrive at random times which are not correlated with the arrival of any other photon. This kind of process is called a Poisson process, and has the special relationship between the mean value  $N$  and the standard deviation  $\sigma_N$

$$\sigma_N = \sqrt{N} \quad (1.5)$$

The standard deviation of power  $\sigma_P$  is

$$\begin{aligned} \sigma_P &= \frac{\sigma_N}{dt} \hbar\omega \\ &= \sqrt{\frac{P dt}{\hbar\omega}} \frac{\hbar\omega}{dt} \\ &= \sqrt{\frac{P \hbar\omega}{dt}} \end{aligned} \quad (1.6)$$

Poisson processes are composed of many independent events and the power spectral density of the fluctuations are white (i.e. the same for all frequencies). Only fluctuations in the power at frequencies below the Nyquist frequency  $\omega_{\text{Nyquist}} = 1/(2dt)$  contribute to the noise measured in a time  $dt$  since the faster fluctuations average to zero. So the variance in measured power  $\sigma_P^2$  over a time  $dt$  is

$$\sigma_P^2 = \int_{-\omega_{\text{Nyquist}}}^{\omega_{\text{Nyquist}}} S_P d\omega \quad (1.7)$$

where  $\sigma_P$  the power spectral density  $S_P$  is a constant. Combining Eqs. 1.6 and 1.7 gives

$$\frac{P\hbar\omega}{dt} = \frac{2}{2dt} S_P \quad (1.8)$$

We then finally arrive at the shot noise expressed in the frequency domain as a power spectral density

$$S_P^{\text{sn}}[\omega] = \hbar\omega P \quad (1.9)$$

Because the integral in Eq. 1.7 goes from  $\omega = -\omega_{\text{Nyquist}}$  to  $\omega = \omega_{\text{Nyquist}}$ , the power spectral density  $S_P^{\text{sn}}[\omega]$  given in Eq. 1.9 is a double-sided PSD. All power spectral densities in this dissertation will be given as double sided. The main goal of this derivation is to show a simple connection between the Poissonian relationship  $\sigma_N = \sqrt{N}$  and the frequency domain result  $S_P^{\text{sn}}[\omega] = \hbar\omega P$ .

When light reflects off of a perfect mirror  $R = 1$ , there are fluctuations in the force due to shot noise. This is called radiation pressure shot noise (RPSN). The conversion between Watts and Newtons is  $\frac{2}{c}$  (Eq. 1.3) so

$$S_F^{\text{sn}} = \left(\frac{2}{c}\right)^2 S_P^{\text{sn}} \quad (1.10)$$

$$= \frac{4\hbar\omega P}{c^2} \quad (1.11)$$

To put the radiation pressure shot noise in perspective, consider the more commonly discussed random force which drives Brownian motion, often called the Langevin force. The Langevin force

$\eta^{\text{th}}(t)$  for a simple harmonic oscillator with equation of motion  $m\ddot{x} + m\gamma\dot{x} + kx = \eta^{\text{th}}(t)$  has a power spectral density of

$$S_F^{\text{th}}[\omega] = 2\gamma m k_B T \tag{1.12}$$

where  $\gamma$  is the mechanical linewidth,  $m$  is the mass,  $k_B$  is Boltzmann's constant, and  $T$  is the temperature.

For the kinds of devices discussed in this dissertation (i.e. silicon nitride membranes at room temperature), the ratio of the radiation pressure shot noise to the Langevin force for 1 Watt of light is  $S_F^{\text{sn}}/S_F^{\text{th}} \approx 10^{-9}$ . So a hundred years after Nichols and Hull first measured the mean radiation pressure, the problem remains that our force sensor is coupled to the environment, and the thermal effects obscure the force of interest.

The remainder of this dissertation is organized as follows:

- The rest of Ch. 1 will discuss various manifestations of the radiation pressure shot noise and its relation to quantum limited measurement.
- Ch. 2 introduces the basic mathematical formalism of cavity optomechanics.
- Ch. 3 describes a scheme to observe RPSN in the presence of a relatively large thermal force.
- Ch. 4 describes the experimental design.
- Ch. 5 gives some preliminary data.

## 1.2 Quantum limited measurement

In the history of radiation pressure, RPSN is important because it limits the ultimate precision of optical interferometric displacement measurements. On the smallest scale, such an interferometric measurement could be the position readout from an atomic force microscope (AFM). On the largest scale it could be a measurement of the distance between test masses kilometers apart in a gravitational wave antenna like those used in the Laser Interferometer Gravitational-Wave Observatory (LIGO). When considering the incredibly small displacements due to gravitational waves, it

is natural to ask what is the smallest detectable oscillation of the LIGO test masses.

Remarkably, much of the early work done on quantum limited measurement was motivated by gravitational wave astronomy. Only kilometer long interferometers measuring at the quantum limits are likely to have the sensitivity to see the feeble ripples in space-time emitted from distant celestial objects like orbiting binary black holes.

A variety of noise sources limit the sensitivity of systems like an AFM or LIGO. Mechanical vibrations of the lab, known as *seismic noise*, are one source of error. Electronic noise in detectors and bit noise in analog to digital converters are examples of *technical noise* which comes in many forms. Brownian motion of the mirrors in an interferometer, Johnson noise in resistive circuits, and thermally stimulated radio frequency and microwave phonons are all kinds of *thermal noise*, which result from the system being at a finite temperature. Seismic and technical noise sources can be reduced through improved engineering. Thermal noise can be reduced by cooling the system using refrigerators or other cooling schemes.

There is a final source of noise, due to quantum mechanics, which cannot be avoided. The mathematical structure of quantum mechanics necessitates certain limits of measurement, and a measurement done so carefully as to bump up against one of these limits is called a quantum limited measurement. Quantum measurement error has two sources. The first source of error is due to the intrinsic uncertainty of the quantum state being measured. For example the uncertainty  $\sigma_A$  of some observable  $\hat{A}$  for the state  $|\psi\rangle$  would be

$$\sigma_A^2 = \text{Var } A = \langle \psi | \left( A - \langle \psi | \hat{A} | \psi \rangle \right)^2 | \psi \rangle \quad (1.13)$$

This is the kind of quantum uncertainty learned about in an introductory quantum mechanics class [30]. The second source of error is due to the measurement scheme, which itself can have quantum properties and add further noise. For an optical detection scheme, this second source of error includes both the statistical imprecision and the measurement back action, because both result from the quantum nature of the measurement tool, and not the object whose displacement is being measured. This kind of error is not typically studied in an introductory quantum mechanics

class.

### 1.3 Examples of quantum limited measurements

The most famous equation in quantum mechanics is the Heisenberg uncertainty equation, shown below for the canonically conjugate variables position  $x$  and momentum  $p_x$

$$\Delta x \Delta p_x \geq \hbar/2 \tag{1.14}$$

It is simple to write down, yet surprising because classically it is unexpected that the uncertainty in these two variables should be related, and that they can't be made arbitrarily small at the same time.

There are several ways to motivate or derive Heisenberg's uncertainty principle. The sophomore physics major may see a justification of the principle by starting with the general inequality for waves:  $\Delta x \Delta k \geq \frac{1}{2}$ . Applying the DeBroglie relation, which says the wave number and momentum are directly proportional (i.e.  $k \equiv \frac{2\pi}{\lambda} = \frac{p}{\hbar}$ ) immediately gives the uncertainty principle. The junior physics major will see a derivation of the equation using operator algebra [30]. In all cases the uncertainty in the measurement is determined by the state of the particle or system being observed, and it must obey the Heisenberg uncertainty principle.

#### Heisenberg's microscope

Heisenberg offered his own intuitive understanding of the uncertainty principle in the form of a gamma ray microscope used to locate an electron by scattering one gamma ray at a time from the electron [31] (see Fig. 1.2). The basic idea is that while the focusing of the lens allows us to spatially resolve the location of the electron, the scattered gamma ray has an uncertainty in momentum because a spread of scattering angles all focus to the same point on the CCD camera. Thus the electron has an uncertainty in its momentum after the measurement. More quantitatively, diffraction of light of wavelength  $\lambda$  by the lens aperture  $\theta$  means the focused light on the camera

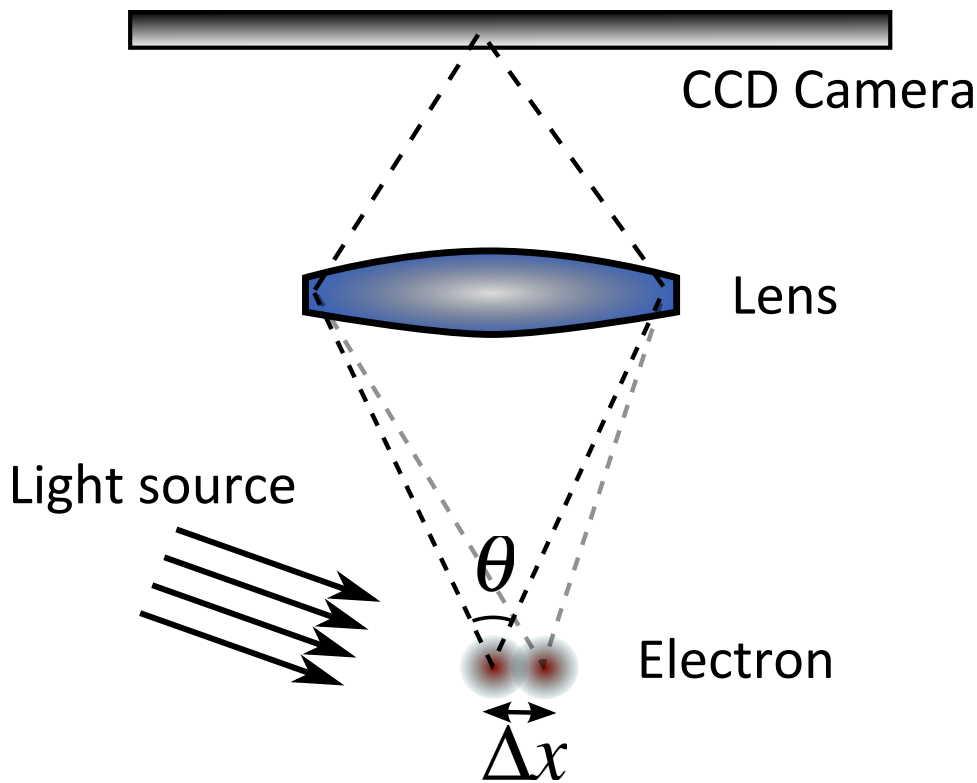


Figure 1.2: Heisenberg's Microscope offers an intuitive origin for the uncertainty relationship. A photon scatters off of an electron and is focused by a lens onto a CCD camera. The aperture of the lens limits the position resolution  $\Delta x$ , while the uncertain direction of the photon recoil causes an uncertainty in the photon's momentum  $\Delta p_x$ , satisfying  $\Delta x \Delta p_x \sim h$ .

has a spatial resolution of

$$\Delta x \approx \frac{\lambda}{\sin \theta} \quad (1.15)$$

while the uncertainty in the  $x$ -component of the momentum is

$$\Delta p_x \approx \frac{h}{\lambda} \sin \theta \quad (1.16)$$

The relative uncertainties in the position and momentum roughly satisfy the uncertainty principle

$$\Delta x \Delta p_x \approx h \quad (1.17)$$

The uncertainty principle is seen not as some intrinsic property of the electron, but of the quantum nature of the measurement tool, which is a gamma ray photon in this example. This argument requires no assumptions about the quantum nature of the electron.

## Interferometric displacement measurements

Very long interferometers make natural candidates for gravitational wave antennae. Interferometers of any length offer very sensitive position resolution. However, the effect of the gravitational wave is in proportion to the length of the interferometer, encouraging the design of kilometer-long interferometers such as LIGO. Even LIGO is expected to undergo extremely small length changes on the order of  $10^{-18}$  m when a gravitational wave passes by. It is necessary to figure out if such precise measurements can be made when considering the error imposed by quantum mechanics. The answer was worked out by Caves [32] and others. Quantum limited measurement in gravitational wave detectors is very important to astronomers, and also provides intuition for the role of radiation pressure shot noise in quantum limited measurement.

Consider now a displacement measurement of a movable mirror as part of the interferometer shown in Fig. 1.3. The powers of the incident, reflected, and transmitted beams are  $P_{\text{in}}$ ,  $P_{\text{refl}}$ , and  $P_{\text{trans}}$  respectively. As the distance between the mirrors (i.e. cavity length) changes, the transmitted power  $P_{\text{trans}}$  also changes. Any fluctuations in  $P_{\text{trans}}$  will be inferred as displacements of the end mirror. However, not all fluctuations in  $P_{\text{trans}}$  are actually due to changes in the mirror's position. Noise in the incident laser beam, such as shot noise, can also cause fluctuations in  $P_{\text{trans}}$ . These fluctuations will be observed in  $P_{\text{trans}}$  independent of the mirror's motion.

If the laser has no noise other than shot noise (also called shot noise-limited), then the double-sided power spectral density of the displacement measurement imprecision  $S_x^{\text{imp}}[\omega]$  for a on-resonance Pound-Drever-Hall measurement is

$$S_x^{\text{imp}}[\omega] = \frac{\pi \hbar c \lambda}{64 P_{\text{in}} F^2} \quad (1.18)$$

where the fluctuations are assumed to be slower than the cavity linewidth ( $\omega \ll \kappa$ ),  $\lambda$  is the laser wavelength, and  $F$  is the cavity finesse [33]. However, shot noise also affects the intracavity intensity, which creates random fluctuations in the radiation pressure on the mirror. The power spectral density of these force fluctuations due to shot noise is derived in Sections 2.8 and 2.10. In the case that the input laser is on resonance with the cavity and we only consider fluctuations much

slower than the cavity linewidth ( $\omega \ll \kappa$ ), then  $S_F^{\text{sn}}[\omega]$  is given by

$$S_F^{\text{sn}}[\omega] = \frac{16\hbar P_{\text{in}} F^2}{\pi c \lambda} \quad (1.19)$$

The following relationship naturally emerges:

$$S_x^{\text{imp}} S_F^{\text{sn}} = \frac{\hbar^2}{4} \quad (1.20)$$

This formula is still the Heisenberg uncertainty relationship, but it is written in a form appropriate for continuous measurements and involves power spectral densities rather than variances  $\sigma_x$  and  $\sigma_{p_x}$ . It is continuous because the position  $x$  is continually monitored in time. While it is sufficient to describe a single measurement by its mean and standard deviation (and possibly higher order moments), a continuously measured quantity calls for a continuous distribution (like the power spectral density) to describe its uncertainty. The exact form of the Heisenberg uncertainty relation for continuous measurements is

$$S_x^{\text{imp}} S_F \geq \frac{\hbar^2}{4} \quad (1.21)$$

(see Ref. [34] or Ch. 6 of Ref. [35] )

Again, in a manner similar to the Heisenberg microscope, we derive a formula very similar to the Heisenberg uncertainty relation. It is not a statement about intrinsic properties of the movable mirror, but rather about the quantum nature of the measurement process. In fact, the quantity  $S_x^{\text{imp}}$  does not represent the full measurement uncertainty in the mirror's position, but only the statistical uncertainty due to shot noise. The displacement imprecision can be made arbitrarily small by increasing the incident laser power  $P_{\text{in}}$ , as can be seen in Eq. 1.18 where  $S_x^{\text{imp}} \rightarrow 0$  as  $P \rightarrow \infty$ . At first glance this may seem to indicate that the position measurement can be made arbitrarily accurate, but this is not so as the next section will discuss.

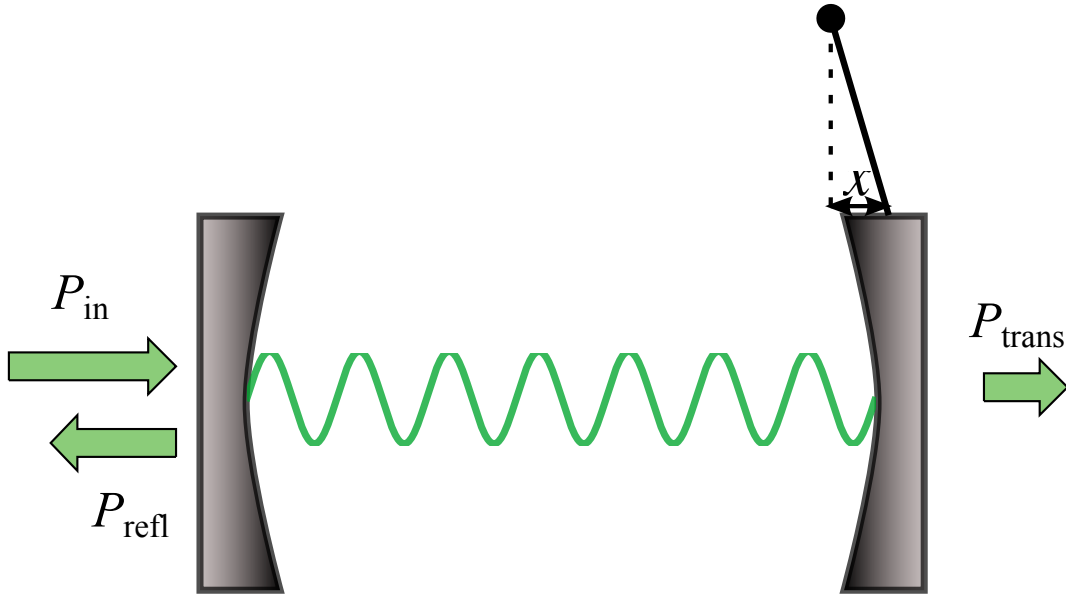


Figure 1.3: Optical cavity with a movable end mirror.

## 1.4 Standard quantum limits

In both the Heisenberg microscope and the optical cavity with a movable end mirror, the measurement probe perturbs the momentum of the electron or end mirror, respectively. This perturbation in momentum, also called *back action*, causes additional fluctuations in the displacement. As the imprecision of the measurement  $S_x^{\text{imp}}$  becomes very small, the back action  $S_F^{\text{back action}}$  becomes very large. When both the imprecision and back action are considered as sources of error in  $x$ , we find there is a minimum total measurement uncertainty, called the *standard quantum limit* (SQL). The standard quantum limit of a displacement measurement of a harmonic oscillator is derived below. A version of the standard quantum limit can also be derived for Heisenberg's microscope (see Ref. [35]).

### SQL of a harmonic oscillator

In a continuous measurement of cavity transmission as in Fig. 1.3, the full measurement error in position has two sources (excluding technical and thermal noise). The first, discussed in Sec. 1.3,

is the measurement imprecision. The second is the measurement back action,

$$S_x^{\text{back action}}[\omega] = |\chi[\omega]|^2 S_F^{\text{back action}}[\omega] \quad (1.22)$$

where

$$\chi[\omega] = m^{-1} (\omega^2 - \omega_m^2 - i\omega\gamma)^{-1} \quad (1.23)$$

$$\approx (2m\omega_m)^{-1} (\omega - \omega_m - i\gamma/2)^{-1} \quad (1.24)$$

is the mechanical susceptibility of an end mirror with mass  $m$ , resonant frequency  $\omega_m$ , and mechanical linewidth  $\gamma$ . The approximate form is for the limit of a mechanical quality factor  $Q \gg 1$ .

Applying the Heisenberg uncertainty principle (Eq. 1.21) gives a power spectral density for the measurement back action force of

$$S_F^{\text{back action}}[\omega] \geq \frac{\hbar^2}{4S_x^{\text{imp}}[\omega]} . \quad (1.25)$$

Combining the statistical and back action uncertainties we get a power spectral density for the total noise in position

$$S_x^{\text{tot}}[\omega] = S_x^{\text{imp}}[\omega] + S_x^{\text{back action}}[\omega] \quad (1.26)$$

$$\geq S_x^{\text{imp}}[\omega] + \frac{1}{4m^2\omega_0^2 ((\omega - \omega_0)^2 + (\gamma/2)^2)} \frac{\hbar^2}{4S_x^{\text{imp}}[\omega]} \quad (1.27)$$

The total error on resonance  $S_x^{\text{tot}}[\omega_m]$  is minimized when

$$S_x^{\text{imp}}[\omega_m] = \frac{\hbar}{2m\omega_m\gamma} \quad (1.28)$$

giving a minimum value for  $S_x^{\text{tot}}[\omega_m]$  of

$$\min(S_x^{\text{tot}}[\omega_m]) = \frac{\hbar}{m\omega_m\gamma} \quad (1.29)$$

This minimum uncertainty is the standard quantum limit

$$S_x^{\text{SQL}}[\omega_m] = \frac{\hbar}{m\omega_m\gamma} \quad (1.30)$$

Although the derivation of the SQL of a harmonic oscillator did not specify a particular measurement scheme, the interferometric scheme has a particularly intuitive interpretation in terms of the radiation pressure shot noise. For optical measurement schemes the back action error is error caused by the radiation pressure shot noise:

$$S_x^{\text{back action}}[\omega] = S_x^{\text{sn}}[\omega]$$

## 1.5 Physical manifestations of the radiation pressure shot noise

### Measurement with an imprecision below the SQL

Any measurement that can claim  $S_x^{\text{imp}} < S_x^{\text{SQL}}$  must be in the regime where  $S_x^{\text{perturb}} > S_x^{\text{imp}}$ . For optomechanical systems this means radiation pressure shot noise dominates the measurement imprecision. To date, two groups have published work demonstrating that they have achieved this regime. Teufel et al. used a nanomechanical beam as a tunable element in a microwave cavity and read out fluctuations in the cavity resonant frequency interferometrically [36]. They have demonstrated  $S_x^{\text{imp}} \approx 0.80S_x^{\text{SQL}}$ . Anetsberger et al. have evanescently coupled silica microtoroids to silicon nitride nanostrings and published displacement imprecisions of  $S_x^{\text{imp}} \approx 0.70S_x^{\text{SQL}}$  [37] and  $S_x^{\text{imp}} \approx 0.47S_x^{\text{SQL}}$  [38]. However, in all cases the total displacement sensitivity on resonance is dominated by thermally driven Brownian motion. In Teufel et al. the mechanical resonator with

$\omega_m = 2\pi \times 1.04$  MHz was cooled in a dilution fridge to 130 mK, or a mean phonon number of about 2600. The measurements of Anetsberger et al. are all at room temperature, so their SiN nanostrings with  $\omega_m \approx 2\pi \times 8$  MHz have a phonon occupation number of  $8 \times 10^5$ .

For comparison with our own earlier work at Yale, Thompson et al. demonstrated  $S_x^{\text{imp}} \approx 0.1S_x^{\text{SQL}}$  using a membrane in the middle cavity where the minimum, but  $S_x^{\text{imp}}$  occurred during significant laser cooling while  $S_x^{\text{SQL}}$  was determined using the bare damping membrane without laser cooling [39].

## RPSN as a limit to laser cooling of atoms and mechanical resonators

Another physical manifestation of the radiation pressure shot noise is that it sets a limit on the lowest possible temperature achievable by laser cooling. The RPSN is a random fluctuating force, which drives a small amount of motion, setting a lower bound on laser cooling [40–42]. More discussion of the relation between RPSN and the limit on laser cooling can be found in Sections 1.6 and 2.9.

The steady state state phonon number of an optically damped mechanical resonator is given in Ref. [40] as

$$\bar{n}_m = \frac{\gamma_m \bar{n}_{\text{th}} + \gamma_{\text{opt}} \bar{n}_m^O}{\gamma_m + \gamma_{\text{opt}}} \quad (1.31)$$

where  $\gamma_m$  and  $\gamma_{\text{opt}}$  are the intrinsic and optomechanical damping factors,  $\bar{n}_{\text{th}}$  is the thermal phonon number before laser cooling, and  $\bar{n}_m^O$  is the lowest achievable phonon number in the limit  $\gamma_{\text{opt}} \gg \gamma_m$ . Once the optical damping is much larger than the intrinsic damping ( $\gamma_{\text{opt}} \gg \gamma_m$ ), there is no additional cooling. Any additional energy loss from a larger damping is matched by an increase in radiation pressure shot noise, which drives the mechanical motion. Figure 1.4 shows a plot of Eq. 1.31.

For an optomechanical system with a mechanical resonant frequency  $\omega_m$ , a cavity decay rate of  $\kappa$ , and a detuning between the cavity and the cooling laser of  $\Delta$ , we can express the minimum achievable phonon number as

$$\bar{n}_m^O = -\frac{(\omega_m + \Delta)^2 + (\kappa/2)^2}{4\omega_m \Delta} \quad (1.32)$$

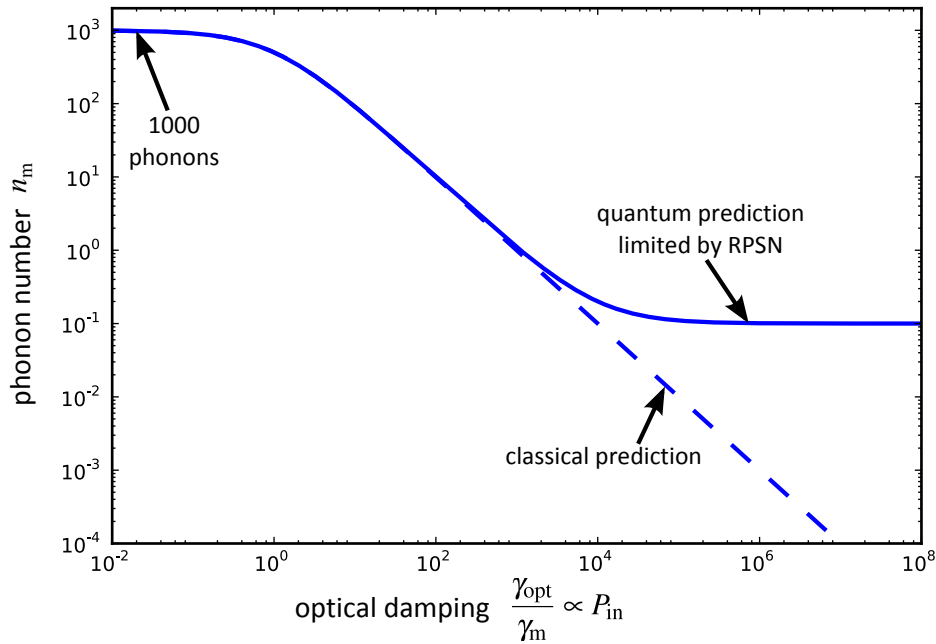


Figure 1.4: Phonon number as a function of the optical damping. For small optical damping (e.g. low laser powers) the phonon number was chosen to be 1000. A classical theory of laser cooling would predict the mean energy of the oscillator would decrease indefinitely, but the radiation pressure shot noise drives a small amount of motion limiting the lowest achievable phonon number. The solid curve is a theoretical plot of Eq. 1.31 with  $\bar{n}_{th} = 1000$  and  $\bar{n}_m^O = 0.1$ .

(see Ref. [40]). The role of quantum fluctuations in the momentum of light causes an analogous limit in the laser cooling of trapped atoms [43, 44].

## RPSN as a limit to linewidth of an optically driven, negatively damped mechanical resonator

Optical damping and laser cooling occur when the laser is red-detuned relative to the cavity resonance. If instead the laser is blue-detuned, the damping becomes negative and the mechanical oscillations will increase in amplitude until the response becomes nonlinear and restricts further increases in amplitude. In this blue-detuned, negative damping regime, the mechanical resonator oscillates with a linewidth much narrower than its natural linewidth. Radiation pressure shot noise imposes a limit on the minimum linewidth in this negative damping regime as determined by Valhala [45]. For instance, in the resolved sideband limit (i.e. the mechanical resonant frequency is

much larger than the cavity decay rate  $\omega_m \gg \kappa$ ) the minimum linewidth is

$$\Delta\omega_{\text{RS}} = \frac{\gamma}{2\bar{n}_c} (\bar{n}_{\text{th}} + 1) \quad (1.33)$$

where  $\gamma$  is the natural mechanical damping rate,  $\bar{n}_{\text{th}}$  is the thermal phonon number, and  $\bar{n}_c$  is the number of phonons in the negative damping steady state. Equation 1.33 shows that the thermal phonon number  $\bar{n}_{\text{th}}$  must be increased by one to account for the effect of the quantum fluctuations of the electromagnetic field. In limit of zero temperature, where  $\bar{n}_{\text{th}} \rightarrow 0$ , there is still a finite linewidth of  $\gamma/2\bar{n}_c$  due to RPSN.

## Observation of RPSN heating an ultracold atomic gas

Murch et al. have reported the observation of RPSN in the collective motion of an ultracold atomic gas trapped inside an optical cavity [46]. In this work, the optical cavity mode contains only a few photons and is far detuned from any atomic transitions of the ultracold atoms. The RPSN in the cavity mode provides random kicks to the ultracold gas, causing the gas to heat up and increasing the loss rate of atoms from the trap. They refer to the process as cavity enhanced diffusive heating.

## Quantum nondemolition measurement of intracavity photon number as a measurement of RPSN

When a movable mirror is displaced by radiation pressure, the mirror's position can be used to determine the power of the incident light. If the movable mirror is part of an optical cavity, then the mirror's position can be used to perform a quantum nondemolition (QND) measurement of the intracavity photon number, as first discussed by Jacobs et al. [47] and further developed by Pinard et al. [48] and Heidmann et al. [49]. Matsko and Vyatchanin considered QND measurements of an arbitrary quadrature of light using a Mach-Zendher interferometer scheme rather than the Fabry-Perot geometry used in the other proposals [50]. Any of these measurement schemes, if achieved, would allow for observations of the fluctuations in intracavity photon number as a direct consequence of the radiation pressure shot noise.

Although no one has yet made a QND measurement of intracavity photon number using optomechanical coupling, Verlot et al. have experimentally demonstrated a scheme which has all the features necessary for a QND measurement [51]. So far they have performed the measurement by adding classical noise to the laser in order to make the classical fluctuations in radiation pressure larger than the thermal fluctuations.

## Squeezing light and changing the RPSN

Some of the earliest work done in cavity optomechanics was in relation to the quantum limited measurement of an interferometer [32], which immediately raises the question: is it possible to do better than the standard quantum limit? The answer is *yes*. Injecting cavities with squeezed light can allow measurements below the standard quantum limit [52–55]. Also, injecting non-linear cavities with coherent states can result in squeezing in the outgoing beams [56, 57]. Any use of an optomechanical system to produce squeezed light would represent both a measurement of the RPSN, and a modification of the quantum statistics of the light and hence the RPSN. It should be noted that the cavity is not essential for squeezing. Heidmann and Reynaud showed that squeezing also occurs for light reflected from a harmonically bound mirror [58]. However, the effect can be greatly enhanced by a cavity.

The key idea is that a cavity with a movable end mirror has an intensity-dependent optical path length, just like a Kerr crystal. The earliest optomechanical nonlinearity was measured in 1983 by Dorsel et al. [28, 59], where they demonstrated the Kerr nonlinearity in a classical steady state (i.e. no dynamics) regime. Such a  $\chi^{(3)}$  nonlinearity is the essential ingredient for the squeezing of light [60] and also for the QND photon number measurements discussed above.

## 1.6 This dissertation in relation to previous work

Many groups are working toward the observation of quantum effects in engineered mechanical systems, including the optomechanical system discussed in this dissertation. Our optomechanical system is composed of a 50 nm-thick silicon nitride (SiN) membrane used as a mechanical resonator,

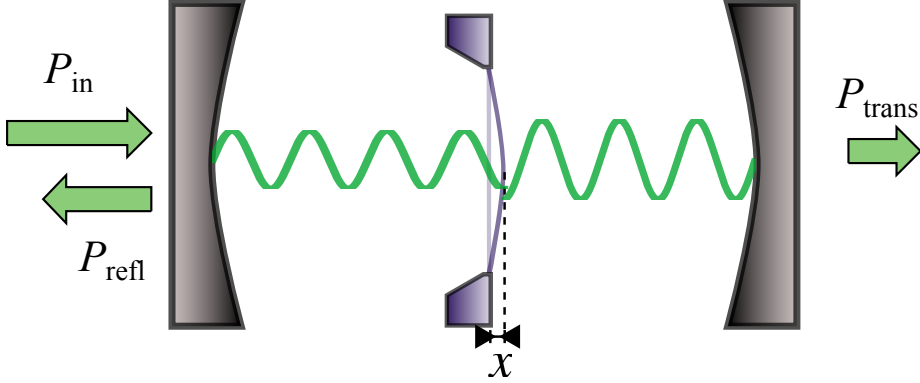


Figure 1.5: Membrane-in-the-middle cavity geometry used in this dissertation.

which is placed in a high-finesse optical cavity as shown in Fig. 1.5. This membrane-in-the-middle geometry can couple the intracavity photons with membrane motion as occurs in the cavity with a movable end mirror (see Fig. 1.3). There are a variety of other optomechanical geometries involving microtoroids [61], microspheres [62], nanostrings [38], microfabricated cantilevers and beams [63], and larger scale systems like LIGO. All are approaching the quantum regime. Typically the most significant obstacle is coupling to the thermal phonon bath, which sets the initial phonon number (for our membranes  $n_{\text{th}} \approx 10^6 - 10^7$  at room temperature). Cryogenic and optical cooling schemes are then employed to reduce the phonon number. The optical cooling in particular works best for low loss resonators because  $T_{\text{final}}/T_{\text{initial}} \approx \gamma_{\text{opt}}/\gamma$  in the classical picture of laser cooling, so given the same amount of optical coupling  $\gamma_{\text{opt}}$ , a lower damping  $\gamma$  resonator, will cool to a lower final effective temperature  $T_{\text{final}}$ . Also, the best cooling is achieved in the resolved sideband limit where the cavity damping rate is much smaller than the mechanical resonant frequency  $\kappa \ll \omega_{\text{M}}$  which motivates low loss optical resonators, and in general the cooling improves for stronger optomechanical couplings. Low optical loss, low mechanical loss, and large optomechanical couplings are key experimental factors

One way to approach to the quantum regime is to first cool the mechanical resonator to the quantum ground state. An optical cavity requires no cooling because even at room temperature the cavity is in the ground state ( $\bar{n}_{\text{cav}}^{\text{th}} = (e^{k_{\text{B}}T/\hbar\omega_{\text{cav}}} - 1)^{-1} \approx 3 \times 10^{-20}$ ). Once the mechanical resonator is in the ground state, purely quantum mechanical interactions between the resonator

and the cavity photons can occur. This can cause entanglement, superposition states, and other quantum phenomena (see Ch. 2). For example, when O’Connell et al. cooled their piezo-electric resonator to the ground state, they were able to observe coherent interactions between the resonator and a qubit [64].

Although quantum effects are easily revealed at optical frequencies, the same is not true for the silicon nitride membrane resonators discussed in this thesis, which have resonant frequencies of  $\omega_m < 2\pi \times 1$  MHz. At room temperature the phonon occupation numbers are about  $\bar{n}_{\text{th}} = k_B T / \hbar \omega_m \sim 10^7$ . In order to reach the ground state, a combination of traditional cryogenics (in this case a  $^3\text{He}$  refrigerator) and laser cooling techniques is required. My Yale colleagues, Andrew Jayich and Jack Sankey, are actively pursuing ground state cooling in this way.

This dissertation discusses an attempted measurement of the radiation pressure shot noise at room temperature. The feasibility of the measurement seems promising, but the details are tricky. In the most naive theory, we could estimate the ratio of the RPSN to the thermal forces using the expressions for  $S_F^{\text{th}}$  and  $S_F^{\text{sn}}$  given in Eqs. 1.12 and 1.19

$$\frac{S_F^{\text{sn}}}{S_F^{\text{th}}} = \frac{8\hbar P_{\text{in}} F^2 Q}{\pi k_B T c \lambda m \omega_m} \quad (1.34)$$

where the incident laser has a power  $P_{\text{in}}$  and wavelength  $\lambda$ , the cavity has a finesse  $F$ , and the mechanical resonator has a mass  $m$ , resonant frequency  $\omega_M$ , and quality factor  $Q$ . Using actual parameters for our optomechanical system, we estimate  $S_F^{\text{sn}}/S_F^{\text{th}} \sim 0.1-1$ . However, Eq. 1.34 ignores a variety of factors. For example, the reflectivity of the silicon nitride membranes is much less than one (typically  $R \approx 0.1$ ), optomechanical nonlinearities limit the maximum input power  $P_{\text{in}}$ , and the cavity filters the shot noise which is especially for fluctuations above the cavity linewidth  $\kappa$ . A more realistic estimate is

$$\frac{S_F^{\text{sn}}}{S_F^{\text{th}}} \sim 10^{-5} - 10^{-3} \quad (1.35)$$

which means distinguishing the effects of the RPSN from the thermally driven motion will be difficult.

## Physical manifestations of the RPSN in our system

### Measurement imprecision below the standard quantum limit

Even achieving this modest ratio of RPSN and thermal forces ( $S_F^{\text{sn}}/S_F^{\text{th}} \lesssim 10^{-3}$ ) implies we will be in a regime where the measurement back action dominates the measurement imprecision (due to shot noise), as in the work of Teufel et al. [36] and Anetsberger et al. [38] where  $S_x^{\text{imp}} < S_x^{\text{SQL}} < S_x^{\text{sn}}$ . If our detection scheme was shot noise-limited (which it is not at present - see Chs. 4 and 5), then we would also be in a position to make a position measurement with an imprecision below the standard quantum limit (i.e.  $S_x^{\text{imp}} < S_x^{\text{SQL}}$ ). For our system, a typical imprecision is closer to

$$(S_x^{\text{imp}})^{1/2} \approx 10^{-15} \text{ m}/\sqrt{Hz} \quad (1.36)$$

while the standard quantum limit on resonance is

$$(S_x^{\text{SQL}})^{1/2} = \frac{\hbar}{m\omega_m\gamma} \approx 3 \times 10^{-16} \text{ m}/\sqrt{Hz} \quad (1.37)$$

The additional noise in the imprecision is due to technical noise in the laser, inefficiencies in the detection optics, and noise in the photodiodes and electronics.

Although Teufel et al. [36] and Anetsberger et al. [38] achieved the impressive imprecision below the standard quantum limit (i.e. where  $S_x^{\text{imp}} < S_x^{\text{SQL}} < S_x^{\text{sn}}$ ), their measurement error was still dominated by thermal fluctuations  $S_x^{\text{sn}} \ll S_x^{\text{th}}$ . Furthermore, they did not have a means to distinguish the dominant thermal fluctuations from those caused by RPSN. We have modified the QND photon number measurement scheme of Verlot et al. [51] to instead measure unique signatures of the RPSN due to correlations in the left and right output beams from the cavity. Although our displacement imprecision is not below the standard quantum limit, the scheme allows the RPSN to be distinguished from sources of technical noise and thermal noise. This correlation scheme was first worked out in detail theoretically by our Yale colleague Kjetil Børkje [4]. This dissertation will discuss the theory (Chs. 2 and 3), apparatus (Ch. 4), and preliminary results (Ch. 5) associated with this measurement scheme.

## RPSN as a limit to laser cooling

When considering Eq. 1.31,

$$\bar{n}_m = \frac{\gamma_m \bar{n}_{\text{th}} + \gamma_{\text{opt}} \bar{n}_m^O}{\gamma_m + \gamma_{\text{opt}}} \quad (1.38)$$

we see there are two contributions to the laser-cooled phonon number. The first is due to thermal noise  $\gamma_m \bar{n}_{\text{th}} / (\gamma_m + \gamma_{\text{opt}})$ ; the second is due to the radiation pressure shot noise  $\gamma_{\text{opt}} \bar{n}_m^O / (\gamma_m + \gamma_{\text{opt}})$ .

When attempting to reach the quantum ground state through laser cooling, the radiation pressure shot noise contribution should be larger than the thermal noise ( $\gamma_{\text{opt}} \bar{n}_m^O \gg \gamma_m \bar{n}_{\text{th}}$ ). We also want the minimum achievable phonon number  $\bar{n}_m^O \ll 1$ , although this is irrelevant if the only goal is to observe the RPSN. The criteria for observing RPSN is to maximize the ratio

$$\frac{\gamma_{\text{opt}} \bar{n}_m^O}{\gamma_m \bar{n}_{\text{th}}} \quad (1.39)$$

which in the bad-cavity limit (i.e.  $\omega, \Delta \ll \kappa$ ) becomes

$$\frac{\gamma_{\text{opt}} \bar{n}_m^O}{\gamma_m \bar{n}_{\text{th}}} = \frac{8\hbar P_{\text{in}} F^2 Q}{\pi k_B T c \lambda m \omega_m} \quad (1.40)$$

This ratio is the same as  $S_F^{\text{sn}}/S_F^{\text{th}}$  given in Eq. 1.34. Since for realistic parameters this ratio is

$$\frac{\gamma_{\text{opt}} \bar{n}_m^O}{\gamma_m \bar{n}_{\text{th}}} \lesssim 10^{-3} \quad (1.41)$$

RPSN will not set a limit on our laser cooling.

## RPSN as a limit to the linewidth in the negative damping regime

The linewidth in the negative damping, blue-detuned regime as determined by Valhala [45] is

$$\Delta\omega_{\text{RS}} = \frac{\gamma}{2\bar{n}_c} (\bar{n}_{\text{th}} + 1) \quad (1.42)$$

The  $\gamma/2\bar{n}_c$  term which remains as  $\bar{n}_{\text{th}} \rightarrow 0$  is the quantum correction due to RPSN. For our room temperature resonators with  $\bar{n}_{\text{th}} \sim 10^7$ , this quantum correction is only one part in  $10^7$ . We have

no way to observe such a small fractional change in linewidth in our current experiment.

### **RPSN heating of ultracold atomic gas**

There are two key differences between the work described in this dissertation and that of Murch et al. in Ref. [46]. First, in Ref. [46] the atoms are ultracold, significantly reducing the effect of thermal forces. Second the optomechanical coupling between the atoms and photons is enormous, and nonlinear optomechanical effects can be seen with just a few intracavity photons. Consequently, the shot noise fluctuations are fractionally very large. Our membrane-in-the-middle cavity requires about  $10^8$  intracavity photons before similar nonlinear optomechanical behavior is observed.

### **RPSN and QND measurement schemes**

The measurement scheme described and implemented in this dissertation is similar to the scheme Verlot et al. have developed for demonstrating a QND measurement of intracavity photon number. However, both our membrane-in-the-middle cavity and the system of Verlot et al. [51] are dominated by thermal motion, so a QND measurement of intracavity photon number is not possible. For simplicity our scheme employs one less input beam to the cavity, which prohibits a QND measurement, but does still allow for observation of the RPSN [4]. The scheme also works for non-zero detunings, in contrast to the scheme in Verlot et al. [51] which only works for zero detuning.

# Chapter 2

## Basic theory of cavity optomechanics

Chapter 1 introduced the two key concepts of radiation pressure and shot noise and showed how together they set a limit on the accuracy of an interferometric displacement measurement, known as the standard quantum limit. The chapter went on to discuss how the radiation pressure shot noise can manifest itself in a variety of ways, any of which would be a conclusive observation of the RPSN. This chapter is concerned with radiation pressure shot noise in cavity optomechanical systems and works through their theoretical description in a much more systematic form than was given in Ch. 1. In one sense, everything in this chapter is entirely known in the literature, so my goals are four-fold:

1. To derive the optomechanical equations of motion from a classical perspective that would be familiar to an undergraduate taking classical mechanics and optics at the level of Hecht [65] or Brooker [66].
2. To summarize the quantum equations of motion and the optomechanical frequency shift and damping of a mechanical resonator.
3. To derive from the quantum equations of motion the forms of the radiation pressure shot noise and thermal force noise.
4. To make a useful reference table of the key variables and equations in cavity optomechanics.

I will first overview many existing results and future possibilities for cavity optomechanical systems. Then the remainder of the chapter will focus on modeling our specific cavity optomechanical system, and deriving key results which are used in the remainder of the dissertation.

## 2.1 Overview of cavity optomechanics

Cavity optomechanics is defined as the study of optical resonators coupled to mechanical resonators via radiation pressure. The first cavity optomechanical systems were radiation pressure-driven interferometers that were proposed as antennae for gravitational waves [32]. Other proposals for quantum cavity optomechanics were already mentioned in Ch. 1, such as QND photon number measurements [47–50] and squeezing light [56, 57, 60, 67]. There are also more exotic (and difficult) proposals: making QND phonon number measurements in dispersively coupled systems [39, 68, 69], entangling an optical and mechanical resonator [70–72], entangling two mechanical resonators [73–75], and creating superposition states of a mechanical resonator [76–79].

A precondition for many of the quantum optomechanical experiments is the ability to cool the mechanical resonator to its quantum ground state. A combination of traditional cryogenics and optical cooling methods has enabled a number of optomechanics groups to approach the ground state with a mean phonon number  $\bar{n} \approx 3 - 30$  [62, 80–82], and it is expected that these systems will soon achieve the ground state, including our own group at Yale.

The idea that radiation pressure could be used to damp the Brownian motion of a resonator (i.e. cool the resonator) dates back to the work of Braginsky and colleagues in the late 1960s and early 1970s [83, 84]. In 1998, Mancini et al. developed a fully quantum model of cooling which used active feedback on the mechanical position via radiation pressure [85]. In 1999, Cohadon et al. experimentally demonstrated an active feedback scheme and achieved laser cooling by a factor of 20 [86]. Modern active feedback schemes have cooled a cantilever with a 30  $\mu\text{m}$  diameter mirror to 135 mK [87] and a 3  $\mu\text{m}$  microsphere to 1.5 mK [88].

Braginsky’s original proposal involved passive feedback by detuning the laser from resonance in analogy with laser cooling of atoms. The first non-static and passive radiation pressure effect on a

mechanical resonator was observed in 2004 by Sheard et al. [89]. They were able to observe a shift in the resonant frequency of a harmonically bound mirror, but did not observe damping. Metzger and Karrai observed passive cooling of a microlever by a factor of 15 due to a photo-thermal force (not radiation pressure) [90]. Our group at Yale observed a similar photo-thermal cooling effect in 2006 and saw cooling by a factor of six [91]. Also, in 2006 a number of groups achieved success with passive laser cooling by radiation pressure [63, 87, 92, 93], and our Yale group joined the crowd in 2008, demonstrating passive cooling by a factor of  $4.4 \times 10^4$  from room temperature to 7 mK [39]. As it became apparent that these cooling schemes, when combined with cryogenics, would likely reach the ground state, it became important to work out the quantum limits on the lowest achievable phonon number. For passive optical cooling schemes the limit is set by radiation pressure shot noise. A number of groups developed the theory [40, 42, 94], with one key result being that ground state cooling requires the resolved sideband limit  $\omega_M \gg \kappa$  where the resonant frequency  $\omega_M$  is much greater than the cavity decay rate (i.e. cavity linewidth)  $\kappa$ . The resolved sideband limit requirement can be relaxed in certain cases like displacement-dependent coupling of the cavity [95].

Lastly, it should be noted that optical damping or similar techniques are not necessary for ground state cooling if the resonator has a sufficiently high resonant frequency and is in a sufficiently cold fridge. O’Connell et al. [64] cooled a 6 GHz piezoelectric resonator in a dilution fridge to a temperature of 0.1 K and achieved a phonon number  $\bar{n} < 0.07$ . Furthermore they demonstrated coherent energy exchange between the resonator and a quantum bit. Their progress represents the first engineered mechanical system in the quantum regime.

In the remainder of this chapter, I will work out the optomechanical equations of motion and use them to derive expressions for the optically induced mechanical frequency shift and damping. I will also derive expressions for the radiation pressure shot noise.

## 2.2 The most basic model: A cavity with one harmonically bound end mirror.

The simplest model of an optomechanical system is a Fabry-Perot cavity where one of the end-mirrors is harmonically bound. Examples of harmonically bound mirrors include mirrors suspended by thin fibers as in LIGO cavities or small mirrors mounted on a microfabricated cantilever [87]. Alternatively the movable mirror could be the vibrational mode of the glass substrate on which the mirror coating is deposited [51]. A general schematic is shown in Fig. 2.1. This system encompasses all of the essential aspects of the radiation pressure shot noise measurement scheme described in Ch. 3.

My goal in this chapter is to derive the key equations describing the system and also to include a number of commonly used equations as a cheat sheet which may be useful for graduate students who comes after me. Table 2.1 gives a minimal set of parameters needed to describe the system. They are chosen because they are simple to understand, but they are certainly not the only choice of parameters and often are not the most handy to use in calculations. Table 2.2 summarizes a variety of alternative parameters which are also common and relates them to the minimal set in Table 2.1. The relationships between the cavity decay rates  $\kappa_i$  and the mirror transmission coefficients  $T_i$  are derived in Sec. 2.3.2, but otherwise the relationships are not explained in any more detail.

## 2.3 Derivation of the cavity equation of motion from the steady-state solution

### 2.3.1 Derivation of the steady-state field amplitudes

The goal of this section is to solve for the reflected, intracavity, and transmitted fields of the cavity in a way similar to an introductory optics book such as Hecht's *Optics* [65] or Brooker's *Modern Classical Optics* [66]. Figure 2.2 shows the basic schematic for the cavity. The cavity axis is assumed to be along the  $z$ -axis with the left mirror at  $z = 0$ . The same set of basic parameters is used to

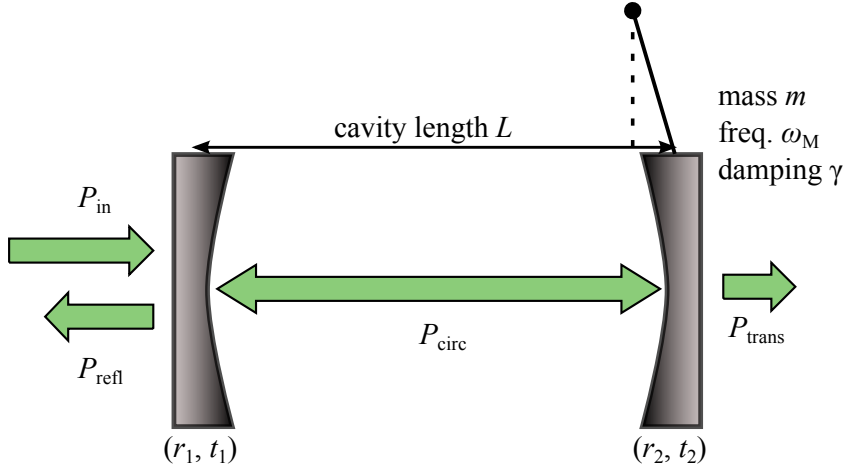


Figure 2.1: Cavity with a harmonically bound end mirror. This is the canonical system in cavity optomechanics. The  $P_i$  refer to the input, reflected, circulating and transmitted laser power. The  $(r_i, t_i)$  pair refers to the amplitude reflection and transmission coefficients for the end mirrors. The mass  $m$ , resonant frequency  $\omega_M$ , and damping constant  $\gamma$  are given for the harmonically bound end mirror.

MECHANICAL PARAMETERS	
$\omega_M$	$2\pi \times$ mechanical resonant frequency of mirror
$\gamma$	mechanical damping rate
$m$	mass of the resonator
OPTICAL PARAMETERS	
$t_1$	amplitude transmission coefficient, fixed mirror
$r_1$	amplitude reflection coefficient, fixed mirror
$t_2$	amplitude transmission coefficient, movable mirror
$r_2$	amplitude reflection coefficient, movable mirror
$L$	cavity length
$P_{\text{in}}$	power incident upon the cavity
$\lambda$	laser wavelength

Table 2.1: Descriptions of the basic cavity optomechanical parameters. This is a (non-unique) minimal set of parameters needed to describe the system. They are chosen because they are conceptually simple, but they are not necessarily the easiest to measure or to include in the theory.

MECHANICAL PARAMETERS				
$Q$	Quality factor of mechanical resonator	$Q = \frac{\omega_m}{\gamma}$		-
OPTICAL PARAMETERS				Units
$\omega_L$	laser wavelength	$\omega_L = 2\pi \frac{c}{\lambda}$	$\omega_L = ck$	$s^{-1}$
$k$	laser wave-number	$k = 2\pi/\lambda$	$k = \omega_L/c$	$m^{-1}$
$\omega_C$	cavity resonant frequency (for the $N$ -th empty cavity mode)	$\omega_C = 2\pi \frac{c}{2L}N$	$\omega_C = 2\pi\nu_{\text{FSR}}N$	$s^{-1}$
$\Delta$	detuning	$\Delta = \omega_L - \omega_C$		$s^{-1}$
$R_i$	power reflectivity for mirror $i$	$R_i =  r_i ^2$		-
$T_i$	power transmission for mirror $i$	$T_i =  t_i ^2$	$T_i = \kappa_i\tau$	-
$A_i$	power absorption for mirror $i$	$R_i + T_i + A_i = 1$		-
$A_M$	absorption via additional intracavity loss			-
$F$	finesse of cavity $\left(F \equiv \frac{\text{Free spectral range in Hz}}{\text{Full linewidth in Hz}} = \frac{\nu_{\text{FSR}}}{\kappa/2\pi}\right)$	$F = \frac{\pi r_1r_r }{1- r_1r_2 }$	$F = \frac{\pi c}{L\kappa} = \frac{\pi c\tau_{\text{decay}}}{L}$	-
$\tau$	cavity round trip time	$\tau = \frac{2L}{c}$		s
$\nu_{\text{FSR}}$	cavity free spectral range	$\nu_{\text{FSR}} = \frac{c}{2L} = \frac{1}{\tau}$		Hz
$\kappa$	cavity decay rate (energy or power)	$\kappa = \kappa_L + \kappa_M + \kappa_R$	$\kappa = \tau_{\text{decay}}^{-1}$	$s^{-1}$
$\kappa_{L,R}$	cavity decay rate from left or right end mirrors	$\kappa_{L,R} = \frac{T_{L,R}}{\tau}$		$s^{-1}$
$\kappa_M$	cavity decay rate from mirror loss $A_{L,R}$ or intracavity loss $A_M$	$\kappa_M = \frac{A_L + A_M + A_R}{\tau}$		$s^{-1}$
$\tau_{\text{decay}}$	power cavity decay time $P_{\text{trans}}(t) = P_{\text{trans}}(0)e^{-t/\tau_{\text{decay}}}$	$\tau_{\text{decay}} = \kappa^{-1}$		s

Table 2.2: Table of derived parameters and the formulas which relate them. Note: Frequencies are listed in Hz, while angular frequencies have units of  $s^{-1}$ .

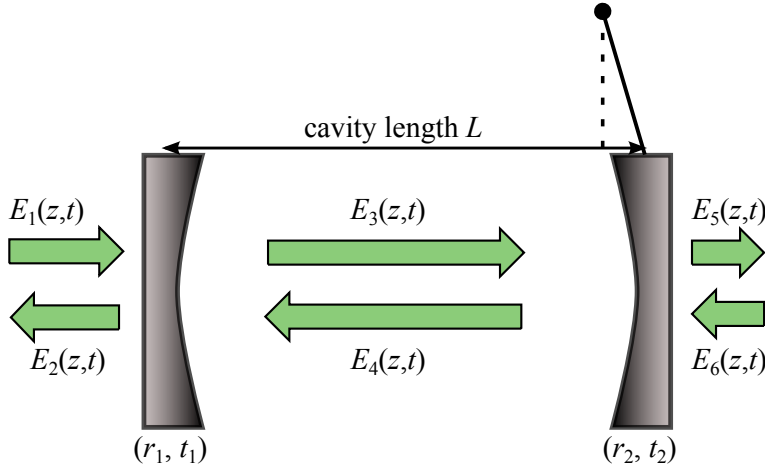


Figure 2.2: Cavity with a movable end mirror. The six electric fields are shown which are used in the steady state derivation for the cavity equations of motion.

describe the cavity as is given in Table 2.1. The transmission and reflection coefficients establish relationships between the amplitudes of the six left- and right-going waves shown in Fig. 2.2.

The goal of this calculation is to solve for the intracavity electric fields  $E_3$  and  $E_4$  in terms of the incident fields  $E_1$  and  $E_6$ . This derivation treats the electric fields as scalars, which is valid if all the fields share the same linear polarization; the vector nature of the field can then be ignored.

The electric fields can be expressed as traveling waves with amplitudes  $A_i$  (note  $A_i$  is different than the mirror absorption coefficient given in Table 2.2), laser frequency  $\omega_L = 2\pi c/\lambda$ , and wave number  $k = 2\pi/\lambda = \omega_L/c$

$$E_i(t, z) = A_i e^{-i\omega_L t} e^{ikz} \text{ for } i = 1, 3, 5 \text{ (Right-going waves)} \quad (2.1)$$

$$E_i(t, z) = A_i e^{-i\omega_L t} e^{-ikz} \text{ for } i = 2, 4, 6 \text{ (Left-going waves)} \quad (2.2)$$

The convention for Fourier transforms in this dissertation is that  $E[\omega] = \int_{-\infty}^{+\infty} E(t) e^{i\omega t}$ , so an electric field with time dependence  $E(t) \propto e^{-i\omega t}$  corresponds to the frequency component  $E[\omega]$ . It should also be noted that the actual electric fields are given by the real part  $\text{Re}((E(t, z)))$ .

The input and output fields of an end mirror can be related by a transfer matrix like

$$\begin{pmatrix} E_3(z=0) \\ E_2(z=0) \end{pmatrix} = \begin{pmatrix} t_1 & r'_1 \\ r_1 & t'_1 \end{pmatrix} \begin{pmatrix} E_1(z=0) \\ E_4(z=0) \end{pmatrix} \quad (2.3)$$

The convention is that  $t_i$  and  $r_i$  are coefficients for the right-going incident waves, and  $t'_i$  and  $r'_i$  are coefficients for the left-going incident waves. For lossless mirrors, the matrix must be unitary, and one common convention is to write it as

$$\begin{pmatrix} E_3(z=0) \\ E_2(z=0) \end{pmatrix} = \begin{pmatrix} t_1 & -r_1 \\ r_1 & t_1 \end{pmatrix} \begin{pmatrix} E_1(z=0) \\ E_4(z=0) \end{pmatrix} \quad (2.4)$$

where  $t_1$  and  $r_1$  are both real and positive. This is the convention used in this dissertation. In the case of lossy end mirrors, the matrix is no longer unitary, but it turns out that the form of Eq. 2.4 with all real coefficients is still acceptable. A full analysis of the constraints in choosing the mirror coefficients for a lossy mirror or beam splitter is given in Ref. [96].

A similar transfer equation relating the input and output fields at the second mirror can be written by evaluating the fields at  $z = L$ . Again the convention is that  $t_2$  and  $r_2$  are both real and positive.

$$\begin{pmatrix} E_5(z=L) \\ E_4(z=L) \end{pmatrix} = \begin{pmatrix} t_2 & -r_2 \\ r_2 & t_2 \end{pmatrix} \begin{pmatrix} E_3(z=L) \\ E_6(z=L) \end{pmatrix} \quad (2.5)$$

The input/output relations given in Eqs. 2.4 and 2.5 for the two mirrors can be rewritten in terms of the field amplitudes  $A_1, \dots, A_6$ . The factors of  $e^{-i\omega_1 t}$  are common to all the terms (see Eqs. 2.1 and 2.2 ) and cancel out. The resulting set of four equations in terms of the amplitudes

$A_i$  is

$$A_2 = -r_1 A_1 + t_1 A_4 \quad (2.6)$$

$$A_3 = t_1 A_1 + r_1 A_4 \quad (2.7)$$

$$A_4 e^{-ikL} = r_2 A_3 e^{ikL} + t_2 A_6 e^{-ikL} \quad (2.8)$$

$$A_5 e^{ikL} = t_2 A_3 e^{ikL} - r_2 A_6 e^{-ikL} \quad (2.9)$$

Solving for the intracavity fields  $A_3$  and  $A_4$  in terms of the input fields  $A_1$  and  $A_6$  gives

$$A_3 = \frac{t_1 A_1 + r_1 t_2 A_6}{1 - r_1 r_2 e^{2ikL}} \quad (2.10)$$

$$A_4 = \frac{t_1 r_2 e^{2ikL} A_1 + t_2 A_6}{1 - r_1 r_2 e^{2ikL}} \quad (2.11)$$

Similarly, the outgoing fields  $A_2$  and  $A_5$  become

$$A_2 = -r_1 A_1 + t_1 A_4 \quad (2.12)$$

$$A_5 = t_2 A_3 - r_2 A_6 e^{-2ikL} \quad (2.13)$$

Next we take the high-reflectivity (i.e. high-finesse) limit so that  $r_1 \rightarrow 1$  and  $r_2 \rightarrow 1$ . We define the resonant cavity length  $L_0$  and wave number  $k_0$  such that  $e^{2ik_0 L_0} = 1$ . Then a cavity with an arbitrary length  $L$  and wave number  $k$  is treated as a small perturbation from resonance:  $L = L_0 + \delta z$  and  $k = k_0 + \delta k$ . The intracavity fields  $A_3$  and  $A_4$ , which become equal in the high-finesse limit, are then

$$A_3 = A_4 = \frac{t_1 A_1 + t_2 A_6}{1 - |r_1 r_2| e^{2ik_0 \delta z} e^{2i\delta k L_0}} \quad (2.14)$$

where the second order term  $e^{iz\delta k} \approx 1$  is omitted. Similarly, the reflected fields in the high-finesse

limit are

$$A_2 = -A_1 + t_1 A_4 \quad (2.15)$$

$$A_5 = -A_6 + t_2 A_3 \quad (2.16)$$

Finally, to be consistent with the nomenclature used later in the full quantum mechanical derivation and throughout this dissertation, the fields are renamed as follows:

$$A_3 = A_4 = A_{\text{cav}} \quad (2.17)$$

$$A_1 = A_{\text{in,L}} \quad (2.18)$$

$$A_6 = A_{\text{in,R}} \quad (2.19)$$

$$A_2 = A_{\text{out,L}} \quad (2.20)$$

$$A_5 = A_{\text{out,R}} \quad (2.21)$$

The final set of equations is then

$$A_{\text{cav}} = \frac{t_1 A_{\text{in,L}} + t_2 A_{\text{in,R}}}{1 - |r_1 r_2| e^{2ikz} e^{2i\delta k L_0}} \quad (2.22)$$

$$A_{\text{out,L}} = -A_{\text{in,L}} + t_1 A_{\text{cav}} \quad (2.23)$$

$$A_{\text{out,R}} = -A_{\text{in,R}} + t_2 A_{\text{cav}} \quad (2.24)$$

Equations 2.22, 2.23, and 2.24 are the standard steady-state solutions for Fabry-Perot cavities. Nearly identical expressions can be found in most optics textbooks. These standard expressions will be used to derive the cavity equations of motion in the following section.

### 2.3.2 From steady-state fields to an equation of motion

Now we take the limit where the mirror displacement from resonance length is small relative to the wavelength  $z \ll \lambda$  (i.e.  $kz \ll 1$ ), and the frequency shift from resonance is small compared to a free spectral range of the cavity  $\Delta = c\delta k \ll c/2L$  (i.e.  $\delta k L_0 \ll 1$ ). This is the standard working condition for these cavities. Equation 2.22 then becomes

$$A_{\text{cav}} = \frac{t_1 A_{\text{in,L}} + t_2 A_{\text{in,R}}}{1 - |r_1 r_2| (1 + 2ik_0 z + 2i\delta k L_0)} \quad (2.25)$$

Recalling that this expression is only valid in the high-finesse limit where reflectivities are almost unity  $|r_1 r_2| \approx 1$  and expressing the wavenumbers in terms of frequencies  $k = \omega_0/c$  and  $\delta k = (\omega - \omega_0)/c$ , we get

$$A_{\text{cav}} = \frac{t_1 A_{\text{in,L}} + t_2 A_{\text{in,R}}}{1 - |r_1 r_2| - 2i\frac{\omega_0}{c}z - 2i\frac{\omega - \omega_0}{c}L_0} \quad (2.26)$$

Equation 2.26 is a steady-state solution for the intracavity field at a particular laser drive frequency  $\omega_L = \omega$ . This can also be thought of as the Fourier component of the intracavity field  $A_{\text{cav}} \rightarrow A_{\text{cav}}[\omega]$  given the incident laser fields  $A_{\text{in,L}} \rightarrow A_{\text{in,L}}[\omega]$  and  $A_{\text{in,R}} \rightarrow A_{\text{in,R}}[\omega]$ . Next we solve for  $-i\omega A_{\text{cav}}[\omega]$  because  $-i\omega A_{\text{cav}}[\omega] \rightarrow \frac{dA_{\text{cav}}(t)}{dt}$  in the Fourier transform

$$-i\omega A_{\text{cav}}[\omega] = \left( -i\omega_0 + i\frac{\omega_0}{L_0}z - \frac{c}{2L_0}(1 - |r_1 r_2|) \right) A_{\text{cav}}[\omega] + \frac{ct_1}{2L_0}A_{\text{in,L}}[\omega] + \frac{ct_2}{2L_0}A_{\text{in,R}}[\omega] \quad (2.27)$$

In the time domain this equation becomes

$$\frac{dA_{\text{cav}}(t)}{dt} = \left( -i\omega_0 + i\frac{\omega_0}{L_0}z - \frac{c}{2L_0}(1 - |r_1 r_2|) \right) A_{\text{cav}}(t) + \frac{ct_1}{2L_0}A_{\text{in,L}}(t) + \frac{ct_2}{2L_0}A_{\text{in,R}}(t) \quad (2.28)$$

Now we can make several simplifications to Eq. 2.28. First,  $2L_0/c$  is the cavity round trip time  $\tau$ . Second, the quantities  $(1 - |r_1 r_2|)/\tau$  and  $t_i/\tau$  can be expressed in terms of cavity decay rates  $\kappa_i$ . From Eq. 2.28 we see the amplitude cavity decay rate (which is defined as  $\kappa/2$ ) is  $\frac{\kappa}{2} = \frac{1 - |r_1 r_2|}{\tau}$ .

The numerator can be rewritten as

$$1 - |r_1 r_2| = 1 - \sqrt{R_1 R_2} \quad (2.29)$$

$$= 1 - \sqrt{(1 - T_1 - A_1)(1 - T_2 - A_2)} \quad (2.30)$$

$$\approx 1 - \left(1 - \frac{1}{2}T_1 - \frac{1}{2}A_1\right) \left(1 - \frac{1}{2}T_2 - \frac{1}{2}A_2\right) \quad (2.31)$$

$$\approx \frac{1}{2}(T_1 + A_1 + T_2 + A_2) \quad (2.32)$$

where it should be noted that  $A_1$  and  $A_2$  are loss terms, and not cavity field amplitudes. Dividing by the cavity round trip time  $\tau$  gives

$$\frac{1 - |r_1 r_2|}{\tau} = \frac{\kappa}{2} = \frac{T_1}{2\tau} + \frac{A_1}{2\tau} + \frac{T_2}{2\tau} + \frac{A_2}{2\tau} \quad (2.33)$$

We can associate a loss term with each of the left and right end mirrors, giving  $\kappa_L = \frac{T_1}{\tau}$  and  $\kappa_R = \frac{T_2}{\tau}$ . The remainder of the absorption loss from the cavity is  $\kappa_M = \frac{A_1 + A_2}{\tau}$  so  $\kappa = \kappa_L + \kappa_R + \kappa_M$ . The coefficients in front of the input fields  $A_{\text{in,L}}$  and  $A_{\text{in,R}}$  then become  $t_1/\tau = \sqrt{\kappa_L/\tau}$  and  $t_2/\tau = \sqrt{\kappa_R/\tau}$ .

Using these new parameters, Eq. 2.28 gives a tidy cavity equation of motion:

$$\frac{dA_{\text{cav}}(t)}{dt} = \left(-i\omega_0 + i\frac{\omega_0}{L_0}z - \frac{\kappa}{2}\right) A_{\text{cav}}(t) + \sqrt{\frac{\kappa_L}{\tau}} A_{\text{in,L}}(t) + \sqrt{\frac{\kappa_R}{\tau}} A_{\text{in,R}}(t) \quad (2.34)$$

At the beginning of this analysis I wasn't explicit about the units on the field amplitudes, but now I would like to define them to be the positive square roots of the powers in each of the traveling waves. So

$$A_{\text{in,R}} = \sqrt{P_{\text{in,R}}} \quad (2.35)$$

$$A_{\text{in,L}} = \sqrt{P_{\text{in,L}}} \quad (2.36)$$

$$A_{\text{in,circ}} = \sqrt{P_{\text{circ}}} \quad (2.37)$$

Now the stored energy in the cavity  $U_{\text{cav}}$  can be expressed as the product of the circulating power and the cavity round trip time  $U_{\text{cav}} = P_{\text{circ}}\tau$ . It is common to rescale the intracavity field by a factor of  $\sqrt{\tau}$ , so that the scaled field  $a_{\text{cav}} = \sqrt{\tau}A_{\text{cav}} = \sqrt{U_{\text{cav}}}$  becomes the square root of energy stored in the cavity, while the incident fields remain square root of powers. The advantages of this scaling are: (1) the cavity round trip time  $\tau$  drops out of the equation; (2) the intracavity field, which is really a standing wave, is more naturally thought of in terms of an energy; (3) the conversion from intracavity field amplitude to photon number is straightforward; (4) the incident field, which is a traveling wave, is more naturally thought of as a flow of energy (power). Using the rescaled field, Eq. 2.34 becomes

$$\frac{da_{\text{cav}}(t)}{dt} = \left(-i\omega_0 + i\frac{\omega_0}{L_0}z - \frac{\kappa}{2}\right) a_{\text{cav}}(t) + \sqrt{\kappa_L}A_{\text{in,L}}(t) + \sqrt{\kappa_R}A_{\text{in,R}}(t) \quad (2.38)$$

At this point it should be noted that Eq. 2.38 describes the response of the intracavity field to a fluctuating drive signal for a fixed cavity length  $L_0 + z$ . It is then somewhat surprising (but true) that the equation of motion is still valid for a cavity with small length fluctuations  $z \ll \lambda/2$  as a consequence of the adiabatic theorem. The small length fluctuation requirement ensures that only one cavity mode is being driven. We then arrive at a cavity equation of motion which only differs from Eq. 2.38 by  $z \rightarrow z(t)$

$$\frac{da_{\text{cav}}(t)}{dt} = \left(-i\omega_0 + i\frac{\omega_0}{L_0}z(t) - \frac{\kappa}{2}\right) a_{\text{cav}}(t) + \sqrt{\kappa_L}A_{\text{in,L}}(t) + \sqrt{\kappa_R}A_{\text{in,R}}(t) \quad (2.39)$$

### 2.3.3 Applying the cavity equation of motion to other optomechanical systems

In general, the equation of motion given in Eq. 2.39 can be applied to other optomechanical systems, including the membrane-in-the-middle cavities used in this dissertation research. Equation 2.39 is of the form  $\dot{a}_{\text{cav}}(t) = (-i\omega - \kappa/2) a_{\text{cav}}(t) + \dots$ , which shows that the cavity resonant frequency  $\omega$  obeys

$$\omega = \omega_0 - \frac{\omega_0}{L_0}z = \omega_0 - \frac{\partial\omega}{\partial z}z \quad (2.40)$$

which is valid for a cavity with a movable end mirror. For the membrane-in-the-middle cavity and other geometries, however,  $\partial\omega/\partial z \neq \omega_0/L_0$ , and we write this more generally as

$$\omega = \omega_0 + Az \tag{2.41}$$

where  $A = \partial\omega/\partial z$ . This gives the final, most general cavity equation of motion:

$$\frac{da_{\text{cav}}(t)}{dt} = \left(-i\omega_0 - iAz(t) - \left(\frac{\kappa_L}{2} + \frac{\kappa_R}{2}\right)\right) a_{\text{cav}}(t) + \sqrt{\kappa_L}A_{\text{in,L}}(t) + \sqrt{\kappa_R}A_{\text{in,R}}(t) \tag{2.42}$$

### 2.3.4 Note: Why a single time varying number is sufficient to describe the intracavity field

The electromagnetic field is described by a vector at each point in space. However, inside a perfectly reflecting cavity, the field can be decomposed into a discrete set of field modes. In most experiments using optical cavities, it is common to consider only one of these cavity modes, ignoring the others. For a finite linewidth cavity  $\Delta\lambda = \frac{c}{\Delta\nu} = \frac{c}{\nu_{FSR}/F} = 2LF$ , we see that the envelope in the waveform resulting from all the wavenumbers can only change on a length scale of  $2LF$ , which is a factor of  $2F$  longer than the cavity. This means for high-finesse cavities the field amplitude is spatially very uniform throughout the cavity, and this amplitude changes on time scales  $1/\kappa$  and longer. Thus even though the intracavity field in general is described by an infinite set of values, in the high-finesse limit a single time varying number is sufficient.

## 2.4 Differences between the movable end mirror and the membrane-in-the-middle geometries

While the cavity geometry with a movable end mirror is conceptually simple and is used in some optomechanical systems (LIGO for instance), at Yale we have focused our efforts on fixed length cavities with thin dielectric slabs in the middle as briefly described in Sec. 1.6 and shown in Fig. 2.3.

This is often called a membrane-in-the-middle geometry, or alternatively, a dispersively coupled membrane and cavity.

### 2.4.1 Advantages of the membrane-in-the-middle geometry

In any optomechanical system, it is desirable to minimize the optical and mechanical losses and to maximize the optomechanical coupling. The traditional cavity geometry with a movable end mirror requires the same optical element to be both a high-reflectivity mirror and a low-loss resonator. This is difficult to achieve, particularly for micromechanical and nanomechanical systems. Low mechanical loss is most commonly achieved in simple mechanical resonators fabricated from a single material, but the typical reflectivity of a single layer of dielectric is very low. High-reflectivity mirrors are formed by stacking many layers of alternating dielectrics which increases the mechanical loss of the element. The membrane-in-the-middle geometry is an attempt to avoid this trade-off between low mechanical loss and low optical loss by using separate optical elements for the high-reflectivity mirrors and the low-loss resonator. For our setup, the cavity end mirrors are stationary and are commercially available high-finesse cavity mirrors with finesse  $F \sim 2 \times 10^4$ . The mechanical element is a single slab of dielectric, which in our case is a very thin ( $\sim 50$  nm), highly stressed silicon nitride  $\text{Si}_3\text{N}_4$  membrane. It is also commercially available and has a mechanical quality factor  $Q \sim 10^5 - 10^6$  at room temperature.

### 2.4.2 Membrane-in-the-middle: Calculation of the steady-state intracavity fields and optomechanical coupling

The one-dimensional model shown in Fig. 2.3 consists of two cavity end mirrors with amplitude reflectivity  $r$  and transmission  $t$ . The two cavity mirrors are assumed identical in this derivation, though the extension to unequal mirrors is straightforward. The dielectric membrane placed between the two end mirrors has thickness  $L_d$  and index of refraction  $n$ . The complex-valued amplitude

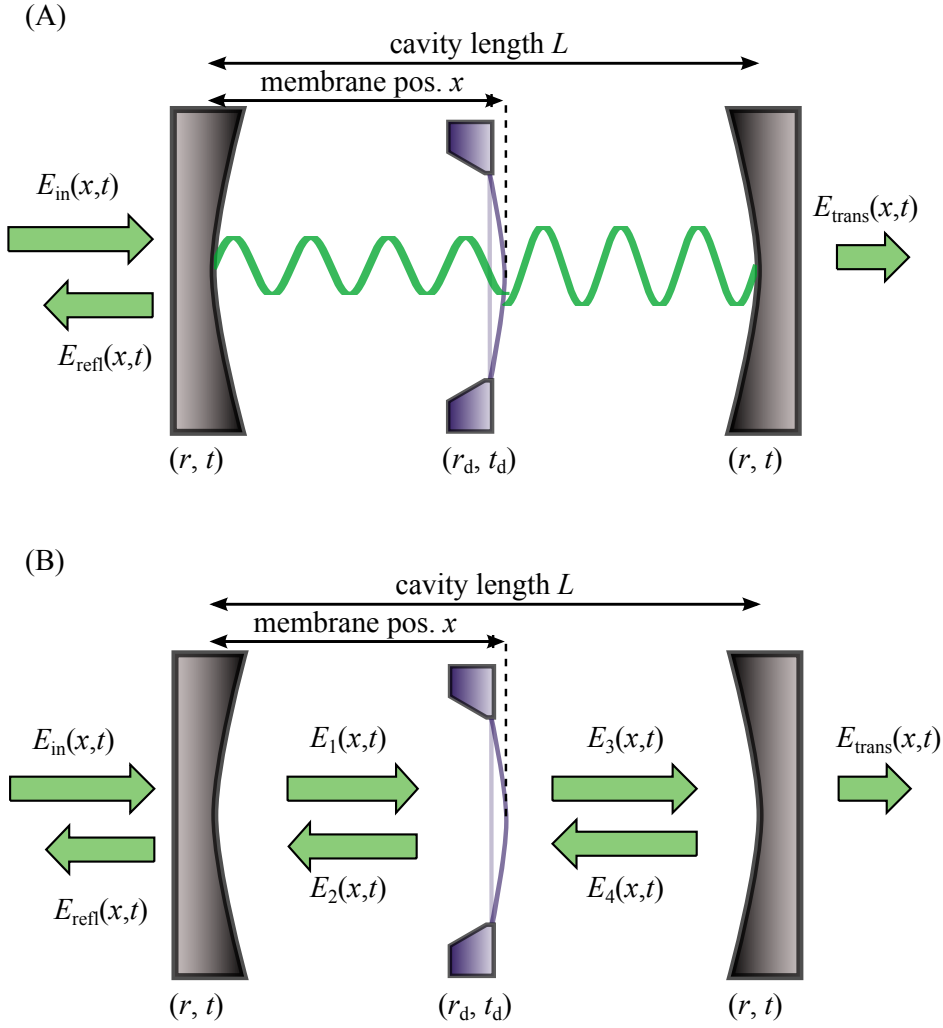


Figure 2.3: Membrane-in-the-middle cavity geometry. A membrane of thickness  $d$  has amplitude reflection and transmission coefficients of  $r_d$  and  $t_d$ , respectively. (A) represents the intracavity field as a standing wave field, showing that the membrane's interaction with the intracavity field will be periodic. (B) represents all the left- and right-going waves needed to describe the system in one dimension.

reflection and transmission coefficients for the dielectric membrane can be written as

$$r_d = \frac{(n^2 - 1) \sin knL_d}{2in \cos knL_d + (n^2 + 1) \sin knL_d} \quad (2.43)$$

$$t_d = \frac{2n}{2in \cos knL_d + (n^2 + 1) \sin knL_d} \quad (2.44)$$

The transmitted, reflected, and intracavity fields can be calculated by solving a system of equations, as was done for the movable end mirror geometry in Sec. 2.3.1. The following brief derivation follows Jayich et al. [97]. The electric fields of incident frequency  $\omega = kc$  can be expressed as traveling waves  $E_i(x, t) = A_i e^{\pm ikx} e^{-i\omega t}$ , where  $+ikx$  is for the right-going waves and  $-ikx$  is for left-going waves. The system of equations for the field amplitudes  $A_i$  is

$$A_1 = itA_{\text{in}} + rA_2 e^{ikL_1} \quad (2.45)$$

$$A_2 = r_d A_1 e^{ikL_1} + it_d A_4 e^{ikL_2} \quad (2.46)$$

$$A_3 = it_d A_1 e^{ikL_1} + r_d A_4 e^{ikL_2} \quad (2.47)$$

$$A_4 = rA_3 e^{ikL_2} \quad (2.48)$$

$$A_{\text{refl}} = itA_2 e^{ikL_1} + rA_{\text{in}} \quad (2.49)$$

$$A_{\text{trans}} = itA_3 e^{ikL_2} \quad (2.50)$$

where  $L_1$  and  $L_2$  are the lengths of the left and right sides of the cavity (as divided by the membrane).

Note that this uses a different convention for the mirror transfer matrix where

$$M = \begin{pmatrix} it & r \\ r & it \end{pmatrix} \quad (2.51)$$

and  $\arg t = \arg r$ .

We must solve the above system of equations in Eqs. 2.45 to 2.50 to obtain the variation in the cavity resonant frequency with membrane position. This can then be used to calculate the optomechanical coupling, which is proportional to  $\partial\omega_C/\partial x$ . From Ref. [97] we find the change in

cavity resonant frequency as a function of membrane position  $x$  to be

$$\omega_C(x) = \nu_{\text{FSR}} \left[ 2\phi_r + 2 \cos^{-1} \left( |r_d| \cos \left( \frac{2\pi}{\lambda/2} x \right) \right) \right] \quad (2.52)$$

where  $r_d$  is the complex amplitude reflection coefficient of the membrane given in Eq. 2.43,  $\phi_r = \arg(r_d)$ , and  $\nu_{\text{FSR}} = c/2L$  is the free spectral range of the cavity. A plot of the theoretical expression for  $\omega_C(x)$  is shown in Fig. 2.4A; experimental data for one of our membrane-in-the-middle cavities is shown in Fig. 2.4B. In the experimental data plot, it is possible to see other faint cavity resonance curves, which represent higher order transverse cavity modes.

The slope of the cavity resonance  $\partial\omega_C/\partial x$  has a particularly simple form in the limit  $|r_d| \ll 1$  because  $\cos^{-1} x \approx \frac{\pi}{2} - x$  in this limit, which gives

$$\omega_C(x) \approx \nu_{\text{FSR}} \left[ 2\phi_r + 2 \left( \frac{\pi}{2} - |r_d| \cos \left( \frac{2\pi}{\lambda/2} x \right) \right) \right] \quad (2.53)$$

Then

$$\frac{\partial\omega_C}{\partial x} \approx \nu_{\text{FSR}} \frac{4\pi}{\lambda} |r_d| \sin \left( \frac{4\pi}{\lambda} x \right) \quad (2.54)$$

Note that  $\nu_{\text{FSR}} \frac{4\pi}{\lambda} = 2\pi c/\lambda L = \omega_L/L$ , which allows us to write

$$\frac{\partial\omega_C}{\partial x} \approx \frac{\omega_L}{L} |r_d| \sin \left( \frac{4\pi}{\lambda} x \right) \quad (2.55)$$

where  $\omega_L$  is the laser frequency. Recall from Eq. 2.40 that for the cavity with a movable end mirror

$$\frac{\partial\omega_C}{\partial x} = -\frac{\omega_L}{L} \quad (2.56)$$

By comparing Eqs. 2.55 and 2.56, we see that the maximum slope for the membrane-in-the-middle geometry is smaller by a factor of  $|r_d| \sin \left( \frac{4\pi}{\lambda} x \right)$ . Also the slope vanishes at the node and antinode of the fields, so there is no linear coupling at these points.

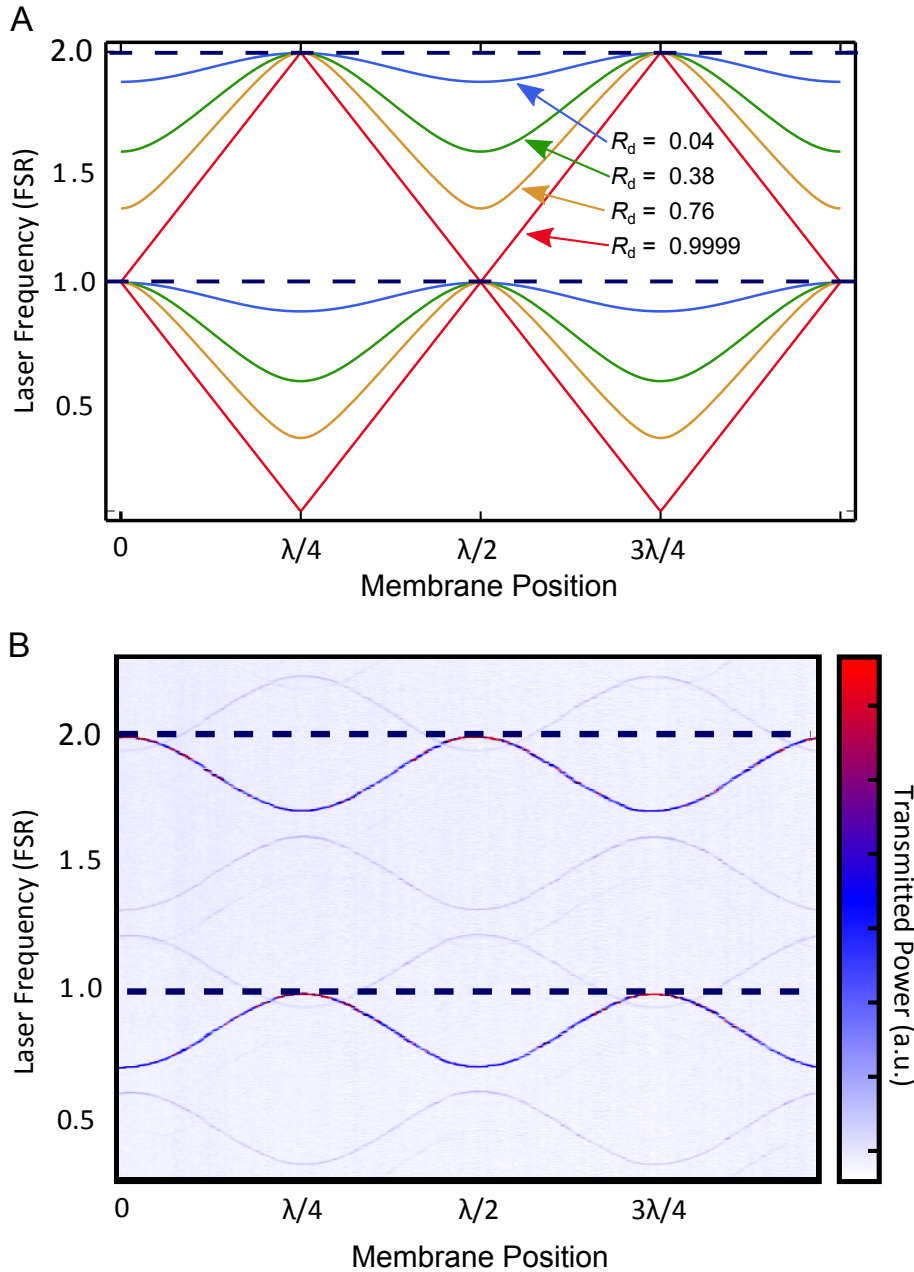


Figure 2.4: (A) A plot of the theoretical variation in cavity resonance frequency  $\omega_C(x)$  as a function of membrane position. The different curves represent different membrane reflectivities. (B) A plot of the cavity transmission for a scan of laser frequency and membrane position. Darker colors correspond to a higher transmission. The darkest line represents the lowest order Gaussian cross-section cavity mode. The dashed lines correspond to the empty cavity modes (i.e. a membrane with zero reflectivity).

### 2.4.3 Other interesting attributes of the membrane-in-the-middle geometry

As far as detecting the radiation pressure shot noise is concerned, the membrane-in-the-middle cavity geometry is identical to the movable end mirror cavity, so long as the coupling is reduced by  $|r_d| \sin\left(\frac{4\pi}{\lambda}x\right)$ . However, for other cavity optomechanical experiments, the membrane-in-the-middle geometry offers some unique advantages. First, the linear optomechanical coupling vanishes at the node and antinode (i.e.  $\partial\omega_C/\partial x = 0$ ). At these points the coupling is purely quadratic, and, given a membrane of sufficiently high reflectivity, it should be possible to do a quantum non-demolition measurement (QND) of the membrane phonon number [39, 97]. A single uniform layer of dielectric will never achieve the necessary reflectivities. However, a multilayer dielectric stack or a photonic crystal patterning of the membrane [98] could achieve the required reflectivities for the QND measurement.

It is possible to create substantially larger quadratic couplings near membrane positions  $x$  where different cavity spatial modes have the same frequency. In general the crossings will be avoided if there is a small coupling between the two cavity modes. This coupling between different cavity spatial modes can be tuned by changing the membrane's position and tilt within the cavity. Although solving for all the spatial modes of a cavity in three dimensions, including the effect of membrane tilt, is in general a computationally difficult problem, the problem simplifies in the limit of a low membrane reflectivity. The effect of the membrane can be calculated as a perturbation of the empty cavity modes as shown by Sankey et al. in Ref. [69]. Furthermore, they experimentally demonstrate the variation of the quadratic coupling strength with membrane tilt and position, and their results show agreement with the perturbative theory [69]. The largest observed quadratic coupling Ref. [69] was three orders of magnitude greater than the coupling at a node or antinode. While this quadratic coupling is still not large enough to observe single jumps in the phonon number, it should be possible to detect the phonon shot noise for a membrane that is driven into a large phonon number coherent state [68, 69].

## 2.5 Mechanical resonator's equation of motion in the high- $Q$ limit

After developing the equation of motion for the cavity from a classical perspective, we will do the same for the mechanical equation of motion. In particular, we will derive an equation of motion for the familiar simple harmonic oscillator, which is similar in form to the quantum equations of motion. The usual quantum equations of motion involve the time evolution of the creation and annihilation operators  $\hat{c}(t)$  and  $\hat{c}^\dagger(t)$  rather than the displacement  $\hat{x}(t)$ .

The starting point is the standard equation of motion for a mechanical resonator with energy damping rate  $\gamma$ , resonant frequency  $\omega_0$ , and mass  $m$  :

$$m\ddot{x} + m\gamma\dot{x} + m\omega_M^2 x = F(t) \quad (2.57)$$

This can be rewritten as two first order differential equations

$$\dot{p} = -\gamma p - m\omega_M^2 x + F(t) \quad (2.58)$$

$$\dot{x} = p/m \quad (2.59)$$

The complex-valued oscillator amplitude, which is a classical version of the annihilation operator, can be defined as

$$c(t) = \sqrt{\frac{m\omega_M}{2\hbar}} \left( x + \frac{ip}{m\omega_M} \right) \quad (2.60)$$

The magnitude of  $c(t)$  is proportional to the square root of the oscillator's energy  $|c(t)| \propto \sqrt{E}$ , and the phase of  $c(t)$  is the phase of the oscillator  $\arg c(t) = \phi$ . So  $c(t)$  can be interpreted as the oscillator's phasor, which is rotating in time with a frequency  $\omega_M$ . The time derivative of  $c(t)$  is

then

$$\dot{c}(t) = \sqrt{\frac{m\omega_M}{2\hbar}} \left( \dot{x} + \frac{i\dot{p}}{m\omega_M} \right) \quad (2.61)$$

$$= \sqrt{\frac{m\omega_M}{2\hbar}} \left( \frac{p}{m} + \frac{i(F(t) - \gamma p - m\omega_M^2 x)}{m\omega_M} \right) \quad (2.62)$$

$$= \sqrt{\frac{m\omega_M}{2\hbar}} \left( \frac{p}{m} - i\omega_M x - \frac{i\gamma p}{m\omega_M} + i \frac{F(t)}{m\omega_M} \right) \quad (2.63)$$

$$= -i\omega_M c(t) - \gamma \sqrt{\frac{m\omega_M}{2\hbar}} \left( \frac{i\gamma p}{m\omega_M} \right) + i \frac{F(t)}{\sqrt{2\hbar m\omega_M}} \quad (2.64)$$

$$= -i\omega_M c(t) - \frac{\gamma}{2} c(t) - \frac{\gamma}{2} c^*(t) + i \frac{F(t)}{\sqrt{2\hbar m\omega_M}} \quad (2.65)$$

So far no approximations have been made. Invoking the high- $Q$  approximation allows us to drop the  $c^*(t)$  term. This is because  $c(t)$  “resonates” at a frequency  $+\omega_M$  and the  $\frac{\gamma}{2}c^*(t)$  term looks like a small driving force, but with a frequency of  $-\omega_M$ , which is detuned from this high- $Q$  resonance by  $2\omega_M \gg \gamma$ . Finally, we get an equation of motion which looks very similar to the quantum version derived later in Eq. 2.70.

$$\dot{c}(t) = - \left( i\omega_0 + \frac{\gamma}{2} \right) c(t) + i \frac{F(t)}{\sqrt{2\hbar m\omega_0}} \quad (2.66)$$

In the cavity optomechanical system, the force  $F(t)$  contains contributions from the thermal force, classical radiation pressure, and radiation pressure shot noise.

## 2.6 Derivation of the quantum equations of motion for a coupled optical cavity and mechanical resonator

The classical derivations of the equations of motion are useful because they show the similarities between the classical and quantum coupled optical and mechanical oscillators. However, a rigorous treatment of the radiation pressure shot noise requires a fully quantum mechanical description of the system. This section outlines derivation of the quantum mechanical equations of motion for the coupled cavity and mechanical oscillators. The solution to the equation of motion is then worked out in detail. The essential change from the classical theory is that the complex-valued amplitudes

for the cavity field,  $a_{\text{cav}}(t)$ , and mechanical oscillator,  $c(t)$ , become operators  $\hat{a}(t)$  and  $\hat{c}(t)$ . Also, the input fields all contain additional fluctuations from the vacuum, which cause photon and phonon shot noise.

The Hamiltonian formalism captures the physics in a straightforward way. The full Hamiltonian of the optomechanical system includes the mechanical energy  $\hbar\omega_{\text{M}}\hat{c}^\dagger\hat{c}$ , the intracavity field energy  $\hbar\omega_{\text{C}}\hat{a}^\dagger\hat{a}$ , the coupling between the membrane motion and the fluctuations in the intracavity field  $\hbar A\hat{z}(\hat{a}^\dagger\hat{a} - \langle\hat{a}^\dagger\hat{a}\rangle)$ , the coupling of the cavity photons to a bath of photons outside the cavity  $\hat{H}_\kappa$ , and the coupling of the membrane phonons to a bath of phonons  $\hat{H}_\gamma$ :

$$\hat{H} = \hbar\omega_{\text{M}}\hat{c}^\dagger\hat{c} + \hbar(\omega_{\text{C}} + A\hat{z})(\hat{a}^\dagger\hat{a} - \langle\hat{a}^\dagger\hat{a}\rangle) + \hat{H}_\kappa + \hat{H}_\gamma \quad (2.67)$$

The bath of photons outside the cavity described by  $\hat{H}_\kappa$  includes a thermal bath plus some modes which are intentionally excited out of thermal equilibrium (i.e. a laser beam incident upon the cavity). The mechanical resonator's bath described by  $\hat{H}_\gamma$  only includes a thermal bath. The coupling constant  $A$  is the slope of the cavity resonance

$$A \equiv \frac{\partial\omega_{\text{cav}}}{\partial z} \quad (2.68)$$

The mechanical resonator's position is coupled to the fluctuations in photon number ( $\hat{a}^\dagger\hat{a} - \langle\hat{a}^\dagger\hat{a}\rangle$ ) because  $z = 0$  is defined to be the equilibrium membrane position including the spring force and the DC radiation pressure force. Adding the constant term  $-\hbar\omega_{\text{C}}\langle\hat{a}^\dagger\hat{a}\rangle$  to the Hamiltonian does not change the equations of motion.

The equations of motion for the intracavity field and mechanical resonator which result from the Hamiltonian in Eq. 2.67 are

$$\dot{\hat{a}} = -\left(\frac{\kappa}{2} + i\omega_{\text{C}}\right)\hat{a} - iA\hat{z}\hat{a} + \sqrt{\kappa_{\text{L}}}\hat{a}_{\text{in,L}} + \sqrt{\kappa_{\text{R}}}\hat{a}_{\text{in,R}} + \sqrt{\kappa_{\text{M}}}\hat{a}_{\text{in,M}} \quad (2.69)$$

$$\dot{\hat{c}} = -\left(\frac{\gamma}{2} + i\omega_{\text{M}}\right)\hat{c} - iA(\hat{a}^\dagger\hat{a} - \langle\hat{a}^\dagger\hat{a}\rangle) + \sqrt{\gamma}\hat{\eta} \quad (2.70)$$

The derivation is fairly straightforward, and is given in wonderful detail in the supplemental mate-

rials of Clerk et al. [34]. The original work by Gardiner and Collett on damped quantum systems is also still very useful [99].

The cavity decay rates out of the left and right end mirrors are related to the mirror transmission coefficients by  $\kappa_L = \sqrt{T_L/\tau}$  and  $\kappa_R = \sqrt{T_R/\tau}$ . The  $\kappa_M$  term accounts for the intracavity loss and end mirror absorption. Also, the cavity input terms  $\hat{a}_{\text{in},i}$  all contain quantum noise in addition to any fields which are driven by a laser. Another important thing to note is that the input fields are normalized so that  $\hat{a}_{\text{in},i}^\dagger \hat{a}_{\text{in},i}$  is the number of incident photons per second, while the intracavity field is normalized so that  $\hat{a}^\dagger \hat{a}$  is the number photons inside the cavity. More will be said about the input fields once we rewrite the equations in the rotating frame in the next subsection.

The mechanical resonator is driven by the fluctuation in radiation pressure in addition to a thermal force  $\hat{\eta}(t)$ . The thermal force obeys the relations

$$\langle \hat{\eta}(t) \hat{\eta}^\dagger(t') \rangle = (n_{\text{th}} + 1) \delta(t - t') \quad (2.71)$$

$$\langle \hat{\eta}^\dagger(t) \hat{\eta}(t') \rangle = n_{\text{th}} \delta(t - t') \quad (2.72)$$

where  $n_{\text{th}} = (e^{\hbar\omega_M/k_B T} - 1)^{-1}$  is the thermal phonon occupation number. Note that when the thermal force  $\hat{\eta}(t)$  is the only force on the membrane, the number of phonons in the mechanical mode will be  $\langle \hat{c}^\dagger \hat{c} \rangle = n_{\text{th}}$ .

The notation used throughout the dissertation for the quantum description is chosen to be consistent with Børkje et al. [4], which contains all the theoretical results for the correlation measurement scheme which is used to detect the RPSN.

### 2.6.1 Linearized cavity equations of motion in the rotating frame

The next step is to rewrite the cavity equation of motion (Eq. 2.69) in terms of small fluctuations about the drive frequency  $\omega_L$  (i.e. in the frame rotating at  $\omega_L$ ). The free evolution of the intracavity field (in the absence of damping, driving, or modulation by mirror motion) has the simple solution

$$\hat{a}(t) = \hat{a}(0)e^{-i\omega_L t}$$

By rewriting the fields in the rotating frame it means we separate the time dependence due to the free evolution of the field  $e^{-i\omega_L t}$  from the more interesting parts due to damping, driving, and modulation by mirror motion. We rewrite the intracavity and incident fields in the rotating frame as

$$\hat{a}(t) = e^{-i\omega_L t} \left( \bar{a} + \hat{d}(t) \right) \quad (2.73)$$

$$\hat{a}_{\text{in,L}}(t) = e^{-i\omega_L t} \left( a_{\text{in}}(t) + \hat{\xi}_{\text{L}}(t) \right) \quad (2.74)$$

$$\hat{a}_{\text{in},i}(t) = e^{-i\omega_L t} \hat{\xi}_i(t), \quad i = \text{R,M} \quad (2.75)$$

The intracavity field in the rotating frame is now  $\hat{d}(t)$  shown in Eq. 2.73, where  $\hat{d}(t)$  contains all the time dependence of the field except for the free evolution  $e^{-i\omega_L t}$ . The left input field  $\hat{a}_{\text{in,L}}(t)$  in the rotating frame in Eq. 2.74 contains two contributions. The first is the classical part

$$a_{\text{in}}(t) = \bar{a}_0 + \delta x(t) + i\delta y(t)$$

where

$$\bar{a}_0 = \sqrt{\frac{P_{\text{in}}}{\hbar\omega_L}} \quad (2.76)$$

is the coherent state amplitude of the incident laser and  $\delta x(t)$  and  $\delta y(t)$  are the classical phase and amplitude modulation noise in the laser, respectively. A phasor diagram of  $a_{\text{in}}(t)$  is shown in Fig. 2.5.

The second contribution to the left input field is the vacuum noise designated by  $\hat{\xi}_{\text{L}}(t)$ . The middle input field  $\hat{a}_{\text{in,M}}(t)$  given in Eq. 2.75 represents any absorption or scattering. It is a loss we cannot couple back into or detect (unlike end mirror transmission loss), so  $\hat{a}_{\text{in,M}}(t)$  only contains the vacuum fluctuations  $\hat{\xi}_{\text{M}}(t)$ . The right input  $\hat{a}_{\text{in,R}}(t)$  also only contains vacuum fluctuations  $\hat{\xi}_{\text{R}}(t)$  because our RPSN measurement scheme does not require we couple light via the right side of the cavity.

In the steady state there are no fluctuations in the intracavity field or membrane position, so  $\hat{d}(t) = 0$  and  $\hat{z}(t) = 0$ , and we ignore all the drive terms except for  $\bar{a}_{\text{in}}$ . Equation 2.69 then allows

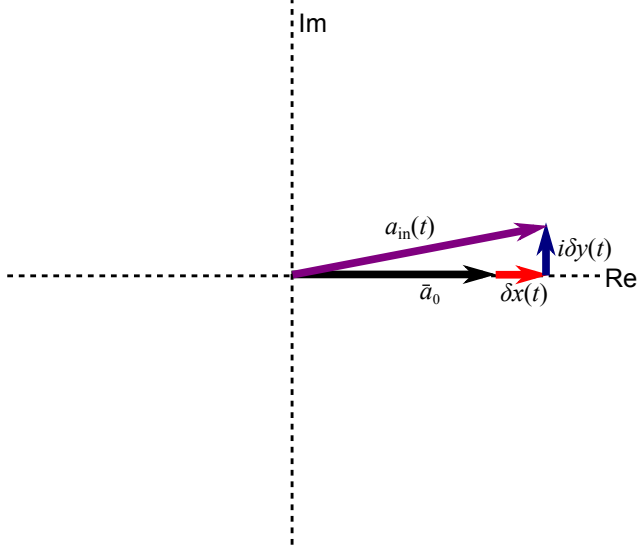


Figure 2.5: A phasor diagram of the classical input field  $a_{\text{in}}(t) = \bar{a}_0 + \delta x(t) + i\delta y(t)$  which is written in in the rotating frame. Note that  $\bar{a}_0$ ,  $\delta x(t)$ , and  $\delta y(t)$  are always assumed to be real valued. The fluctuations  $\delta x(t)$  have the same phasor orientation as the mean amplitude  $\bar{a}_0$ , which implies they are amplitude fluctuations. Similarly the fluctuations  $i\delta y(t)$  have a phasor orientation orthogonal to the mean amplitude  $\bar{a}_0$ , which implies they are phase fluctuations.

us to solve for the mean cavity amplitude  $\bar{a}$  in terms of the mean incident power  $\bar{a}_{\text{in}}$  :

$$-i\omega_L \bar{a} = -\left(\frac{\kappa}{2} + i\omega_C\right) \bar{a} + \sqrt{\kappa_L} \bar{a}_{\text{in}} \quad (2.77)$$

or

$$\bar{a} = \langle \hat{a} \rangle = \frac{\sqrt{\kappa_L}}{\frac{\kappa}{2} - i\Delta} \bar{a}_{\text{in}} \quad (2.78)$$

Substituting Eqs. 2.73-2.75 into the equation of motion for the cavity, Eq. 2.69, gives

$$\begin{aligned} -i\omega_L \left(\bar{a} + \hat{d}(t)\right) + \dot{\hat{d}}(t) = & -\left(\frac{\kappa}{2} + i\omega_C\right) \left(\bar{a} + \hat{d}(t)\right) - iA\hat{z} \left(\bar{a} + \hat{d}(t)\right) \\ & + \sqrt{\kappa_L} \left(\bar{a}_0 + \delta x(t) + i\delta y(t) + \hat{\xi}_L(t)\right) \\ & + \sqrt{\kappa_R} \hat{\xi}_R(t) + \sqrt{\kappa_M} \hat{\xi}_M(t) \quad (2.79) \end{aligned}$$

Substituting in the steady state solution in Eq. 2.77 will make some terms vanish. If we linearize

this equation of motion, we can drop the small term  $\hat{z}(t)\hat{d}(t)$  because  $\hat{z}(t)\hat{d}(t) \ll \hat{z}\bar{a}$ . Finally, we obtain the linearized cavity equation of motion in the rotating frame

$$\dot{\hat{d}} = -\left(\frac{\kappa}{2} - i\Delta\right)\hat{d} - i\alpha\hat{z} + \sqrt{\kappa_L}\left(\delta x + i\delta y + \hat{\xi}_L\right) + \sqrt{\kappa_R}\hat{\xi}_R + \sqrt{\kappa_M}\hat{\xi}_M \quad (2.80)$$

where  $\alpha = A\bar{a}$  is the optomechanical coupling and  $\Delta = \omega_L - \omega_C$  is the detuning.

## 2.6.2 Linearized mechanical equation of motion in the rotating (optical) frame

When considering the mechanical equation of motion given in Eq. 2.70, the only term which needs to be evaluated in the rotating optical frame and then linearized is  $\hat{a}^\dagger\hat{a} - \langle\hat{a}^\dagger\hat{a}\rangle$ . First note that

$$\hat{a}^\dagger\hat{a} = e^{+i\omega_D t}\left(\bar{a}^* + \hat{d}^\dagger\right)e^{-i\omega_D t}\left(\bar{a} + \hat{d}\right) \quad (2.81)$$

$$= |\bar{a}|^2 + \bar{a}^*\hat{d} + \bar{a}\hat{d}^\dagger + \hat{d}^\dagger\hat{d} \quad (2.82)$$

By definition,  $\hat{d}(t)$  represents only the fluctuating part of the intracavity field, so  $\langle\hat{d}(t)\rangle = 0$  giving

$$\hat{a}^\dagger\hat{a} - \langle\hat{a}^\dagger\hat{a}\rangle = |\bar{a}|^2 + \bar{a}^*\hat{d} + \bar{a}\hat{d}^\dagger + \hat{d}^\dagger\hat{d} - \langle|\bar{a}|^2 + \bar{a}^*\hat{d} + \bar{a}\hat{d}^\dagger + \hat{d}^\dagger\hat{d}\rangle \quad (2.83)$$

$$= \bar{a}^*\hat{d} + \bar{a}\hat{d}^\dagger + \hat{d}^\dagger\hat{d} - \langle\hat{d}^\dagger\hat{d}\rangle \quad (2.84)$$

$$\approx \bar{a}^*\hat{d} + \bar{a}\hat{d}^\dagger \quad (2.85)$$

In the last step the linearized approximation is made, and we neglect the  $\hat{d}^\dagger\hat{d}$  and  $\langle\hat{d}^\dagger\hat{d}\rangle$  terms. The mechanical equation of motion is then

$$\begin{aligned} \dot{\hat{c}} &= -\left(\frac{\gamma}{2} + i\omega_M\right)\hat{c} - iA\left(\bar{a}^*\hat{d} + \bar{a}\hat{d}^\dagger\right) + \sqrt{\gamma}\hat{\eta} \\ &= -\left(\frac{\gamma}{2} + i\omega_M\right)\hat{c} - i\left(\alpha^*\hat{d} + \alpha\hat{d}^\dagger\right) + \sqrt{\gamma}\hat{\eta} \end{aligned} \quad (2.86)$$

where  $\alpha = A\bar{a}$ .

### 2.6.3 Solution to cavity linearized equation of motion in the Fourier domain

Expressed in Fourier space, the linearized cavity equation of motion in the rotating (optical) frame given in Eq. 2.80 becomes

$$-i\omega\hat{d}[\omega] = -\left(\frac{\kappa}{2} - i\Delta\right)\hat{d}[\omega] - i\alpha\hat{z}[\omega] + \sqrt{\kappa_L}\left(\delta x[\omega] + i\delta y[\omega] + \hat{\xi}_L[\omega]\right) + \sqrt{\kappa_R}\hat{\xi}_R[\omega] + \sqrt{\kappa_M}\hat{\xi}_M[\omega] \quad (2.87)$$

Solving for  $\hat{d}[\omega]$  gives

$$\hat{d}[\omega] = \frac{1}{\frac{\kappa}{2} - i(\omega + \Delta)} \quad (2.88)$$

$$\begin{aligned} &\times \left[-i\alpha\hat{z}[\omega] + \sqrt{\kappa_L}\left(\delta x[\omega] + i\delta y[\omega] + \hat{\xi}_L[\omega]\right) + \sqrt{\kappa_R}\hat{\xi}_R[\omega] + \sqrt{\kappa_M}\hat{\xi}_M[\omega]\right] \\ &= -\chi_C[\omega]\left(i\alpha\hat{z}[\omega] - \hat{\zeta}[\omega]\right) \end{aligned} \quad (2.89)$$

where we define the cavity susceptibility  $\chi_C[\omega]$  to be

$$\chi_C[\omega] = \frac{1}{\frac{\kappa}{2} - i(\omega + \Delta)} \quad (2.90)$$

The  $\hat{\zeta}[\omega]$  term represents the classical and quantum noise which couples into the cavity and is defined by

$$\hat{\zeta}[\omega] = \sqrt{\kappa_L}\left(\delta x[\omega] + i\delta y[\omega] + \hat{\xi}_L[\omega]\right) + \sqrt{\kappa_R}\hat{\xi}_R[\omega] + \sqrt{\kappa_M}\hat{\xi}_M[\omega] \quad (2.91)$$

### 2.6.4 Solution to the mechanical equation of motion in the Fourier domain

Expressed in Fourier space, the mechanical equation of motion given in Eq. 2.86 becomes

$$-i\omega\hat{c}[\omega] = -\left(\frac{\gamma}{2} + i\omega_M\right)\hat{c}[\omega] - i\left(\alpha^*\hat{d}[\omega] + \alpha\hat{d}^\dagger[\omega]\right) + \sqrt{\gamma}\hat{\eta}[\omega] \quad (2.92)$$

This has a solution of

$$\hat{c}[\omega] = \frac{1}{\frac{\gamma}{2} - i(\omega - \omega_M)} \left[ -i\left(\alpha^*\hat{d}[\omega] + \alpha\hat{d}^\dagger[\omega]\right) + \sqrt{\gamma}\hat{\eta}[\omega] \right] \quad (2.93)$$

$$= \chi_M[\omega] \left[ -i\left(\alpha^*\hat{d}[\omega] + \alpha\hat{d}^\dagger[\omega]\right) + \sqrt{\gamma}\hat{\eta}[\omega] \right] \quad (2.94)$$

where the mechanical susceptibility  $\chi_M[\omega]$  is defined as

$$\chi_M[\omega] \equiv \frac{1}{\gamma/2 - i(\omega - \omega_M)} \quad (2.95)$$

Equation 2.94 gives the solution for the mechanical annihilation operator  $\hat{c}[\omega]$ , but we really want the solution for  $\hat{z}[\omega] = \hat{c}[\omega] + \hat{c}^\dagger[\omega]$ . First we take the Hermitian conjugate of the mechanical equation of motion in the time domain given by Eq. 2.86, which gives

$$\dot{\hat{c}}^\dagger = -\left(\frac{\gamma}{2} - i\omega_M\right)\hat{c}^\dagger + i\left(\alpha\hat{d}^\dagger + \alpha^*\hat{d}\right) + \sqrt{\gamma}\hat{\eta}^\dagger \quad (2.96)$$

In Fourier space this equation of motion becomes

$$-i\omega\hat{c}^\dagger[\omega] = -\left(\frac{\gamma}{2} - i\omega_M\right)\hat{c}^\dagger[\omega] + i\left(\alpha\hat{d}^\dagger[\omega] + \alpha^*\hat{d}[\omega]\right) + \sqrt{\gamma}\hat{\eta}^\dagger[\omega] \quad (2.97)$$

Solving for  $\hat{c}^\dagger[\omega]$  gives

$$\hat{c}^\dagger[\omega] = \frac{1}{\frac{\gamma}{2} - i(\omega + \omega_M)} \left[ i\left(\alpha\hat{d}^\dagger[\omega] + \alpha^*\hat{d}[\omega]\right) + \sqrt{\gamma}\hat{\eta}^\dagger[\omega] \right] \quad (2.98)$$

$$= \chi_M^*[-\omega] \left[ i\left(\alpha\hat{d}^\dagger[\omega] + \alpha^*\hat{d}[\omega]\right) + \sqrt{\gamma}\hat{\eta}^\dagger[\omega] \right] \quad (2.99)$$

Then  $\hat{z}[\omega] = \hat{c}[\omega] + \hat{c}^\dagger[\omega]$  becomes

$$\hat{z}[\omega] = \hat{c}[\omega] + \hat{c}^\dagger[\omega] \quad (2.100)$$

$$\begin{aligned} &= \chi_M[\omega] \left[ -i \left( \alpha^* \hat{d}[\omega] + \alpha \hat{d}^\dagger[\omega] \right) + \sqrt{\gamma} \hat{\eta}[\omega] \right] \\ &\quad + \chi_M^*[-\omega] \left[ i \left( \alpha \hat{d}^\dagger[\omega] + \alpha^* \hat{d}[\omega] \right) + \sqrt{\gamma} \hat{\eta}^\dagger[\omega] \right] \end{aligned} \quad (2.101)$$

Both terms in Eq. 2.101 contain the expression  $\alpha^* \hat{d}[\omega] + \alpha \hat{d}^\dagger[\omega]$ . Rewriting  $\hat{d}^\dagger[\omega]$  in terms of incident fields and mechanical motion via Eq. 2.88 gives

$$\begin{aligned} \alpha^* \hat{d}[\omega] + \alpha \hat{d}^\dagger[\omega] &= -\alpha^* \chi_C[\omega] \left( i \alpha \hat{z}[\omega] - \hat{\zeta}[\omega] \right) \\ &\quad + \alpha \chi_C^*[-\omega] \left( i \alpha^* \hat{z}[\omega] + \hat{\zeta}^\dagger[\omega] \right) \end{aligned} \quad (2.102)$$

$$\begin{aligned} &= i |\alpha|^2 \hat{z}[\omega] (-\chi_C[\omega] + \chi_C^*[-\omega]) \\ &\quad + \left( \alpha^* \chi_C[\omega] \hat{\zeta}[\omega] + \alpha \chi_C^*[-\omega] \hat{\zeta}^\dagger[\omega] \right) \end{aligned} \quad (2.103)$$

Substituting this into Eq. 2.101 gives

$$\begin{aligned} \hat{z}[\omega] &= \chi_M[\omega] \left[ |\alpha|^2 \hat{z}[\omega] (-\chi_C[\omega] + \chi_C^*[-\omega]) \right. \\ &\quad \left. - i \left( \alpha^* \chi_C[\omega] \hat{\zeta}[\omega] + \alpha \chi_C^*[-\omega] \hat{\zeta}^\dagger[\omega] \right) + \sqrt{\gamma} \hat{\eta}[\omega] \right] \\ &\quad + \chi_M^*[-\omega] \left[ -|\alpha|^2 \hat{z}[\omega] (-\chi_C[\omega] + \chi_C^*[-\omega]) \right. \\ &\quad \left. + i \left( \alpha^* \chi_C[\omega] \hat{\zeta}[\omega] + \alpha \chi_C^*[-\omega] \hat{\zeta}^\dagger[\omega] \right) + \sqrt{\gamma} \hat{\eta}^\dagger[\omega] \right] \end{aligned} \quad (2.104)$$

Collecting the  $\hat{z}[\omega]$  terms gives

$$\begin{aligned} \hat{z}[\omega] \left[ 1 - |\alpha|^2 (-\chi_C[\omega] + \chi_C^*[-\omega]) (\chi_M[\omega] - \chi_M^*[-\omega]) \right] &= \\ -i (\chi_M[\omega] - \chi_M^*[-\omega]) \left( \alpha^* \chi_C[\omega] \hat{\zeta}[\omega] + \alpha \chi_C^*[-\omega] \hat{\zeta}^\dagger[\omega] \right) & \\ + \sqrt{\gamma} (\chi_M[\omega] \hat{\eta}[\omega] + \chi_M^*[-\omega] \hat{\eta}^\dagger[\omega]) & \quad (2.105) \end{aligned}$$

Now we solve for  $\hat{z}[\omega]$  and multiply numerator and denominator by  $\chi_M[\omega]^{-1}\chi_M^*[-\omega]^{-1}$ :

$$\hat{z}[\omega] = \frac{-i(\chi_M[-\omega]^{-1} - \chi_M[\omega]^{-1}) \left( \alpha^* \chi_C[\omega] \hat{\zeta}[\omega] + \alpha \chi_C^*[-\omega] \hat{\zeta}^\dagger[\omega] \right)}{\chi_M[\omega]^{-1} \chi_M^*[-\omega]^{-1} - |\alpha|^2 (-\chi_C[\omega] + \chi_C^*[-\omega]) (\chi_M[-\omega]^{-1} - \chi_M[\omega]^{-1})} + \frac{\sqrt{\gamma} (\chi_M^*[-\omega]^{-1} \hat{\eta}[\omega] + \chi_M[\omega]^{-1} \hat{\eta}^\dagger[\omega])}{\chi_M[\omega]^{-1} \chi_M^*[-\omega]^{-1} - |\alpha|^2 (-\chi_C[\omega] + \chi_C^*[-\omega]) (\chi_M[-\omega]^{-1} - \chi_M[\omega]^{-1})} \quad (2.106)$$

Noting that

$$\chi_M^*[-\omega]^{-1} - \chi_M[\omega]^{-1} = (\gamma/2 + i(-\omega - \omega_M)) - (\gamma/2 - i(\omega - \omega_M)) = -2i\omega_M \quad (2.107)$$

we get a slightly simpler form for  $\hat{z}[\omega]$ :

$$\hat{z}[\omega] = \frac{-i(-2i\omega_M) \left( \alpha^* \chi_C[\omega] \hat{\zeta}[\omega] + \alpha \chi_C^*[-\omega] \hat{\zeta}^\dagger[\omega] \right)}{\chi_M[\omega]^{-1} \chi_M^*[-\omega]^{-1} - |\alpha|^2 (-\chi_C[\omega] + \chi_C^*[-\omega]) (-2i\omega_M)} + \frac{\sqrt{\gamma} (\chi_M^*[-\omega]^{-1} \hat{\eta}[\omega] + \chi_M[\omega]^{-1} \hat{\eta}^\dagger[\omega])}{\chi_M[\omega]^{-1} \chi_M^*[-\omega]^{-1} - |\alpha|^2 (-\chi_C[\omega] + \chi_C^*[-\omega]) (-2i\omega_M)} \quad (2.108)$$

Lastly, we define the functions

$$\Sigma[\omega] = -i|\alpha|^2 (\chi_C[\omega] - \chi_C^*[-\omega]) \quad (2.109)$$

$$N[\omega] = \chi_M[\omega]^{-1} \chi_M^*[-\omega]^{-1} + 2\omega_M \Sigma[\omega] \quad (2.110)$$

which gives a nice expression for the mechanical position

$$\hat{z}[\omega] = \frac{1}{N[\omega]} \left[ \sqrt{\gamma} (\chi_M^*[-\omega]^{-1} \hat{\eta}[\omega] + \chi_M[\omega]^{-1} \hat{\eta}^\dagger[\omega]) - 2\omega_M \left( \alpha^* \chi_C[\omega] \hat{\zeta}[\omega] + \alpha \chi_C^*[-\omega] \hat{\zeta}^\dagger[\omega] \right) \right] \quad (2.111)$$

## 2.7 Optical resonant frequency shift and optical damping

### 2.7.1 Effective susceptibility of the resonator

Having the solution for the position fluctuations  $\hat{z}[\omega]$  in terms of the drive forces allows us to sensibly define an effective mechanical susceptibility  $\chi_{M,\text{eff}}[\omega]$ , which represents changes to the bare susceptibility  $\chi_M[\omega]$  due to an optical spring and damping caused by radiation pressure. In order to determine this effective optomechanical susceptibility, we consider only the first term in the expression for  $\hat{z}[\omega]$  given above in Eq. 2.111:

$$\frac{1}{N[\omega]} \sqrt{\gamma} (\chi_M^*[-\omega]^{-1} \hat{\eta}[\omega]) = \frac{\chi_M^*[-\omega]^{-1}}{N[\omega]} \sqrt{\gamma} \hat{\eta}[\omega] \quad (2.112)$$

The  $\sqrt{\gamma} \hat{\eta}[\omega]$  term is the Langevin force due to being coupled to a bath of phonons. The prefactor is then the effective susceptibility of the resonator, which includes the modifications of the resonant frequency and damping due to radiation pressure:

$$\chi_{M,\text{eff}}[\omega] \equiv \frac{\chi_M^*[-\omega]^{-1}}{N[\omega]} \quad (2.113)$$

The remainder of this section is devoted to simplifying the effective susceptibility  $\chi_{M,\text{eff}}[\omega]$  given in Eq. 2.113 and getting explicit formulas for the optical resonant frequency shift and optical damping. First, expand out  $\chi_{M,\text{eff}}[\omega]$  in terms of  $\omega$ 's,  $\gamma$ , and  $\Sigma[\omega]$ :

$$\chi_{M,\text{eff}}[\omega] = \frac{1}{N[\omega]} \chi_M^*[-\omega]^{-1} \quad (2.114)$$

$$= \frac{\left(\frac{\gamma}{2} - i(\omega + \omega_M)\right)}{\left(\frac{\gamma}{2} - i(\omega + \omega_M)\right) \left(\frac{\gamma}{2} - i(\omega - \omega_M)\right) + 2\omega_M \Sigma[\omega]} \quad (2.115)$$

$$= \frac{1}{\left(\frac{\gamma}{2} - i(\omega - \omega_M)\right) + 2\omega_M \Sigma[\omega] / \left(\frac{\gamma}{2} - i(\omega + \omega_M)\right)} \quad (2.116)$$

The inverse of the effective mechanical susceptibility can be rewritten as

$$\chi_{M,\text{eff}}^{-1}[\omega] = \left( \frac{\gamma}{2} + i(-\omega + \omega_M) \right) + 2\omega_M \Sigma[\omega] / \left( \frac{\gamma}{2} - i(\omega + \omega_M) \right) \quad (2.117)$$

$$= \chi_M^{-1}[\omega] + 2\omega_M \Sigma[\omega] \chi_M^*[-\omega] \quad (2.118)$$

In the weak coupling limit where  $|\gamma_{\text{opt}}| \ll \kappa, \omega_M$ ,  $\chi_{M,\text{eff}}[\omega]$  is very small except near  $\omega_M$ . Also, over this small range of frequencies near  $\omega_M$ ,  $\Sigma[\omega]$  and  $\chi_M^*[-\omega]$  can be treated as constants where  $\Sigma[\omega] \approx \Sigma[\omega_M]$  and  $\chi_M^*[-\omega_M] \approx 1/(-2i\omega_M)$ . Then Eq. 2.117 becomes

$$\chi_{M,\text{eff}}^{-1}[\omega] = \left( \frac{\gamma}{2} + i(-\omega + \omega_M) \right) + i\Sigma[\omega_M] \quad (2.119)$$

We can immediately write the radiation pressure induced frequency shift  $\delta\omega_M$  and optical damping  $\gamma_{\text{opt}}$  as

$$\delta\omega_M = \text{Re}\Sigma[\omega_M] \quad (2.120)$$

$$\gamma_{\text{opt}} = -2\text{Im}\Sigma[\omega_M] \quad (2.121)$$

The effective mechanical resonant frequency  $\tilde{\omega}_M$  and effective damping  $\tilde{\gamma}_M$  are

$$\tilde{\omega}_M = \omega_M + \delta\omega_M \quad (2.122)$$

$$\tilde{\gamma} = \gamma + \gamma_{\text{opt}} \quad (2.123)$$

A plot of the resonant frequency shift  $\delta\omega_M$  and damping  $\gamma_{\text{opt}}$  due to the radiation pressure is given in Fig. 2.6. Both the frequency shift  $\delta\omega_M$  and damping  $\gamma_{\text{opt}}$  depend on the detuning  $\Delta$ , but the qualitative nature of this relationship depends on the ratio of the cavity linewidth  $\kappa$  and the mechanical resonant frequency  $\omega_M$ . If  $\kappa/\omega_M \ll 1$ , which is called the “good-cavity” or “resolved sideband limit,” then there are distinct sharp features at  $\Delta = 0, \pm\omega_M$ . In particular, the damping  $\gamma_{\text{opt}}$  has a maximum at  $\Delta = -\omega_M$ , indicating that this is the detuning for optimal laser cooling. The other extreme limit, where the cavity linewidth greatly exceeds the mechanical

resonance frequency  $\kappa/\omega_M \gg 1$ , is sometimes called the “bad-cavity limit.” In the bad-cavity limit the frequency shift and damping are both proportional to the slope of the Lorentzian line shape of the cavity  $\delta\omega_M, \gamma_{\text{opt}} \propto \Delta / \left(1 + \left(\frac{\Delta}{\kappa/2}\right)^2\right)$ . This bad-cavity limit is the nearly-adiabatic limit that was first observed and explained theoretically by Karrai et. al. The membrane-in-the-middle cavity used for this dissertation has a ratio of  $\kappa/\omega_M \approx 1.1$  (the red curve in Fig. 2.6A and 2.6B), which is in neither the good-cavity nor the bad-cavity limit.

## 2.7.2 Longer expressions for the frequency shift and optical damping

Before moving on to a discussion of the radiation pressure shot noise, it is convenient to have the optical frequency shift  $\delta\omega_M$  and  $\gamma_{\text{opt}}$ , given by Eqs. 2.120 and 2.121, written out explicitly in terms of  $\kappa$ ,  $\omega_M$ , and  $\Delta$ . Inserting the definitions for  $\Sigma[\omega]$  (Eq. 2.109) and  $\chi_C[\omega]$  (Eq. 2.90) into Eq. 2.120 for  $\delta\omega_M$  and Eq. 2.121 for  $\gamma_{\text{opt}}$  and performing some algebra gives

$$\delta\omega_M = \text{Re}\Sigma[\omega_M] \quad (2.124)$$

$$= \text{Re} \left[ -i |\alpha|^2 (\chi_C[\omega_M] - \chi_C^*[-\omega_M]) \right] \quad (2.125)$$

$$= \text{Re} \left[ -i |\alpha|^2 \left( \frac{1}{\frac{\kappa}{2} - i(\omega_M + \Delta)} - \frac{1}{\frac{\kappa}{2} + i(-\omega_M + \Delta)} \right) \right] \quad (2.126)$$

$$= \text{Re} \left[ -i |\alpha|^2 \left( \frac{\frac{\kappa}{2} + i(\omega_M + \Delta)}{\left(\frac{\kappa}{2}\right)^2 + (\omega_M + \Delta)^2} - \frac{\frac{\kappa}{2} - i(-\omega_M + \Delta)}{\left(\frac{\kappa}{2}\right)^2 + (-\omega_M + \Delta)^2} \right) \right] \quad (2.127)$$

$$= |\alpha|^2 \left( \frac{\omega_M + \Delta}{\left(\frac{\kappa}{2}\right)^2 + (\omega_M + \Delta)^2} + \frac{-\omega_M + \Delta}{\left(\frac{\kappa}{2}\right)^2 + (-\omega_M + \Delta)^2} \right) \quad (2.128)$$

and

$$\gamma_{\text{opt}} = -2\text{Im}\Sigma[\omega_M] \quad (2.129)$$

$$= -2\text{Im} \left[ -i |\alpha|^2 \left( \frac{\frac{\kappa}{2} + i(\omega_M + \Delta)}{\left(\frac{\kappa}{2}\right)^2 + (\omega_M + \Delta)^2} - \frac{\frac{\kappa}{2} - i(-\omega_M + \Delta)}{\left(\frac{\kappa}{2}\right)^2 + (-\omega_M + \Delta)^2} \right) \right] \quad (2.130)$$

$$= 2 |\alpha|^2 \frac{\kappa}{2} \left( \frac{1}{\left(\frac{\kappa}{2}\right)^2 + (\omega_M + \Delta)^2} - \frac{1}{\left(\frac{\kappa}{2}\right)^2 + (-\omega_M + \Delta)^2} \right) \quad (2.131)$$

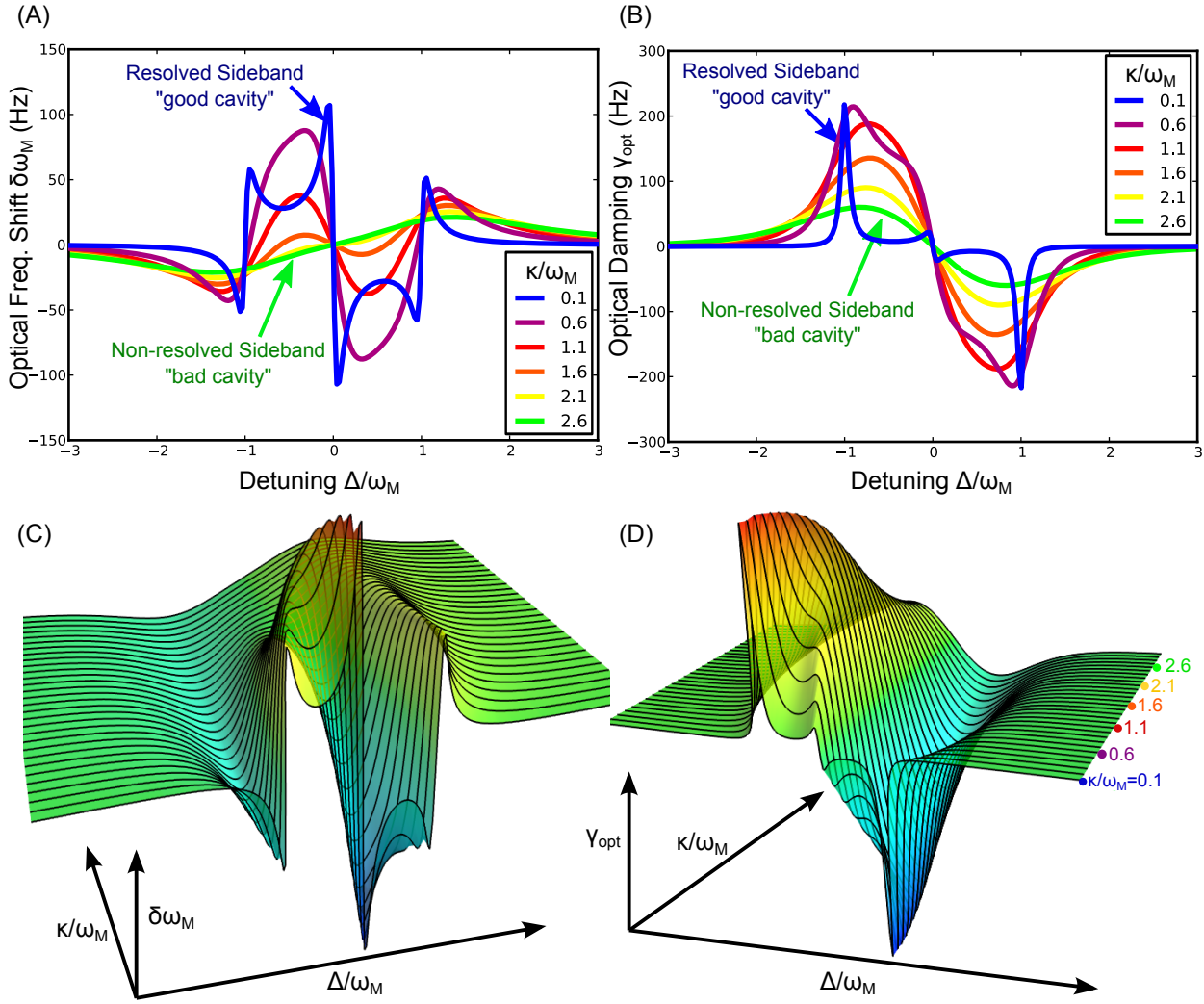


Figure 2.6: Plots of the radiation pressure induced changes to the mechanical resonant frequency  $\delta\omega_M$  (in subplots A and C) and damping  $\gamma_{opt}$  (in subplots B and D). The 3D subplots in C and D show the transition from the resolved sideband regime  $\kappa/\omega_M = 0.1$  to the non-resolved sideband regime  $\kappa/\omega_M = 3.0$ . Only the cavity damping rate  $\kappa$  and the detuning  $\Delta$  are varied. All other parameters are held constant. The magnitude of the optomechanical coupling which can be varied by changing the incident power  $P_{in}$  and the slope  $\partial\omega_{CSV}/\partial z$  acts as a vertical scaling factor for the curves, but otherwise does not change the shape.

The magnitude of the optomechanical coupling strength  $|\alpha|$  is given by

$$|\alpha|^2 = |\bar{a}|^2 A^2 \quad (2.132)$$

$$= \frac{\kappa_L |a_{\text{in}}|^2}{\left(\frac{\kappa}{2}\right)^2 + \Delta^2} \left| \frac{\partial \omega_{\text{cav}}}{\partial z} \right|^2 \quad (2.133)$$

$$= \frac{\kappa_L \frac{P_{\text{in}}}{\hbar \omega_L}}{\left(\frac{\kappa}{2}\right)^2 + \Delta^2} x_{\text{zpt}}^2 \left| \frac{\partial \omega_{\text{cav}}}{\partial \tilde{z}} \right|^2 \quad (2.134)$$

$$= \frac{\kappa_L}{\left(\frac{\kappa}{2}\right)^2 + \Delta^2} \frac{P_{\text{in}}}{\hbar \omega_L} \frac{\hbar}{2m\omega_M} \left| \frac{\partial \omega_{\text{cav}}}{\partial \tilde{z}} \right|^2 \quad (2.135)$$

The mean intracavity field  $\bar{a}$  is given in Eq. 2.78, and the coupling constant  $A = \partial \omega_{\text{cav}} / \partial z$  was defined in Eq. 2.68. The input field strength  $|a_{\text{in}}|^2 = P_{\text{in}} / \hbar \omega_L$  is the number of photons incident on the cavity per second and was defined in Eq. 2.76. The position  $\tilde{z} = x_{\text{zpt}} z$  has been rescaled by the zero point fluctuation displacement  $x_{\text{zpt}}$  to convert the position back into length units, rather than the unitless scaled position  $\hat{z} = \hat{c} + \hat{c}^\dagger$ .

## 2.8 Derivation of the position power spectral density $S_z[\omega]$

Calculating the position power spectral density  $S_z[\omega]$  gives us an easy way to interpret equations of the form  $S_z[\omega] = \chi_{M,\text{eff}}[\omega] (S_F^{\text{th}}[\omega] + S_F^{\text{sp}}[\omega])$ . It also allows us to pick out the force power spectral densities for RPSN  $S_F^{\text{sp}}[\omega]$  and the thermal force  $S_F^{\text{th}}[\omega]$ .

The solution for  $\hat{z}[\omega]$  in Eq. 2.101 can be rewritten in terms of the effective susceptibility  $\chi_{M,\text{eff}}[\omega] = \chi_M^*[-\omega]^{-1} / N[\omega]$  given in Eq. 2.113:

$$\begin{aligned} \hat{z}[\omega] &= \frac{1}{N[\omega]} \left[ \sqrt{\gamma} (\chi_M^*[-\omega]^{-1} \hat{\eta}[\omega] + \chi_M[\omega]^{-1} \hat{\eta}^\dagger[\omega]) \right. \\ &\quad \left. - 2\omega_M (\alpha^* \chi_C[\omega] \hat{\zeta}[\omega] + \alpha \chi_C^*[-\omega] \hat{\zeta}^\dagger[\omega]) \right] \end{aligned} \quad (2.136)$$

$$\begin{aligned} &= \chi_{M,\text{eff}}[\omega] \left[ \sqrt{\gamma} \hat{\eta}[\omega] - \chi_M^*[-\omega] (2\omega_M \alpha^* \chi_C[\omega] \hat{\zeta}[\omega]) \right] \\ &\quad + \chi_{M,\text{eff}}^*[-\omega] \left[ \sqrt{\gamma} \hat{\eta}^\dagger[\omega] - \chi_M[\omega]^{-1} (2\omega_M \alpha \chi_C^*[-\omega] \hat{\zeta}^\dagger[\omega]) \right] \end{aligned} \quad (2.137)$$

$$= \chi_{M,\text{eff}}[\omega] \left[ \sqrt{\gamma} \hat{\eta}[\omega] - i\alpha^* \chi_C[\omega] \hat{\zeta}[\omega] \right] + \chi_{M,\text{eff}}^*[-\omega] \left[ \sqrt{\gamma} \hat{\eta}^\dagger[\omega] + i\alpha \chi_C^*[-\omega] \hat{\zeta}^\dagger[\omega] \right] \quad (2.138)$$

In the last step we used the fact that in the high- $Q$  approximation, only frequencies near  $\omega_M$  are considered, and  $\chi_M^*[-\omega]$  and  $\chi_M[\omega]^{-1}$  are approximately constant near  $\omega = +\omega_M$ :

$$\chi_M^*[-\omega_M] = \frac{1}{\frac{\gamma}{2} - i(\omega_M + \omega_M)} \approx \frac{i}{2\omega_M} \quad (2.139)$$

$$\chi_M^*[-\omega_M] = \frac{1}{\frac{\gamma}{2} - i(\omega_M + \omega_M)} \approx \frac{i}{2\omega_M} \quad (2.140)$$

Comparing Eq. 2.138 to  $\hat{z}[\omega] = \hat{c}[\omega] + \hat{c}^\dagger[\omega]$ , we see that

$$\hat{c}[\omega] = \chi_{M,\text{eff}}[\omega] \left[ \sqrt{\gamma} \hat{\eta}[\omega] - i\alpha^* \chi_C[\omega] \hat{\zeta}[\omega] \right] \quad (2.141)$$

$$\hat{c}^\dagger[\omega] = \chi_{M,\text{eff}}^*[-\omega] \left[ \sqrt{\gamma} \hat{\eta}^\dagger[\omega] + i\alpha \chi_C^*[-\omega] \hat{\zeta}^\dagger[\omega] \right] \quad (2.142)$$

Next, the definition of the power spectral density is given by

$$S_z[\omega] = \frac{1}{4\pi} \int_{-\infty}^{\infty} d\omega' \langle \{ \hat{z}[\omega], \hat{z}[\omega'] \} \rangle \quad (2.143)$$

$$= \frac{1}{2\pi} \int_{-\infty}^{\infty} d\omega' \langle \hat{z}[\omega] \hat{z}[\omega'] \rangle \quad (2.144)$$

$$= \frac{1}{2\pi} \int_{-\infty}^{\infty} d\omega' \langle (\hat{c}[\omega] + \hat{c}^\dagger[\omega]) (\hat{c}[\omega'] + \hat{c}^\dagger[\omega']) \rangle \quad (2.145)$$

$$= \frac{1}{2\pi} \int_{-\infty}^{\infty} d\omega' \langle \hat{c}[\omega] \hat{c}^\dagger[\omega'] + \hat{c}^\dagger[\omega] \hat{c}[\omega'] \rangle \quad (2.146)$$

The anticommutator in Eq. 2.143 becomes a factor of two because  $\hat{z}[\omega] = \hat{c}[\omega] + \hat{c}^\dagger[\omega]$  is Hermitian.

The terms  $\langle \hat{c}[\omega]\hat{c}[\omega'] \rangle$  and  $\langle \hat{c}^\dagger[\omega]\hat{c}^\dagger[\omega'] \rangle$  are both zero. The remaining terms become

$$\begin{aligned} \frac{1}{2\pi} \int_{-\infty}^{\infty} d\omega' \langle \hat{c}[\omega]\hat{c}^\dagger[\omega'] \rangle &= \frac{1}{2\pi} \int_{-\infty}^{\infty} d\omega' \left\langle \chi_{M,\text{eff}}[\omega] \left[ \sqrt{\gamma}\hat{\eta}[\omega] - i\alpha^* \chi_C[\omega]\hat{\zeta}[\omega] \right] \right. \\ &\quad \left. \times \chi_{M,\text{eff}}^*[-\omega'] \left[ \sqrt{\gamma}\hat{\eta}^\dagger[\omega'] + i\alpha \chi_C^*[-\omega']\hat{\zeta}^\dagger[\omega'] \right] \right\rangle \end{aligned} \quad (2.147)$$

$$\begin{aligned} &= \frac{1}{2\pi} \int_{-\infty}^{\infty} d\omega' \chi_{M,\text{eff}}[\omega] \chi_{M,\text{eff}}^*[-\omega'] \\ &\quad \left[ \gamma \langle \hat{\eta}[\omega]\hat{\eta}^\dagger[\omega'] \rangle + |\alpha|^2 \chi_C[\omega]\chi_C^*[-\omega'] \langle \hat{\zeta}[\omega]\hat{\zeta}^\dagger[\omega'] \rangle \right] \end{aligned} \quad (2.148)$$

$$\begin{aligned} &= \frac{1}{2\pi} \int_{-\infty}^{\infty} d\omega' \chi_{M,\text{eff}}[\omega] \chi_{M,\text{eff}}^*[-\omega'] \\ &\quad \left[ \gamma (n_{\text{th}} + 1) 2\pi\delta(\omega + \omega') + |\alpha|^2 \chi_C[\omega]\chi_C^*[-\omega'] \kappa 2\pi\delta(\omega + \omega') \right] \end{aligned} \quad (2.149)$$

$$= \frac{1}{2\pi} \chi_{M,\text{eff}}^*[\omega] \chi_{M,\text{eff}}[\omega] \left[ 2\pi\gamma (n_{\text{th}} + 1) + 2\pi\kappa |\alpha|^2 \chi_C[\omega]\chi_C^*[\omega] \right] \quad (2.150)$$

$$= |\chi_{M,\text{eff}}[\omega]|^2 \left[ \gamma (n_{\text{th}} + 1) + \kappa |\alpha|^2 |\chi_C[\omega]|^2 \right] \quad (2.151)$$

and

$$\begin{aligned} \frac{1}{2\pi} \int_{-\infty}^{\infty} d\omega' \langle \hat{c}^\dagger[\omega]\hat{c}[\omega'] \rangle &= \frac{1}{2\pi} \int_{-\infty}^{\infty} d\omega' \left\langle \chi_{M,\text{eff}}^*[-\omega] \left[ \sqrt{\gamma}\hat{\eta}^\dagger[\omega] + i\alpha \chi_C^*[-\omega]\hat{\zeta}^\dagger[\omega] \right] \right. \\ &\quad \left. \times \chi_{M,\text{eff}}[\omega'] \left[ \sqrt{\gamma}\hat{\eta}[\omega'] - i\alpha^* \chi_C[\omega']\hat{\zeta}[\omega'] \right] \right\rangle \end{aligned} \quad (2.152)$$

$$\begin{aligned} &= \frac{1}{2\pi} \int_{-\infty}^{\infty} d\omega' \chi_{M,\text{eff}}^*[-\omega] \chi_{M,\text{eff}}[\omega'] \\ &\quad \times \left[ \gamma \langle \hat{\eta}^\dagger[\omega]\hat{\eta}[\omega'] \rangle + |\alpha|^2 \chi_C^*[-\omega]\chi_C[\omega'] \langle \hat{\zeta}^\dagger[\omega]\hat{\zeta}[\omega'] \rangle \right] \end{aligned} \quad (2.153)$$

$$\begin{aligned} &= \frac{1}{2\pi} \int_{-\infty}^{\infty} d\omega' \chi_{M,\text{eff}}^*[-\omega] \chi_{M,\text{eff}}[\omega'] \\ &\quad \left[ \gamma (n_{\text{th}}) 2\pi\delta(\omega + \omega') + |\alpha|^2 \chi_C^*[-\omega]\chi_C[\omega'] \kappa 2\pi\delta(\omega + \omega') \right] \end{aligned} \quad (2.154)$$

$$= \frac{1}{2\pi} \chi_{M,\text{eff}}^*[-\omega] \chi_{M,\text{eff}}[-\omega] \left[ 2\pi\gamma n_{\text{th}} + 2\pi\kappa |\alpha|^2 \chi_C[-\omega]\chi_C^*[-\omega] \right] \quad (2.155)$$

$$= |\chi_{M,\text{eff}}[-\omega]|^2 \left[ \gamma n_{\text{th}} + \kappa |\alpha|^2 |\chi_C[-\omega]|^2 \right] \quad (2.156)$$

The full expression for the power spectral density of the position fluctuations  $S_z[\omega]$  due to the RPSN

and thermal force is then

$$S_z[\omega] = |\chi_{M,\text{eff}}[\omega]|^2 [\gamma (n_{\text{th}} + 1) + \kappa |\alpha|^2 |\chi_C[\omega]|^2] + |\chi_{M,\text{eff}}[-\omega]|^2 [\gamma n_{\text{th}} + \kappa |\alpha|^2 |\chi_C[-\omega]|^2] \quad (2.157)$$

where the classical (thermal) and quantum Langevin force noise is

$$S_F^{\text{th}}[\omega] = \gamma \left( n_{\text{th}} + \frac{1}{2} \right) \quad (2.158)$$

and the radiation pressure shot noise is

$$S_F^{\text{sn}}[\omega] = \kappa |\alpha|^2 |\chi_C[\omega]|^2 \quad (2.159)$$

## 2.9 Radiation pressure shot noise as a limit to laser cooling

The expression for  $S_z[\omega]$  given in Eq. 2.157 can be used to derive the laser cooling limit due to RPSN. First we rewrite  $S_z[\omega]$  in terms of an effective damping and phonon number:

$$S_z[\omega] = |\chi_{M,\text{eff}}[\omega]|^2 [\tilde{\gamma} (\bar{n}_M + 1)] + |\chi_{M,\text{eff}}[-\omega]|^2 [\tilde{\gamma} \bar{n}_M] \quad (2.160)$$

where  $\tilde{\gamma} = \gamma + \gamma_{\text{opt}}$  is the effective damping constant and  $\bar{n}_M$  is the final phonon number. Then the ratio of  $(\bar{n}_M + 1)/\bar{n}_M$  is found by comparing Eqs. 2.160 and 2.157

$$\frac{\bar{n}_M + 1}{\bar{n}_M} = \frac{\gamma (n_{\text{th}} + 1) + \kappa |\alpha|^2 |\chi_C[\omega]|^2}{\gamma n_{\text{th}} + \kappa |\alpha|^2 |\chi_C[-\omega]|^2} \quad (2.161)$$

Solving for  $\bar{n}_M$  gives

$$\bar{n}_M = \frac{\gamma n_{\text{th}} + \kappa |\alpha|^2 |\chi_C[-\omega]|^2}{\gamma + \kappa |\alpha|^2 [|\chi_C[\omega_M]|^2 - |\chi_C[-\omega_M]|^2]} \quad (2.162)$$

Next we note that the optical damping  $\gamma_{\text{opt}}$  given in Eq. 2.131 can be written as

$$\gamma_{\text{opt}} = \kappa |\alpha|^2 (|\chi_C[\omega_M]|^2 - |\chi_C[-\omega_M]|^2) \quad (2.163)$$

which gives

$$\bar{n}_M = \frac{\gamma n_{\text{th}} + \kappa |\alpha|^2 |\chi_C[-\omega]|^2}{\gamma + \gamma_{\text{opt}}} \quad (2.164)$$

In the limit of large optical damping  $\gamma_{\text{opt}} \gg \gamma$  the phonon number approaches the limit

$$\bar{n}_M \rightarrow \frac{\kappa |\alpha|^2 |\chi_C[-\omega]|^2}{\gamma_{\text{opt}}} \quad (2.165)$$

$$= \frac{\kappa |\alpha|^2 |\chi_C[-\omega]|^2}{\kappa |\alpha|^2 [|\chi_C[\omega]|^2 - |\chi_C[-\omega]|^2]} \quad (2.166)$$

$$= \frac{(\omega_M + \Delta)^2 + \left(\frac{\kappa}{2}\right)^2}{-4\omega_M \Delta} \quad (2.167)$$

We define this minimum phonon number to be

$$\bar{n}_M^O = \left[ (\omega_M + \Delta)^2 + \left(\frac{\kappa}{2}\right)^2 \right] / (-4\omega_M \Delta) \quad (2.168)$$

In general,  $\bar{n}_M^O$  is minimized when the laser is detuned to the negative sideband  $\Delta = -\omega_M$ . In this special case

$$\bar{n}_M^O = \left( \frac{\kappa}{4\omega_M} \right)^2 \quad (2.169)$$

It is clear that to make the phonon number arbitrarily small we need  $\omega_M \gg \kappa$  (i.e. the resolved sideband limit), but even for  $\kappa = \omega_M$  the minimum phonon number is  $\bar{n}_M^O = \frac{1}{16} \ll 1$ . Thus it is seen that the limit on minimum phonon number is a result of the additional random force on the mechanical resonator due to the RPSN,  $S_F^{\text{sn}} = \kappa |\alpha|^2 |\chi_C[\omega]|^2$ .

## 2.10 Ratio of the radiation pressure shot noise and thermal force

The ratio of the radiation pressure shot noise and thermal force can now be written using the force power spectral densities  $S_F^{\text{th}}[\omega]$  and  $S_F^{\text{sn}}[\omega]$  given in Eqs. 2.158 and 2.159:

$$\frac{S_F^{\text{sn}}[\omega]}{S_F^{\text{th}}[\omega]} = \frac{\kappa |\alpha|^2 |\chi_C[\omega]|^2}{\gamma (n_{\text{th}} + 1)} \quad (2.170)$$

where  $|\alpha|^2$  is given in Eq. 2.135, and we have used

$$|\chi_C[\omega]|^2 = \frac{1}{(\omega + \Delta)^2 + (\kappa/2)^2} \quad (2.171)$$

and

$$n_{\text{th}} = [e^{\hbar\omega_M/k_B T} - 1]^{-1} \quad (2.172)$$

Next we consider the ratio in two special cases. The first case is when the laser is on resonance ( $\Delta = 0$ ) and the membrane motion is slow compared to the cavity decay rate (i.e.  $\omega \ll \kappa$ ). This was the intuitive limit considered in the initial discussion of the RPSN in Sec. 1.6. The second limit is for arbitrary detuning  $\Delta$  but only considering force fluctuations near the mechanical resonant frequency  $\omega \approx \omega_M$ , which is the frequency range where most of the mechanical motion occurs. This second limit of  $\omega \approx \omega_M$  is the one relevant to our experimental setup, as we will see later on.

### 2.10.1 Special case of on resonance $\Delta = 0$ and slow fluctuations $\omega \ll \kappa$

We now want to simplify Eq. 2.170 in order to recover Eq. 1.34 given in the introductory chapter:

$$\frac{S_F^{\text{sn}}}{S_F^{\text{th}}} = \frac{8\hbar P_{\text{in}} F^2 Q}{\pi k_B T c \lambda m \omega_m} \quad (2.173)$$

This requires the following list of assumptions:

1. On resonance detuning  $\Delta = 0$ , which maximizes the radiation pressure shot noise.

2. A lossless and symmetric cavity so that  $\kappa_L = \kappa_R = \kappa/2$  and  $\kappa_M = 0$ .
3. Low frequency fluctuations  $\omega \ll \kappa$ .
4. A hot membrane  $k_B T \gg \hbar \omega_M$  so that  $n_{\text{th}} = [e^{\hbar \omega_M / k_B T} - 1]^{-1} \approx k_B T / \hbar \omega_M \gg 1$ .
5. The end mirror is the mechanical oscillator so that  $|\frac{\partial \omega_{\text{cav}}}{\partial \tilde{z}}| = \frac{\omega_L}{L} = \frac{2\pi c}{\lambda L}$ .

Applying assumptions 1, 2, and 3 to the definition of  $\chi_C[\omega]$  (Eq. 2.90) gives

$$|\chi_C[0]|^2 = \left(\frac{2}{\kappa}\right)^2 \quad (2.174)$$

Applying assumptions 1, 2, and 5 to the optomechanical coupling strength  $\alpha = \bar{a}A$  gives

$$|\alpha|^2 = \frac{2}{\kappa} \frac{P_{\text{in}}}{\hbar \omega_L} \frac{\hbar}{2m\omega_M} \left(\frac{\omega_L}{L}\right)^2 \quad (2.175)$$

Then

$$\frac{S_F^{\text{sn}}[0]}{S_F^{\text{th}}[0]} = \frac{\kappa |\alpha|^2 |\chi_C[0]|^2}{\gamma (n_{\text{th}} + \frac{1}{2})} \quad (2.176)$$

$$= \frac{4\hbar P_{\text{in}} \omega_M \omega_L}{\gamma m \omega_M \kappa^2 L^2 k_B T} \quad (2.177)$$

Lastly, using  $\gamma = \omega_M/Q$ ,  $\omega_L = 2\pi c/\lambda$ , and  $\kappa = \pi c/LF$  we recover Eq. 1.34:

$$\left[ \frac{S_F^{\text{sn}}[0]}{S_F^{\text{th}}[0]} \right]_{\text{LL,sym},\Delta=0} \equiv \frac{8\hbar P_{\text{in}} F^2 Q}{\pi k_B T c \lambda m \omega_M} \quad (2.178)$$

The subscript LL,sym, $\Delta = 0$  refers to a lossless, symmetric, on resonance cavity.

### 2.10.2 Special case of $\omega \approx \omega_M$

We now want to simplify Eq. 2.170 given a less restrictive set of assumptions:

1. Arbitrary detuning  $\Delta$ .
2. The cavity is not lossless and symmetric.

3. We are only looking at low frequency fluctuations so  $\omega \approx \omega_M$ .
4. The membrane is hot ( $k_B T \gg \hbar \omega_M$ ) so that  $n_{\text{th}} = [e^{\hbar \omega_M / k_B T} - 1]^{-1} \approx k_B T / \hbar \omega_M \gg 1$ .
5.  $|\frac{\partial \omega_{\text{cav}}}{\partial \tilde{z}}| = \beta \frac{\omega_L}{L}$  where  $\beta \leq 1$  (for our membranes  $\beta \approx 0.3$ ).

Then Eq. 2.170 becomes

$$\begin{aligned} \frac{S_F^{\text{sn}}[\omega_M]}{S_F^{\text{th}}[\omega_M]} &= \frac{\kappa |\alpha|^2 |\chi_C[\omega_M]|^2}{\gamma (n_{\text{th}} + \frac{1}{2})} \tag{2.179} \\ &= \kappa \left( \frac{\kappa_L}{(\frac{\kappa}{2})^2 + \Delta^2} \frac{P_{\text{in}}}{\hbar \omega_L} \frac{\hbar}{2m\omega_M} \left| \frac{\partial \omega_{\text{cav}}}{\partial \tilde{z}} \right|^2 \right) \left( \frac{1}{(\frac{\kappa}{2})^2 + (\Delta + \omega_M)^2} \right) \left( \frac{1}{\gamma} \right) \left( \frac{\hbar \omega_M}{k_B T} \right) \tag{2.180} \end{aligned}$$

Defining  $\beta$  through the equation  $|\frac{\partial \omega_{\text{cav}}}{\partial \tilde{z}}| = \beta \frac{\omega_L}{L}$ , and using the same change of variables:  $\gamma = \omega_M / Q$ ,  $\omega_L = 2\pi c / \lambda$ , and  $\kappa = \pi c / LF$  gives

$$\frac{S_F^{\text{sn}}[\omega_M]}{S_F^{\text{th}}[\omega_M]} = \left( \frac{1}{1 + \left(\frac{\Delta}{\kappa/2}\right)^2} \right) \left( \frac{1}{1 + \left(\frac{\Delta + \omega_M}{\kappa/2}\right)^2} \right) \left( \frac{\kappa_L}{\kappa/2} \right) \beta^2 \frac{8\hbar P_{\text{in}} F^2 Q}{\pi m \omega_M c \lambda k_B T} \tag{2.181}$$

which simplifies to

$$\frac{S_F^{\text{sn}}[\omega_M]}{S_F^{\text{th}}[\omega_M]} = \left( \frac{1}{1 + \left(\frac{\Delta}{\kappa/2}\right)^2} \right) \left( \frac{1}{1 + \left(\frac{\Delta + \omega_M}{\kappa/2}\right)^2} \right) \left( \frac{\kappa_L}{\kappa/2} \right) \beta^2 \left[ \frac{S_F^{\text{sn}}[0]}{S_F^{\text{th}}[0]} \right]_{\text{LL, sym, } \Delta=0} \tag{2.182}$$

We see that the more relevant experimental result of the ratio of force noises near the mechanical resonance is a scaling of Eq. 2.178 for a lossless, symmetric cavity with a movable end mirror. The prefactor  $\left(1 + \left(\frac{\Delta}{\kappa/2}\right)^2\right)^{-1}$  is due to the reduced coupling into the cavity for non-zero detuning. The prefactor  $\left(1 + \left(\frac{\Delta + \omega_M}{\kappa/2}\right)^2\right)^{-1}$  accounts for passive filtering of fluctuations due to the finite cavity linewidth (which is a larger effect in the resolved sideband limit). The prefactor  $\left(\frac{\kappa_L}{\kappa/2}\right)$  accounts for potentially non-symmetric and lossy cavities ( $\frac{\kappa_L}{\kappa/2} = 1$  for lossless symmetric cavities). Lastly, the prefactor  $\beta^2 < 1$  accounts for effects like finite membrane reflectivity and the position dependence of the slope  $\partial \omega_{\text{cav}} / \partial z$ .

Figure 2.7 shows the effect of detuning  $\Delta$  and cavity decay rate  $\kappa$  on the ratio of the RPSN and thermal force  $S_F^{\text{sn}}[\omega_M]/S_F^{\text{th}}[\omega_M]$ . The  $\Delta$  and  $\kappa$  dependence is given by

$$\frac{S_F^{\text{sn}}[\omega_M]}{S_F^{\text{th}}[\omega_M]} \propto \left( \frac{1}{1 + \left(\frac{\Delta}{\kappa/2}\right)^2} \right) \left( \frac{1}{1 + \left(\frac{\Delta + \omega_M}{\kappa/2}\right)^2} \right) \kappa^2 \quad (2.183)$$

It might be naively supposed that an increase in finesse is always beneficial for improving the ratio  $S_F^{\text{sn}}[\omega_M]/S_F^{\text{th}}[\omega_M]$  because the radiation pressure force is multiplied by the finesse. However, this benefit is canceled out by the cavity filtering of the fluctuations around  $\omega_M \gg \kappa$  which drives the mechanical motion. Figure 2.7 shows that the ratio reaches a maximum when  $\kappa = \omega_M$ . Any subsequent improvement in finesse will cause narrower peaks in the RPSN, but will not increase the overall magnitude. This suggests that  $\kappa \approx \omega_M$  is a reasonable choice for the cavity optomechanical system.

Although the RPSN at the mechanical resonant frequency  $\omega_M$  does not increase with finesse once the resolved sideband limit is reached ( $\kappa \ll \omega_M$ ), there may be other advantages to designing a setup for the resolved sideband regime in the future. The first advantage of the resolved sideband regime is that the stronger optomechanical damping could make the membrane dynamics more stable. In this dissertation most of the data was taken close to zero detuning which means small perturbations in the membrane position pushed the membrane into a blue detuned optical heating regime. Optical heating would be less likely to happen if the mean laser detuning was far from resonance (such as  $\Delta = -\omega_M$  for optimal cooling). Second advantage is that as the cavity linewidth becomes smaller than the effective mechanical linewidth ( $\kappa < \gamma_{\text{eff}} = \gamma + \gamma_{\text{opt}}$ ) the frequency spectrum of the RPSN is no longer constant over the mechanical linewidth, which distinguishes it from the white thermal force. The power spectral density of the membrane's motion will no longer look Lorentzian, and this distortion could be a means to convincingly observe the RPSN.

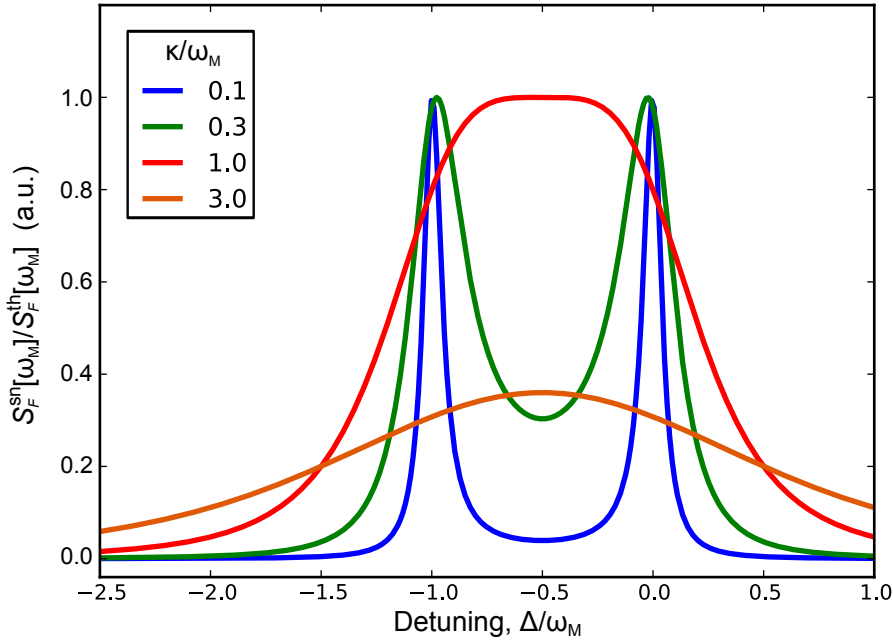


Figure 2.7: Ratio of RPSN to thermal force noise. The series of plots show that as  $\kappa$  decreases (finesse increases) there is no increase in the ratio beyond  $\kappa = \omega_M$ .

### 2.10.3 Power spectral densities in SI units

It is useful to rewrite the force and position noises in SI units for comparison with the standard formulas for the Langevin force. The resonator position  $\hat{z} = \hat{c} + \hat{c}^\dagger$  is unitless, and to return it to SI units we should multiply it by  $x_{\text{zpt}}$ , the zero point motion. The tilde used below denotes quantities converted into SI units:

$$\tilde{z} = x_{\text{zpt}} z = \sqrt{\frac{\hbar}{2m\omega}} z \quad (2.184)$$

The power spectral density is like  $z[\omega]^2$  so it scales by  $x_{\text{zpt}}^2$ :

$$\tilde{S}_z[\omega] = x_{\text{zpt}}^2 S_z[\omega] \quad (2.185)$$

The mechanical susceptibility and force power spectral density scales as follows:

$$\tilde{\chi}_M[\omega] = \frac{i}{2\omega_M} \chi_M[\omega] \quad (2.186)$$

$$\tilde{S}_F[\omega] = 2m\hbar\omega_M S_F[\omega] \quad (2.187)$$

The familiar power spectral density for the single-sided thermal force  $\tilde{S}_F^{\text{th}}$  is then

$$\tilde{S}_F^{\text{th}}[\omega] = 2m\hbar\omega_M S_F^{\text{th}} \quad (2.188)$$

$$= 2m\hbar\omega_M \gamma \left( n_{\text{th}} + \frac{1}{2} \right) \quad (2.189)$$

$$= 2m\gamma k_B T \quad (2.190)$$

where in the last line we used the relation  $k_B T \approx \hbar\omega_M n_{\text{th}}$ , which is a very accurate approximation in the limit  $n_{\text{th}} \gg 1$ .

## 2.11 Useful formulas for the noise terms $\eta[\omega]$ and $\xi_i[\omega]$

For completeness, here are the expectation values of the correlations between the different noise sources in the Fourier domain:

$$\langle \hat{\eta}[\omega] \hat{\eta}^\dagger[\omega'] \rangle = (n_{\text{th}} + 1) 2\pi \delta(\omega + \omega') \quad (2.191)$$

$$\langle \hat{\eta}^\dagger[\omega] \hat{\eta}[\omega'] \rangle = n_{\text{th}} 2\pi \delta(\omega + \omega') \quad (2.192)$$

$$\langle \hat{\xi}_i[\omega] \hat{\xi}_i^\dagger[\omega'] \rangle = (n_c + 1) 2\pi \delta(\omega + \omega') \quad (2.193)$$

where  $n_c$  is the cavity thermal photon number  $n_c = [e^{\hbar\omega/k_B T} - 1]^{-1}$ .

# Chapter 3

## Correlation scheme to measure the radiation pressure shot noise

### 3.1 Introduction

Observation of the radiation pressure shot noise (RPSN), which can be equivalently thought of as the quantum back action of an interferometric displacement measurement, is a major goal for cavity optomechanics, and is the primary goal of this dissertation research. The shot noise in the beam incident upon the cavity drives mechanical fluctuations in the harmonically bound mirror via radiation pressure. One straightforward way to measure the RPSN would be to observe correlations between the intensity fluctuations (shot noise) in the incident beam and the random fluctuations in the displacement of the mechanical resonator. Heidmann et al. [49] describe such a scheme using two optical beams. The strong signal beam induces fluctuations in the mechanical oscillator, while a weaker meter beam measures the position fluctuations of the oscillator. If the beams are both exactly on resonance, the signal beam intensity and meter beam phase quadrature will have correlations due to RPSN alone (thermal effects go to zero for long averaging times).

The idea presented by Heidmann et al. was experimentally tested in the classical domain by Verlot et al. [51], who added classical amplitude noise to the signal beam using an electro-optic modulator. The classical amplitude modulation was essential in order to have a correlation dom-

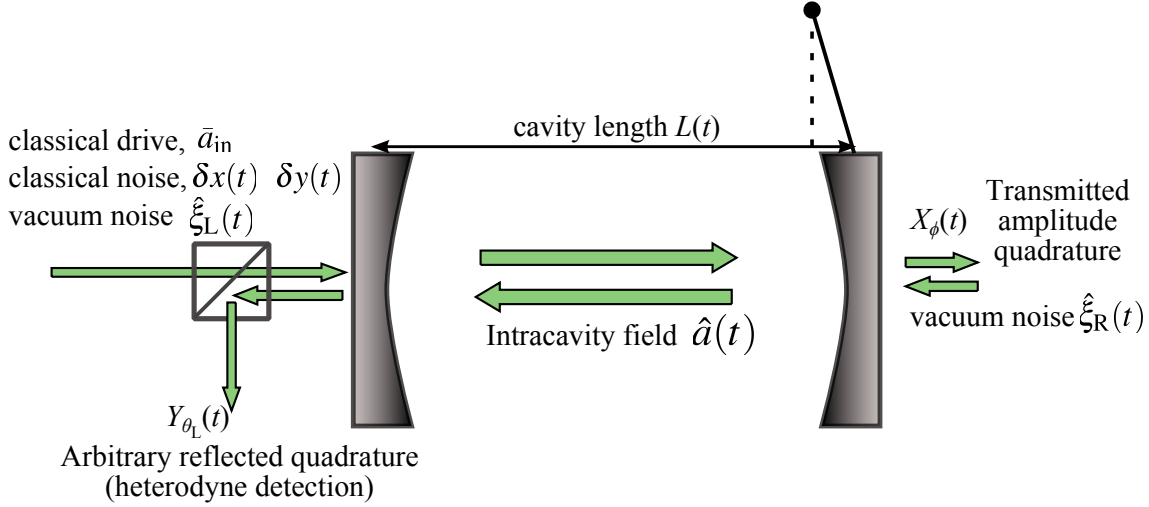


Figure 3.1: Radiation pressure shot noise measurement scheme developed by Børkje et al. [4]. The scheme involves a single beam incident upon the cavity. The correlation will be calculated between an arbitrary quadrature of the reflected field  $Y_{\theta_L}[\omega]$  and the transmitted amplitude quadrature  $X_{\phi}[\omega]$ .

inated by fluctuations in the radiation pressure, and not by thermally driven Brownian motion. Correlations due to the smaller quantum shot noise were not observed.

The scheme described in this chapter was developed by our Yale colleague Kjetil Børkje [4] and is shown in Fig. 3.1. It is distinguished from that of Heidmann et al. in three ways. First, our scheme only relies on one beam, and the correlations are between the reflected and transmitted beams. Second, the scheme works both at zero detuning and at finite detunings. Third, a specific quadrature of the reflected beam (the quadrature angle depends on detuning) must be measured, rather than the phase quadrature. This chapter will build on the optomechanical model given in Ch. 2 and will review the key theoretical results of the scheme from Børkje et al. Chapter 4 will discuss how the correlation scheme was experimentally implemented.

## 3.2 Correlation scheme on resonance

### 3.2.1 The basic idea for classical amplitude noise input on the cavity

The basic idea behind the scheme of Heidmann et al. (see Ref. [49]) can be illustrated by considering the effect of classical amplitude noise  $\delta x(t)$  when the incident beam is on resonance with the cavity ( $\Delta = 0$ ). On resonance, the linear response of the transmitted intensity to membrane motion vanishes, so to first order the transmitted beam carries no information about the membrane motion. The reflected phase (as measured using Pound-Drever-Hall (PDH) locking for instance [33]) is very sensitive to the fluctuations in mirror position  $z(t)$ , but is totally insensitive to the amplitude fluctuations in the incident beam  $\delta x(t)$ . Thus we can measure the intracavity radiation pressure  $F^{\text{sn}}(t) \propto \delta I_{\text{trans}} \propto \delta x(t)$  and independently measure the resonator's displacement  $z(t)$  (e.g. using the PDH error signal). Any correlations between  $\delta x(t)$  and  $z(t)$  are due to the radiation pressure. Next I follow Børkje et al. and review the full quantum treatment of the correlation measurement and its generalization to finite detuning.

### 3.2.2 Expected form for the RPSN-induced correlation

I now introduce  $\delta X_\phi(t) \propto \delta I_{\text{trans}}(t)$  for the transmitted intensity quadrature ( $\phi$  denotes amplitude quadrature as opposed to some other arbitrary quadrature of the transmitted field). I also introduce  $\delta Y_{\theta_L}(t)$  for an arbitrary quadrature of the left-side reflected beam. At zero detuning, the interesting signature of fluctuations in radiation pressure comes from the real part of the correlation between the transmitted intensity  $i\delta X_\phi(t) \propto F^{\text{sn}}(t)$  and the reflected phase  $Y_{\phi+\pi/2}(t) \propto z(t)$ . Thermal effects average to zero in this correlation because at zero detuning there is no lowest order contribution to the transmission fluctuations  $\delta X_\phi(t)$  caused by thermally driven position fluctuations. In the

frequency domain, the correlation can be expressed as

$$\begin{aligned}
\text{Re} (F^{\text{sn}}[\omega]z^*[\omega]) &\propto \text{Re} (\delta X_\phi[\omega]\delta Y_{\pi/2}^*[\omega]) \\
&\propto \text{Re} (\delta X_\phi[\omega] (-i\chi_M^*[\omega]\delta X_\phi^*[\omega])) \\
&\propto |\delta X_\phi[\omega]|^2 \text{Re} \left( \frac{-i}{\frac{\gamma}{2} + i(\omega - \omega_M)} \right) \\
&= |\delta X_\phi[\omega]|^2 \frac{-(\omega - \omega_M)}{\left(\frac{\gamma}{2}\right)^2 + (\omega - \omega_M)^2}
\end{aligned} \tag{3.1}$$

where the mechanical susceptibility  $\chi_M[\omega]$  connects the position and force fluctuations

$$z[\omega] = \chi_M[-\omega]F^{\text{sn}}[\omega] \propto i\chi_M[-\omega]\delta X_\phi[\omega] \tag{3.2}$$

and Eq. 2.86 shows the origin of the imaginary  $i$  in  $F^{\text{sn}}(t) \propto i\delta X_\phi(t)$ . Figure 3.2 is a plot of the real part of the correlation given by Eq. 3.1. The amplitude noise  $\delta X_\phi[\omega]$  is assumed to be white noise over the narrow range of frequencies around the mechanical resonance. The correlation is seen to be purely antisymmetric.

### 3.2.3 Definition of arbitrary quadratures of transmitted and reflected beams

A calculation of the correlation which is useful for non-zero detuning, and which includes both classical and quantum noise, requires that we detect arbitrary quadratures of the transmitted and reflected beams. The arbitrary quadratures of the transmitted and reflected beams are a generalization of the expressions for the transmitted intensity. The out-going fields from the cavity are the sum of the part which leaks out through the end mirror and the promptly reflected part:

$$\hat{a}_{\text{out},\text{R}}(t) = \sqrt{\kappa_{\text{R}}}\hat{a}(t) - \hat{a}_{\text{in},\text{R}}(t) \tag{3.3}$$

$$\hat{a}_{\text{out},\text{L}}(t) = \sqrt{\kappa_{\text{L}}}\hat{a}(t) - \hat{a}_{\text{in},\text{L}}(t) \tag{3.4}$$

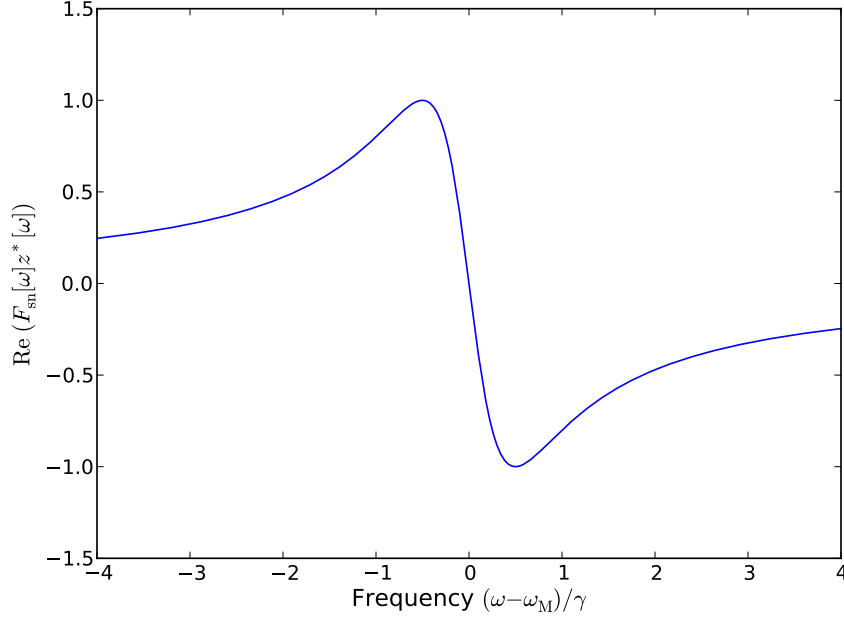


Figure 3.2: Plot of the correlation between the transmitted intensity fluctuations and reflected phase given in Eq. 3.1. The laser is assumed to be on resonance ( $\Delta = 0$ ) and only noise considered is classical amplitude noise on the laser. The vertical axis scale is normalized to have a maximum correlation of one.

We can rewrite these output fields in terms of fluctuations in a rotating frame:

$$\hat{a}_{\text{out},i}(t) = e^{-i\omega_{\text{D}}t} \left( \bar{a}_{\text{out},i} + \hat{d}_{\text{out},i}(t) \right) \quad (3.5)$$

The fluctuations in the output fields in the rotating frame  $\hat{d}_{\text{out},\text{R}}(t)$  and  $\hat{d}_{\text{out},\text{L}}(t)$  are given by

$$\hat{d}_{\text{out},\text{R}}(t) = \sqrt{\kappa_{\text{R}}} \hat{d}(t) - \hat{\xi}_{\text{R}}(t) \quad (3.6)$$

$$\hat{d}_{\text{out},\text{L}}(t) = \sqrt{\kappa_{\text{L}}} \hat{d}(t) - \left( \delta x(t) + i\delta y(t) + \hat{\xi}_{\text{L}}(t) \right) \quad (3.7)$$

The The cavity is only driven from the left side, so there is classical and vacuum noise in  $\hat{d}_{\text{out},\text{L}}(t)$  (Eq. 3.7), but only vacuum noise in  $\hat{d}_{\text{out},\text{R}}(t)$  (Eq. 3.6).

In order to motivate the expression for an arbitrary quadrature of the reflected field, we first calculate the fluctuations in the transmitted intensity  $I_{\text{trans}}(t) = \hat{a}_{\text{out},\text{R}}^\dagger(t) \hat{a}_{\text{out},\text{R}}(t)$  by substituting in

Eqs. 3.5 and 3.6 for  $\hat{a}_{\text{out,R}}(t)$  and only keeping fluctuations first order in  $\hat{d}_{\text{out,R}}(t)$  to obtain  $\delta I_{\text{trans}}(t)$ :

$$\begin{aligned}\delta I_{\text{trans}}(t) &= \kappa_{\text{R}} \left( \bar{a} \hat{d}^\dagger(t) + \bar{a}^* \hat{d}(t) \right) - \sqrt{\kappa_{\text{R}}} \left( \bar{a} \hat{\xi}_{\text{R}}^\dagger(t) + \bar{a}^* \hat{\xi}_{\text{R}}(t) \right) \\ &= \sqrt{\kappa_{\text{R}}} \left( \bar{a}^* \hat{d}_{\text{out,R}}(t) + \bar{a} \hat{d}_{\text{out,R}}^\dagger(t) \right)\end{aligned}\quad (3.8)$$

where  $\bar{a} = \langle \hat{a} \rangle = \frac{\sqrt{\kappa_{\text{L}}}}{\frac{\kappa}{2} - i\Delta} \bar{a}_{\text{in}}$  is given in Eq. 2.78. Equation 3.8 can be generalized to an arbitrary quadrature of the transmitted beam  $\delta X_{\theta_{\text{R}}}(t)$  and the reflected beam  $\delta Y_{\theta_{\text{L}}}(t)$ :

$$\delta \hat{X}_{\theta_{\text{R}}}(t) = e^{-i\theta_{\text{R}}} \hat{d}_{\text{out,R}}(t) + e^{i\theta_{\text{R}}} \hat{d}_{\text{out,R}}^\dagger(t) \quad (3.9)$$

$$\delta \hat{Y}_{\theta_{\text{L}}}(t) = e^{-i\theta_{\text{L}}} \hat{d}_{\text{out,L}}(t) + e^{i\theta_{\text{L}}} \hat{d}_{\text{out,L}}^\dagger(t) \quad (3.10)$$

where  $\theta_{\text{L}}$  and  $\theta_{\text{R}}$  are the quadrature angles. Comparing the expression for  $\delta I_{\text{trans}}(t)$  in Eq. 3.8 with the arbitrary amplitude quadrature in Eq. 3.9 we see that the transmitted intensity quadrature is  $\theta_{\text{R}} = \arg \bar{a} = \arctan \frac{2\Delta}{\kappa} \equiv \phi$ . The phase  $\phi$  is defined to be the phase shift of the intracavity beam relative to the incident beam:

$$\phi = \arctan \frac{2\Delta}{\kappa} \quad (3.11)$$

### 3.2.4 Transmitted intensity quadrature on resonance using the quantum formulation

I now want to show that the two claims made in Sec. 3.2.1 about the transmitted intensity (i.e. that  $\delta I_{\text{trans}}[\omega]$  is a measure of the radiation pressure fluctuations, and that  $\delta I_{\text{trans}}[\omega]$  doesn't contain any signal from the Brownian motion) are consistent with a fully quantum mechanical calculation of  $\delta I_{\text{trans}}(t)$ . First, we need to express  $\delta I_{\text{trans}}(t)$  in terms of the solution for  $\hat{d}[\omega]$  given in Eq. 2.88:

$$\hat{d}[\omega] = \chi_{\text{C}}[\omega] \left( i\alpha \hat{z}[\omega] - \hat{\zeta}[\omega] \right) \quad (3.12)$$

Then Eq. 3.8 for  $\delta I_{\text{trans}}[\omega]$  becomes

$$\delta I_{\text{trans}}[\omega] = \sqrt{\kappa_{\text{R}}} \left( \bar{a}^* \hat{d}_{\text{out,R}}[\omega] + \bar{a} \hat{d}_{\text{out,R}}^\dagger[\omega] \right) \quad (3.13)$$

$$= \sqrt{\kappa_{\text{R}}} \left( \bar{a}^* \left( \sqrt{\kappa_{\text{R}}} \hat{d}[\omega] - \hat{\xi}_{\text{R}}[\omega] \right) + \bar{a} \left( \sqrt{\kappa_{\text{R}}} \hat{d}^\dagger[\omega] - \hat{\xi}_{\text{R}}^\dagger[\omega] \right) \right) \quad (3.14)$$

$$= \sqrt{\kappa_{\text{R}}} \bar{a}^* \left( \sqrt{\kappa_{\text{R}}} \chi_{\text{C}}[\omega] \left( -i\alpha \hat{z}[\omega] + \hat{\zeta}[\omega] \right) - \hat{\xi}_{\text{R}}[\omega] \right) \\ + \sqrt{\kappa_{\text{R}}} \bar{a} \left( \sqrt{\kappa_{\text{R}}} \chi_{\text{C}}^*[-\omega] \left( i\alpha^* \hat{z}[\omega] + \hat{\zeta}^\dagger[\omega] \right) - \hat{\xi}_{\text{R}}^\dagger[\omega] \right) \quad (3.15)$$

$$= \sqrt{\kappa_{\text{R}}} \sqrt{\kappa_{\text{R}}} \left( -i\bar{a}^* \alpha \chi_{\text{C}}[\omega] + i\bar{a} \alpha^* \chi_{\text{C}}^*[-\omega] \right) \hat{z}[\omega] \\ + \sqrt{\kappa_{\text{R}}} \left( \sqrt{\kappa_{\text{R}}} \bar{a}^* \chi_{\text{C}}[\omega] \hat{\zeta}[\omega] - \bar{a}^* \hat{\xi}_{\text{R}}[\omega] + \sqrt{\kappa_{\text{R}}} \bar{a} \chi_{\text{C}}^*[-\omega] \hat{\zeta}^\dagger[\omega] - \bar{a} \hat{\xi}_{\text{R}}^\dagger[\omega] \right) \quad (3.16)$$

When on resonance ( $\Delta = 0$ ) the mean intracavity field  $\bar{a}$  is real and equal to

$$\bar{a} = \frac{\sqrt{\kappa_{\text{L}}}}{\kappa/2} \bar{a}_{\text{in}} \quad (3.17)$$

Also, the optomechanical coupling  $\alpha = \bar{a}A$  is real. The cavity susceptibility (when  $\Delta = 0$ ) simplifies to

$$\chi_{\text{C}}[\omega] = \frac{1}{\frac{\kappa}{2} - i\omega} \quad (3.18)$$

and in this special case  $\chi_{\text{C}}[\omega] = \chi_{\text{C}}^*[-\omega]$ . Applying these simplifications to Eq. 3.16 gives

$$\delta I_{\text{trans}}[\omega] = \sqrt{\kappa_{\text{R}}} \left[ \left( \sqrt{\kappa_{\text{R}}} \bar{a} \chi_{\text{C}}[\omega] \left( \hat{\zeta}[\omega] + \hat{\zeta}^\dagger[\omega] \right) - \bar{a} \left( \hat{\xi}_{\text{R}}[\omega] + \hat{\xi}_{\text{R}}^\dagger[\omega] \right) \right) \right] \quad (3.19)$$

where the term containing  $\left( \hat{\zeta}[\omega] + \hat{\zeta}^\dagger[\omega] \right)$  is proportional to the intracavity intensity fluctuations and hence the force  $F(t)$ . The second term  $-\bar{a} \left( \hat{\xi}_{\text{R}}[\omega] + \hat{\xi}_{\text{R}}^\dagger[\omega] \right)$  is proportional to the intensity fluctuations in the right side incident beam. Notice, as expected, the fluctuations in the membrane position  $\hat{z}[\omega]$  vanish on resonance so transmission contains no evidence of the thermally driven Brownian motion.

### 3.2.5 Reflected phase quadrature on resonance using the quantum formulation

I now want to show that the two claims made in Sec. 3.2.1 about the reflected phase measurement (i.e.  $\delta Y_{\phi+\pi/2}(t) \propto z(t)$  and  $\delta Y_{\phi+\pi/2}(t)$  does not contain any information about the radiation pressure fluctuations) are consistent with a fully quantum mechanical calculation of  $\delta Y_{\phi+\pi/2}(t)$ . We need to express  $\delta Y_{\phi+\pi/2}(t)$  in terms of the solution for  $\hat{d}[\omega]$  given in Eq. 2.88:

$$\hat{d}_{\text{out,L}}(t) = \sqrt{\kappa_{\text{R}}}\hat{d}(t) - \left( \delta x(t) + i\delta y(t) + \hat{\xi}_{\text{L}}(t) \right) \quad (3.20)$$

For  $\Delta = 0$  and  $\theta_{\text{L}} = \pi/2$ , we have  $\phi = 0$ , and the quadrature  $Y_{\pi/2}[\omega]$  will be

$$\delta Y_{\phi+\pi/2}(t) = e^{-i\frac{\pi}{2}}\hat{d}_{\text{out,L}}(t) + e^{i\frac{\pi}{2}}\hat{d}_{\text{out,L}}^\dagger(t) \quad (3.21)$$

$$= -i\hat{d}_{\text{out,L}}(t) + i\hat{d}_{\text{out,L}}^\dagger(t) \quad (3.22)$$

$$= -i \left[ \sqrt{\kappa_{\text{L}}}\hat{d}(t) - \left( \delta x(t) + i\delta y(t) + \hat{\xi}_{\text{L}}(t) \right) \right] \\ + i \left[ \sqrt{\kappa_{\text{L}}}\hat{d}^\dagger(t) - \left( \delta x(t) - i\delta y(t) + \hat{\xi}_{\text{L}}^\dagger(t) \right) \right] \quad (3.23)$$

$$= i\sqrt{\kappa_{\text{L}}} \left( -\hat{d}(t) + \hat{d}^\dagger(t) \right) + 2\delta y(t) - i\hat{\xi}_{\text{L}}(t) + i\hat{\xi}_{\text{L}}^\dagger(t) \quad (3.24)$$

Changing this expression into the frequency domain and substituting in the solution for  $\hat{d}[\omega]$  (Eq. 2.88) gives

$$\delta Y_{\phi+\pi/2}[\omega] = i\sqrt{\kappa_{\text{L}}} \left( \chi_{\text{C}}[\omega] \left( i\alpha\hat{z}[\omega] - \hat{\zeta}[\omega] \right) + \chi_{\text{C}}^*[-\omega] \left( i\alpha^*\hat{z}[\omega] + \hat{\zeta}^\dagger[\omega] \right) \right) \\ + 2\delta y[\omega] - i\hat{\xi}_{\text{L}}[\omega], + i\hat{\xi}_{\text{L}}^\dagger[\omega] \quad (3.25)$$

$$= i\sqrt{\kappa_{\text{L}}}\chi_{\text{C}}[\omega] \left( 2i\alpha\hat{z}[\omega] + \left( -\hat{\zeta}[\omega] + \hat{\zeta}^\dagger[\omega] \right) \right) + 2\delta y[\omega] - i\hat{\xi}_{\text{L}}[\omega], + i\hat{\xi}_{\text{L}}^\dagger[\omega] \quad (3.26)$$

We can see that the reflected phase quadrature contains a signal proportional to the position  $\hat{z}[\omega]$ , the classical phase noise  $\delta y[\omega]$ , and the incident vacuum noise  $\hat{\xi}_{\text{L}}[\omega]$  and  $\hat{\xi}_{\text{R}}[\omega]$ . The question naturally arises: When will the signal from the position fluctuations  $\hat{z}[\omega]$  (which are induced by radiation pressure fluctuations) be bigger than the shot noise contribution from  $\hat{\xi}_{\text{L}}[\omega]$  and  $\hat{\xi}_{\text{R}}[\omega]$ ?

These two sources of fluctuations are exactly the back action noise term (due to RPSN) and shot noise term which are involved in the discussion of the standard quantum limit in Sec. 1.3. Since the RPSN part is proportional to the coupling strength  $\alpha \propto \sqrt{P_{\text{in}}}$ , we can rephrase this question and ask, “At what incident power will the signal from the position fluctuations be bigger than the shot noise contribution?” These two sources of fluctuations become equal at a particular power  $P_{\text{in}} = P_{\text{SQL}}$  when the total measurement imprecision is minimized. For input powers exceeding the standard quantum limit power ( $P_{\text{in}} > P_{\text{SQL}}$ ), the RPSN term (i.e. measurement back-action) will dominate.

### 3.3 Non-zero detuning correlation scheme

Two are two nice things about the zero detuning correlation scheme described in Sec. 3.2. First, for long time averages the symmetric contribution to the thermally-driven Brownian motion does not contribute to the real part of the correlation. Second, the antisymmetric form of the RPSN correlation is distinct from the symmetric contribution of the Brownian motion. It is reasonable to ask if the same advantages exist for a correlation between reflected and transmitted beams at non-zero detuning. The answer is: sort of. A choice of reflected quadrature  $\theta_L$  and transmitted quadrature  $\theta_R$  can always be found which makes the correlation due to Brownian motion vanish. However, the second advantage, that the RPSN signal is purely antisymmetric, is a condition only sometimes met. Børkje derives a figure of merit for the “antisymmetric-ness” of the RPSN signal, which is given below in Eq. 3.61.

#### 3.3.1 Derivation of the critical angle $\theta_C$

A short derivation of the conditions which make the thermal contribution to the correlation vanish is given below. We start by assuming the transmitted quadrature is always the intensity quadrature  $\theta_R = \phi$ . We then seek the reflected quadrature  $\theta_L$  which causes the real part of the contribution of the Brownian motion to vanish. We define this special choice of  $\theta_L$  to be  $\theta_C$ , the critical angle.

Assume the laser incident upon the cavity is noiseless. The only fluctuations in the transmitted

field  $\delta X_{\theta_R}[\omega]$  and reflected field  $\delta Y_{\theta_L}[\omega]$  are then caused by the mechanical resonator's motion  $z[\omega]$ . Also, both quadratures are proportional to the intracavity fluctuations via the end mirror coupling constants  $\sqrt{\kappa_L}$  and  $\sqrt{\kappa_R}$ , so it is sufficient to consider the correlation between two arbitrary quadratures of the intracavity field, rather than transmission and reflection. An arbitrary quadrature of the intracavity field is defined by

$$Z_\theta[\omega] = e^{-i\theta}d[\omega] + e^{i\theta}d^\dagger[\omega] \quad (3.27)$$

where  $Z_\phi[\omega]$  is the intracavity amplitude fluctuation quadrature, and  $Z_{\phi+\pi/2}[\omega]$  is the intracavity phase quadrature. Ignoring all the input fluctuations  $\hat{\zeta}[\omega]$  and only considering the effect of the mechanical displacement  $\hat{z}[\omega]$ , we obtain the solutions for  $\hat{d}[\omega]$  and  $\hat{d}^\dagger[\omega]$  (from Eq. 3.12):

$$d[\omega] = -\chi_C[\omega] (i\alpha z[\omega]) \quad (3.28)$$

$$d^\dagger[\omega] = \chi_C^*[-\omega] (i\alpha^* z[\omega]) \quad (3.29)$$

The intensity quadrature occurs at the angle  $\phi = \arg \bar{a}$ . Then

$$Z_\phi[\omega] = e^{-i\phi}d[\omega] + e^{i\phi}d^\dagger[\omega] \quad (3.30)$$

$$= D(-\chi_C[\omega] + \chi_C^*[-\omega])z[\omega] \quad (3.31)$$

$$= 2iD \frac{-\Delta}{\left(\frac{\kappa}{2}\right)^2 - \omega^2 + \Delta^2 - i\kappa\omega} z[\omega] \quad (3.32)$$

where  $e^{i\phi} = \frac{\bar{a}}{|\bar{a}|}$  and

$$D = i\alpha e^{-i\phi} = iA\bar{a} \frac{\bar{a}^*}{|\bar{a}|} = iA|\bar{a}| \quad (3.33)$$

A similar expression can be derived for the intracavity phase quadrature  $Z_{\phi+\pi/2}[\omega]$ :

$$Z_{\phi+\pi/2}[\omega] = e^{-i(\phi+\pi/2)}d[\omega] + e^{i(\phi+\pi/2)}d^\dagger[\omega] \quad (3.34)$$

$$= D(i\chi_C[\omega] + i\chi_C^*[-\omega])z[\omega] \quad (3.35)$$

$$= 2iD \frac{\frac{\kappa}{2} - i\omega}{\left(\frac{\kappa}{2}\right)^2 - \omega^2 + \Delta^2 - i\kappa\omega} z[\omega] \quad (3.36)$$

An arbitrary quadrature of the intracavity field at  $\theta = \phi + \theta'$  is then given by

$$Z_\phi[\omega] = e^{-i(\phi+\theta')}d[\omega] + e^{i(\phi+\theta')}d^\dagger[\omega] \quad (3.37)$$

$$= \cos \theta' X[\omega] + \sin \theta' Y[\omega] \quad (3.38)$$

$$= 2iD \frac{-\Delta \cos \theta' + \left(\frac{\kappa}{2} - i\omega\right) \sin \theta'}{\left(\frac{\kappa}{2}\right)^2 - \omega^2 + \Delta^2 - i\kappa\omega} z[\omega] \quad (3.39)$$

Lastly, the correlation between the amplitude quadrature  $Z_\phi[\omega]$  and the arbitrary quadrature  $Z_{\phi+\theta'}[\omega]$  is

$$Z_\phi[\omega]Z_{\phi+\theta'}^*[\omega] = \frac{4|D|^2\Delta}{\left|\left(\frac{\kappa}{2}\right)^2 - \omega^2 + \Delta^2 - i\kappa\omega\right|^2} \left(\Delta \cos \theta' - \left(\frac{\kappa}{2} + i\omega\right) \sin \theta'\right) |z[\omega]|^2 \quad (3.40)$$

While there is no choice of  $\theta'$  which makes the  $|z[\omega]|^2$  contribution vanish, it is possible to make the real part of the correlation vanish.  $\text{Re}(Z[\omega]Z_{\phi+\theta'}^*[\omega])$  vanishes when

$$\Delta \cos \theta' - \frac{\kappa}{2} \sin \theta' = 0 \quad (3.41)$$

or

$$\theta' = \arctan \frac{2\Delta}{\kappa} = \phi \quad (3.42)$$

We then define the critical quadrature to be this choice of quadrature that causes the thermal contribution to the correlation to be purely imaginary:

$$\theta_C = \phi + \theta' \quad (3.43)$$

$$= 2\phi \quad (3.44)$$

$$= 2 \arctan \frac{2\Delta}{\kappa} \quad (3.45)$$

where  $\theta'$  is from Eq. 3.42.

### 3.4 A full expression for the correlation between $\delta\hat{X}_\phi[\omega]$ and $\delta\hat{Y}_{\theta_L}[\omega]$

The simple expression for the correlation given in Eq. 3.40 neglects the classical and quantum noise in the incident beams. In order to make sense of the various contributions to the correlation, it is helpful to express the reflected quadrature  $\delta\hat{Y}_{\theta_L}[\omega]$  and the transmitted quadrature  $\delta\hat{X}_\phi[\omega]$  in terms of the mechanical displacement  $\hat{z}[\omega]$  and the input fields to the cavity  $\delta x[\omega]$ ,  $\delta y[\omega]$ , and  $\hat{\xi}_i[\omega]$ :

$$\delta\hat{Y}_{\theta_L}[\omega] = e^{-i\theta_L}\hat{d}_{\text{out,L}}[\omega] + e^{i\theta_L}\hat{d}_{\text{out,L}}^\dagger[\omega] \quad (3.46)$$

$$\begin{aligned} &= e^{-i\theta_L} \left[ \sqrt{\kappa_L}\hat{d}[\omega] - \left( \delta x[\omega] + i\delta y[\omega] + \hat{\xi}_L[\omega] \right) \right] \\ &+ e^{i\theta_L} \left[ \sqrt{\kappa_L}\hat{d}^\dagger[\omega] - \left( \delta x[\omega] - i\delta y[\omega] + \hat{\xi}_L^\dagger[\omega] \right) \right] \end{aligned} \quad (3.47)$$

$$\begin{aligned} &= e^{-i\theta_L} \left[ -\sqrt{\kappa_L}\chi_C[\omega] \left( i\alpha\hat{z}[\omega] - \hat{\zeta}[\omega] \right) - \delta x[\omega] - i\delta y[\omega] - \hat{\xi}_L[\omega] \right] \\ &+ e^{i\theta_L} \left[ \sqrt{\kappa_L}\chi_C^*[-\omega] \left( i\alpha^*\hat{z}[\omega] - \hat{\zeta}^\dagger[\omega] \right) - \delta x[\omega] + i\delta y[\omega] - \hat{\xi}_L^\dagger[\omega] \right] \end{aligned} \quad (3.48)$$

where  $\hat{d}_{\text{out,L}}[\omega]$  comes from Eq. 3.7 and the solution for  $\hat{d}[\omega]$  is given by Eq. 3.12. The expression for the transmitted amplitude quadrature  $\delta\hat{X}_\phi$  is similar, except that there is no classical noise incident on the right side of the cavity

$$\delta\hat{X}_\phi[\omega] = e^{-i\phi}\hat{d}_{\text{out,R}}[\omega] + e^{i\phi}\hat{d}_{\text{out,R}}^\dagger[\omega] \quad (3.49)$$

$$\begin{aligned} &= e^{-i\theta_R} \left[ -\sqrt{\kappa_R}\chi_C[\omega] \left( i\alpha\hat{z}[\omega] - \hat{\zeta}[\omega] \right) - \hat{\xi}_R[\omega] \right] \\ &+ e^{i\theta_R} \left[ \sqrt{\kappa_R}\chi_C^*[-\omega] \left( i\alpha^*\hat{z}[\omega] - \hat{\zeta}^\dagger[\omega] \right) - \hat{\xi}_R^\dagger[\omega] \right] \end{aligned} \quad (3.50)$$

The expression for the correlation in the frequency domain [4] is then

$$S[\omega] = \frac{1}{4\pi} \int_{-\infty}^{\infty} d\omega' \langle \{ \delta X_{\theta_R}[\omega], \delta Y_{\theta_L}[\omega'] \} \rangle \quad (3.51)$$

The entire correlation can be expressed in terms of correlations between pairs of the various input fluctuations:  $\xi_L[\omega]$ ,  $\xi_M[\omega]$ ,  $\xi_R[\omega]$ ,  $\delta x[\omega]$ ,  $\delta y[\omega]$ , and  $\hat{\eta}[\omega]$  and their complex conjugates. The noise sources are assumed to be totally uncorrelated, so all of the cross-correlations vanish. For example,  $\langle \hat{\xi}_L[\omega] \hat{\xi}_M^\dagger[\omega'] \rangle = 0$ . The six expectation values for the self-correlations between noise sources are:

$$\langle \hat{\xi}_j[\omega] \hat{\xi}_j^\dagger[\omega'] \rangle = \frac{1}{2\pi} \delta(\omega + \omega') \text{ for } j \in \{L, M, R\} \quad (3.52)$$

$$\langle \hat{\xi}_j^\dagger[\omega] \hat{\xi}_j[\omega'] \rangle = 0 \text{ for } j \in \{L, M, R\} \quad (3.53)$$

$$\langle \hat{\eta}[\omega] \hat{\eta}^\dagger[\omega'] \rangle = \frac{1}{2\pi} (n_{\text{th}} + 1) \delta(\omega + \omega') \quad (3.54)$$

$$\langle \hat{\eta}^\dagger[\omega] \hat{\eta}[\omega'] \rangle = \frac{1}{2\pi} n_{\text{th}} \delta(\omega + \omega') \quad (3.55)$$

$$\langle \delta x[\omega] \delta x[\omega'] \rangle = \frac{1}{2\pi} C_X \delta(\omega + \omega') \quad (3.56)$$

$$\langle \delta y[\omega] \delta y[\omega'] \rangle = \frac{1}{2\pi} C_Y \delta(\omega + \omega') \quad (3.57)$$

Given these six self-correlations in Eqs. 3.52-3.57, we can explicitly write an expression for the correlation  $S[\omega]$  given in Eq. 3.51. However, there are many terms to be collected and made sense of, so for tidy expressions I defer to those already published in Børkje et al. [4].

### 3.5 Key results from Børkje et al.

The first step taken by Børkje in simplifying the long expression for the integrand in Eq. 3.51  $\langle \delta X_{\theta_R}[\omega] \delta Y_{\theta_L}[\omega'] \rangle$  is to separate it into different contributions according to the source of fluctuations:

$$\begin{aligned} \langle \delta X_{\theta_R}[\omega] \delta Y_{\theta_L}[\omega'] \rangle &= \langle \delta X_{\theta_R}[\omega] \delta Y_{\theta_L}[\omega'] \rangle_{\text{q,q}} + \langle \delta X_{\theta_R}[\omega] \delta Y_{\theta_L}[\omega'] \rangle_{\text{cl,cl}} + \langle \delta X_{\theta_R}[\omega] \delta Y_{\theta_L}[\omega'] \rangle_{\text{q,z}} \\ &\quad + \langle \delta X_{\theta_R}[\omega] \delta Y_{\theta_L}[\omega'] \rangle_{\text{cl,z}} + \langle \delta X_{\theta_R}[\omega] \delta Y_{\theta_L}[\omega'] \rangle_{\text{z,z}} \end{aligned} \quad (3.58)$$

The label “q” refers to quantum fields  $\xi_j[\omega]$ , “cl” refers to classical field  $\delta x[\omega]$  and  $\delta y[\omega]$ , and “z” refers to the position  $\hat{z}[\omega]$ . A description of each of the terms in Eq. 3.58 follows:

- $\langle \delta X_{\theta_R}[\omega] \delta Y_{\theta_L}[\omega'] \rangle_{\text{q,q}}$  is the vanishing correlation between the shot noise in the two quadratures. This includes terms like  $\langle \hat{\xi}_j[\omega] \hat{\xi}_j^\dagger[\omega'] \rangle$ , but does not include the additional correlations resulting

from the position being driven by radiation pressure. It is a general fact that when a coherent state is incident upon a beam splitter, the outputs are uncorrelated. Our cavity is a just beam splitter whose transmission-reflection split depends on frequency. Thus the “q,q” term vanishes for any choice of  $\theta_L$ .

- $\langle \delta X_{\theta_R}[\omega] \delta Y_{\theta_L}[\omega'] \rangle_{q,z}$  is the correlation between shot noise and the resulting fluctuations in mechanical displacement  $\hat{z}[\omega]$  due to the RPSN. Similar to the “q,q” term, it involves terms like  $\langle \hat{\xi}_j[\omega] \hat{\xi}_j^\dagger[\omega'] \rangle$ , but they are scaled by the mechanical susceptibility and the optomechanical coupling  $\alpha$ . *This is the term of interest which is due to the RPSN.*
- $\langle \delta X_{\theta_R}[\omega] \delta Y_{\theta_L}[\omega'] \rangle_{cl,cl}$  is the correlation between classical noise in the two quadratures and involves terms like  $\langle \delta x[\omega] \delta x[\omega'] \rangle$  and  $\langle \delta y[\omega] \delta y[\omega'] \rangle$ . When classical noise is incident upon a beam splitter (like our cavity) the outputs are correlated, so this term does not vanish.
- $\langle \delta X_{\theta_R}[\omega] \delta Y_{\theta_L}[\omega'] \rangle_{cl,z}$  is the correlation between classical laser fluctuations and the resulting fluctuations in mechanical displacement  $\hat{z}[\omega]$ . Similar to the “cl,cl” term, it involves terms like  $\langle \delta x[\omega] \delta x[\omega'] \rangle$  and  $\langle \delta y[\omega] \delta y[\omega'] \rangle$ , but they are scaled by the mechanical susceptibility and the optomechanical coupling  $\alpha$ .
- $\langle \delta X_{\theta_R}[\omega] \delta Y_{\theta_L}[\omega'] \rangle_{z,z}$  is the correlation between the mechanical displacement  $\hat{z}[\omega]$  in the two quadratures. It involves terms like  $\langle \hat{z}[\omega] \hat{z}[\omega'] \rangle$ , which are further reducible into terms due to shot noise, classical laser noise, and thermal noise. *The thermal contribution to this “z,z” term can be very large compared to the RPSN signal contained in the “q,z” term.*

The quantity which is measured in the lab is the symmetrized correlation  $S[\omega]$  given in Eq. 3.51.  $S[\omega]$  can then be split up into the same terms depending on the source of the fluctuations:

$$S[\omega] = S_{q,z}[\omega] + S_{cl,cl}[\omega] + S_{cl,z}[\omega] + S_{z,z}[\omega] \quad (3.59)$$

Again, there would be a  $S_{q,q}[\omega]$  term but it is identically zero in the limit of infinite measurement times.

Finally, we denote the real part of the correlation by  $R[\omega] = \text{Re } S[\omega]$ . The same notation is used for the sub-terms such as  $R_{q,z}[\omega] = \text{Re } S_{q,z}[\omega]$ .

## 3.6 Plots near zero detuning

Figure 3.3 shows the different components of the correlation  $R[\omega] = R_{q,z}[\omega] + R_{\text{cl,cl}}[\omega] + R_{\text{cl,z}}[\omega] + R_{z,z}[\omega]$  when the laser is very close to zero detuning. The plots were generated using the parameters from our experimental system. Here is a list of key observations from Fig. 3.3:

- The real part of the correlation due to RPSN  $R_{q,z}[\omega]$  is antisymmetric, which distinguishes it from the classical laser noise and thermal effects.
- Even for a very small detuning  $\Delta = -2\pi \times 1.0$  Hz the contribution due to Brownian motion in  $R_{z,z}[\omega]$  is still an order of magnitude larger than the correlation in  $R_{q,z}[\omega]$ , which contains the terms resulting from RPSN.
- The unwanted Brownian motion signal  $R_{z,z}[\omega]$  is proportional to the detuning  $\Delta$ . When the detuning is changed from  $-0.1$  Hz to  $-1.0$  Hz, we see a factor of 10 increase in  $R_{z,z}[\omega]$ .
- The other terms,  $R_{q,z}$ ,  $R_{\text{cl,z}}$ , and  $R_{\text{cl,cl}}$ , do not depend on the detuning  $\Delta$  to first order, so remain unchanged as the detuning is changed from  $-0.1$  Hz to  $-1.0$  Hz.
- $R_{\text{cl,cl}}[\omega]$  vanishes on resonance because the transmitted intensity is proportional to the incident classical amplitude noise  $\delta x[\omega]$ , while the reflected phase is proportional to the incident classical phase noise  $\delta y[\omega]$  and these two classical noises are assumed to be uncorrelated.

### 3.6.1 Figure of merit near zero detuning

One of the convenient results presented in Børkje et al. is a figure of merit for the ratio of the magnitude of the antisymmetric RPSN term  $R_{q,z}$  (defined as  $P_q$ ) to the symmetric Brownian motion term  $R_{z,z}$  (defined as  $M$ ):

$$\frac{P_q}{M} = \frac{(\kappa/2)^2 + \omega_M^2}{2(n_M + 1/2)\kappa|\Delta|} \quad (3.60)$$

$$\Delta/\kappa \approx -0.000 \quad \theta \approx 1.571$$

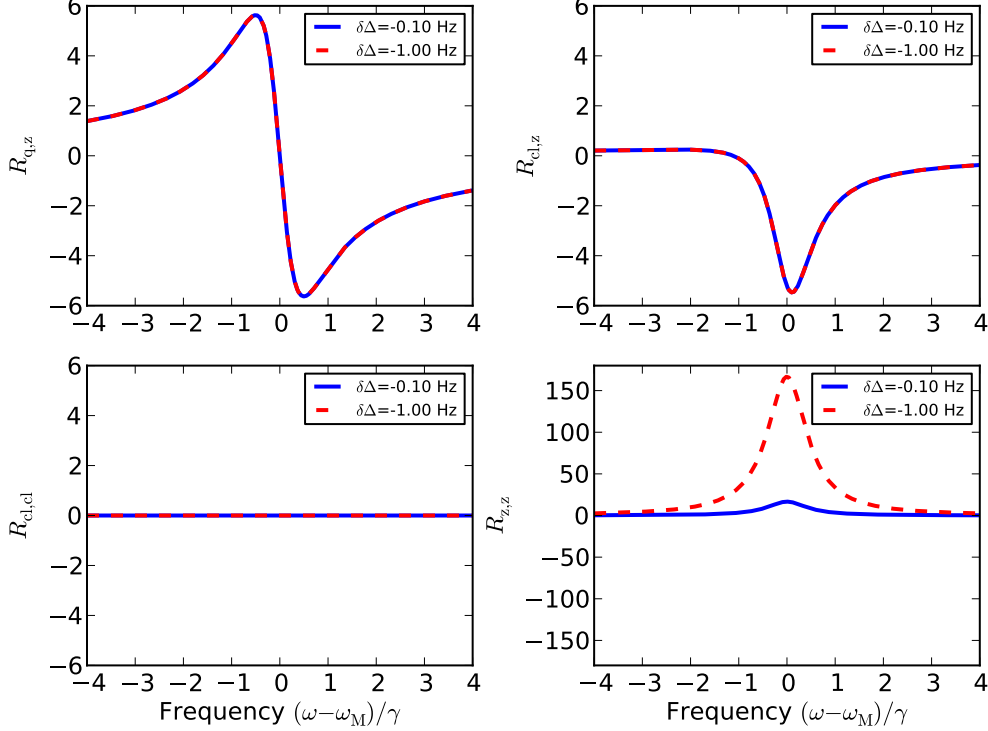


Figure 3.3: Theoretical plots of the various contributions to the correlation  $R[\omega]$ . The detuning is  $\Delta = \Delta_0 + \delta\Delta$  where  $\Delta_0 \approx 0$ , and  $\delta\Delta = -2\pi \times 0.1$  Hz for the blue curve, and  $\delta\Delta = -2\pi \times 1.0$  Hz for the red curve. The reflected heterodyne quadrature is  $\theta = \pi/2$ . The frequency axis is centered about the bare resonant frequency  $\omega_M = 2\pi \times 788$  kHz and scaled by the bare mechanical linewidth  $\gamma = 2\pi \times 1.1$  Hz. The incident power is  $P_{\text{in}} = 10 \mu\text{W}$ .  $\kappa = 4.45 \times 10^6 \text{ s}^{-1}$  and  $\kappa_L = 0.155\kappa$ .  $T = 295\text{K}$ . The membrane is positioned about 10 nm from a node of the intracavity field. The classical amplitude and phase noise have the same magnitude as the quantum noise ( $C_X = C_Y = 1$ , where  $C_X$  and  $C_Y$  are defined in Eqs. 3.56 and 3.57).

For the optomechanical parameters given in Fig. 3.3, the figure of merit formula indicates the detuning should be  $\Delta \leq 0.06$  Hz in order to make the thermal correlation  $R_{z,z}$  as small as the RPSN correlation  $R_{q,z}$ .

One important feature of this figure of merit is that it does not depend on the laser power. This implies the RPSN and thermal contributions scale in the same way with laser power. While increasing the laser power changes the ratio of the forces  $S_F^{\text{sn}}[\omega]/S_F^{\text{th}}[\omega]$ , it doesn't change the relative magnitudes of the correlations  $R_{q,z}/R_{z,z}$ . Because the ratio of the quantum and classical contributions to the correlation  $R_{q,z}/R_{z,z}$  is independent of laser power, the choice of laser power is guided by a number of technical considerations. One of the main advantages of higher laser power is that the shot noise becomes larger relative to the detector dark noise. Possible disadvantages of higher laser power include increased membrane absorption (which can lead to heating), optomechanical bistability (which can make stably locking the laser to the cavity difficult), and increased classical laser noise relative to shot noise. The balance of these considerations depends on properties of the membrane (absorption coefficient), the photodiodes (noise equivalent power), and the laser (classical amplitude and phase noise).

### 3.7 Plots at large, finite detuning ( $\Delta = -3.1\kappa$ )

Figure 3.4 shows the different components of the correlation  $R[\omega] = R_{q,z}[\omega] + R_{\text{cl,cl}}[\omega] + R_{\text{cl,z}}[\omega] + R_{z,z}[\omega]$  when the laser has a large detuning from the cavity resonance  $\Delta \approx -3.1\kappa$ , and the heterodyne quadrature angle is chosen to be very near the critical value of  $\theta_C = \arctan(2\Delta/\kappa)$ . The exact value  $\Delta \approx 3.1\kappa$  is arbitrary, but is representative of the case  $\Delta \gg \kappa, \omega_M$ . The plots were generated using the parameters from our experimental system (given in the figure caption), and except for the detuning, they are the same as in Sec. 3.6. Here is a list of key observation from Fig. 3.4:

- *Most importantly, the term of interest  $R_{q,z}[\omega]$  is still antisymmetric as in the case of zero detuning, which distinguishes it from the symmetric thermal contribution.* However, the contribution from the classical laser noise  $R_{\text{cl,z}}$  is now basically indistinguishable from the RPSN term  $R_{q,z}$ . This suggests that we need a shot noise-limited laser with  $C_X, C_Y \ll 1$  (where  $C_X$

and  $C_Y$  are defined in Eqs. 3.56 and 3.57).

- The thermal contribution  $R_{z,z}[\omega]$  is proportional to the error in detuning  $\delta\Delta$ , where  $\Delta = \Delta_0 + \delta\Delta$  and the critical quadrature  $\theta_C = 2 \arctan(2\Delta_0/\kappa)$ . When the detuning error is increased from 0.1 Hz to 1.0 Hz, there is a 10-fold increase in  $R_{z,z}[\omega]$ .
- For the parameters used in Fig. 3.4,  $R_{q,z}[\omega] \approx R_{z,z}[\omega]$  when the error in detuning is  $\delta\Delta_0 \approx 0.1 \times 2\pi$  Hz (solid blue lines).
- The other terms,  $R_{q,z}$ ,  $R_{cl,z}$ , and  $R_{cl,cl}$ , do not depend on the detuning  $\Delta$  to first order, so they remain unchanged as the error in detuning is changed from 0.1 to 1.0 Hz.
- $R_{cl,cl}$  does not change with  $\omega$ , and so is easy to distinguish from  $R_{q,z}$ .

### 3.8 Plots at half-linewidth detuning

Figure 3.5 shows the different components of the correlation  $R[\omega] = R_{q,z}[\omega] + R_{cl,cl}[\omega] + R_{cl,z}[\omega] + R_{z,z}[\omega]$  when the laser is detuned by a half linewidth from the cavity resonance ( $\Delta \approx -0.5\kappa$ ). The reflected heterodyne quadrature is chosen to be  $\theta = \theta_C(\Delta_0)$ , where  $\Delta_0 = -\kappa/2$ . The error in detuning is  $\delta\Delta = 0.1$  Hz or  $\delta\Delta = 1.0$  Hz, where  $\Delta = \Delta_0 + \delta\Delta$ . This regime is different from very small detuning  $\Delta \approx 0$  and large detuning  $\Delta \gg \omega_M, \kappa$  in that the RPSN term  $R_{q,z}$  is no longer antisymmetric, and thus it is much more difficult to distinguish from the thermal component. Børkje et al. derives a condition, which if met, ensures  $R_{q,z}$  is antisymmetric:

$$\frac{\omega_M \kappa}{|(\kappa/2)^2 + \Delta^2 - \omega_M^2|} \ll 1 \quad (3.61)$$

For the parameters in Fig. 3.5 this is

$$\frac{\omega_M \kappa}{|(\kappa/2)^2 + \Delta^2 - \omega_M^2|} \approx 1.5 \quad (3.62)$$

$$\Delta/\kappa \approx -3.14 \quad \theta \approx 0.316$$

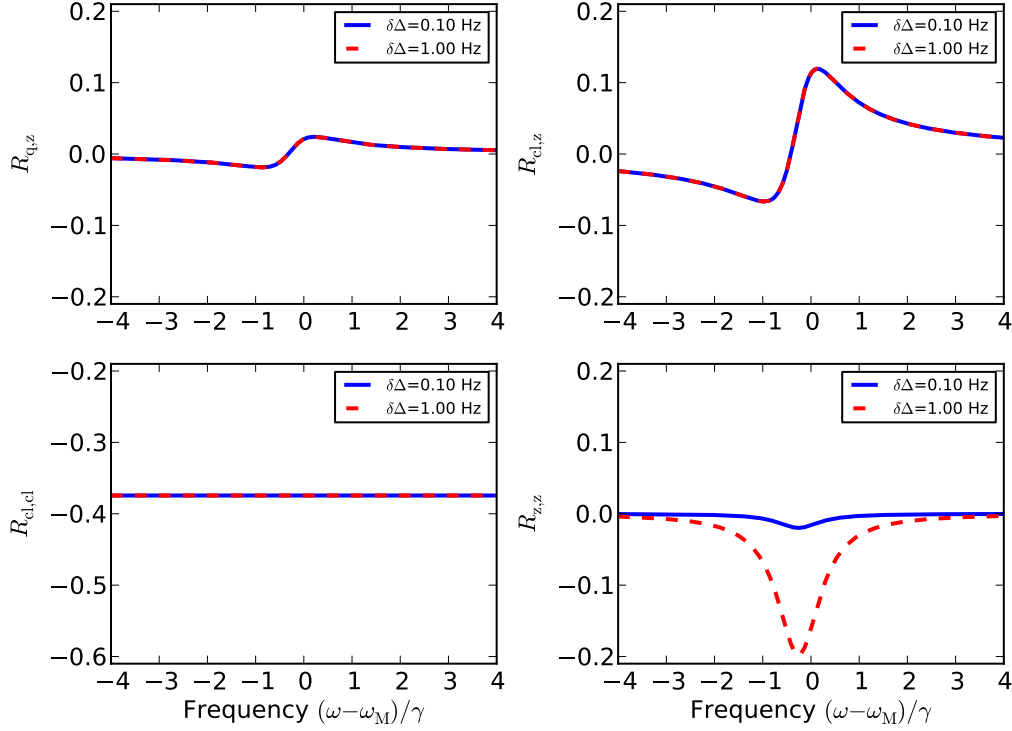


Figure 3.4: Theoretical plots of the various contributions to the correlation  $R[\omega]$ . The detuning is  $\Delta = \Delta_0 + \delta\Delta$  where  $\Delta_0 \approx -3.1\kappa$ , and  $\delta\Delta = 0.1 \times 2\pi$  Hz for the blue curve, and  $\delta\Delta = 1.0 \times 2\pi$  Hz for the red curve. The reflected heterodyne quadrature was  $\theta = \theta_C(\Delta_0)$ . The frequency axis is centered about the bare resonant frequency  $\omega_M = 2\pi \times 788$  kHz and scaled by the bare mechanical linewidth  $\gamma = 2\pi \times 1.1$  Hz. The incident power is  $P_{in} = 10 \mu\text{W}$ .  $\kappa = 4.45 \times 10^6 \text{ s}^{-1}$  and  $\kappa_L = 0.155\kappa$ .  $T = 295$  K. The membrane is positioned about 10 nm from a node of the intracavity field. The classical amplitude and phase noise is the same magnitude as the quantum noise ( $C_X = C_Y = 1$ ).

$$\Delta/\kappa \approx -0.5 \quad \theta \approx -1.57$$

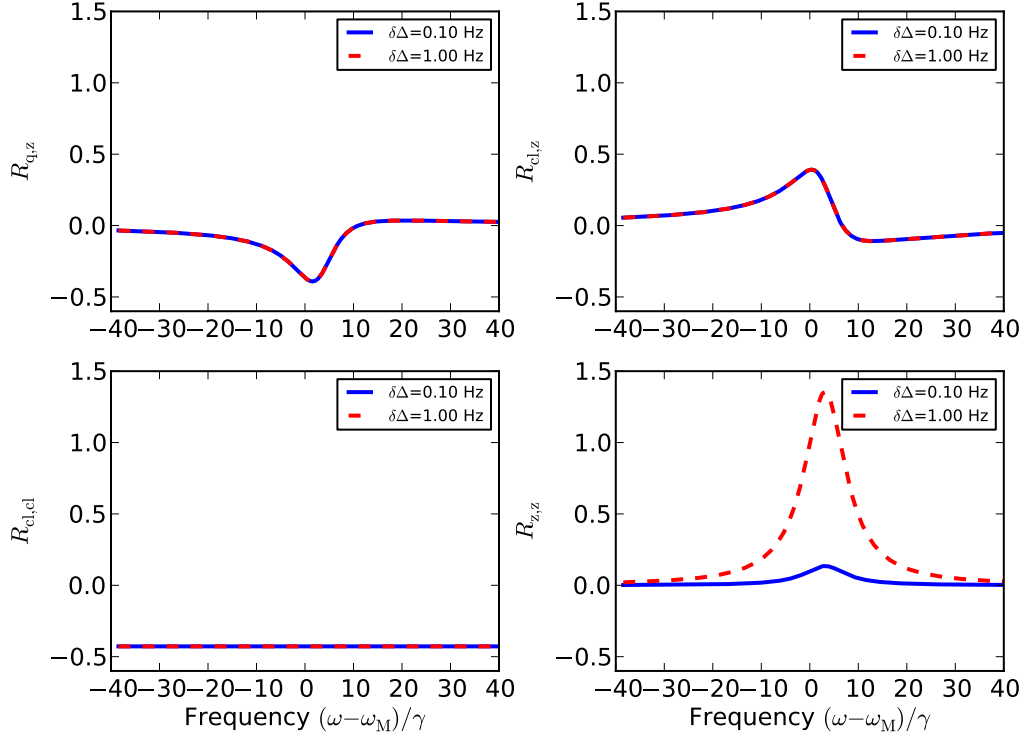


Figure 3.5: Theoretical plots of the various contributions to the correlation  $R[\omega]$ . The detuning is  $\Delta = \Delta_0 + \delta\Delta$  where  $\Delta_0 = -0.5\kappa$ , and  $\delta\Delta = 0.1 \times 2\pi$  Hz for the blue curve, and  $\delta\Delta = 1.0 \times 2\pi$  Hz for the red curve. The reflected heterodyne quadrature was  $\theta = \theta_C(\Delta_0)$ . The frequency axis is centered about the bare resonant frequency  $\omega_M = 2\pi \times 788$  kHz and scaled by the bare mechanical linewidth  $\gamma = 2\pi \times 1.1$  Hz. The incident power is  $P_{\text{in}} = 10 \mu\text{W}$ .  $\kappa = 4.45 \times 10^6 \text{ s}^{-1}$  and  $\kappa_L = 0.155\kappa$ .  $T = 295$  K. The membrane is positioned about 10 nm from a node of the intracavity field. The classical amplitude and phase noise is the same magnitude as the quantum noise ( $C_X = C_Y = 1$ ).

Thus, for  $\Delta \approx -0.5\kappa$ , the criteria for having an antisymmetric  $R_{q,z}$  is not satisfied, and it is no surprise that  $R_{q,z}$  does not appear antisymmetric in Fig. 3.5.

## 3.9 Effect of finite measurement time

### 3.9.1 Averaging time on resonance

The above plots in Figs. 3.3, 3.4, and 3.5 are for an infinite measurement time, where correlations like  $\langle \xi_i[\omega]\eta[\omega] \rangle$  vanish. However, any measurement in the lab takes a finite measurement time, and these correlations won't be zero. We must then determine how long of a measurement time is needed.

It is easiest to estimate the measurement time needed in the on resonance case  $\Delta = 0$ . Suppose we want to generate a plot of  $R_{q,z}[\omega]$  with  $N_{\text{res}}$  points per linewidth  $\gamma/2\pi$  (where “res” stand for resolution), so the frequency resolution is  $\delta f = \gamma/2\pi N_{\text{res}}$ . The measurement time required to achieve this frequency resolution  $\tau_{\text{meas},1}$  is given by

$$\tau_{\text{meas},1} = \frac{1}{\delta f} = \frac{2\pi N_{\text{res}}}{\gamma} \quad (3.63)$$

This is the measurement time needed to observe  $R_{q,z}[\omega]$  with a frequency resolution  $\delta f$ .

However, for a measurement at finite temperature, the fluctuations in resonator displacement  $z[\omega]$  are mostly due to thermal force noise, rather than RPSN. Thus the fluctuations in the reflected heterodyne signal  $Y_{\phi+\pi/2}[\omega]$  due to thermally driven Brownian motion are larger than the fluctuations caused by the RPSN by a factor of  $\sqrt{S_F^{\text{th}}[\omega]/S_F^{\text{sn}}[\omega]}$ . Averaging  $N_{\text{avg}}$  data points will improve the ratio of the signal (RPSN induced fluctuations in  $Y_{\phi+\pi/2}[\omega]$ ) to noise (thermally induced fluctuations in  $Y_{\phi+\pi/2}[\omega]$ ) by a factor of  $\sqrt{N_{\text{avg}}}$  giving

$$\frac{\text{signal}}{\text{noise}} \equiv G = \sqrt{N_{\text{avg}}} \sqrt{\frac{S_F^{\text{sn}}[\omega]}{S_F^{\text{th}}[\omega]}} \quad (3.64)$$

The time required to have the frequency resolution  $\delta\omega = \gamma/N_{\text{res}}$  and a signal to noise ratio  $G$  (after averaging) is

$$\tau_{\text{meas},2} = N_{\text{avg}} \tau_{\text{meas},1} \quad (3.65)$$

$$= \tau_{\text{meas},1} G \sqrt{\frac{S_F^{\text{th}}[\omega]}{S_F^{\text{sn}}[\omega]}} \quad (3.66)$$

$$= \frac{N_{\text{res}}}{\gamma/2\pi} G \sqrt{\frac{S_F^{\text{th}}[\omega]}{S_F^{\text{sn}}[\omega]}} \quad (3.67)$$

For reasonable parameters like those used to generate Fig. 3.3

$$S_F^{\text{th}}[\omega]/S_F^{\text{sn}}[\omega] \approx 5 \times 10^6 \quad (3.68)$$

where the ratio of thermal and RPSN forces is evaluated using Eq. 2.170. For a signal to noise ratio of  $G = 1$ , a mechanical linewidth  $\gamma/2\pi = 1$  Hz, and  $N_{\text{res}} = 10$  points per linewidth, the minimum averaging time is

$$\tau_{\text{meas},2} \gtrsim 2 \times 10^4 \text{ s} \quad (3.69)$$

or about six hours. This only includes additional noise in the reflected phase quadrature due to Brownian motion, which we expect is the largest source of noise. In situations where the technical noise in the laser and photodiodes can be ignored, it is advantageous to increase  $\gamma$  by optomechanical damping since the measurement time  $\tau_{\text{meas},2} \propto \gamma^{-1}$ . In practice, this will reduce the absolute scale of the position fluctuations, and hence also reduce the fluctuations in the reflected heterodyne signal  $Y_{\phi+\pi/2}[\omega]$ . The advantage of increasing  $\gamma$  may be lost if the heterodyne fluctuations become smaller than dark noise in the photodiodes.

Similarly, any additional noise in the measured transmitted amplitude quadrature, such as detector dark noise, will cause the averaging time  $\tau_{\text{meas},2}$  to increase. Noise in the transmitted intensity measurement is discussed in more detail in Sec. 5.6 where it is presented along with measurements of the correlation for finite measurement times.

# Chapter 4

## Experimental Design

The goal of this chapter is to describe the setup in sufficient detail that the experiment could be reproduced.

### 4.1 Mechanical resonator: Silicon nitride membrane

The mechanical resonator used in our optomechanical system was a commercially available silicon nitride ( $\text{Si}_3\text{N}_4$ ) membrane from Norcada Inc. [100]. Silicon nitride is an amorphous insulator. The membranes are formed by depositing a silicon nitride layer on a silicon substrate. The silicon substrate is then etched out in a square pattern, leaving a square silicon frame with a silicon nitride membrane stretched across it. The membrane used here was a 50 nm-thick, 1 mm square silicon nitride membrane deposited on a 200  $\mu\text{m}$ -thick, 5 mm square silicon frame.

The silicon nitride film is always highly stressed due to a mismatch in the atomic spacings between the silicon substrate and the silicon nitride film. The degree of stress can be changed by an order of magnitude by adjusting deposition conditions, including the ratio between silicon and nitrogen. In this experiment we used stoichiometric silicon nitride membranes, meaning the film was designed to have an exact silicon to nitrogen ratio of 3:4. Stoichiometric  $\text{Si}_3\text{N}_4$  is the highest-stress film commercially available ( $\sigma \approx 900$  MPa), and this high stress makes the stoichiometric membranes more brittle and less desirable for most of their intended purposes. However, we chose the high-stress stoichiometric membranes because they have lower optical loss than the lower-stress

$\sigma$	stress	$900 \times 10^6$	N/m <sup>2</sup>
$t_m$	membrane thickness	50	nm
$L$	membrane side length	1.0	mm
$\rho$	density	$3.0 \times 10^3$	kg/m <sup>3</sup>
$m_{\text{eff}}$	effective mass	$3.75 \times 10^{-11}$	kg
$k_{1,1}$	spring constant	220	N/m
$\omega_{1,1}$	resonant frequency of the fundamental	$2\pi \times 387.$	kHz
$\kappa$	thermal conductivity	3.2	W K <sup>-1</sup> m <sup>-1</sup>
$\alpha$	thermal expansion coefficient	$3 \times 10^{-6}$	K <sup>-1</sup>
$E_Y$	Young's modulus	$126 \times 10^9$	N/m <sup>2</sup>
$\nu_P$	Poisson ratio	0.25	—

Table 4.1: Materials data for the high-stress stoichiometric silicon nitride membrane used in this dissertation. Unless otherwise specified, these will be the assumed membrane parameters for the dissertation. Some of the parameters ( $\kappa$ ,  $\alpha$ ,  $E_Y$ , and  $\nu_P$ ) are based on measurements in published literature because they are not specified by Norcada, nor were they measured by us.

membranes.

Even the “low-stress” silicon nitride membranes typically have a stress  $\sigma \gtrsim 100$  MPa, which is sufficiently high that the internal elasticity provides a negligible contribution to the restoring force compared to the stress applied by the silicon frame. As a result, the mechanical modes of the membrane of side length  $L$  take on the particularly simple form of a tightly stretched square drum head:

$$z_{m,n}(x, y, t) = z_0(t) \sin\left(\frac{\pi m x}{L}\right) \sin\left(\frac{\pi n y}{L}\right) \quad (4.1)$$

where  $z_0(t)$  is the time varying amplitude of the mode, and  $m \geq 1$  and  $n \geq 1$  are integer mode indices. The membrane’s effective spring constant  $k_{m,n}$ , effective mass  $m_{\text{eff}}$ , and resonant frequency  $\omega_{m,n}$  are derived in Appendix A. The results are quoted below. Materials parameters for silicon nitride are given in Table 4.1.

$$k_{m,n} = \frac{\pi^2 \sigma t_m}{4} (m^2 + n^2) \quad (4.2)$$

$$m_{\text{eff}} = \frac{1}{4} \rho t_m L^2 = \frac{1}{4} m \quad (4.3)$$

$$\omega_{m,n} = \sqrt{\frac{k_{m,n}}{m_{\text{eff}}}} = \sqrt{\frac{\pi^2 \sigma (m^2 + n^2)}{\rho L^2}} \quad (4.4)$$

### 4.1.1 Mechanical loss in silicon nitride membranes

The intended applications of silicon nitride membranes as sample holders for transmission electron microscopy and as x-ray vacuum windows relies on the strength of their thin film against static loads. When our Yale group tested the dynamic properties of the membranes we were pleasantly surprised to find mechanical quality factors of  $Q \sim 10^6$  at room temperature and  $Q \sim 10^7$  at cryogenic temperatures [39, 101]. Figure 4.1 (from Zwickl et al. [101]) shows the decaying oscillation amplitude of the fundamental mechanical mode for two low-stress silicon nitride membranes at room temperature and cryogenic temperatures (300 mK).

While it was initially surprising to find such high quality factors in amorphous membranes, it seems likely that the stress, which increases the energy stored in the membrane, does not increase the mechanical loss per oscillation by the same proportion. Thus, the mechanical loss rate will be lower for more highly stressed membranes.

For example, thermo-elastic dissipation is a loss mechanism which does not scale with the stress [102–105]. Thermo-elastic dissipation is not proportional to strain, but rather to the strain gradient, so the loss does not increase with the externally applied stress, though the energy does. The quality factor when limited only by thermo-elastic dissipation,  $Q_{\text{TED}}$ , in a highly stressed membrane becomes

$$Q_{\text{TED}m,n} = \frac{\sqrt{\rho\sigma}\pi^3\kappa L^3(1-\nu_{\text{P}}^2)}{32(m^2+n^2)^{3/2}T\alpha^2 E^2 t_{\text{m}}^4} \quad (4.5)$$

where  $L$  is the side length of the square membrane,  $t_{\text{m}}$  is the membrane thickness,  $T$  is the temperature,  $\kappa$  is the thermal conductivity,  $\nu_{\text{P}}$  is the Poisson ratio of silicon nitride,  $\alpha$  is the thermal expansion coefficient,  $E_{\text{Y}}$  is the Young’s modulus of the membrane material,  $\rho$  is the density, and  $\sigma$  is the uniform stress of the membrane. A full derivation Eq. 4.5 is given in Appendix B. Assuming the material parameters listed in Table 4.1, Eq. 4.5 gives a room temperature, TED-limited quality factor for the (1,1) mode of  $Q_{\text{TED}1,1} \approx 5 \times 10^{11}$ . Since our observed mechanical quality factors have never exceeded  $10^7$ , it is clear that thermo-elastic dissipation is negligible compared to other loss mechanisms.

While thermoelastic dissipation is totally negligible, one significant factor in finding low-loss

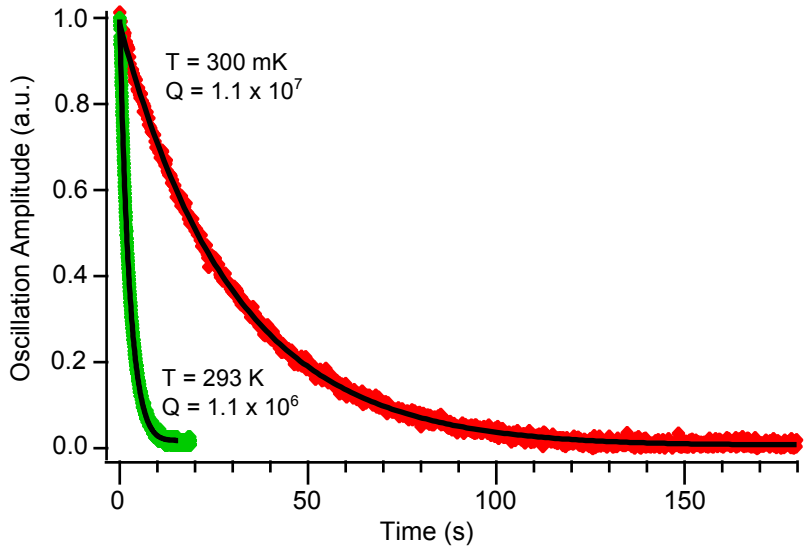


Figure 4.1: Ring-down of the fundamental mechanical mode of silicon nitride membranes at room temperature (green) and cryogenic temperatures (red). The membranes were 1 mm square, 50 nm-thick Norcada low-stress silicon nitride membranes with a fundamental resonant frequency of about 130 kHz.

membranes appears to be the mounting method. We have tried clipping down membranes without using epoxy, epoxying only a portion of the frame, and epoxying the entire frame. In general, the results have not been consistent enough to claim that one method routinely yield better results. Depending on the membrane and mounting method, we have found that the fundamental mode quality factor varies over three orders of magnitude ( $Q_{1,1} \sim 10^3 - 10^6$ ). Typically the higher-order modes have higher quality factors as shown in Fig. 4.2. This wide variation in quality factor is consistent with similar work on stoichiometric silicon nitride membranes published by Wilson et al. at Caltech [106]. Wilson et al. consistently found the highest quality factors when using no epoxy or clamping, but letting the membrane frame rest in a concave mirror substrate. Two undergraduate researchers in our Yale group, Sydney Schreppler and Israel Kositsky, have designed, built, and operated a dedicated vacuum chamber with optical access to multiple membranes to help us to characterize the high-stress membranes and to develop a repeatably good mounting scheme.

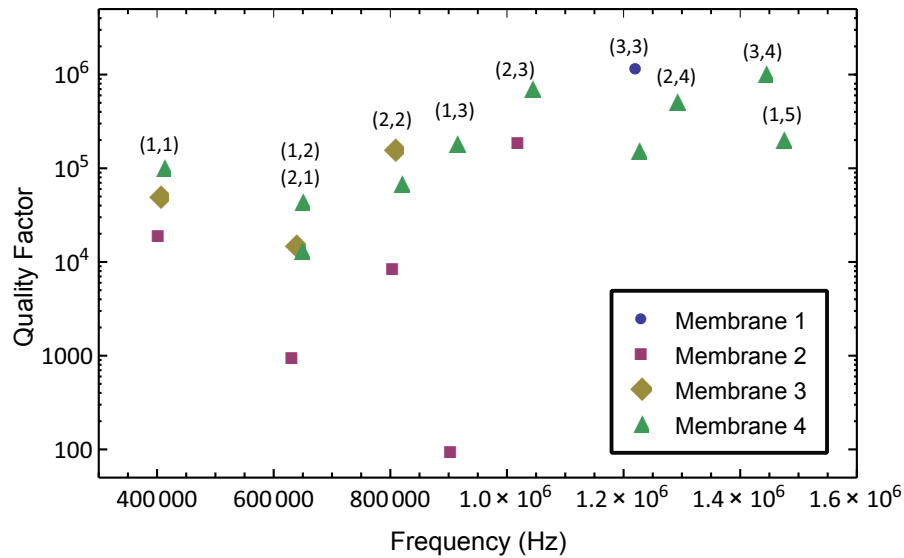


Figure 4.2: Measured quality factor for different mechanical modes of four 1 mm square, 50 nm-thick, high-stress stoichiometric membranes used over the period of a month. The mountings all used epoxy, but amount and location of the epoxy joint differed between membranes. The measurements were made by driving the membrane and sweeping the drive across the mechanical resonant frequency and measuring the width of the resonance peak. The estimates are relatively crude when compared to the ring-down measurements in Fig. 4.1. The most significant point is that higher frequency mechanical modes tend to have higher quality factors.

### 4.1.2 Optical loss in silicon nitride membranes

In general, silicon nitride membranes have low optical loss. Table 4.2 shows upper bounds on absorption loss for a number of silicon nitride membranes. The loss is usually characterized using an optical ring-down technique where a well-coupled incident laser beam is chopped very quickly ( $\sim 10$  ns), whereupon a photodiode captures the decay of the intracavity field by monitoring the light leaking out through the end mirrors. In our case, the cavity ring-downs were most often monitored using the transmitted intensity and a 150 MHz bandwidth photodiode (Thorlabs PDA10CF). The high bandwidth is important so that the short cavity decay time  $\tau_{\text{decay}} \sim 10^{-7}$  s is not distorted by the photodiode response time.

Figure 4.4 shows a cavity ring-down at a node and an antinode. The data is fit to an exponential of the form

$$P_{\text{trans}}(t) = P_0 e^{-t/\tau_{\text{decay}}} \quad (4.6)$$

where  $P_0$  is the power at  $t = 0$  and  $\tau_{\text{decay}}$  is the cavity decay time. The decay time  $\tau_{\text{decay}}$  is related to the cavity finesse  $F$  according to

$$F = \frac{\pi c \tau_{\text{decay}}}{L} \quad (4.7)$$

where  $c$  is the speed of light and  $L$  is the cavity length.

An upper bound on the absorption and scattering loss due to the membrane can be set by comparing the loss when the membrane is positioned at a node (minimum field, negligible absorption) and at an antinode (maximum field and absorption). The round-trip absorption in the membrane  $A_{\text{mem}}$  can be expressed in two ways. The first way relates the round-trip fractional absorption  $A_{\text{mem}}$  to the finesse at the node and antinode:

$$A_{\text{mem}} = \frac{\pi}{F_{\text{antinode}}} - \frac{\pi}{F_{\text{node}}} \quad (4.8)$$

The second way relates the absorption  $A_{\text{mem}}$  to the absorption loss passing through twice the membrane thickness:

$$A_{\text{mem}} = \frac{4\pi \text{Im}(n) t_m}{\lambda} \quad (4.9)$$

	$F_{\text{node}}$	$F_{\text{antinode}}$	$\text{Im}(n)$	$\lambda$ (nm)	Reference
Low Stress (Yale)	16,800	7,100	$\lesssim 1.6 \times 10^{-4}$	1064	Ref. [101]
High Stress (Yale)			$\lesssim 1.5 \times 10^{-6}$	1064	Ref. [69]
High Stress (Caltech)			$\lesssim 10^{-5}$	935	Ref. [106]
High Stress (Thesis)	57,000	29,000	$\lesssim 9 \times 10^{-5}$	1064	See Figs. 4.3 and 4.4

Table 4.2: Comparison of upper bounds on membrane absorption for a variety of silicon nitride membranes tested by our Yale group and by the Caltech group.

Solving for the imaginary part of the index of refraction  $\text{Im}(n)$  gives

$$\text{Im}(n) = \frac{\lambda}{4t_m} \left( \frac{1}{F_{\text{antinode}}} - \frac{1}{F_{\text{node}}} \right) \quad (4.10)$$

When Eq. 4.10 is applied to the data in Fig. 4.3, we determine a value of  $\text{Im}(n) \lesssim 9 \times 10^{-5}$ . Table 4.2 compares this result with other estimates of optical loss in silicon nitride membranes. While the estimate given in this thesis is smaller than the absorption of low stress silicon nitride membranes determined in Ref. [101], it is an order of magnitude larger than the high stress absorptions determined in Refs. [69, 106]. Because the membrane comes from the same batch of high stress membranes as used in Ref. [69], the additional loss is likely explained by contamination of the membrane surface rather than an intrinsic property of the silicon nitride.

## 4.2 The cavity and optical mount

The cavity end mirrors were nominally identical. The substrates had a diameter of 0.5 inches, a radius of curvature  $R = 5$  cm, and thickness of 0.165 inches. Advanced Thin Films of Boulder, CO coated the end mirrors with a low-loss, high-reflectivity laser line coating for 1064 nm.

The cavity length was  $L = 7$  mm, giving a beam waist  $w_0$  for the Gaussian-cross-section  $\text{TEM}_{00}$  mode of

$$w_0 = \left( \frac{2R}{L} - 1 \right)^{1/4} \left( \frac{\lambda L}{2\pi} \right)^{1/2} \quad (4.11)$$

Using  $R = 5$  cm,  $L = 7$  mm, and a laser wavelength of  $\lambda = 1064$  nm gives a beam waist of  $w_0 = 65 \mu\text{m}$ . Since our membrane is a 1 mm square, clipping of the beam should not limit the finesse in any way, unless the beam is positioned significantly off-center of the membrane.

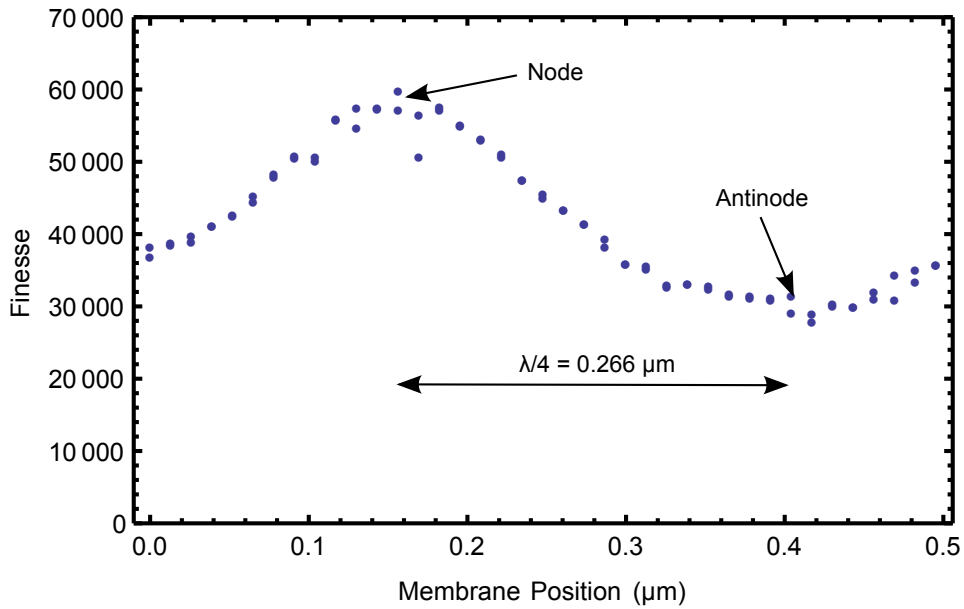


Figure 4.3: Position dependence of cavity finesse for a high-stress stoichiometric membrane inside the  $L = 7$  mm cavity. Each of the points is measured by taking an optical ring-down similar to Fig. 4.4. The variation in finesse from node to antinode is used to determine an upper limit on membrane absorption of  $\text{Im}(n) \lesssim 9 \times 10^{-5}$  using Eq. 4.10. Table 4.2 compares this result with previous estimates of membrane absorption.

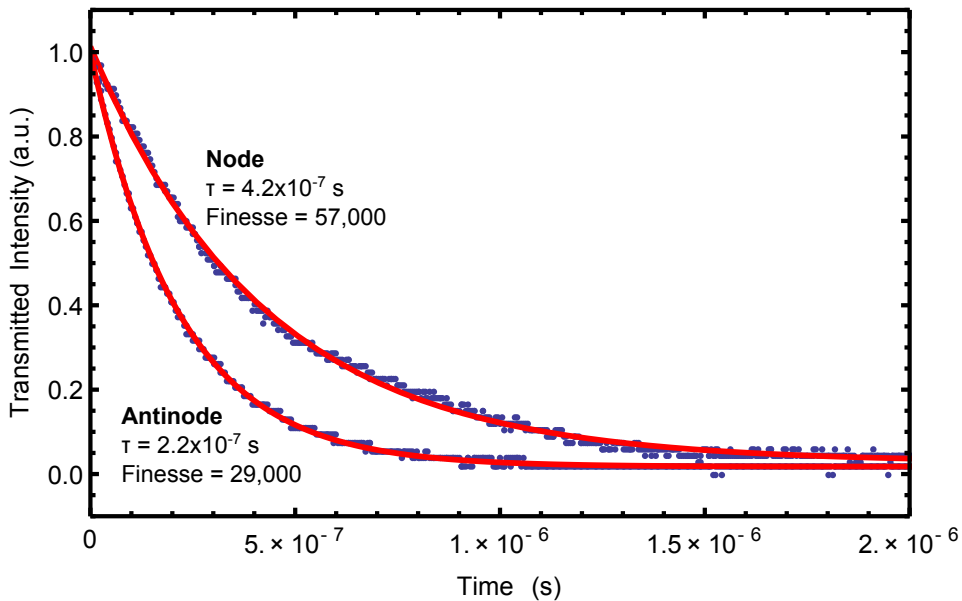


Figure 4.4: Cavity ring-downs at the node and antinode.

The cavity and membrane mount is shown in Fig. 4.5. The cavity spacer was machined from Invar, chosen for its low coefficient of thermal expansion compared to stainless steel or aluminum. The membrane was epoxied to a thin removable aluminum bridge which could be slid in between the end mirrors. In order to center the membrane on the intracavity beam, the membrane has a rough adjustment actuated by screws in the plane parallel to the membrane. Fine adjustment in the  $z$ -direction along the cavity axis is provided by a kinematic mirror mount (modified Thorlabs KS2). The three standard 1/4"-80 adjustment screws were replaced by vacuum compatible motorized actuators (Thorlabs Z606V), which have a minimum step size of about 50 nm and a 6 mm range. Since the membrane should ideally be positioned with  $\sim 1$  nm resolution, the aluminum bridge upon which the membrane is mounted is supported a pair of piezo-electric actuators (one on each end of the bridge). These miniature multilayer piezo stack actuators (Physik Instrumente PICMA PL055) have a 5 mm square base and are 2 mm thick. The piezo actuators have a 2.2  $\mu\text{m}$  range over 0 – 100 V, which spans about four periods of the intracavity standing wave.

The angular alignment of the membrane is also controlled via the Thorlabs KS2 kinematic mirror mount. Angular alignment is essential for achieving low optical loss and can also be used to tune the optomechanical coupling as shown by Sankey et al. [69].

## 4.3 Optics Setup

This section will describe the optical setup. It will refer to the diagram shown in Fig. 4.6.

### 4.3.1 Stage 1

The laser source is an Nd:YAG laser (Innolight Prometheus) which produces about 1 Watt of 1064 nm light with a free-running linewidth of about 1 kHz. The first stage of optics passes the beam through an optical isolator to protect the laser from back-reflections. The isolated beam is then split by a non-polarizing beam splitter, with part of the beam going to the RPSN experiment, and part going to other experiments. Next, a half wave plate and polarizing beam splitter are employed for controlling the laser power. Finally the beam diameter and direction are modified by lenses and

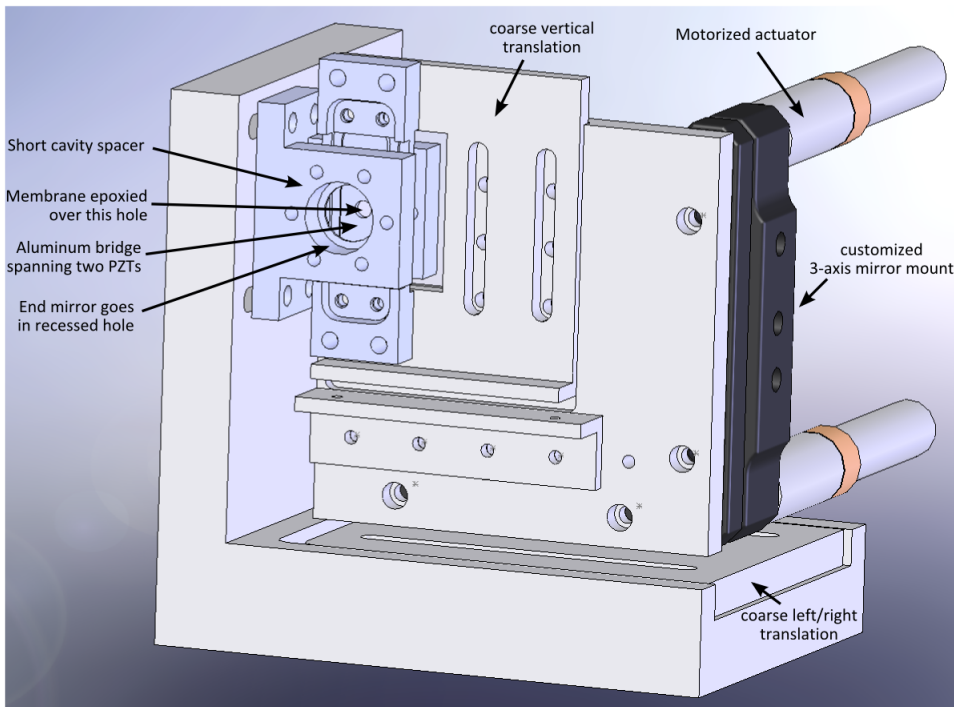


Figure 4.5: Diagram of the cavity spacer, membrane mount, and associated positioning optomechanics.

mirrors to couple efficiently into a collimator (Thorlabs FiberPort). A polarization-maintaining fiber (Thorlabs PM980-HP) takes the 1064 nm light to the second stage of optics.

### 4.3.2 Stage 2

The second stage begins with another collimator (Thorlabs FiberPort PAF-X-7-C), which sends out collimated light from the fiber. The diameter of the collimator output was chosen to be as large as possible without clipping the beam on any of the subsequent optics. The aperture is limited by the 1 mm-tall crystal in the acousto-optic modulator. The beam will later be recoupled into another collimator without any additional lenses, so a wider beam with less divergence is desired. After emerging from the collimator, the beam is split in two using a half-wave plate and a polarizing beam splitter to adjust the split ratio. The reflected beam will be the local oscillator beam for a heterodyne detection scheme of the light reflected from the cavity. The transmitted beam will be the signal beam.

The signal beam passes through an electro-optic modulator (EOM, ConOptics M360-40), which is aligned for phase modulation of the beam. The phase modulation sidebands are used for a

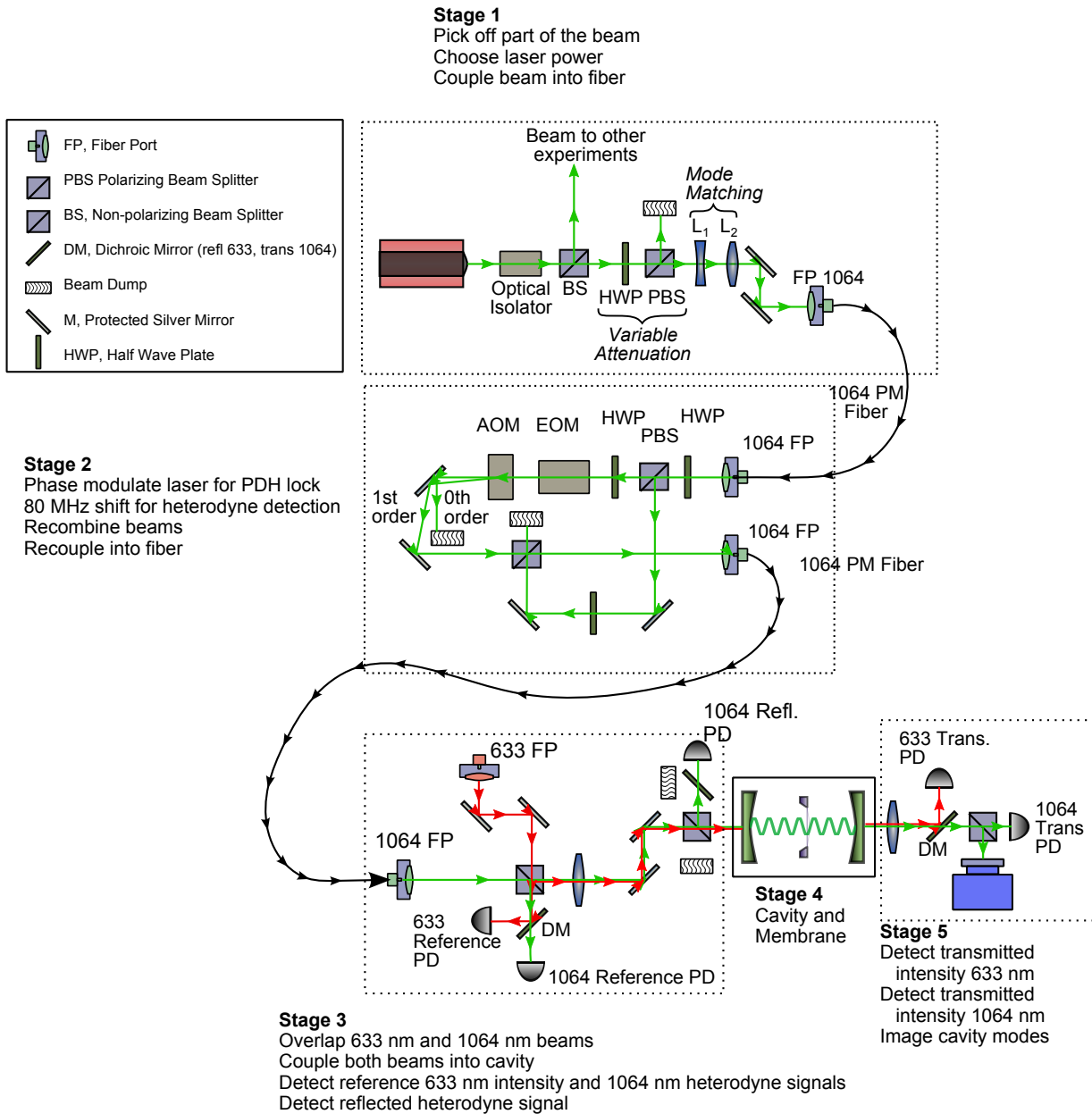


Figure 4.6: Schematic of the optics from laser to cavity to photodiodes.

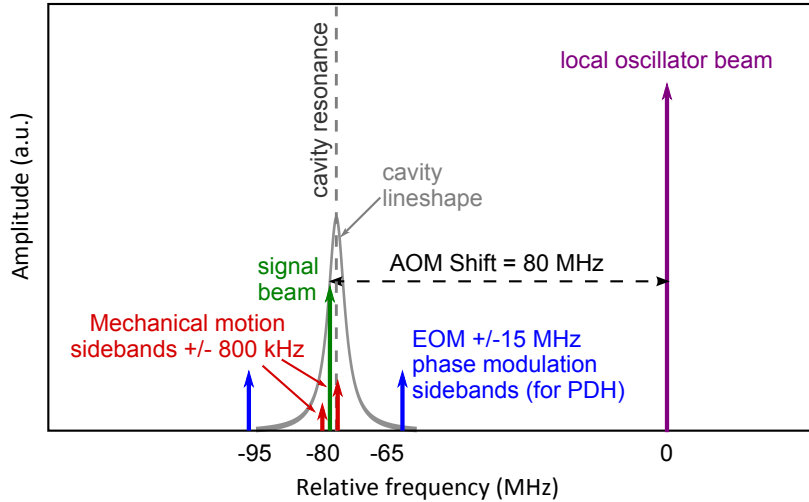


Figure 4.7: Diagram of the main optical signals. The local oscillator beam (purple), the signal beam (green), and the phase modulation sidebands of the signal beam (blue) are all incident upon the cavity (gray, dashed line). The reflected beam has the additional  $\pm 800$  kHz modulation of the signal beam (shown in red), which results from the membrane’s Brownian motion modulating the intracavity field.

Pound-Drever-Hall (PDH) detection scheme to measure the relative detuning between the laser and cavity [33]. Next, the carrier and phase modulation sidebands are passed through an acousto-optic modulator (AOM, NEOS 46080-1-1.06) to shift the carrier and sidebands of the beam by about 80 MHz. The zeroth order (undeflected) beam is blocked.

The frequency-shifted, phase-modulated signal beam is recombined with the local oscillator beam, and both beams are then recoupled into another polarization-maintaining fiber. Figure 4.7 graphically summarizes the end result of the AOM and EOM modulation which occurs in Stage 2.

### 4.3.3 Stage 3

The 1064 nm beam is overlapped with a 633 nm beam from a fiber-coupled stabilized HeNe laser, and both are coupled into the cavity. The 1064 nm beam is responsible for the optomechanics and for the very sensitive displacement measurements. The 633 nm beam detects nanometer-scale displacements of the membrane, and the signal is used to provide feedback on the membrane position via the piezo actuators, keeping the membrane at a fixed position in the intracavity field. A dichroic beam splitter separates the 633 nm and 1064 nm reference beams which are not incident upon the

cavity. The 633 nm reference beam monitors power fluctuations in the diode laser so they are not confused with position fluctuation in the membrane. The 1064 nm reference photodiode (Thorlabs PDA10CF) is used to measure the  $\sim 80$  MHz heterodyne beat note before entering the cavity and to detect phase shifts between the signal and local oscillator beam in Stage 2. Such a phase shift between the signal beam and local oscillator beam can be caused by thermal expansion of the optical breadboard and/or vibrations the mirrors.

Lastly, the reflected 1064 nm photodiode (Thorlabs PDA10CF) detects beat notes due to PDH (15 MHz) and heterodyne mixing (80 MHz). A dichroic mirror is used to reject 633 nm light from the reflected 1064 nm photodiode. For any of the heterodyne photodiodes, care must be taken to limit the total incident optical power to about  $200 \mu\text{W}$  to maintain a linear response from the photodiode.

Regarding mode matching to the cavity, the mirror substrates are plano-concave and act like diverging lenses, which means the input beam needs some effective beam waist  $w_{\text{eff}}$  and effective position  $z_{0,\text{eff}}$ , such that after going through the diverging lens, the true intracavity beam waist and position will be achieved. Kogelnik and Li [107] wrote the classic reference for Gaussian beams and cavity modes, and the following equations for the effective beam waist and position are quoted from them:

$$w_{0,\text{eff}} = \sqrt{\frac{\lambda R \sqrt{L(2R - L)}}{\pi (2R + L)(n^2 - 1)}} \quad (4.12)$$

$$z_{0,\text{eff}} = \frac{L}{2} - \frac{nLR}{2R - L(n^2 - 1)} \quad (4.13)$$

For our cavity with length  $L = 7$  mm, mirror radius of curvature  $R = 5$  cm, index of refraction for the fused silica substrate  $n = 1.46$ , and wavelength  $\lambda = 1064$  nm we obtain

$$w_{\text{eff}} = 63 \mu\text{m} \quad (4.14)$$

and

$$z_{0,\text{eff}} = -2 \text{ mm} \quad (4.15)$$

Thus the deviation from the cavity mode waist of  $w_0 = 66 \mu\text{m}$  is minimal for such a short cavity.

Note that in the limit  $L \ll R$ , the equation for the intracavity beam waist given in Eq. 4.11 and the effective beam waist given in Eq. 4.12 become equal.

#### 4.3.4 Stage 4

The 1064 nm and 633 nm beams enter the cavity and are modulated by the membrane motion. Light leaks out of the cavity through the end mirrors and is detected by the reflected heterodyne photodiode or the transmitted intensity photodiodes.

#### 4.3.5 Stage 5

The transmitted 633 nm beam is sensitive to large scale ( $> 1$  nm) motion of the membrane. The intensity of the transmitted 1064 nm beam, along with the reflected heterodyne signal, are the two signals needed for the correlation measurement. A camera is also used to image the cavity modes in transmission to determine which mode the incident beam is exciting inside the cavity.

### 4.4 Vacuum systems

The cavity and membrane are under continuous vacuum provided by an ion pump. The internal pressure is about  $10^{-6}$  Torr.

### 4.5 Electronic signal processing and data acquisition

Table 4.3 summarizes the many signals that we would like to simultaneously and synchronously acquire. For the correlation measurement  $S[\omega] = X_\phi[\omega]Y_{\theta_l}^*[\omega]$ , we must acquire the membrane position fluctuations in the reflected heterodyne signal (near 79.2 MHz and 80.8 MHz) and the fluctuations in transmitted intensity near the mechanical resonance (800 kHz). The reference heterodyne beat note at 80 MHz is needed to measure fluctuations in the phase between the local oscillator and signal beams. The reflected heterodyne beat note at 80 MHz is used to measure low frequency (zero to a few kHz) detuning fluctuations. The PDH error signal (zero to a few kHz) and the 633 nm

transmitted intensity (zero to a few kHz) can be used to characterize the membrane vibrations due to acoustic and seismic noise.

In addition to simultaneously acquiring many channels, we also need long averaging times. The mechanical linewidth of the membrane is about 1 Hz, necessitating measurement times much longer than a second to resolve the mechanical resonance. To sufficiently suppress the thermal effects below the RPSN-induced  $R_{q,z}[\omega]$  term, a measurement time of an hour or longer may be needed (see Sec. 3.9).

We used a Zurich Instruments HF2 Lock-in Amplifier in order to synchronously capture the narrow-bandwidth signals in Table 4.3. The ZI-HF2 has two 50 MHz bandwidth inputs, six independently controllable internal oscillators, and six internal mixers which can be combined in an arbitrary arrangement. There are also two 100 kHz bandwidth auxiliary inputs which are not mixed or filtered. Because the heterodyne beat note is around 80 MHz (optimal diffraction efficiency for AOM), which is above the 50 MHz bandwidth of the ZI-HF2, we mix the heterodyne signals with a 100 MHz local oscillator to shift all the heterodyne signals closer to 20 MHz, well within the ZI-HF2's bandwidth. The 80 MHz AOM drive is created by mixing a 20 MHz ZI-HF2 output with the same 100 MHz local oscillator. A schematic of the electronic detection scheme is shown in Fig. 4.8. Because many of the signals are widely separated in frequency (0 kHz, 800 kHz, 19.2 MHz, 20.0 MHz, 20.8 MHz), these signals can be summed and connected to the same input on the ZI-HF2.

## 4.6 Using a heterodyne measurement to detect an arbitrary quadrature

A heterodyne measurement involves the beating (mixing) of a strong, noise-free oscillation, and a weaker oscillation containing a signal of interest. The technique can be used to measure an arbitrary quadrature of the signal.

In an *optical* heterodyne measurement the two oscillations are typically laser beams, and the mixing is accomplished by overlapping the beams on the same photodiode. The strong and noise-free beam is called the *local oscillator beam*. The weaker beam containing the signal of interest is

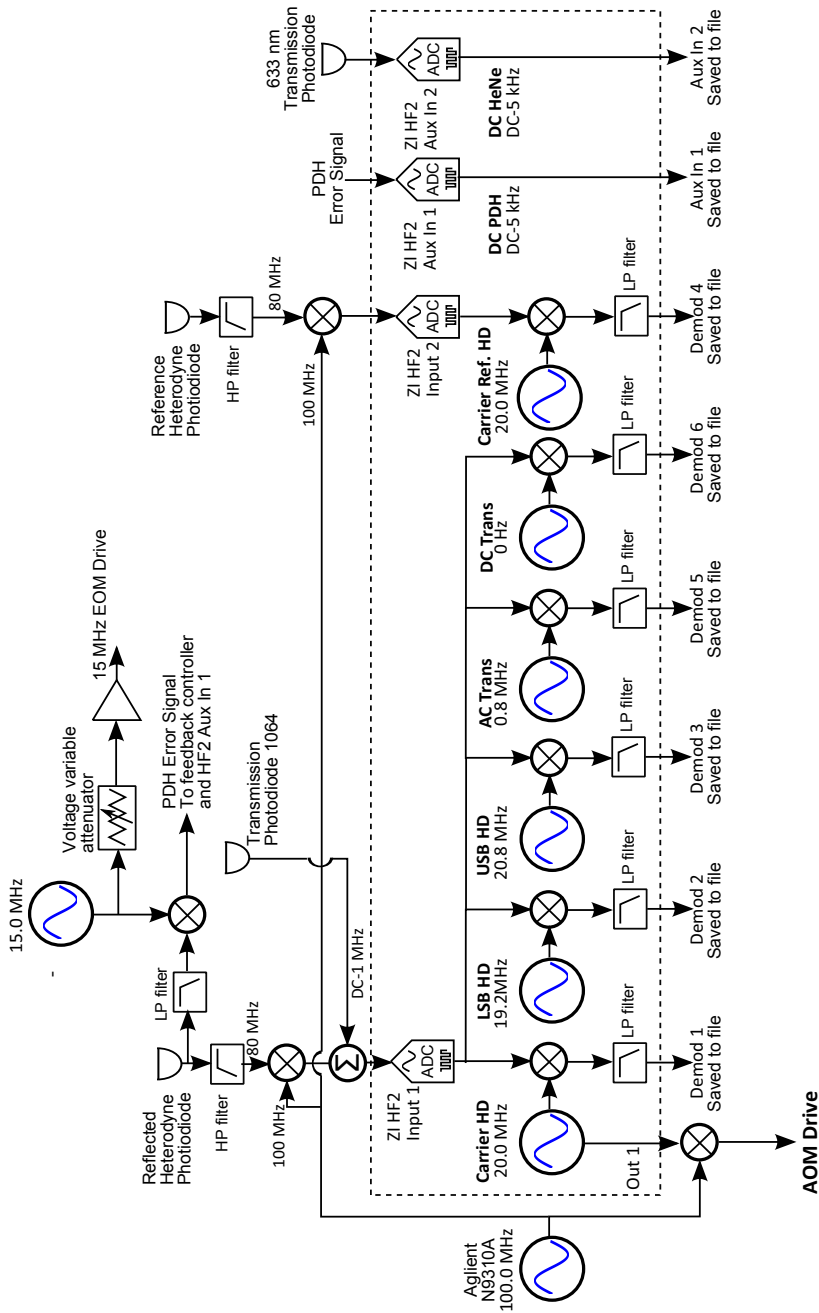


Figure 4.8: Electronic Detection Scheme. The portion inside the dashed rectangle in the Zurich Instruments HF2. The diagram tracks the signals from the various photodiodes (also shown in the optical schematic Fig. 4.6) to the final mixed down quadratures from the ZI-HF2. Omitted from the diagram are a number of attenuators and amplifiers needed for adjusting the signal strengths to appropriate levels for mixers and the ZI-HF2 inputs.

	Input	Demod. No.	Sig. Freq. (MHz)	Input/Demod Freq. (MHz)
Reflected HD Carrier	1	1	80.0	20.0
HD Mechanical USB	1	2	79.2	20.8
HD Mechanical LSB	1	3	80.8	19.2
Reference HD Carrier	2	4	80.0	20.0
Transmission Mechanical	1	5	0.8	0.8
Transmission DC	1	6	0	0
Pound-Drever-Hall Error Signal DC	Aux-in 1	-	-	-
633 nm Transmission DC	Aux-in 2	-	-	-

Table 4.3: Summary of the eight input signals to the ZI-HF2. The table matches what is explained graphically in Fig. 4.8. The column “Sig. Freq.” is the frequency of the heterodyne beat note on the photodiode. The column “Input/Demod Freq.” is the frequency of the signal at the input to the ZI-HF2, which for the heterodyne signals involves mixing the photodiode signal with a 100 MHz oscillator before going to the ZI-HF2. The input frequency is the same (to within 1 kHz) as the demodulator frequency, which is why the column is labeled “Input/Demod. Freq.”

called the *signal beam*. When the two beams are detected on a photodiode, the photodiode output is proportional to the square of the instantaneous electric field (low-passed by the photodiode’s bandwidth). The photodiode’s output signal is proportional to

$$I(t) \propto (E_{\text{LO}}(t) + E_{\text{sig}}(t))^2 \quad (4.16)$$

The cross-term  $E_{\text{LO}}(t)E_{\text{sig}}(t)$  is the mixing process.

I now want to calculate the reflected heterodyne mixing term  $V_{\text{HD}}[\omega]$  in terms of the local oscillator beam  $E_{\text{LO}}(t)$  and the reflected signal beam  $\hat{d}_{\text{out,L}}(t)$ . First, we express the local oscillator with frequency  $\omega_{\text{LO}}$  and phase shift  $\psi$  as

$$E_{\text{LO}}(t) = E_{\text{LO}} \cos(\omega_{\text{LO}}t - \psi) \quad (4.17)$$

The local oscillator can be treated as a classical signal because shot noise in the stronger local oscillator beam makes a negligible contribution to the heterodyne mixing term. The signal beam  $\hat{E}_{\text{sig}}$  can be written as

$$\hat{E}_{\text{sig}}(t) = \hat{a}_{\text{out,L}}(t) + \hat{a}_{\text{out,L}}^\dagger(t) \quad (4.18)$$

In the Fourier domain Eq. 4.17 becomes

$$E_{\text{LO}}[\omega] = E_{\text{LO}}\pi \left( e^{-i\psi} \delta(\omega + \omega_{\text{LO}}) + e^{i\psi} \delta(\omega - \omega_{\text{LO}}) \right) \quad (4.19)$$

Similarly, the signal beam fluctuations given by Eq. 4.18 becomes

$$\hat{a}_{\text{out,L}}[\omega] + \hat{a}_{\text{out,L}}^\dagger[\omega] = \sqrt{\kappa_{\text{L}}}\bar{a} \left( 2\pi\delta(\omega - \omega_{\text{D}}) + \hat{d}_{\text{out,L}}[\omega - \omega_{\text{D}}] \right) \quad (4.20)$$

$$+ \sqrt{\kappa_{\text{L}}}\bar{a}^* \left( 2\pi\delta(\omega + \omega_{\text{D}}) + \hat{d}_{\text{out,L}}^\dagger[\omega + \omega_{\text{D}}] \right) \quad (4.21)$$

Then the photodiode output  $V_{\text{HD}}[\omega]$ , which results from the heterodyne beating of the local oscillator and the signal beam, can be found via the convolution theorem:

$$V_{\text{HD}}[\omega] = \frac{1}{2\pi} \int_{-\infty}^{\infty} d\omega' E_{\text{LO}}[\omega'] \left( \hat{a}_{\text{out,L}}[\omega - \omega'] + \hat{a}_{\text{out,L}}^\dagger[\omega - \omega'] \right) \quad (4.22)$$

$$= \frac{1}{2\pi} E_{\text{LO}}\pi e^{-i\psi} \left[ \sqrt{\kappa_{\text{L}}}\bar{a} \left( 2\pi\delta(\omega + \omega_{\text{LO}} - \omega_{\text{D}}) + \hat{d}_{\text{out,L}}[\omega + \omega_{\text{LO}} - \omega_{\text{D}}] \right) \right. \\ \left. + \sqrt{\kappa_{\text{L}}}\bar{a}^* \left( 2\pi\delta(\omega + \omega_{\text{LO}} + \omega_{\text{D}}) + \hat{d}_{\text{out,L}}^\dagger[\omega + \omega_{\text{LO}} + \omega_{\text{D}}] \right) \right] \\ + \frac{1}{2\pi} E_{\text{LO}}\pi e^{i\psi} \left[ \sqrt{\kappa_{\text{L}}}\bar{a} \left( 2\pi\delta(\omega - \omega_{\text{LO}} - \omega_{\text{D}}) + \hat{d}_{\text{out,L}}[\omega - \omega_{\text{LO}} - \omega_{\text{D}}] \right) \right. \\ \left. + \sqrt{\kappa_{\text{L}}}\bar{a}^* \left( 2\pi\delta(\omega - \omega_{\text{LO}} + \omega_{\text{D}}) + \hat{d}_{\text{out,L}}^\dagger[\omega - \omega_{\text{LO}} + \omega_{\text{D}}] \right) \right] \quad (4.23)$$

The photodiode output only responds to intensity fluctuations within the photodiode bandwidth ( $< 150$  MHz), so the frequency-summed beating terms at  $\omega_{\text{LO}} + \omega_{\text{D}} \approx 2\pi \times 10^{15}$  Hz are not detected by the photodiode.

Lastly, we define the difference beat frequency  $\omega_{\text{B}} = \omega_{\text{D}} - \omega_{\text{LO}}$ . Then the reflected heterodyne mixing term becomes

$$V_{\text{HD}}[\omega] = \frac{1}{2\pi} E_{\text{LO}}\pi \left[ e^{-i\psi} \sqrt{\kappa_{\text{L}}}\bar{a} \left( 2\pi\delta(\omega - \omega_{\text{B}}) + \hat{d}_{\text{out,L}}[\omega - \omega_{\text{B}}] \right) \right. \\ \left. + e^{i\psi} \sqrt{\kappa_{\text{L}}}\bar{a}^* \left( 2\pi\delta(\omega + \omega_{\text{B}}) + \hat{d}_{\text{out,L}}^\dagger[\omega + \omega_{\text{B}}] \right) \right] \quad (4.24)$$

## 4.7 Converting the ZI-HF2 demodulator into the correlation signal

This section will describe how the photodiode output  $V_{\text{HD}}[\omega]$  given by Eq. 4.24 is processed and saved to file by the ZI-HF2 Lock-in Amplifier. This section will also describe how the data saved by the ZI-HF2 is converted to the arbitrary reflected quadrature  $Y_{\theta_L}[\omega]$  and transmitted intensity quadrature  $X_{\phi}[\omega]$ . The correlation  $S[\omega]$  can then be computed as:

$$S[\omega] = \delta X_{\phi}[\omega] \delta Y_{\theta}^*[\omega] \quad (4.25)$$

Since we are only interested in fluctuations in a narrow bandwidth around  $\omega_M$ , it is natural to shift the signal to a much lower frequency in order to reduce the sample rate of the data acquisition. First, I want to consider how the ZI-HF2 transforms the input signal into saved data.

Let  $V(t)$  be the input signal to the ZI-HF2, and let the  $i$ -th demodulator be set to a frequency  $\Omega_i$ . The input signal  $V(t)$  first passes into a high speed ( $\approx 200$  MS/s) analog-to-digital converter. The digitized signal is then multiplied by  $e^{i\Omega t} = \cos \Omega t + i \sin \Omega t$  and filtered by a low pass filter with a time constant  $\tau_C$ , which gives

$$V_X(t) = \int_{-\infty}^t e^{-t'/\tau_C} V(t-t') \cos \Omega(t-t') dt' \quad (4.26)$$

$$V_Y(t) = \int_{-\infty}^t e^{-t'/\tau_C} V(t-t') \sin \Omega(t-t') dt' \quad (4.27)$$

The two time traces  $V_X(t)$  and  $V_Y(t)$  are then written to file at a sample rate much smaller than  $\Omega/2\pi$  (typically about 7 kHz).

To recover the original input signal  $V(t)$  from the saved time traces  $V_X(t)$  and  $V_Y(t)$ , first form the complex quantity

$$V_Z(t) = V_X(t) + iV_Y(t) \quad (4.28)$$

which in the Fourier domain becomes

$$V_Z[\omega] = \int_{-\infty}^{\infty} V_Z(t) e^{i\omega t} dt \quad (4.29)$$

$$= \int e^{-t'/\tau_C} V(t-t') e^{i\Omega(t-t')} e^{i\omega t} dt dt' \quad (4.30)$$

$$= \int e^{-t'/\tau_C} e^{i\omega t'} V(t-t') e^{i\Omega(t-t')} e^{i\omega(t-t')} dt dt' \quad (4.31)$$

$$= \int e^{-t'/\tau_C} e^{i\omega t'} V[\omega] 2\pi \delta(\Omega + \omega - \omega') d\omega' dt' \quad (4.32)$$

$$= \int e^{-t'/\tau_C} e^{i\omega t'} V[\omega + \Omega] dt' \quad (4.33)$$

$$= \frac{1}{\frac{1}{\tau_C} - i\omega} V[\omega + \Omega] \quad (4.34)$$

Similarly, the Fourier transform of  $V_{Z^*}(t) = V_Z(t) - iV_Y(t)$  is

$$V_{Z^*}[\omega] = \frac{1}{\frac{1}{\tau_C} - i\omega} V[\omega - \Omega] \quad (4.35)$$

Ignoring the low-pass filtering, we obtain an approximation for the Fourier transform of the original input  $V[\omega]$ , which is valid within the bandwidth of the low-pass filter:

$$V[\omega + \Omega] \approx V_Z[\omega] \quad (4.36)$$

and

$$V[\omega - \Omega] \approx V_Z^*[\omega] \quad (4.37)$$

where  $V_Z^*[\omega]$  denotes that the complex conjugation of the time trace  $V_Z(t) = V_X(t) + iV_Y(t)$  is happens *before* the Fourier transform rather than  $V_Z[\omega]^*$  where the complex conjugation happens *after* the Fourier transform.

## 4.8 Reconstructing the transmitted intensity fluctuations $\delta X_\phi[\omega]$

The following sections will use a notation consistent with the schematic for the electronic detection scheme shown in Fig. 4.8. Demodulator 5 is used to measure fluctuations near  $\omega_M$ . The demodulator

frequency  $\Omega_5$  is shifted from mechanical resonance  $\omega_M$  by an amount  $\delta\omega$  (i.e.  $\Omega_5 = \omega_M + \delta\omega$ ). Typically the offset  $\delta\omega$  is chosen to be about  $2\pi \times 1$  kHz. Recovering the transmitted intensity fluctuations  $\delta X_\phi[\omega]$  from the demodulator outputs  $X_5(t)$  and  $Y_5(t)$  is straightforward because the only role of the ZI-HF2 in this case is to shift the input signal to a lower frequency. The Fourier transform of  $Z_5(t) = X_5(t) + iY_5(t)$  is related to the input signal  $\delta X_\phi[\omega]$  by Eq. 4.36 giving

$$\delta X_\phi[\omega + \Omega_5] = Z_5[\omega] \quad (4.38)$$

## 4.9 Reconstructing the reflected fluctuations in an arbitrary quadrature $\delta Y_{\theta_L}[\omega]$ (Ideal measurement)

Next, we want to reconstruct an arbitrary quadrature of the reflected heterodyne signal  $Y_{\theta_L}[\omega] = e^{-i\theta_L} \hat{d}_{\text{out,L}}[\omega] + e^{i\theta_L} \hat{d}_{\text{out,L}}^\dagger[\omega]$  from the photodiode output  $V_{\text{HD}}[\omega]$  given in Eq. 4.24 (and copied below)

$$\begin{aligned} V_{\text{HD}}[\omega] = & \frac{1}{2\pi} E_{\text{LO}} \pi \left[ e^{-i\psi} \sqrt{\kappa_L} \bar{a} \left( 2\pi \delta(\omega - \omega_B) + \hat{d}_{\text{out,L}}[\omega - \omega_B] \right) \right. \\ & \left. + e^{i\psi} \sqrt{\kappa_L} \bar{a}^* \left( 2\pi \delta(\omega + \omega_B) + \hat{d}_{\text{out,L}}^\dagger[\omega + \omega_B] \right) \right] \end{aligned} \quad (4.39)$$

Because the heterodyne beat note is above the input bandwidth of the ZI-HF2, we must first perform an intermediate stage of mixing. The photodiode signal  $V_{\text{HD}}[\omega]$  is mixed with a 100 MHz oscillation to bring the 80 MHz beat note down to around 20 MHz. We define the difference frequency  $\omega_F$ :

$$\omega_F/2\pi = 100 \text{ MHz} - 80 \text{ MHz} = 20 \text{ MHz} \quad (4.40)$$

The mixed-down version of  $V_{\text{HD}}[\omega]$  that is input to the ZI-HF2,  $V_{\text{HD,M}}[\omega]$ , is

$$\begin{aligned} V_{\text{HD,M}}[\omega] = & \frac{1}{2\pi} E_{\text{LO}} \pi \left[ e^{-i\psi} \sqrt{\kappa_L} \bar{a} \left( 2\pi \delta(\omega + \omega_F) + \hat{d}_{\text{out,L}}[\omega + \omega_F] \right) \right. \\ & \left. + e^{i\psi} \sqrt{\kappa_L} \bar{a}^* \left( 2\pi \delta(\omega - \omega_M) + \hat{d}_{\text{out,L}}^\dagger[\omega - \omega_F] \right) \right] \end{aligned} \quad (4.41)$$

In order to capture the narrow-band mechanical motion in the heterodyne signal  $V_{\text{HD,M}}[\omega]$ , we need two of the ZI-HF2 demodulators set near the upper and lower mechanical motion sidebands (near 20.8 MHz and 19.2 MHz). We capture the upper sideband with demodulator 2 set to a frequency  $\Omega_2 = \omega_{\text{F}} + \Omega_5$  and capture the lower sideband with demodulator 3 set to  $\Omega_3 = \omega_{\text{F}} - \Omega_5$ . In a narrow bandwidth ( $|\omega| \ll \Omega_5 \ll \Omega_2$ ) around  $\Omega_2$ , the mixed heterodyne signal can be written as:

$$V_{\text{HD,M}}[\omega + \Omega_2] = \frac{1}{2\pi} E_{\text{LO}} \pi \left[ e^{-i\psi} \sqrt{\kappa_{\text{L}}} \bar{a} \left( 2\pi\delta(\omega + \Omega_2 + \omega_{\text{F}}) + \hat{d}_{\text{out,L}}[\omega + \Omega_2 + \omega_{\text{F}}] \right) \right. \quad (4.42)$$

$$\left. + e^{i\psi} \sqrt{\kappa_{\text{L}}} \bar{a}^* \left( 2\pi\delta(\omega + \Omega_2 - \omega_{\text{F}}) + \hat{d}_{\text{out,L}}^\dagger[\omega + \Omega_2 - \omega_{\text{F}}] \right) \right] \quad (4.43)$$

$$= \frac{1}{2\pi} E_{\text{LO}} \pi \left[ e^{-i\psi} \sqrt{\kappa_{\text{L}}} \bar{a} \left( 2\pi\delta(\omega + \Omega_5 + 2\omega_{\text{F}}) + \hat{d}_{\text{out,L}}[\omega + \Omega_5 + 2\omega_{\text{F}}] \right) \right. \quad (4.44)$$

$$\left. + e^{i\psi} \sqrt{\kappa_{\text{L}}} \bar{a}^* \left( 2\pi\delta(\omega + \Omega_5) + \hat{d}_{\text{out,L}}^\dagger[\omega + \Omega_5] \right) \right] \quad (4.45)$$

$$\approx \frac{1}{2\pi} E_{\text{LO}} \pi e^{i\psi} \sqrt{\kappa_{\text{L}}} \bar{a}^* \hat{d}_{\text{out,L}}^\dagger[\omega + \Omega_5] \quad (4.46)$$

$$\approx V_{Z2}[\omega] \quad (4.47)$$

The simplification in Eq. 4.46 occurs because of the narrow bandwidth approximation ( $|\omega| \ll \Omega_5 \ll \Omega_2$ ). Equation 4.47 comes from Eq. 4.36. The key result is the relationship between  $\hat{d}_{\text{out,L}}^\dagger[\omega + \Omega_5]$  in Eq. 4.46 and  $V_{Z2}[\omega]$  in Eq. 4.47.

Similarly  $V_{\text{HD,M}}[\omega - \Omega_2]$  becomes

$$V_{\text{HD,M}}[\omega - \Omega_2] = \frac{1}{2\pi} E_{\text{LO}} \pi e^{-i\psi} \sqrt{\kappa_{\text{L}}} \bar{a} \hat{d}_{\text{out,L}}[\omega - \Omega_5] \quad (4.48)$$

$$= V_{Z2}^*[\omega] \quad (4.49)$$

For demodulator 3 set near the lower sideband  $\Omega_3 = \omega_{\text{F}} - \Omega_5$  we get

$$V_{\text{HD,M}}[\omega + \Omega_3] = \frac{1}{2\pi} E_{\text{LO}} \pi e^{i\psi} \sqrt{\kappa_{\text{L}}} \bar{a} \hat{d}_{\text{out,L}}^\dagger[\omega - \Omega_5] \quad (4.50)$$

$$= V_{Z3}[\omega] \quad (4.51)$$

And similarly  $V_{\text{HD,M}}[\omega - \Omega_3]$  becomes

$$V_{\text{HD,M}}[\omega - \Omega_3] = \frac{1}{2\pi} E_{\text{LO}} \pi e^{-i\psi} \sqrt{\kappa_{\text{L}}} \bar{a} \hat{d}_{\text{out,L}}[\omega + \Omega_5] \quad (4.52)$$

$$= V_{Z_3}^*[\omega] \quad (4.53)$$

The four equations relating the fluctuations in the output field  $\hat{d}_{\text{out,L}}[\omega]$  to the ZI-HF2 demodulated signals  $V_{Z_2}[\omega]$  and  $V_{Z_3}[\omega]$  can be summarized compactly by defining the constant  $C = \frac{2e^{i\psi}}{E_{\text{LO}} \bar{a} \sqrt{\kappa_{\text{L}}}} = |C| e^{-i\psi_{\text{L}}}$ :

$$\hat{d}_{\text{out,L}}[\omega - \Omega_5] = |C| e^{-i\psi_{\text{L}}} V_{Z_2}^*[\omega] \quad (4.54)$$

$$\hat{d}_{\text{out,L}}^\dagger[\omega + \Omega_5] = |C| e^{i\psi_{\text{L}}} V_{Z_2}[\omega] \quad (4.55)$$

$$\hat{d}_{\text{out,L}}[\omega + \Omega_5] = |C| e^{-i\psi_{\text{L}}} V_{Z_3}^*[\omega] \quad (4.56)$$

$$\hat{d}_{\text{out,L}}^\dagger[\omega - \Omega_5] = |C| e^{i\psi_{\text{L}}} V_{Z_3}[\omega] \quad (4.57)$$

Now we can relate the arbitrary quadrature of the reflected field  $Y_{\theta_{\text{L}}}[\omega]$  in the frequency range around the mechanical resonant frequency  $\omega_{\text{M}} \approx \Omega_5$  to the Fourier transforms of the saved output files from the ZI-HF2  $V_{Z_2}[\omega]$  and  $V_{Z_3}[\omega]$ :

$$Y_{\theta_{\text{L}}}[\omega + \Omega_5] = e^{-i\theta_{\text{L}}} \hat{d}_{\text{out,L}}[\omega + \Omega_5] + e^{i\theta_{\text{L}}} \hat{d}_{\text{out,L}}^\dagger[\omega + \Omega_5] \quad (4.58)$$

$$= |C| e^{-i(\theta_{\text{L}} + \psi_{\text{L}})} V_{Z_3}^*[\omega] + |C| e^{i(\theta_{\text{L}} + \psi_{\text{L}})} V_{Z_2}[\omega] \quad (4.59)$$

Similarly for the negative frequency term around  $-\Omega_5$  we obtain

$$Y_{\theta_{\text{L}}}[\omega - \Omega_5] = e^{-i\theta_{\text{L}}} \hat{d}_{\text{out,L}}[\omega - \Omega_5] + e^{i\theta_{\text{L}}} \hat{d}_{\text{out,L}}^\dagger[\omega - \Omega_5] \quad (4.60)$$

$$= |C| e^{-i(\theta_{\text{L}} + \psi_{\text{L}})} V_{Z_2}^*[\omega] + |C| e^{i(\theta_{\text{L}} + \psi_{\text{L}})} V_{Z_3}[\omega] \quad (4.61)$$

Equations 4.59 and 4.61 are equivalent and can be related using two properties: (1)  $\hat{Y}_{\theta_{\text{L}}}$  is Hermitian

so  $\hat{Y}_{\theta_L}[\Omega] = \hat{Y}_{\theta_L}[-\Omega]^\dagger$  and (2)  $V_{Z3}[\omega] = V_{Z3}^*[-\omega]^*$ . A derivation is given below:

$$Y_{\theta_L}[\omega - \Omega_5] = Y_{\theta_L}[-\omega + \Omega_5]^\dagger \quad (4.62)$$

$$= (|C| e^{-i(\theta_L + \psi_L)} V_{Z3}^*[-\omega] + |C| e^{i(\theta_L + \psi_L)} V_{Z2}[-\omega])^\dagger \quad (4.63)$$

$$= |C| e^{i(\theta_L + \psi_L)} V_{Z3}^*[-\omega]^* + |C| e^{-i(\theta_L + \psi_L)} V_{Z2}[-\omega]^* \quad (4.64)$$

$$= |C| e^{i(\theta_L + \psi_L)} V_{Z3}[\omega] + |C| e^{-i(\theta_L + \psi_L)} V_{Z2}^*[\omega] \quad (4.65)$$

## 4.10 Reconstructing the reflected fluctuations in an arbitrary quadrature $\delta Y_{\theta_L}[\omega]$ (Actual measurement)

The actual reconstruction of the reflected heterodyne signal near the mechanical resonant frequency  $Y_{\theta_L}[\omega + \Omega_5]$  differs from the ideal expression given in Eq. 4.59. This section describes the corrections to the ideal expression.

### 4.10.1 Correction #1 - Phase changes between the local oscillator and signal beams

A time varying phase shift  $\psi(t)$  between the local oscillator and signal beams will cause the heterodyne measurement to have a time varying heterodyne phase  $\theta_L + \psi(t) + \phi$  in Eq. 4.59. A time varying phase shift  $\psi(t)$  can be caused by path length variations between the signal and local oscillators beams. These path length variations can be caused either by mechanical vibrations of the mirrors or by thermal expansion of the aluminum breadboard on top of which the optics are located. The other contribution to the heterodyne phase is  $\phi = \arg \bar{a}$ , which is the phase shift between the incident beam and the intracavity field. The phase  $\phi$  depends on the detuning of the incident laser relative to the cavity resonance. If the Pound-Drever-Hall lock is working well, then the detuning  $\Delta$  is constant, and  $\phi = \arctan(2\Delta/\kappa)$  should also be constant.

Figure 4.9 shows fluctuations in the relative phase between the local oscillator beam and the signal beam. The reference phase is reconstructed from the  $X$  and  $Y$  quadratures of the fourth

demodulator of the ZI-HF2  $V_{X4}(t)$  and  $V_{Y4}(t)$  using

$$\psi_{\text{ref}} = \arg(V_{Z4}(t)) = \arg(V_{X4}(t) + iV_{Y4}(t)) \quad (4.66)$$

Similarly, the reflected phase is computed using the  $X$  and  $Y$  quadratures of the first demodulator  $V_{X1}(t)$  and  $V_{Y1}(t)$  :

$$\psi_{\text{refl}}(t) = \arg(V_{Z1}(t)) = \arg(V_{X1}(t) + iV_{Y1}(t)) \quad (4.67)$$

Several things should be noted about Fig. 4.9. First, during the 20 seconds the data was recorded, the reference phase fluctuates by about 0.2 radians, which is equivalent to a path length fluctuation of about 30 nm. Second, the fluctuations in the reflected phase match the fluctuations in the reference phase, which means the reference phase should be subtracted off. Third, the reflected phase has additional phase fluctuations at higher frequencies which are caused by acoustically-driven membrane motion in the sub-kHz frequency range.

Before the reflected heterodyne signals  $V_{Z1}(t)$ ,  $V_{Z2}(t)$  (upper mechanical sideband), or  $V_{Z3}(t)$  (lower mechanical sideband) are converted into the frequency domain, the time varying reference phase  $\psi_{\text{ref}}(t)$  must be subtracted off. The additional subscript “cor” denotes a “corrected” signal which has the phase appropriately subtracted:

$$V_{Zi,\text{cor}}(t) = e^{-i\psi_{\text{ref}}(t)} V_{Zi} \text{ for } i = 1, 2, 3 \quad (4.68)$$

Then Eq. 4.59 for  $Y_{\theta_L}[\omega + \Omega_5]$  becomes

$$Y_{\theta_L}[\omega + \Omega_5] = |C| e^{-i(\theta_L + \psi_L)} V_{Z3,\text{cor}}^*[\omega] + |C| e^{i(\theta_L + \psi_L)} V_{Z2,\text{cor}}[\omega] \quad (4.69)$$

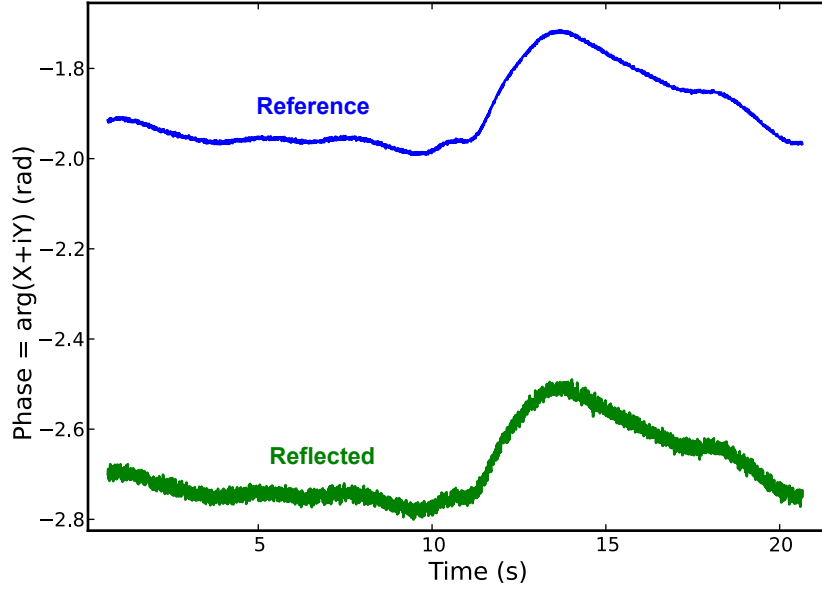


Figure 4.9: A plot of the reference heterodyne phase and the reflected heterodyne phase as a function of time. The reflected phase appears noisier because it is measuring low frequency  $< 3$  kHz position fluctuations of the membrane which are driven by acoustic noise.

#### 4.10.2 Correction #2 - A constant phase offset in the heterodyne phase

$$\theta_{\text{offset}}$$

Even after the time varying phase shift  $\psi_{\text{ref}}(t)$  is subtracted off, there is still a DC offset in the heterodyne phase shift. This could be either optical or electronic in origin. There is a 80 MHz frequency difference between the signal and local oscillator beams, which corresponds to a relative phase shift of  $2\pi$  every 3.75 meters of optical path length. Since there is no simple way to predict this phase offset, a calibration is performed by phase modulating the signal beam at the frequency of demodulator 5,  $\Omega_5$ , which is very near the mechanical resonance frequency. The phase modulation of the signal beam is created using the same electro-optic modulator used to create phase modulation sidebands for the Pound-Drever-Hall locking scheme. If the signal beam is far off resonance, then the reflected signal beam should still have pure phase modulation at  $\Omega_5$ . The offset phase  $\theta_{\text{offset}}$  is chosen to maximize the phase modulation signal  $Y_{\pi/2}[\Omega_5]$ :

$$Y_{\frac{\pi}{2}}[\Omega_5] = |C| e^{-i(\pi/2+\theta_{\text{offset}})} V_{Z3,\text{cor}}^*[\Omega_5] + |C| e^{i(\pi/2+\theta_{\text{offset}})} V_{Z2,\text{cor}}[\Omega_5] \quad (4.70)$$

### 4.10.3 Correction #3 - A variation in amplifier gain over the 2 MHz bandwidth between the upper and lower mechanical sidebands

The signals near the upper side band demodulator  $\Omega_3 = \omega_F + \Omega_5 \approx 2\pi \times 20.8$  MHz and lower side band demodulator  $\Omega_2 = \omega_F - \Omega_5 \approx 2\pi \times 19.2$  MHz are separated by almost 2 MHz. Any variation in the photodiode response or gain in any subsequent amplifiers over this 2 MHz bandwidth will scale the two sidebands differently. Thus we should calibrate this variation in gain between the upper and lower sidebands and parametrize it by a parameter  $\beta$ :

$$Y_{\frac{\pi}{2}}[\Omega_5] = |C| \beta e^{-i(\pi/2 + \theta_{\text{offset}})} V_{Z3, \text{cor}}^*[\Omega_5] + |C| e^{i(\pi/2 + \theta_{\text{offset}})} V_{Z2, \text{cor}}[\Omega_5] \quad (4.71)$$

The calibration method, calibration data, and estimated value for  $\beta$  are given in Sec. 5.1.2.

### 4.10.4 Correction #4 - An overall phase shift to reflected heterodyne quadrature $Y_{\theta_L}[\omega] \rightarrow e^{i\theta_g} Y_{\theta_L}[\omega]$

A global phase shift to the reflected heterodyne quadrature  $Y_{\theta_L}[\omega] \rightarrow e^{i\theta_g} Y_{\theta_L}[\omega]$  will cause a phase shift in the correlation  $S[\omega] = X_\phi[\omega] Y_{\theta_L}^*[\omega] \rightarrow e^{-i\theta_g} S[\omega]$ . Since the signature of the RPSN is contained in the real part of  $S[\omega]$ , if this global phase shift is not accounted for then the detected signal will be a combination of the desired real part of  $S[\omega]$  and an undesired imaginary part. A global phase shift can be caused by relative phase shifts between the internal local oscillators in the ZI-HF2 responsible for demodulating the heterodyne carrier at  $\Omega_1$ , the heterodyne sidebands demodulators at  $\Omega_2$  and  $\Omega_3$ , and the transmitted signal at  $\Omega_5$ . As a result,

$$Y_{\theta_L}[\omega + \Omega_5] = e^{-i\theta_g} (|C| \beta e^{-i(\theta_L + \theta_{\text{offset}})} V_{Z3, \text{cor}}^*[\omega] + |C| e^{i(\theta_L + \theta_{\text{offset}})} V_{Z2, \text{cor}}[\omega]) \quad (4.72)$$

which contrasts with the uncorrected expression given in Eq. 4.59:

$$Y_{\theta_L}[\omega + \Omega_5] = |C| e^{-i(\theta_L + \psi_L)} V_{Z3}^*[\omega] + |C| e^{i(\theta_L + \psi_L)} V_{Z2}[\omega] \quad (4.73)$$

Equation 4.72 will be used throughout the final chapter in all measurements involving the heterodyne detection scheme.

The calibration method, calibration data, and estimated value for  $\theta_g$  are given in Sec. 5.1.3.

# Chapter 5

## Preliminary Results and Discussion

### 5.1 Calibrating the measurement scheme

As described in detail in Sec. 4.10, there are three calibration parameters which must be determined in order to reconstruct the reflected heterodyne quadrature and the real part of the correlation  $R[\omega]$ .

These three calibration parameters are:

1.  $\theta_{\text{offset}}$ , the constant phase offset between the local oscillator and signal beams (Sec. 4.10.2).
2.  $\beta$ , the variation in gain over the 2 MHz bandwidth separating the upper and lower sidebands produced by mechanical motion (Sec. 4.10.3).
3.  $\theta_g$ , a global phase shift between the transmitted and reflected signals (Sec. 4.10.4) caused by relative phase shifts between the internal local oscillators in the ZI-HF2 responsible for demodulating the heterodyne carrier at  $\Omega_1$ , the heterodyne sidebands demodulators at  $\Omega_2$  and  $\Omega_3$ , and the transmitted signal at  $\Omega_5$ .

These calibration constants need to be determined during each data-taking run. The next three subsections present the calibration data and estimated calibration parameters which are used in the subsequent data analysis in this chapter. A summary of the measured calibration constants is given in Table 5.1.

$\theta_{\text{offset}}$	1.623
$\beta$	1.0020
$\theta_{\text{g}}$	5.55
$\theta_{\text{car}}$	-0.90986

Table 5.1: Summary of the important calibration constants.  $\theta_{\text{offset}}$ ,  $\beta$ , and  $\theta_{\text{g}}$  were described in Sec. 5.1. The heterodyne phase (not quadrature angle) of the carrier  $\theta_{\text{car}}$  is measured by taking the mean value of  $\arg(X_{\text{car}} + iY_{\text{car}})$  where  $X_{\text{car}}$  and  $Y_{\text{car}}$  are the quadratures recorded by the ZI-HF2 at the heterodyne beat note frequency (demodulator 2).

### 5.1.1 Calibration of $\theta_{\text{offset}}$

A calibration of  $\theta_{\text{offset}}$  is performed by phase-modulating the signal beam at  $\Omega_5$  (the frequency of demodulator 5), which is very near the mechanical resonance frequency  $\omega_{\text{M}}$ . The phase modulation of the signal beam is created using the same electro-optic modulator used to create phase modulation sidebands for the Pound-Drever-Hall locking scheme. Figure 5.1 A shows a plot of the power spectral density of the phase modulation signal as detected by the heterodyne measurement scheme. If there was no phase offset between the local oscillator and signal beams, then this pure phase modulation signal would be maximized for a heterodyne quadrature of  $\theta = \pi/2$ , and the heterodyne signal would vanish at  $\theta = 0, \pi, \dots$ . However, as Fig. 5.1 B shows, the modulation signal vanishes at  $\theta = 1.623$ , which means  $\theta_{\text{offset}} = 1.623$ .

### 5.1.2 Calibration of $\beta$

#### 5.1.2.1 Method 1: Laser far-detuned from cavity resonance

In this measurement, the laser is far-detuned from resonance so both phase modulation sidebands at  $\Omega_5$  reflect off of the cavity with the same phase shift and amplitude. In this case, the power in the two reflected sidebands should be equal. If an inequality is observed, it could be from either (a) one sideband coupling to a higher-order mode of the cavity or (b) a non-flat response of the heterodyne measurement over the 2 MHz bandwidth spanned by the sidebands. The possibility of a higher-order mode can be ruled out by ensuring there is no transmission through the cavity as detected by a camera or photodiode. Second, coupling to a higher-order mode can be ruled out by slightly adjusting the detuning so as to shift the sideband from the possible resonance

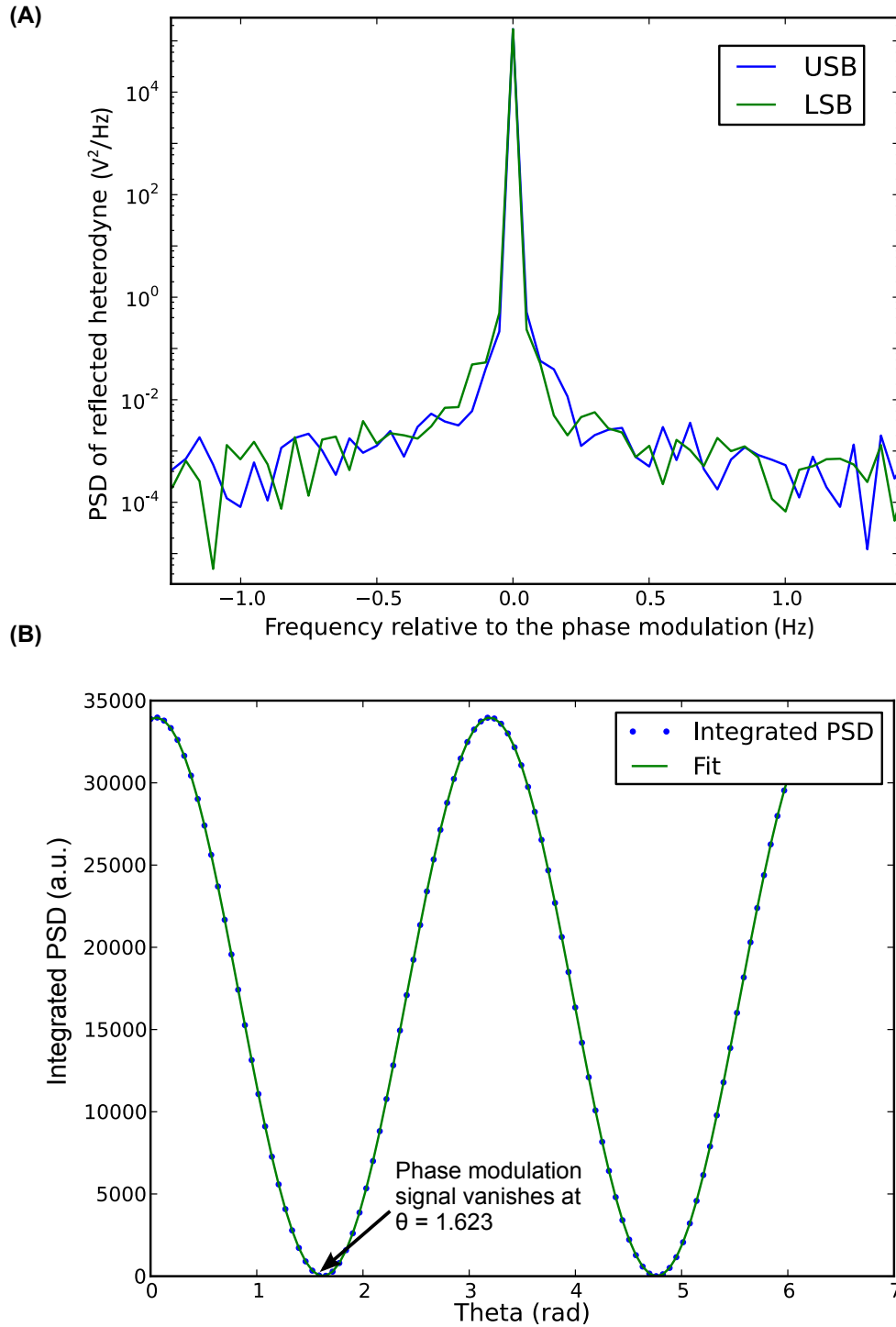


Figure 5.1: (A) The power in the upper and lower sidebands. The frequency is the deviation from the sideband frequency, so that the USB and LSB overlap for easy comparison. In this case the integrated power is the same to about 0.4 percent, meaning  $\beta = 1.002$ . (B) Integrated power (at the modulation frequency) in a quadrature of the reflected field as the quadrature angle is varied. The USB and LSB data whose PSDs are shown in (A) have been used to reconstruct an arbitrary quadrature of the reflected field.

and looking for a change in the sidebands. Third, the higher-order modes should be of reduced significance for an input laser which is geometrically well-coupled to the TEM<sub>00</sub> cavity mode. Since coupling to higher-order modes can be ruled out for a variety of reasons, any remaining inequality in sideband amplitude is assumed to be caused by a non-uniform frequency response in the heterodyne measurement. I parametrize this non-ideality as

$$\beta = \sqrt{\frac{P_{\text{USB}}}{P_{\text{LSB}}}} \quad (5.1)$$

where  $P_{\text{USB}}$  and  $P_{\text{LSB}}$  are the powers in the upper and lower sidebands, respectively. For the far-detuned calibration data shown in Fig. 5.1 A  $\beta = 1.0025$ . The ratio of the powers is computed by integrating the upper and lower sideband power spectral densities over a very narrow bandwidth ( $\pm 2$  Hz) around the modulation frequency.

### 5.1.2.2 Method 2: Ratio of sidebands at zero detuning

Just as in the far-detuned case, it is also true that the reflected phase modulation sidebands should have equal amplitudes at zero detuning. However, zero detuning requires locking the laser, which is prone to offsets in the error signal, offering a slightly less accurate method of estimating  $\beta$ . We can tell which data sets are closest to zero detuning in a few different ways, but one good option is to choose data sets which minimize the membrane Brownian motion observed in the transmitted intensity. At zero detuning there should be no signal in the transmission due to membrane motion to lowest order. Figure 5.2 shows the integrated Brownian motion for a number of data sets taken at different detunings. The phase modulation ratio is defined in the same way as  $\beta$ , i.e.  $\sqrt{\frac{P_{\text{USB}}}{P_{\text{LSB}}}}$ . Table 5.2 shows the estimated values of  $\beta$  for the three data sets closest to zero detuning and they are all within one percent of the estimates given from the far-detuned data. These values are consistent with a red-detuning of  $0.005\kappa$  to  $0.025\kappa$ . Because the the far-detuned calibration method does not rely of having the laser locked precisely at zero detuning, I will use  $\beta = 1.0025$  for the remaining analysis in the dissertation.

Data set	$\beta$
50	0.990
51	0.995
55	0.997

Table 5.2: Calibration constant  $\beta$  estimated from the ratio of powers in reflected phase modulation sidebands. Data sets 50, 51, and 55 represent the three data sets closest to zero detuning.

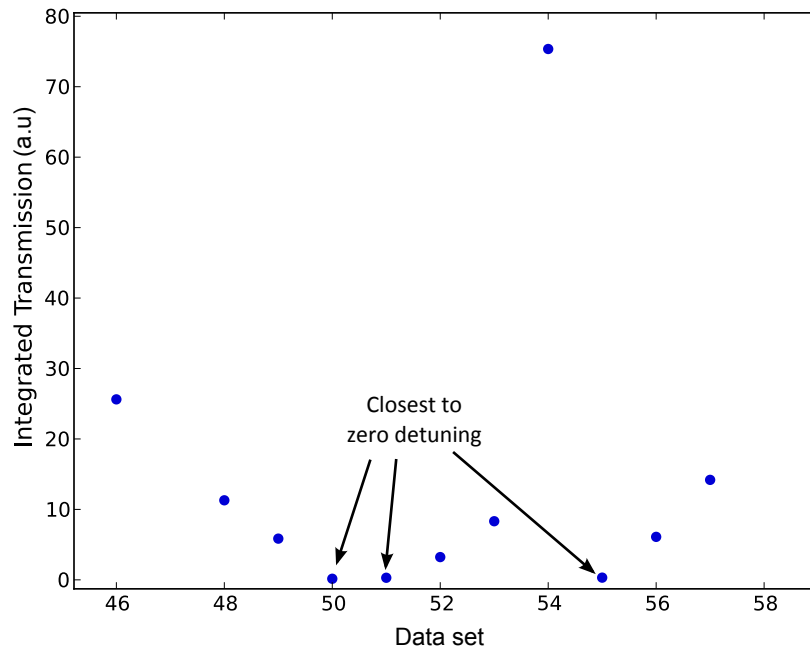


Figure 5.2: Plot showing the variation of the integrated Brownian motion signal in transmission, for a series of data sets taken at different detunings. The data sets closest to zero detuning should correspond to the smallest Brownian motion signal.

### 5.1.3 Calibration of $\theta_g$

A global phase shift of the reflected heterodyne quadrature  $Y_{\theta_L}[\omega] \rightarrow e^{i\theta_g} Y_{\theta_L}[\omega]$  will occur due to the arbitrary (but constant) phase shifts of the ZI-HF2's internal oscillators that are demodulating the heterodyne carrier and sidebands. The phase shift  $e^{i\theta_g}$  will cause a phase shift in the correlation  $S[\omega] = X_\phi[\omega]Y_{\theta_L}^*[\omega] \rightarrow e^{-i\theta_g} S[\omega]$ . However, by using one data set at zero detuning, we can calibrate this phase. According to Børkje et al. [4], for small detunings, the ratio of the real and imaginary parts of the correlation have a simple relation:

$$\frac{\text{Re}(S_{z,z}[\omega])}{\text{Im}(S_{z,z}[\omega])} \equiv \frac{R_1^{(\text{th})}[\omega]}{I_1^{(\text{th})}[\omega]} = \frac{\kappa}{2\omega_M} \approx 0.45 \quad (5.2)$$

where the cavity decay rate  $\kappa \approx 4.45 \times 10^6 \text{ s}^{-1}$  as determined in Sec. 5.2, and  $\omega_M \approx 2\pi \times 785 \text{ kHz}$  is the resonant frequency of the membrane's (2,2) mode. The result is valid as the detuning goes to zero, because even though  $S_{z,z}[\omega] \rightarrow 0$ , the ratio of the real and imaginary parts obeys Eq. 5.2. Also, the ratio given in Eq. 5.2 is independent of  $\omega$ , meaning the real and imaginary parts of the correlation can be integrated over  $\omega$  and ratio will still be  $\kappa/2\omega_M$ .

We can estimate the ratio of thermal contributions in Eq. 5.2 as

$$\frac{\text{Re}(S_{z,z}[\omega])}{\text{Im}(S_{z,z}[\omega])} \approx \frac{\text{Re}S[\omega]}{\text{Im}S[\omega]} \equiv \frac{R[\omega]}{I[\omega]} \approx \frac{\kappa}{2\omega_M} \quad (5.3)$$

because the thermal contribution to the correlation is much larger than the contribution from either classical or quantum radiation pressure noise. Then we need to find the choice of  $\theta_g$  which yields the ratio

$$\frac{R_1^{(\text{th})}[\omega]}{I_1^{(\text{th})}[\omega]} \approx \frac{R[\omega]}{I[\omega]} \approx 0.45 \quad (5.4)$$

Once  $\theta_g$  is calibrated for a data set near zero detuning, the same  $\theta_g$  is used in all subsequent data analysis at all detunings.

Figure 5.3 shows a plot of the ratio of the integrated real and imaginary parts of the correlation as a function of the heterodyne quadrature angle. The integration was taken over a bandwidth of about  $\pm 100 \text{ Hz}$  from the mechanical resonant frequency. Since the data set was not exactly at

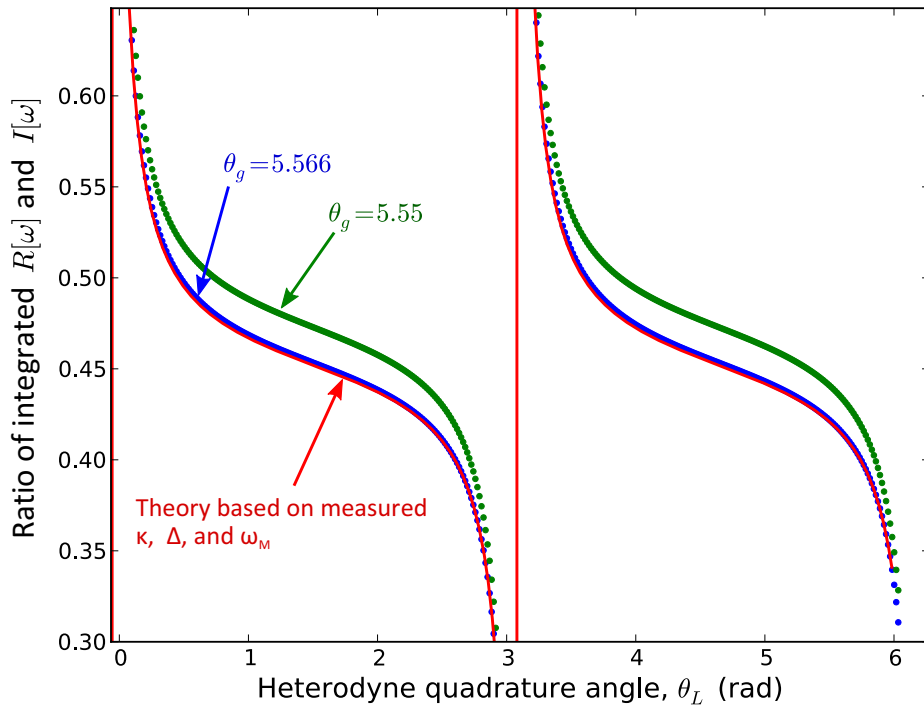


Figure 5.3: Ratio of real and imaginary parts of the correlation integrated over frequencies near the mechanical resonant frequency. The data set is near zero detuning ( $\Delta = -0.03\kappa$ ). When the detuning is not exactly zero, the ratio depends on the heterodyne angle. The optimal fit gives a calibration of  $\theta_g = 5.566$ . A value of  $\theta_g = 5.55$ , determined from an earlier analysis, is used in all subsequent analysis of correlation data for all detunings. Both estimates of  $\theta_g$  are consistent with a 2% uncertainty in  $\kappa$ .

zero detuning, there is some heterodyne angle dependence of the ratio. The best fit curve gives a value of  $\theta_g = 5.566$ . A value of  $\theta_g = 5.55$ , determined by a more primitive analysis, is used in all subsequent analysis. In the future, only the method described here and shown in Fig. 5.3 should be used because it gives a more precise determination of  $\theta_g$ . Both values of  $\theta_g$  are consistent with a 2% uncertainty in  $\kappa$ .

## 5.2 Determining cavity decay rates $\kappa$ and $\kappa_L$

The overall cavity decay rate  $\kappa$  and the decay rate out of the left end mirror  $\kappa_L$  must both be known in order to compare any observed optomechanical effects with theory. In general,  $\kappa$  can depend sensitively on position due a variety of mechanisms such as scattering or absorption of

the membrane. For the optomechanical cavity discussed in this work,  $\kappa$  varied by a factor of two between the node and antinode as seen in Figs. 4.3 and 4.4. Also large  $\kappa$  gradients  $\partial\kappa/\partial x$  can occur near avoided crossings of different transverse modes as was shown by Sankey et al. [69]. Because of the position dependence of the cavity decay rates, it is important to measure  $\kappa$  and  $\kappa_L$  any time the membrane is repositioned.

In Figs. 4.3 and 4.4, the cavity decay rate  $\kappa$  was determined by a ring-down measurement. However, the ring-down measurement doesn't give any information about  $\kappa_L$ . Instead, we used heterodyne detection to simultaneously measure the total cavity decay rate  $\kappa$  and the transmission decay through the left end mirror  $\kappa_L$  by sweeping the laser through the cavity resonance and measuring the variation in the reflected phase and amplitude as a function of detuning.

Sweeping the laser through resonance, but over an uncertain range in detunings, is sufficient to determine the ratio  $\kappa_L/\kappa$ , but the detuning range must be calibrated to measure  $\kappa$  and  $\kappa_L$  independently. This is accomplished by using phase modulation sidebands at a known modulation frequency as yardsticks for the detuning sweep. The complex reflection coefficient  $r$  can be derived from the steady state solution of the cavity equation of motion given in Eq. 2.69. The complex reflection coefficient  $r$  is given by

$$r(\Delta) = \frac{\frac{\kappa_L}{\kappa/2} + i\frac{\Delta}{\kappa/2} - 1}{1 - i\frac{\Delta}{\kappa/2}} \quad (5.5)$$

The data is shown in Figs. 5.4 and 5.5. The fits (solid lines) follow Eq. 5.5, where  $\kappa$  and  $\kappa_L$  are fit parameters, and the laser detuning  $\Delta$  is assumed to be linearly varying in time, i.e.  $\Delta(t) = at + b$ , where  $a$  and  $b$  are also fit parameters. The phase modulation frequency was 1 MHz. The membrane position was very near the cavity node and should represent the highest finesse achievable in our cavity. Ten sweeps of the cavity resonance gave fit values of  $\kappa = (4.45 \pm .03) \times 10^6 \text{ s}^{-1}$  and  $\kappa_L/\kappa = 0.155 \pm .002$ .

### 5.3 Measurement of detuning

The detuning between the cavity and the laser is controlled through a Pound-Drever-Hall (PDH) locking scheme. The PDH error signal can also be used as an estimate of detuning. However,

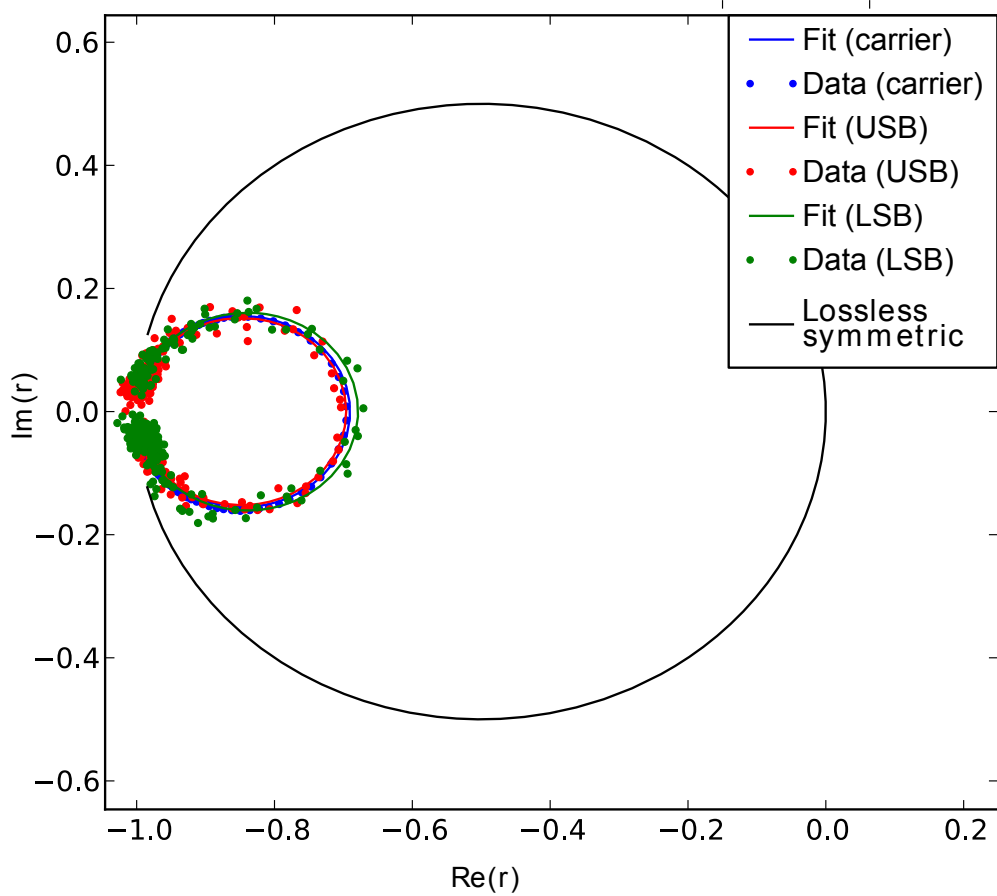


Figure 5.4: Plot of the cavity's complex-valued reflection coefficient as a function of laser frequency,  $r[\omega_{\text{laser}}]$ . The data is shown for just one sweep of the carrier laser frequency through the cavity's resonance. The three colors represent the carrier (blue) and two phase modulation sidebands (red and green). The theoretical reflection coefficient for the case of a lossless, symmetric cavity is shown for comparison (black solid line).

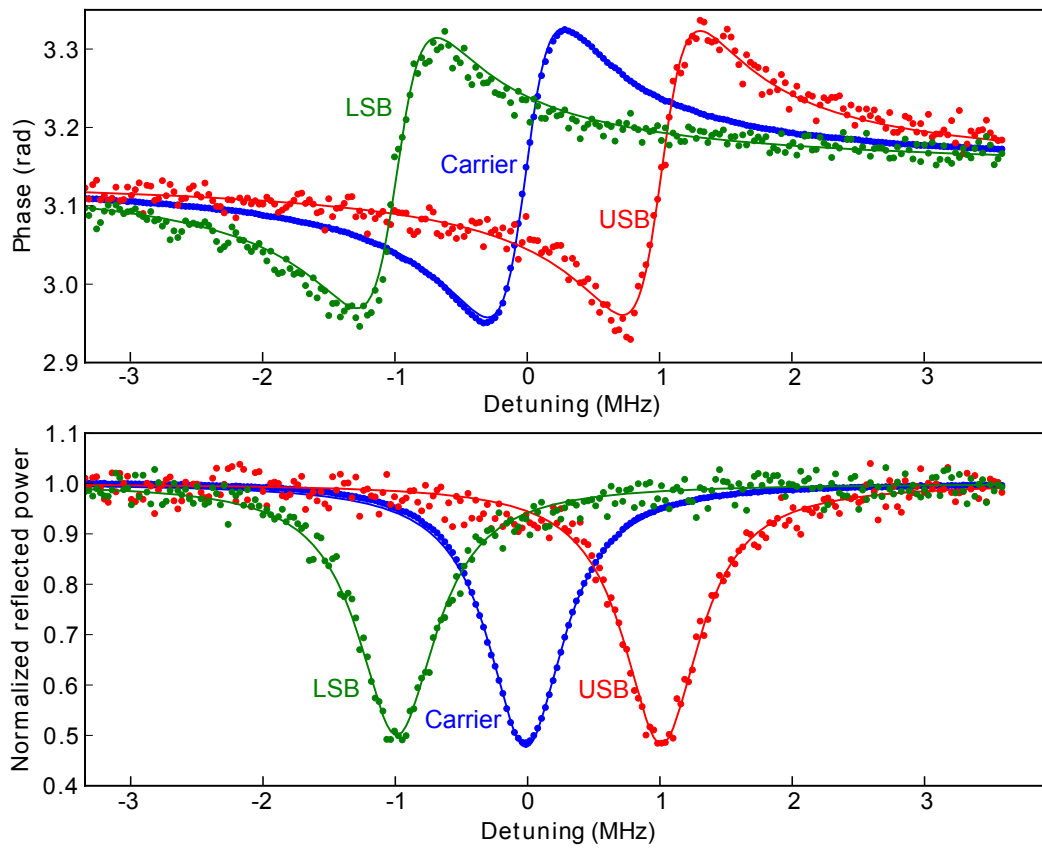


Figure 5.5: Reflected phase and amplitude vs laser detuning. Fits are solid lines, dots are data. Blue shows the carrier, which is the largest signal with best signal-to-noise ratio. Red and green are the phase modulation sidebands at  $\pm 1$  MHz from the carrier.

because the PDH error signal scales with the incident laser power  $P_{\text{in}}$ , it is inconvenient to use the error signal as a measure of non-zero detunings. The commonly cited advantage, that PDH locking is insensitive to power fluctuations in the laser, occurs because the PDH error signal is exactly zero at  $\Delta = 0$  for any laser power  $P_{\text{in}}$ .

In this section I discuss three alternative ways to measure the detuning, none of which depend on  $P_{\text{in}}$ . The first two methods require that the cavity decay rates  $\kappa$  and  $\kappa_L$  are already determined using the methods described in Sec. 5.2.

### 5.3.1 Method 1: Phase shift of the reflected heterodyne carrier

A measurement of the phase shift of the reflected heterodyne signal carrier  $\alpha_{\text{carrier}}$  is sufficient to determine the detuning. The phase shift  $\alpha_{\text{carrier}}$  is given by

$$\alpha_{\text{carrier}} = \arctan \left( \frac{\Delta \kappa_L}{\frac{\kappa}{2} (\kappa_L - \frac{\kappa}{2}) - \Delta^2} \right) \quad (5.6)$$

Inverting to find the detuning  $\Delta$  gives

$$\Delta = \frac{-\kappa_L \cot \alpha_{\text{carrier}} \pm \sqrt{(\kappa_L \cot \alpha_{\text{carrier}})^2 + 4 \frac{\kappa}{2} (\kappa_L - \frac{\kappa}{2})}}{2} \quad (5.7)$$

Note that Eq. 5.7 only depends on the phase measurement and is insensitive to the overall optical power being used.

Figure 5.6 shows the measured phase shift of the reflected signal beam carrier  $\alpha_{\text{carrier}}$  as a function of detuning. Using  $\kappa_L = 0.132\kappa$  (green dashed curve) provided the best fit to the data, but is about 15 percent smaller than the  $\kappa_L$  measured in Sec. 5.2. A future experiment should be directed at determining whether the difference in  $\kappa_L$  is real and is the result of some effect like a position dependent cavity decay rate, or if instead, it represents an error in the reflected phase shift determined via the heterodyne measurement.

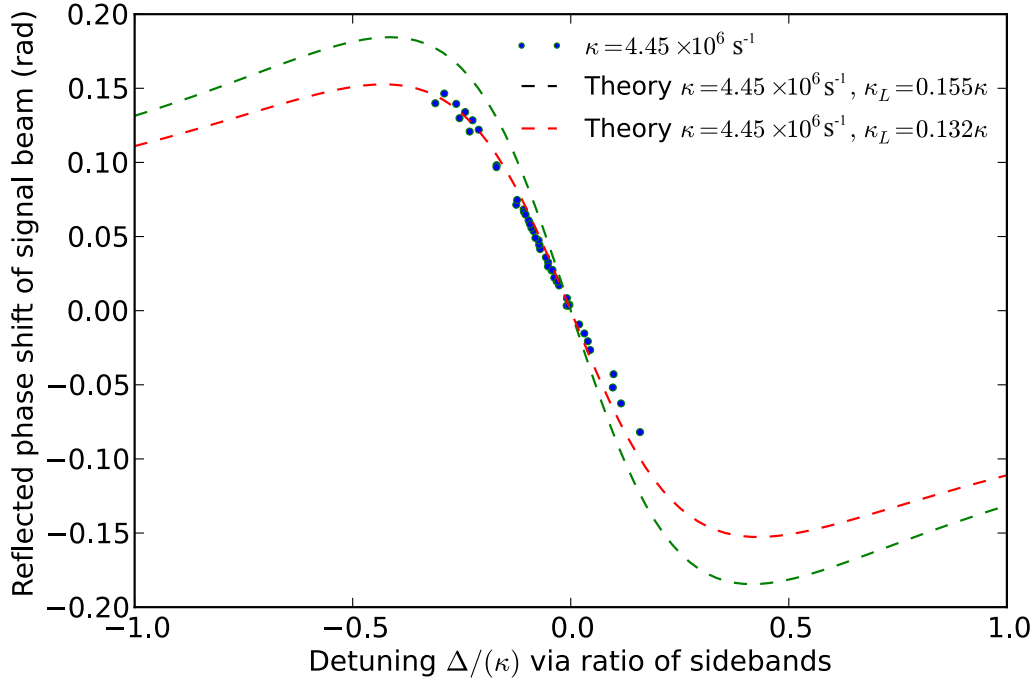


Figure 5.6: Plot of the phase shift of the reflected signal beam measured using the heterodyne detection. The measured data (blue dots) agrees best with the red theory curve using parameters  $\kappa = 4.45 \times 10^6 \text{ s}^{-1}$  and  $\kappa_L = 0.132\kappa$ . The green theory curve uses  $\kappa = 4.45 \times 10^6 \text{ s}^{-1}$  and  $\kappa_L = 0.155\kappa$ , which were determined from the data shown in Figs. 5.4 and 5.5.

### 5.3.2 Method 2: Phase shift of the reflected phase modulation sidebands

In principle, the phase shift of the reflected phase modulation sidebands could be used to determine the detuning in the same way as the carrier. However, the signal-to-noise ratio for the sidebands is worse than the carrier for two reasons. First, the power in the sidebands  $P_s$  is typically much smaller than the power in the carrier  $P_c$  ( $P_s < 0.05P_c$ ). Second, the reflected phase shift changes most sensitively with detuning near zero ( $\partial\alpha_{\text{carrier}}/\partial\Delta$  is largest near  $\Delta = 0$ ). The phase modulation frequency is very near  $\omega_m = 2\pi \times 784 \text{ kHz}$ , and for typical cavity parameters the sensitivity  $\partial\alpha_{\text{carrier}}/\partial\Delta$  at  $\Delta \approx \omega_m$  is ten times smaller than the sensitivity at zero detuning. The reduced signal-to-noise ratio in the reflected sidebands relative to the carrier is easily seen in Fig. 5.5.

### 5.3.3 Method 3: Ratio of the mechanical motion-induced sidebands

A third method uses the ratio of the powers of the sidebands induced by mechanical motion (Brownian motion). One advantage of this scheme is that it only relies on the power in the two sidebands

and is independent of phase shifts. It depends on the calibration factor  $\beta$  and on the cavity decay rate  $\kappa$ , but does not depend on the phase calibration or  $\kappa_L$ . The theoretical expression for the ratio of the powers in the upper and lower sidebands is given by the ratio of two Lorentzians of width  $\kappa$ . The upper sideband is detuned by  $\Delta + \Omega$ , and the lower sideband is detuned by  $\Delta - \Omega$ . The ratio of the sidebands  $R_{SB}$  is then

$$R_{SB} = \frac{P_{USB}}{P_{LSB}} = \frac{(\Delta - \Omega)^2 + \left(\frac{\kappa}{2}\right)^2}{(\Delta + \Omega)^2 + \left(\frac{\kappa}{2}\right)^2} \quad (5.8)$$

Inverting and solving for the detuning  $\Delta$  in terms of the ratio of sidebands  $R_{SB}$  gives

$$\Delta = \frac{-\omega_M(R_{SB} + 1) \pm \sqrt{\omega_M^2(R_{SB} + 1)^2 - (R_{SB} - 1)^2 \left(\omega_M^2 + \left(\frac{\kappa}{2}\right)^2\right)}}{R_{SB} - 1} \quad (5.9)$$

### 5.3.4 Agreement of Methods 1 and 3

Figure 5.7 shows a plot of the detuning as estimated by methods 1 and 3. The phase shift of the heterodyne carrier depends only on the carrier, and the ratio of the sidebands depends only on the sidebands and not on the carrier. Thus the methods give two independent ways of measuring the detuning. However, method 1, which uses the ratio of sidebands produced by mechanical motion, does not require the sophisticated calibration procedure required for the heterodyne measurement, so I believe it is the simpler and more reliable method. Throughout the remainder of the dissertation all detuning estimates are given using method 3 (i.e., the ratio of sidebands).

Also, though using  $\kappa_L = 0.132\kappa$  produced better agreement between the two detuning estimates as shown in Fig. 5.7 this is 15% smaller than the earlier estimate of  $\kappa_L = 0.155\kappa$  based on the swept data in Fig. 5.5. However, the swept data set had a detuning range of  $-3\kappa < \Delta < 3\kappa$ , whereas the data in Fig. 5.7 shows the locked detuning range was much smaller (about  $-0.3\kappa < \Delta < 0.2\kappa$ ). Because the swept method offers a more complete set of fitable data and is simpler to analyze, the left end mirror decay rate will be assumed to be  $\kappa_L = 0.155\kappa$ .

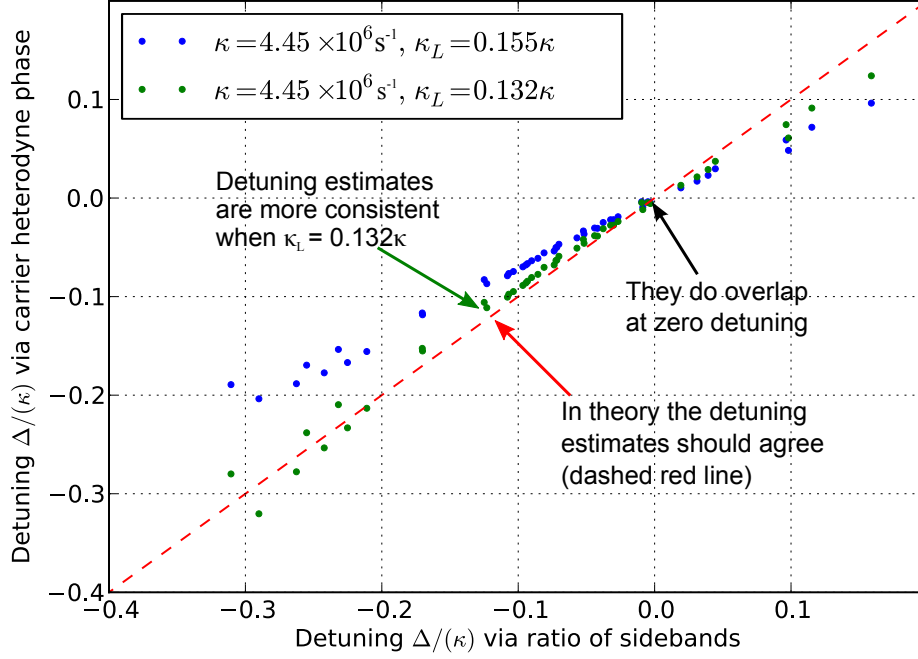


Figure 5.7: Comparison of the detuning as estimated by the ratio of the power in the upper and lower mechanical motion-induced sidebands ( $x$ -axis) and as estimated by the carrier heterodyne phase shift  $\alpha_{\text{carrier}}$  ( $y$ -axis).

## 5.4 Optomechanics

The optically-induced shift in mechanical resonant frequency and damping was derived in Sec. 2.7.

The results for  $\delta\omega_{\text{M}}$  and  $\gamma_{\text{opt}}$  are given in Eqs. 2.128 and 2.131 and repeated here for convenience:

$$\delta\omega_{\text{M}} = |\alpha|^2 \left( \frac{\omega_{\text{M}} + \Delta}{\left(\frac{\kappa}{2}\right)^2 + (\omega_{\text{M}} + \Delta)^2} + \frac{-\omega_{\text{M}} + \Delta}{\left(\frac{\kappa}{2}\right)^2 + (-\omega_{\text{M}} + \Delta)^2} \right) \quad (5.10)$$

$$\gamma_{\text{opt}} = 2|\alpha|^2 \frac{\kappa}{2} \left( \frac{1}{\left(\frac{\kappa}{2}\right)^2 + (\omega_{\text{M}} + \Delta)^2} - \frac{1}{\left(\frac{\kappa}{2}\right)^2 + (-\omega_{\text{M}} + \Delta)^2} \right) \quad (5.11)$$

The optomechanical coupling strength  $|\alpha|^2$  is given in Eq. 2.135 and repeated here:

$$|\alpha|^2 = \frac{\kappa_{\text{L}}}{\left(\frac{\kappa}{2}\right)^2 + \Delta^2} \frac{P_{\text{in}}}{\hbar\omega_{\text{L}}} \frac{\hbar}{2m\omega_{\text{M}}} \left| \frac{\partial\omega_{\text{cav}}}{\partial\tilde{z}} \right|^2 \quad (5.12)$$

The slope is given in Eq. 2.55 and repeated here:

$$\frac{\partial\omega_C}{\partial\tilde{z}} \approx \frac{\omega_L}{L} |r_d| \sin\left(\frac{4\pi}{\lambda} \tilde{z}\right)$$

The parameters are straight-forward to determine experimentally except for the displacement of the membrane relative to a cavity node  $\tilde{z}$  which determines the slope  $|\frac{\partial\omega_{cav}}{\partial\tilde{z}}|$ . The cavity decay rates  $\kappa = 4.45 \times 10^6 \text{ s}^{-1}$  and  $\kappa_L = 0.155\kappa$  were determined in Sec. 5.2. The detuning  $\Delta$  is estimated using the simpler (compared to the heterodyne measurement) ratio of sidebands on the signal beam induced by the Brownian motion of the membrane as described in Sec. 5.3.3. The power incident on the cavity was measured to be  $P_{in} \approx 1 \times 10^{-5} \text{ W}$ . The mechanical resonant frequency is  $\omega_M/2\pi = 784 \text{ kHz}$ . The laser wavelength, as mentioned elsewhere, was  $\lambda = 1064 \text{ nm}$ . The cavity length was  $L = 7 \text{ mm}$ . The approximate amplitude reflectivity for the membrane was  $|r_d| \approx 0.27$ . We estimated that the membrane was between 5 nm and 15 nm from the node, and the value of  $\tilde{z}$  which created the best overlap with the data shown in Fig. 5.10 was 12 nm. We chose to keep the membrane close to a node as a way to reduce our sensitivity to audio frequency mechanical vibration of the membrane's in-situ alignment system. The slope  $|\partial\omega_C/\partial\tilde{z}|$  is over an order of magnitude smaller at  $\tilde{z} = 12 \text{ nm}$  compared to the maximum slope at  $\tilde{z} = 266 \text{ nm}$  allowing the PDH feedback to keep the laser locked to the cavity more cleanly and for longer times.

The resonant frequencies and linewidths were determined by fitting the membrane's Brownian motion as measured by the reflected heterodyne measurement. Three such power spectral densities are shown in Fig. 5.8 along with their fits.

One difficulty in comparing the optomechanical theory with the measured data is that the resonant frequency of the membrane drifted up about 14 Hz over an hour, which, if the drift is assumed to be uniform, amounts to 0.26 Hz per minute. Figure 5.9 shows a plot of the resonant frequency as a function of time. The drift did not significantly affect the measurement of mechanical linewidth because each data set only represented 20 seconds of data, or an estimated frequency drift of about 0.08 Hz. However, the frequency drift during the hour of measurements did exceed the expected optomechanical induced frequency shift. Figure 5.10 shows a plot of the uncorrected

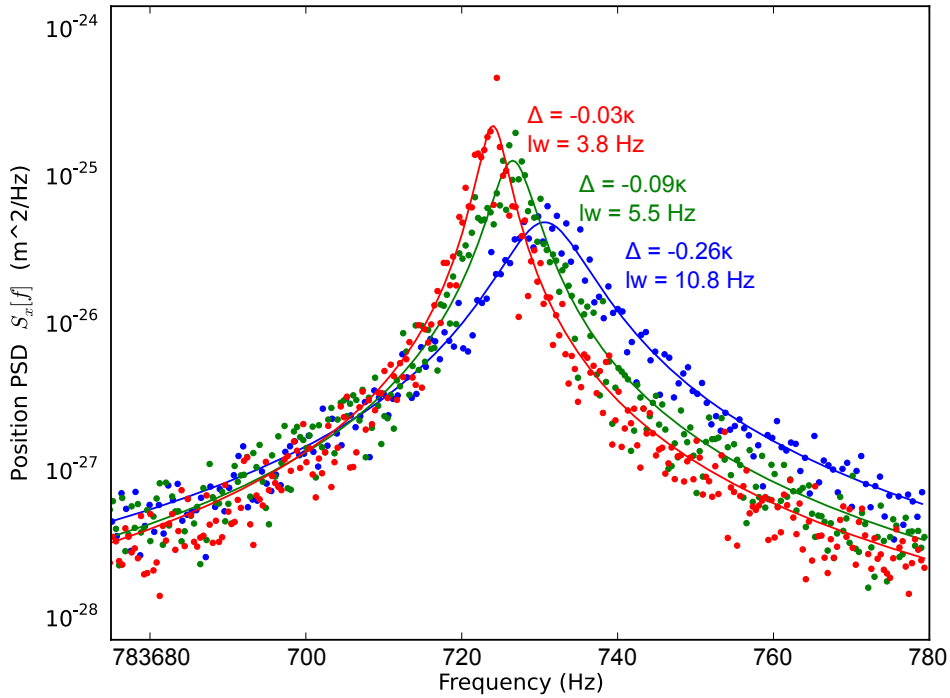


Figure 5.8: Power spectral densities of the Brownian motion of the membrane for three detunings. As the detuning becomes increasingly negative, the linewidth increases and the resonant frequency shifts due to optical damping and the optical frequency shift.

resonant frequency shift and the resonant frequency shift with a uniform 0.26 Hz/minute drift subtracted. The fit to theory improves substantially.

A mechanism for the frequency drift is unclear. During the months the membrane was under vacuum the resonant frequency decreased by at least 5 kHz. Such a decrease, if due to mass change alone, would correspond to adding about 7 atomic layers of water (a 2 nm thick layer). However, it seems surprising that pumping longer would end up with more mass deposited on the membrane. Also, the short term drift in Fig. 5.9 shows an *increase* in resonant frequency, which is the opposite of the long term drift. The short term drift is consistent with the laser heating and vaporizing a small amount of the depositions from the membrane surface, though no causal relationship can be inferred from this limited amount of data. In the future it would be good to test this hypothesis by observing how the drift rate changes as a function of incident laser power.

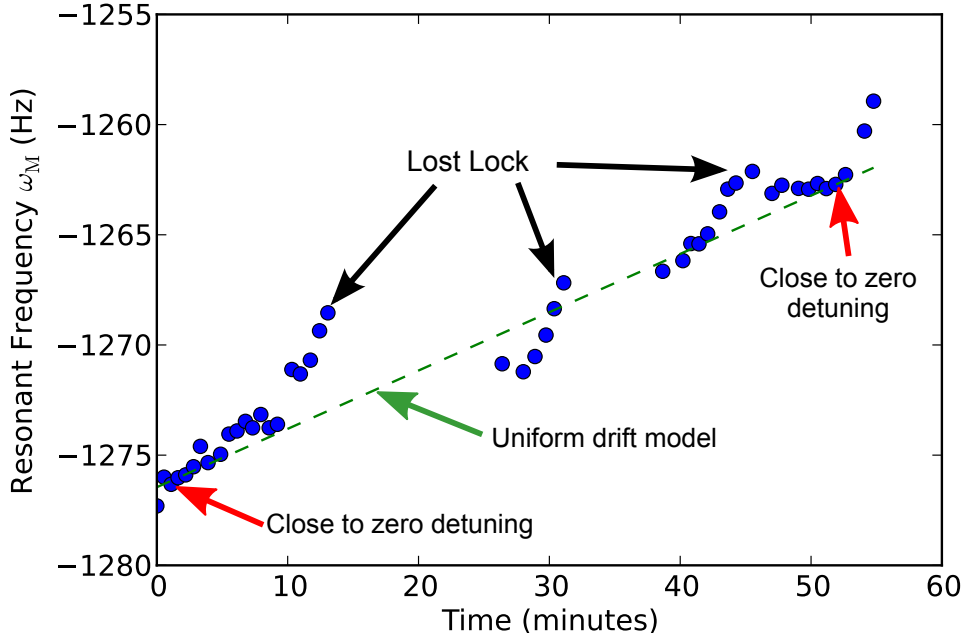


Figure 5.9: Resonant frequency drift of the membrane over an hour of measurements. Two data sets near zero detuning (meaning the optomechanical frequency shift was also zero) were chosen as the two points to define the uniform drift estimate (green dashed line). The laser became unlocked from the cavity at times labeled “Lost Lock.”

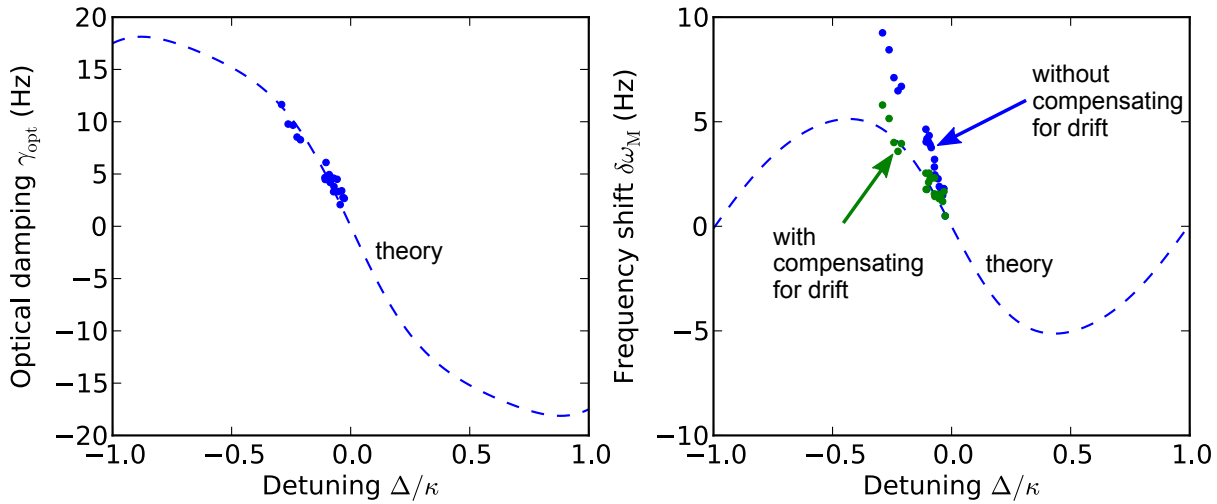


Figure 5.10: Measured optical damping and frequency shift as a function detuning. The theory curve has one free parameter, the distance of the membrane from a node of the intracavity field, which was difficult to determined experimentally. This parameter essentially sets the strength of the optomechanical coupling, and the best fit value was 12 nm. A value between 5 and 15 nm was expected. There was a drift in the resonant frequency during the measurement. The green frequency drift data has had a uniform drift subtracted, as is detailed in Fig. 5.9.

## 5.5 Measurement of the critical quadrature

The correlation measurement scheme predicted by Børkje et al. in Ref. [4] makes a simple prediction that the real part of the correlation caused by thermally-induced Brownian motion  $R_{z,z}[\omega]$  will vanish if the reflected heterodyne quadrature angle is chosen to have a particular value, known as the “critical quadrature”  $\theta_C$ , given by

$$\theta_C = 2 \arctan \frac{2\Delta}{\kappa} \quad (5.13)$$

Similarly, the imaginary part of the thermal correlation  $R_{z,z}[\omega]$  will vanish at a quadrature angle

$$\theta = \arctan \frac{2\Delta}{\kappa} \quad (5.14)$$

The angle in Eq. 5.14 that causes the imaginary part of the correlation  $\text{Im}S_{z,z}[\omega]$  to vanish is included for comparison with experimental data. However, the imaginary part of the RPSN-induced correlation  $\text{Im}S_{q,z}[\omega]$  is not antisymmetric, so even though  $\text{Im}S_{z,z}[\omega]$  vanishes, this heterodyne quadrature is less useful for observing the RPSN.

Both angles in Eqs. 5.13 and 5.14 depend only on the detuning  $\Delta$  and the total cavity decay rate  $\kappa$ , which means they are insensitive to many parameters such as laser input power, membrane position (as long as  $\kappa$  remains constant), and optomechanical effects.

Since our measurements are all in the regime where the thermal contributions are much larger than any effect from classical or quantum radiation pressure noise, we have  $R[\omega] \approx R_{z,z}[\omega]$ . At the critical quadrature we should see the real part of the measured correlation get significantly smaller. Figure 5.11 shows the real part of the correlation for different quadrature angles. The curve labeled  $\theta = \theta_C$  significantly reduces the correlation. At an angle  $\theta = \theta_C \pm \pi/2$  the thermal contribution to the correlation  $R_{z,z}[\omega]$  attains a maximum value. These heterodyne quadrature angles which minimize  $\text{Re}S[\omega]$  and  $\text{Im}S[\omega]$  can be empirically determined and compared against the theoretical predictions in Eqs. 5.13 and 5.14, respectively.

Figure 5.12 shows a plot of the empirically determined values of the heterodyne quadrature angles

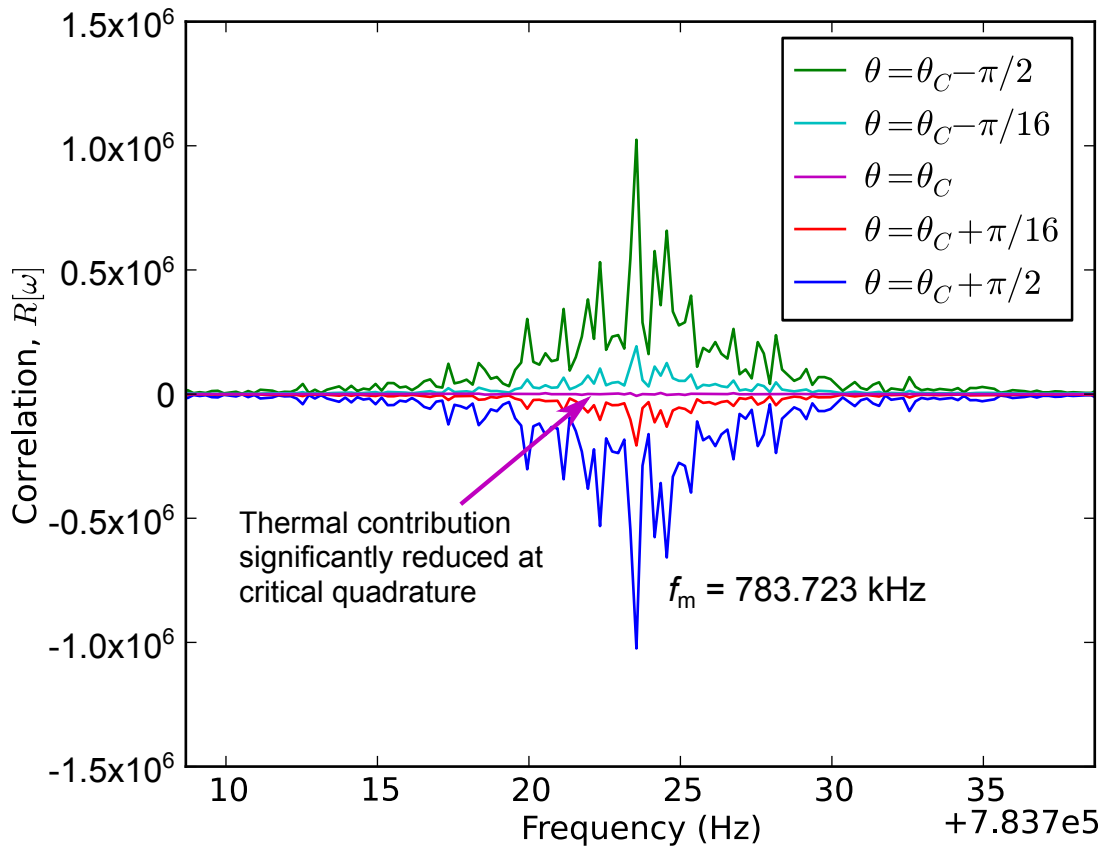


Figure 5.11: Measured real part of the correlation  $R[\omega] = \text{Re}S[\omega]$  for different heterodyne quadratures. When the heterodyne quadrature angle is chosen to be the critical quadrature, the real part of the correlation is substantially reduced. The resonant frequency  $f_m = 783.723 \text{ kHz}$ .

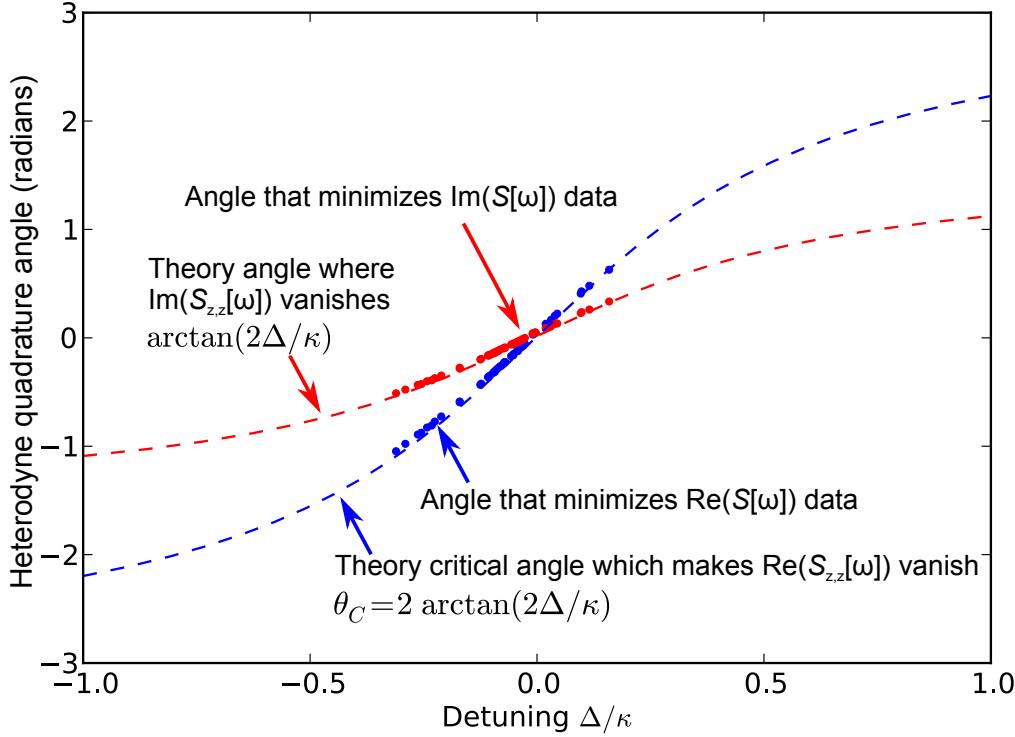


Figure 5.12: Plot of the measured critical quadrature as a function of detuning. The theoretical prediction that  $\theta_C = \arctan(2\Delta/\kappa)$  is plotted as the blue dashed line. The blue circle data points represent the heterodyne quadratures which minimized the real part of the correlation  $R[\omega]$ . A similar relationship can be measured for the imaginary part of the correlation, and the theory (dashed line) and data (circles) is plotted in red.

which minimize the real part  $R[\omega]$  and imaginary part of the correlation  $\text{Im}S[\omega]$  for many different detunings. The dashed lines show the theoretical predictions given by Eqs. 5.13 and 5.14. The agreement is good, which confirms the effectiveness of the calibration scheme and experimentally measures the critical quadrature predicted by Børkje et al. in Ref. [4].

However, the entire purpose for measuring the correlation using this particular critical quadrature is that the thermal noise can be suppressed enough to observe the interesting quantum correlation. The next section will present data showing the degree to which the thermal contribution was suppressed and discuss whether this seems reasonable. The averaging time required to observe the desired RPSN-induced  $R_{q,z}[\omega]$  correlation will also be discussed.

## 5.6 Suppression of the thermal contribution to the correlation

Now we want to quantify the degree of suppression of the thermal contribution to the correlation  $R_{z,z}[\omega]$ . Figure 5.13 A shows the desired  $R_{q,z}[\omega]$  contribution, which has a magnitude of  $\sim 0.1$ . Figure 5.13 C shows the observed suppression of the thermal contribution which still shows fluctuations with magnitude  $\sim 10^4$ . Figure 5.13 B shows  $R[\omega]$  at  $\theta = \theta_C + \pi/2$ , which is the quadrature angle creating largest thermally-induced correlation and is used to calibrate the correlation data to the same scale as theory.

This factor of  $10^5$  between the desired  $R_{q,z}[\omega]$  term and the observed correlation at critical quadrature in Fig. 5.13 C has two contributions. The first, due to thermally driven Brownian motion detected by the reflected quadrature, was described in Sec. 3.9. There it was argued that, prior to averaging, the amplitude of fluctuations in the correlation should be a factor of

$$\sqrt{\frac{S_F^{\text{th}}[\omega]}{S_F^{\text{sn}}[\omega]}} \approx 2000 \quad (5.15)$$

larger than the desired  $R_{q,z}[\omega]$  contribution (though for an infinite measurement time these fluctuation average to zero). The second source of noise is in the measurement of transmitted intensity. In Sec. 3.9 it was assumed that the transmitted amplitude quadrature  $X_\phi[\omega]$  measurement was shot noise-limited. However, as Fig. 5.14 shows, the actual noise floor of the transmission photodetector is a factor of  $5 \times 10^4$  larger than the predicted shot noise. The specified detector dark noise is about  $2 \times 10^3$  larger than shot noise, implying more noise is added between the photodiode output and the ZI-HF2, possibly during the summing of the transmission signal with the heterodyne signal. This additional dark noise causes fluctuations in  $R[\omega]$  which are an additional factor of  $\sqrt{5 \times 10^4} \approx 220$  greater than the desired  $R_{q,z}[\omega]$  contribution. When combined, the expected size of these unaveraged fluctuations would be about  $2000 \times 220 \approx 4 \times 10^5$  larger than the desired  $R_{q,z}[\omega]$ , which is in close agreement with Fig. 5.13.

In Sec. 3.9 it was calculated that an averaging time of nine hours would be needed to achieve a signal-to-noise ratio of unity assuming the membrane temperature was  $T = 300$  K and the photodiodes were shot noise-limited. The additional noise caused by the non-shot noise-limited transmission

detection system photodiode causes an increase in the averaging time by a factor of  $\sqrt{5 \times 10^4} \approx 220$ , so the measurement shown in Fig. 5.13 would take about 1200 hours to achieve a signal to noise of unity.

There are multiple approaches to using the correlation measurement scheme of the RPSN in a more reasonable time. First, the detectors should be shot noise-limited. This can be accomplished by using photodiodes with a lower noise equivalent power and/or increasing the amount of power landing on the photodiode. In the current setup, the optical power can be increased by removing the beam splitter (for mode imaging) before the photodiode and by increasing the power incident upon the cavity. Also, a heterodyne or homodyne detection scheme could be used in transmission to scale up the shot noise fluctuations by the local oscillator signal. Second, the ratio of the RPSN and thermal forces can be made more favorable through changing many parameters in the setup. For example, one straightforward way is to make the system colder. The averaging time is proportional to  $\sqrt{S_{FF}^{\text{th}}/S_{FF}^{\text{sn}}} \propto \sqrt{T}$ . By lowering the temperature from 300 K to 300 mK, which is achievable in a  $^3\text{He}$  refrigerator, the averaging time is reduced by a factor of 32. Chapter 6 will explore in more detail a variety of changes to the optomechanical system which could increase the RPSN effects relative to the thermal effects. Third, if a resonator with a larger mechanical linewidth ( $\gamma \rightarrow a\gamma$ ) is used, then the measurement time required to resolve the mechanical line shape decreases by this same factor ( $T_{\text{meas}} \rightarrow T_{\text{meas}}/a$ ). This effect is particularly significant when the optical damping is used to increase the linewidth of the mechanical resonator (which avoids increasing the thermal Langevin force), but is also helpful for smaller membranes such as for the proposed fiber cavity optomechanical systems ( $\omega_M/2\pi = 3 - 100$  MHz) described in Ch. 6.

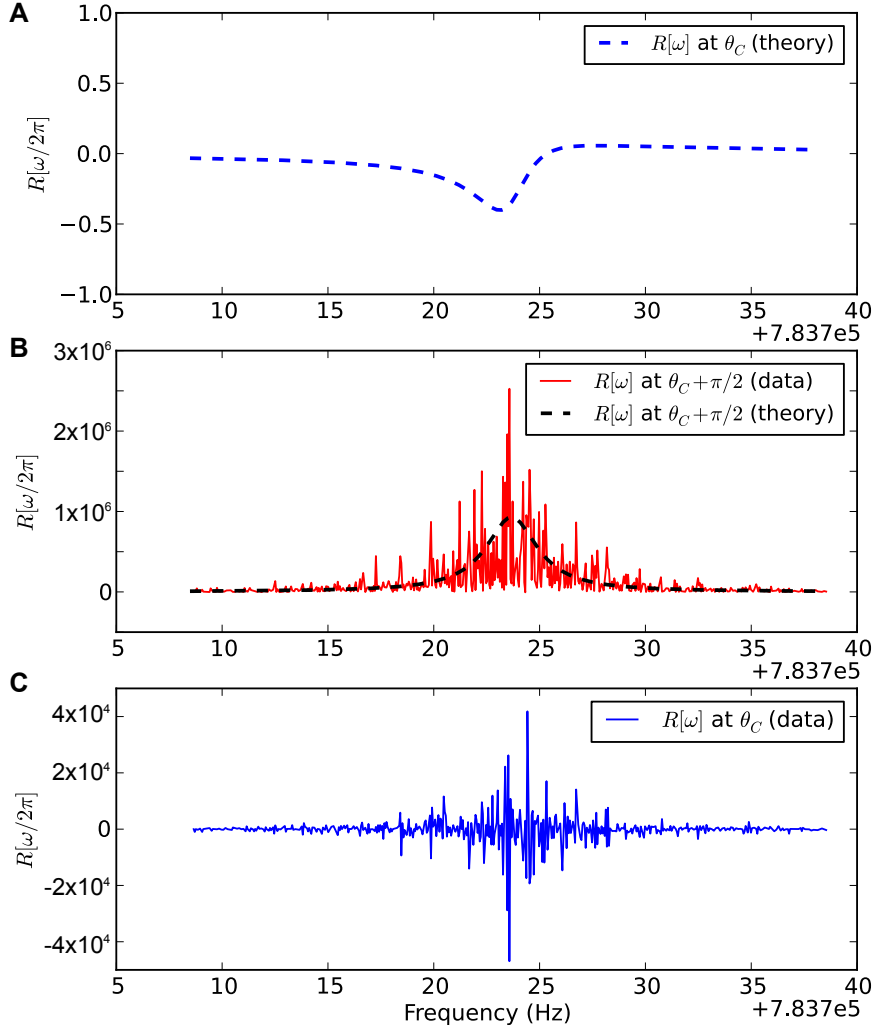


Figure 5.13: (A) The theoretically expected profile of the real part of the correlation  $R[\omega]$  at the critical quadrature for a detuning of  $\Delta \approx -0.037\kappa$ . (B) The dashed line is a plot of the theoretical expectation for the real part of the correlation at  $\theta_C + \pi/2$  in the limit of an infinite measurement time. This is the quadrature that maximizes the correlation due to Brownian motion, and is used to calibrate the scale of the measured correlation data (shown in red). (C) Measured real part of the correlation  $R[\omega]$  at critical quadrature  $\theta_C$ . The vertical axis is in the same units as the top plot, showing that there are still fluctuations about  $10^4$  times larger than the desired quantum signal.

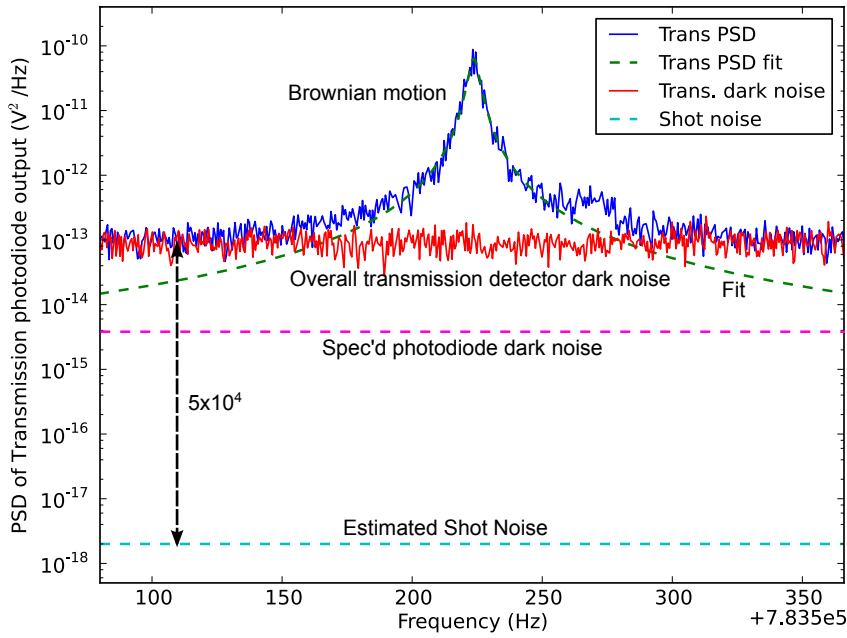


Figure 5.14: Plot of the Brownian motion in transmission. The dark noise of the transmitted detector is a factor of  $5 \times 10^4$  larger than the estimated shot noise for a power of 800 nW incident upon the detector. The dark noise was measured using an unlocked and far-detuned data set with no transmission. The specified photodiode dark noise is  $4 \times 10^{-15} \text{ V}^2/\text{Hz}$ . The total dark noise in the transmission detection scheme was a factor of 30 larger than the specified dark noise of the photodiode indicating additional noise was added after the photodiode. The detuning for the locked near-resonance transmission data (blue and dashed green) was  $\Delta = -0.037\kappa$ .

# Chapter 6

## Future directions and conclusions

### 6.1 Optimization of optomechanical parameters

Chapter 5 concluded with the sobering thought that the cavity optomechanical system used in this dissertation would require a measurement time of 700 hours in order to detect the correlation signature of RPSN with a signal-to-noise ratio of unity. In this section I describe how the system could be modified to perform the measurement in a more reasonable time. The ratio of RPSN and thermal forces given by Eq. 2.181 (copied below for convenience) is our guide:

$$\frac{S_F^{\text{sn}}[\omega_M]}{S_F^{\text{th}}[\omega_M]} = \left( \frac{1}{1 + \left(\frac{\Delta}{\kappa/2}\right)^2} \right) \left( \frac{1}{1 + \left(\frac{\Delta + \omega_M}{\kappa/2}\right)^2} \right) \left( \frac{\kappa_L}{\kappa/2} \right) \beta^2 \frac{8\hbar P_{\text{in}} F^2 Q}{\pi m \omega_M c \lambda k_B T} \quad (6.1)$$

Writing the cavity decay rate  $\kappa$  as

$$\kappa = \frac{\pi c}{LF} \quad (6.2)$$

and writing the left end-mirror coupling efficiency  $\eta_{\text{eff}}$  as

$$\eta_{\text{eff}} = \frac{\kappa_L}{\kappa/2} \quad (6.3)$$

we get

$$\frac{S_F^{\text{sn}}[\omega_M]}{S_F^{\text{th}}[\omega_M]} = \frac{\left(\frac{\pi c}{2LF}\right)^4}{\left(\left(\frac{\pi c}{2LF}\right)^2 + \Delta^2\right) \left(\left(\frac{\pi c}{2LF}\right)^2 + (\Delta + \omega_M)^2\right)} \eta_{\text{eff}} \beta^2 \frac{4\hbar P_{\text{in}} F^2 \omega_L Q}{\pi^2 c^2 m \omega_M k_B T} \quad (6.4)$$

One immediate consideration is that the ratio in Eq. 6.4 is proportional to the incident laser power  $P_{\text{in}}$ . One reasonable upper limit for the laser power is the power at which the optomechanical system has a static bistability, meaning there are multiple steady state solutions of the membrane's unstretched position as a function of the laser power. The onset of bistability occurs when the maximum DC optical spring constant is equal to the spring constant of the lowest order mechanical mode  $k_0$ . The maximum DC spring constant is given by

$$k_{\text{opt}}^{(\text{max})} = \frac{3\sqrt{3}\eta_{\text{eff}} F^2 \beta^2 \omega_L P_{\text{in}}}{2\pi^2 c^2} \quad (6.5)$$

Then the optomechanical bistability occurs when  $k_{\text{opt}}^{(\text{max})} = k_0 \equiv m\omega_{M,0}^2$ , where  $k_0$  is the spring constant of the lowest order mechanical mode with resonant frequency  $\omega_{M,0}$ . Solving for the incident power  $P_{\text{in}}^{\text{BS}}$  at which the bistability condition is met (called the bistability power) we get

$$P_{\text{in}}^{\text{BS}} = \frac{2\pi^2 c^2 m \omega_{M,0}^2}{3\sqrt{3}\eta_{\text{eff}} F^2 \beta^2 \omega_L} \quad (6.6)$$

Substituting  $P_{\text{in}}^{\text{BS}}$  from Eq. 6.6 into Eq. 6.4 gives

$$\frac{S_F^{\text{sn}}[\omega_M]}{S_F^{\text{th}}[\omega_M]} = \frac{\left(\frac{\pi c}{2LF}\right)^4}{\left(\left(\frac{\pi c}{2LF}\right)^2 + \Delta^2\right) \left(\left(\frac{\pi c}{2LF}\right)^2 + (\Delta + \omega_M)^2\right)} \frac{8\hbar Q}{3\sqrt{3}k_B T} \frac{\omega_{M,0}^2}{\omega_M} \quad (6.7)$$

This is a useful figure of merit for comparing systems and can be used to estimate the measurement time required to resolve the RPSN signature in the correlation measurement as in Sec. 3.9. The figure of merit no longer depends on the optomechanical coupling parameter  $\beta$ , assuming the power can always be increased up to the bistability power  $P_{\text{in}}^{\text{BS}}$ .

### 6.1.1 Relevance of the static radiation pressure bistability to the experiments in this dissertation

For a 50-nm thick membrane displaced 12 nm from the node (as in Ch. 5), the factor  $\beta$  is

$$\beta = \frac{\partial\omega_{\text{cav}}}{\partial\tilde{z}} \times \frac{L}{\omega_{\text{cav}}} \approx 0.02 \quad (6.8)$$

The bistability power given by Eq. 6.6 for the optomechanical parameters in this thesis is  $P_{\text{in}}^{\text{BS}} = 400 \text{ mW}$ , which is  $4 \times 10^4$  times higher than the  $10 \mu\text{W}$  of incident optical power actually used in the experiments. Had the membrane been at a position of largest optomechanical coupling  $\partial\omega_{\text{cav}}/\partial\tilde{z}$  (halfway between a node and antinode) the bistability power would have only been  $P_{\text{in}}^{\text{BS}} = 1.7 \text{ mW}$ .

Because the estimated power at the onset of bistability is about a hundred times larger than the actual incident power, the primary obstacle to locking is almost certainly large mechanical vibrations of the membrane in the audio frequency range which is caused by the membrane's in-situ tilt-translation mount. Occasionally these vibrations move the membrane to a position of blue-detuning, which causes anti-damping and creates large oscillations of the membrane. These large oscillations cause the laser to lose lock with the cavity. The fact that an occasional blue detuning is the primary cause of the laser unlocking suggests a significant advantage to locking at large red-detunings. Section 3.7 showed that the regime of large red-detuning ( $\Delta \gg \kappa, \omega_{\text{M}}$ ) also offers a good (antisymmetric) signature of the RPSN using the correlation measurement scheme.

Table 6.1 shows the effect of making successive improvements to the system used for the measurements in Ch. 5, but without changing optomechanical parameters. The measurement time at room temperature can be reduced to three minutes if the following three changes are made: (1) the incident power is increased to the bistability limit, (2) the optomechanical coupling is maximized (as it is halfway between a node and antinode), and (3) the detectors are shot noise-limited.

If the membrane optomechanical parameters are also allowed to vary and the incident power is pushed to the bistability threshold, then Eq. 6.7 gives us some idea of how to optimize parameters.

First note that the first factor resulting from cavity filtering is always less than one:

$$\frac{\left(\frac{\pi c}{2LF}\right)^4}{\left(\left(\frac{\pi c}{2LF}\right)^2 + \Delta^2\right) \left(\left(\frac{\pi c}{2LF}\right)^2 + (\Delta + \omega_M)^2\right)} \leq 1 \quad (6.9)$$

and the upper limit of one is reached when  $\Delta, \omega_M \ll \kappa = \pi c/LF$ . Second, note that in this limit, the only remaining optomechanical parameter which is easily varied is  $\omega_M$  (the mechanical quality factor  $Q$  is not easy to vary). The ratio of RPSN and thermal forces is then proportional to  $\omega_M$ :

$$\frac{S_F^{\text{sn}}[\omega_M]}{S_F^{\text{th}}[\omega_M]} \propto \omega_M \quad (6.10)$$

The measurement would be improved by using membranes with higher resonant frequency as long as  $\omega_M \ll \kappa$ . The cavity decay rate  $\kappa$  can be kept large by using shorter cavities or decreasing the finesse. Decreasing the finesse, however, has the potentially undesirable consequence of requiring larger incident laser powers to accomplish the same optomechanical effect. The Stage 1 fiber cavity in Table 6.2, under development by Nathan Flowers-Jacobs and Jack Harris, is an example of a cavity which has moved towards higher  $\omega_M$ , and shorter cavity lengths. The Stage 1 fiber cavity should be able to achieve a ratio  $S_F^{\text{SN}}[\omega_M]/S_F^{\text{th}}[\omega_M] \approx 1$  for 1 mW of incident power. The Stage 1 fiber cavity system should be able to observe directly the effects of RPSN as an additional random force on the membrane of comparable size to the thermal Langevin force.

## 6.2 Conclusion

It has been over 100 years since the first conclusive demonstration of radiation pressure by Lebedev [1] and Nichols and Hull [2, 3]. The past decade has seen the development of a variety of tabletop-scale optomechanical systems which offer a test bed for the mechanical properties of light. In these recent optomechanical systems, light is not only causing a steady state deflection of a mirror, but is creating a rich array of dynamical effects such as the shifts in mechanical resonant frequency and the optical damping as were demonstrated in this thesis.

During these same 100 years we have also learned much more about the (quantum) nature

	Transmission photodiode	Mirror efficiency $\eta = \frac{2\kappa_L}{\kappa}$	$T$ (K)	$P_{\text{in}}$ ( $\mu\text{W}$ )	Displacement from node (nm)	$\frac{S_F^{\text{SN}}[\omega_M]}{S_F^{\text{th}}[\omega_M]}$	Measurement time for $S/N = 1$
Thesis data	current	0.3	300	10	12	$2 \times 10^{-7}$	1200 hours
Thesis + optimal detectors	shot noise-limited	0.3	300	10	12	$2 \times 10^{-7}$	6 hours
Thesis + optimal detectors + more optomechanical coupling	shot noise-limited	0.3	300	10	24	$10^{-6}$	3 hours
Thesis + optimal detectors + max optomechanical coupling	shot noise-limited	0.3	300	10	266	$4 \times 10^{-5}$	25 min.
Thesis + optimal detectors + max optomechanical coupling + max incident power	shot noise-limited	1.0	300	500	266	$6 \times 10^{-3}$	2 min
Thesis + optimal detectors + max optomechanical coupling + max incident power + cryogenics	shot noise-limited	1.0	0.3	500	266	6	10 sec (a)

Table 6.1: A comparison of the measurement time required to observe the RPSN signature  $R_{q,z}[\omega]$  with a signal-to-noise ratio of unity. The comparison shows the effect of successive improvements to the measurement while keeping the cavity and membrane parameters the same. All setups assume finesse  $F = 30000$ , cavity length  $L = 0.007$  m, mechanical quality factor  $Q = 8 \times 10^5$ , mechanical resonant frequency  $\omega_M/2\pi = 784$  kHz, the membrane dimensions are  $1 \text{ mm} \times 1 \text{ mm} \times 50 \text{ nm}$ , and the detuning is  $\Delta = 0$ . *Notes:* (a) For the cryogenic setup, the 10 second measurement time is set by the time required to resolve the resonance. No averaging is required since the signal-to-noise ratio already exceeds unity.

	Transmission photo- diode	Finesse	Cavity Length $L$ (mm)	$\frac{\omega_M}{2\pi}$ (MHz)	$Q$	Mem- brane side ( $\mu\text{m}$ )	Mem- brane thick- ness (nm)	$P_{\text{in}}$ (W)	$\frac{S_F^{\text{SN}}[\omega_M]}{S_F^{\text{th}}[\omega_M]}$ at $P_{\text{in}}^{\text{BS}}$	Meas. time for $S/N = 1$
Thesis	current	30000	7	0.8	$8 \times 10^5$	1000	50	$10^{-5}$	$2 \times 10^{-7}$	1200 hours
Thesis + optimal detectors	shot noise- limited	30000	7	0.8	$8 \times 10^5$	1000	50	$10^{-5}$	$2 \times 10^{-7}$	6 hours
Stage 1 fiber cavity	shot noise- limited	30000	0.4	3.0	$10^6$	100	200	$10^{-3}$	1.3	3 sec. (a)
Stage 2 fiber cavity	shot noise- limited	2000	0.2	100	$10^6$	10	200	$10^{-1}$	1.7	0.1 sec. (a)

Table 6.2: A comparison of the measurement time required to observe the RPSN signature  $R_{q,z}[\omega]$  with a signal-to-noise ratio of unity. The comparison shows the improvement which can be achieved by significantly reducing the physical dimensions of the cavity and membrane. The parameters are based on current and future designs for fiber cavities in development by my Harris Lab colleagues Nathan Flowers-Jacobs and Scott Hoch. All devices are assumed to be at room temperature  $T = 294$  K and at zero detuning  $\Delta = 0$ . *Notes:* (a) For the fiber cavities, the measurement time is set by the time required to resolve the resonance. No averaging is required since the signal-to-noise ratio already exceeds unity.

of light. This thesis was an attempt to observe radiation pressure shot noise—an effect which is simultaneously quantum (photon statistics) and mechanical (via radiation pressure). Cavity optomechanical systems offer a promising route towards observing the RPSN. Though the system described in this thesis was unsuccessful in observing the RPSN, the path to observation is well-defined. Continuing work in the Harris Lab by Nathan Flowers-Jacobs and Scott Hoch on fiber cavity optomechanical systems will offer a direct observation of the RPSN and much more. These fiber cavity systems should enable the production of squeezed light. Also, many groups (including the Harris Lab) are rapidly approaching the ground state of a mechanical resonator, and it is expected that one of these groups using laser cooling will observe RPSN as the limit to their lowest achievable phonon number. In short, conclusive observation of the RPSN is just around the corner.

So what did we learn from all this? As a technical accomplishment it was the first optical heterodyne measurement employed by our lab. The correlation measurement scheme was one of the most sophisticated optomechanical measurement schemes implemented in our lab. The Zurich Instruments HF-2 lock-in was found to be a versatile and indispensable device for implementing the correlation measurement scheme, and has now become an integrated part of all the optomechanical projects in the lab.

As a confirmation of theory, basic predictions of optical spring and damping agreed with our data. More importantly, in agreement with the predictions of Børkje et al. [4], we minimized the effect of thermally driven motion in the correlation measurement using the critical heterodyne quadrature of the reflected beam. Although the suppression of thermal effects wasn't sufficient to observe the RPSN, the discrepancy was consistent with the finite averaging time and with the additional noise in the non-shot noise-limited detectors. Achieving shot noise-limited detection and locking the laser with larger optomechanical couplings (higher powers and larger  $\partial\omega_{\text{cav}}/\partial\tilde{z}$ ) could reduce the required measurement time from hundreds of hours to about 10 minutes. Although these improvements are possible, they will not be pursued because there are more exciting physics goals awaiting the fiber cavity system and the cryogenic system. If all goes well, my Harris lab colleagues will soon be creating squeezed light via the fiber cavity and cooling a membrane near the ground state in the cryogenic system.

# Appendix A

## Calculations of stressed membrane properties

Notes to calculate the spring constant of a square stressed membrane of

- side length  $L$
- thickness  $t$
- stress  $\sigma$

### A.1 Calculation of spring constant

For a membrane under a high stress, the Young's modulus of the material contributes little to the restoring force, and the mechanical eigenmodes become very simple:

$$z_{m,n}(x, y, t) = z_0(t) \sin\left(\frac{\pi m x}{L}\right) \sin\left(\frac{\pi n y}{L}\right) \quad (\text{A.1})$$

The modes in Eq. A.1 are the two dimensional versions of the vibrational modes of a string under tension studied in introductory college physics. The derivation of the mode shapes can proceed in a similar way as for a vibrating string under tension.

The work done to stretch a membrane by an amount  $\Delta A$  is just  $E = \sigma t \Delta A$ . For a membrane mode shape  $z(x, y)$ , the area becomes

$$\Delta A = \int_0^L dx \int_0^L dy \left( \sqrt{1 + \left(\frac{\partial z}{\partial x}\right)^2 + \left(\frac{\partial z}{\partial y}\right)^2} - 1 \right) \quad (\text{A.2})$$

which for small amplitudes of motion we can assume the partial derivatives of  $z$  are small, and the expression simplifies to

$$\Delta A = \frac{1}{2} \int_0^L dx \int_0^L dy \left( \left(\frac{\partial z}{\partial x}\right)^2 + \left(\frac{\partial z}{\partial y}\right)^2 \right) \quad (\text{A.3})$$

Plugging in the definition of  $z_{m,n}(x, y)$  gives

$$\Delta A = \frac{\pi^2}{8} (m^2 + n^2) z_0(t)^2 \quad (\text{A.4})$$

Potential energy is then

$$U = \sigma t \Delta A = \frac{\pi^2 \sigma t_m}{8} (m^2 + n^2) z_0(t)^2 \quad (\text{A.5})$$

Defining the spring constant so that  $U = \frac{1}{2} k_{m,n} z_0^2$ , we get

$$k_{m,n} = \frac{\pi^2 \sigma t_m}{4} (m^2 + n^2) \quad (\text{A.6})$$

Assuming  $\sigma = 125$  MPa,  $t_m = 50$  nm,  $m = n = 1$ , we get  $k = 30$  N/m. In practice  $\sigma$  is a fit parameter that is chosen to predict agree with the spectrum of measured resonant frequencies. I forget what Norcada claims typical error bars on stress are, but they might be as large as a 50%.

## A.2 Calculation of Kinetic Energy, Effective Mass, and Resonant Frequency

The time dependent solution will look like

$$z_{m,n}(x, y, t) = z_0(t) \sin\left(\frac{\pi m x}{L}\right) \sin\left(\frac{\pi n y}{L}\right) \quad (\text{A.7})$$

The kinetic energy is then

$$T = \frac{1}{2} \int_0^L dx \int_0^L dy \rho t_m \left( \frac{dz_{m,n}(x, y, t)}{dt} \right)^2 \quad (\text{A.8})$$

$$= \frac{1}{2} \int_0^L dx \int_0^L dy \rho t_m \left( \frac{dz_0(t)}{dt} \right)^2 \sin^2\left(\frac{\pi m x}{L}\right) \sin^2\left(\frac{\pi n y}{L}\right) \quad (\text{A.9})$$

$$= \frac{1}{2} \rho t_m \dot{z}_0(t)^2 \left( \frac{L}{2} \right)^2 \quad (\text{A.10})$$

$$= \frac{1}{2} m_{\text{eff}} \dot{z}_0(t)^2 \quad (\text{A.11})$$

where  $m_{\text{eff}} = \frac{1}{4} \rho t_m L^2 = \frac{1}{4} m$  is the effective mass, and is one quarter of the actual mass of the membrane. So the full expression for the energy is

$$E = T + U \quad (\text{A.12})$$

$$= \frac{1}{2} m_{\text{eff}} \dot{z}_0(t)^2 + \frac{1}{2} k_{m,n} z_0^2 \quad (\text{A.13})$$

Then the resonant frequency is

$$\omega_{m,n} = \sqrt{\frac{k_{m,n}}{m_{\text{eff}}}} \quad (\text{A.14})$$

$$= \sqrt{\frac{\pi^2 \sigma t_m (m^2 + n^2)/4}{\rho t_m L^2/4}} \quad (\text{A.15})$$

$$= \sqrt{\frac{\pi^2 \sigma (m^2 + n^2)}{\rho L^2}} \quad (\text{A.16})$$

# Appendix B

## Derivation of thermo-elastic dissipation limited $Q$

### B.1 Introduction

One of the few forms of damping which is calculable from first principles is thermo-elastic dissipation (TED). As a material is strained there is a change in temperature related by the thermal expansion coefficient  $\alpha$ . If there is a bending strain as is the case for oscillating beams and membranes then there is a strain gradient across the thickness of the beam which sets up a thermal gradient in the beam. As for any thermal gradient, there will be a heat flow from the warmer side to the cooler side. Any energy which is transported as a heat conducting from warm to cooler is an irreversible change. This irreversible heat transfer is a conversion of mechanical energy into heat. The goal of this calculation is to find a formula for  $Q_{\text{TED}}$ , the thermo-elastic dissipation limited mechanical quality factor.

## B.2 Derivation

### B.2.1 Modifications of argument in Norris and Photiadis

This derivation is a hybrid of the  $Q_{\text{TED}}$  derivations given by Norris and Photiadis [105] and original theory by Zener [102, 103]. Norris and Photiadis have very clear formalism for deriving  $Q_{\text{TED}}$  based on general thermodynamic principles for continuous media. The results are very general, but a little longer computationally (at least for me). Zener's derivation is more direct, but less general. Since I only wanted  $Q_{\text{TED}}$  for a particular known vibrational mode, Zener's approach gave a quicker route to the final result. Here are some general simplifications used in this derivation compared to Norris and Photiadis.

1. The medium is assumed to be isotropic (as it is for amorphous silicon nitride) so all the material constants like the thermal expansion coefficient  $\alpha$ , the thermal conductivity  $\mathbf{K}$ , Poisson's ratio  $\nu$ , and Young's Modulus  $E_Y$  are all assumed to be scalars or if they are treated as tensors, they have the simple form such as a diagonal matrix with identical values (e.g.,  $\alpha = \alpha \text{diag}(1, 1, 1)$ ).
2. The energy of the oscillator undergoing oscillations of amplitude  $A_0$  is assumed to have the simple form for a membrane under tension given in Eq. B.2. Norris and Photiadis assume there is no externally applied stress so the energy given by Norris and Photiadis is Norris and Photiadis Eq. 4.3.
3. I take the limit that the thermal relaxation time  $\tau_r$  goes to zero which recovers the Kirchoff theory of heat diffusion (which I believe is used by Zener also). I am not sure how to estimate  $\tau_r$ . I don't think it is related to the thermal conductivity.

### B.2.2 Setting up the basic equations to solve

This derivation is based heavily on formalism in Norris and Photiadis [105]. Refer to Table B.1 for a list of the symbols used because they may be different than in the rest of the dissertation.

$\boldsymbol{\sigma}(\vec{x}, t)$	stress tensor
$\mathbf{e}(\vec{x}, t)$	strain tensor
$\theta(\vec{x}, t)$	temperature deviation from equilibrium
$\boldsymbol{\alpha}$	thermal expansion coeff.
$\epsilon(\vec{x}, t)$	energy loss per unit volume
$\mathbf{K}$	thermal conductivity tensor

Table B.1: List of symbols used in  $Q_{\text{TED}}$  derivation. The list is consistent with notation in Norris and Photiadis [105].

$\rho$	density	$3 \times 10^3$	kg/m <sup>3</sup>
$\sigma_{\text{ext}}$	external stress	$897 \times 10^6$	N/m <sup>2</sup>
$L$	side length	$10^{-3}$	m
$\nu$	Poisson's ratio	0.25	-
$\theta_a$	Average temperature	294	K
$\alpha$	thermal expansion coeff	$3 \times 10^{-6}$	K <sup>-1</sup>
$E_Y$	Young's Modulus	$126 \times 10^9$	N/m <sup>2</sup>
$K$	Thermal conductivity	3.2	W/m K
$h$	Membrane thickness	$50 \times 10^{-9}$	m
$C_p$	heat capacity at constant stress	$2.1 \times 10^6$	J/m <sup>3</sup> /K

Table B.2: List of material parameters used in derivation

In order to calculate the mechanical quality factor  $Q_{\text{TED}}$  we need to calculate the quantity

$$Q = \frac{\omega_M E}{\bar{\dot{E}}} \quad (\text{B.1})$$

where  $\omega_M$  is the resonant frequency of a mechanical mode,  $E$  is the energy of the mechanical mode, and  $\bar{\dot{E}}$  is the mean energy loss during one oscillation. In general  $\dot{E}$  oscillates with the membrane motion which is why the mean over a period must be taken. The resonant frequency  $\omega_M$  and energy  $E$  of the  $(m, n)$  vibrational mode for a square membrane under tension is given in Appendix A as

$$E = \frac{\pi^2 \sigma_{\text{ext}} h}{8} (m^2 + n^2) A_0^2 \quad (\text{B.2})$$

where  $h$  is the membrane thickness,  $\sigma_{\text{ext}}$  is the externally applied stress, and  $A_0$  is the amplitude of oscillation. The resonant frequency  $\omega_{m,n}$  of that same mode is

$$\omega_{m,n} = \sqrt{\frac{\pi^2 \sigma_{\text{ext}} (m^2 + n^2)}{\rho L^2}} \quad (\text{B.3})$$

where  $\rho$  is the density, and the side length of the square membrane is  $L$ . The only remaining thing to calculate is the mean energy loss over an oscillation cycle  $\bar{E}$ .

Because the loss mechanism in thermoelastic dissipation depends on strain gradients which occur where there is bending, the energy loss is greatest at points where there is the most curvature in the mode shape (antinodes) and zero at the positions of least curvature (nodes). This means the energy loss per cycle is not spatially uniform. There is more energy lost near the antinodes, so we need to first calculate  $\bar{\epsilon}$ , the energy loss per unit volume time-averaged over an oscillation.  $\bar{\epsilon}$  is then integrated over the volume of the membrane to give  $\bar{E}$ . The basic thermodynamics of thermoelastic dissipation is nicely reviewed in Norris and Photiadis, so I will not review it. The energy loss density averaged over an oscillation cycle is given by Norris and Photiadis Eq. 3.9:

$$\bar{\epsilon} = -\overline{\theta(\vec{x}, t) \boldsymbol{\alpha} \cdot \dot{\boldsymbol{\sigma}}(\vec{x}, t)} \quad (\text{B.4})$$

### B.2.3 Calculating the temperature field $\theta(\vec{x}, t)$ (part 1)

The temperature field is calculated from the stress  $\boldsymbol{\sigma}$  via the equation of motion for  $\theta(t)$  which is given by Norris and Photiadis Eq. 2.11

$$C_p \dot{\theta} - \nabla \cdot (\mathbf{K} \nabla \theta) = -\theta_a \boldsymbol{\alpha} \cdot \dot{\boldsymbol{\sigma}} \quad (\text{B.5})$$

We try a separable series solution to of the form (given by Norris and Photiadis Eq. 3.5)

$$\theta(\vec{x}, t) = \sum_{n=0}^{\infty} \theta_n(t) \phi_n(\vec{x}) \quad (\text{B.6})$$

where  $\theta_n(t)$  and  $\phi_n(\vec{x})$  satisfy an equations of motion (given by Norris and Photiadis Eq. 3.6 and 3.7)

$$\frac{1}{C_p} \text{div}(\mathbf{K} \nabla \phi_n) + \frac{1}{\tau_n} \phi_n = 0 \quad (\text{B.7})$$

$$\dot{\theta}_n + \frac{1}{\tau_n} \theta_n = -\frac{\theta_a}{C_p} \langle \phi_n, \boldsymbol{\alpha} \cdot \dot{\boldsymbol{\sigma}} \rangle \quad (\text{B.8})$$

where  $\langle f, g \rangle = \int dV f(\vec{x})g(\vec{x})$ .

## B.2.4 Calculating $\alpha \cdot \sigma$

For an isotropic medium the thermal expansion coefficient tensor is given by

$$\boldsymbol{\alpha} = \alpha \begin{pmatrix} 1 & 0 & 0 \\ 0 & 1 & 0 \\ 0 & 0 & 1 \end{pmatrix} \quad (\text{B.9})$$

and the Poisson ratio  $\nu$  and Young's modulus  $E_Y$  are regarded as scalars. The product  $\boldsymbol{\alpha} \cdot \boldsymbol{\sigma}$  (basically given by Norris and Photiadis Eq 4.1) is

$$\boldsymbol{\alpha} \cdot \boldsymbol{\sigma} = \alpha (\sigma_{xx} + \sigma_{yy}) \quad (\text{B.10})$$

$$= \frac{z}{1 - \nu^2} [(1 + \nu)E\alpha(\kappa_{xx} + \kappa_{yy})] \quad (\text{B.11})$$

$$= \frac{z}{1 - \nu} E\alpha(\kappa_{xx} + \kappa_{yy}) \quad (\text{B.12})$$

where the curvature tensor  $\kappa_{ij}$  (Norris and Photiadis Eq. 4.2) is

$$\kappa_{ij} = \frac{\partial^2 w(x, y)}{\partial x_i \partial x_j} \quad (\text{B.13})$$

The mechanical modes of an externally stressed membrane are given by

$$z(t)w_{m,n}(x, y) = z(t) \sin \frac{m\pi x}{L} \sin \frac{n\pi y}{L} \quad (\text{B.14})$$

so

$$\kappa_{xx} = -\frac{\partial^2 w_{m,n}}{\partial x^2} = z(t) \left(\frac{m\pi}{L}\right)^2 \sin \frac{m\pi x}{L} \sin \frac{n\pi y}{L} \quad (\text{B.15})$$

$$\kappa_{yy} = -\frac{\partial^2 w_{m,n}}{\partial y^2} = z(t) \left(\frac{n\pi}{L}\right)^2 \sin \frac{m\pi x}{L} \sin \frac{n\pi y}{L} \quad (\text{B.16})$$

and the time derivatives (which are needed later for calculating  $\theta(\vec{x}, t)$ ) are

$$\dot{\kappa}_{xx} = \dot{z}(t) \left(\frac{m\pi}{L}\right)^2 \sin \frac{m\pi x}{L} \sin \frac{n\pi y}{L} \quad (\text{B.17})$$

$$\dot{\kappa}_{yy} = \dot{z}(t) \left(\frac{n\pi}{L}\right)^2 \sin \frac{m\pi x}{L} \sin \frac{n\pi y}{L} \quad (\text{B.18})$$

and the quantity  $\boldsymbol{\alpha} \cdot \dot{\boldsymbol{\sigma}}$  is

$$\boldsymbol{\alpha} \cdot \dot{\boldsymbol{\sigma}} = \frac{z}{1-\nu} E \alpha (\dot{\kappa}_{xx} + \dot{\kappa}_{yy}) \quad (\text{B.19})$$

$$= \frac{z}{1-\nu} E \alpha \dot{z}(t) \left(\frac{\pi}{L}\right)^2 \sin \frac{m\pi x}{L} \sin \frac{n\pi y}{L} (m^2 + n^2) \quad (\text{B.20})$$

### B.2.5 Calculating the temperature field $\theta(\vec{x}, t)$ (Part 2)

The temperature field must satisfy Eq. B.5:

$$C_p \dot{\theta} - \nabla \cdot (\mathbf{K} \nabla \theta) = -\theta_a \boldsymbol{\alpha} \cdot \dot{\boldsymbol{\sigma}} \quad (\text{B.21})$$

$$= -\theta_a \frac{z}{1-\nu} E \alpha (\dot{\kappa}_{xx} + \dot{\kappa}_{yy}) \quad (\text{B.22})$$

$$= -\theta_a \frac{z}{1-\nu} E \alpha \dot{z}(t) \left(\frac{\pi}{L}\right)^2 \sin \frac{m\pi x}{L} \sin \frac{n\pi y}{L} (m^2 + n^2) \quad (\text{B.23})$$

In the thin plate limit the heat flow in transverse directions can be ignored (discussed in more detail in Ref. [105]) so the left hand side of the equation simplifies to  $C_p \dot{\theta} - K \frac{\partial^2 \theta}{\partial z^2}$  so

$$C_p \dot{\theta} - K \frac{\partial^2 \theta}{\partial z^2} = -\theta_a \frac{z}{1-\nu} E \alpha \dot{z}(t) \left(\frac{\pi}{L}\right)^2 \sin \frac{m\pi x}{L} \sin \frac{n\pi y}{L} (m^2 + n^2) \quad (\text{B.24})$$

Now assume that the membrane motion is oscillatory so the amplitude of motion  $z(t)$  has the form

$$z(t) = A_0 \sin(\omega_{m,n} t) \quad (\text{B.25})$$

Substituting  $z(t) = A_0 \sin(\omega_{m,n}t)$  into the equation of motion for  $\theta$  given in Eq. B.24 gives

$$C_p \dot{\theta} - K \frac{\partial^2 \theta}{\partial z^2} = -\theta_a \frac{z}{1-\nu} E \alpha A_0 \omega_{m,n} \cos(\omega_{m,n}t) \times \left(\frac{\pi}{L}\right)^2 \sin \frac{m\pi x}{L} \sin \frac{n\pi y}{L} (m^2 + n^2) \quad (\text{B.26})$$

Try the separable solutions of the form

$$\theta(\vec{x}, t) = \sum_{i=0}^{\infty} \theta_i(t) \phi_i(\vec{x}) \quad (\text{B.27})$$

$$= \sum_{i=0}^{\infty} \theta_i(t) \left(\frac{2}{h}\right)^{1/2} \sin(2i+1) \frac{\pi z}{h} \quad (\text{B.28})$$

The spatial part of the temperature field

$$\phi_i(\vec{x}) = \left(\frac{2}{h}\right)^{1/2} \sin(2i+1) \frac{\pi z}{h} \quad (\text{B.29})$$

is anti-symmetric because the symmetric solutions don't create any damping (recall the damping is proportional to the inner product of the (symmetric) stress field and the temperature field in Eq. B.8). Also, the solution for  $\phi_i(\vec{x})$  given in Eq. B.28 was chosen so that  $\theta(\vec{x}, t)$  would satisfy the appropriate boundary conditions, which according to Zener [102] is that the temperature field must satisfy

$$\frac{\partial \theta}{\partial z} = 0 \text{ at } z = \pm \frac{h}{2}$$

Substituting the solution in Eq. B.28 into Eq. B.26 gives

$$\begin{aligned} \sum_{i=0}^{\infty} C_p \dot{\theta}_i(t) \left(\frac{2}{h}\right)^{1/2} \sin(2i+1) \frac{\pi z}{h} - K \theta_i(t) \left(\frac{(2i+1)\pi}{h}\right)^2 \left(\frac{2}{h}\right)^{1/2} \sin(2i+1) \frac{\pi z}{h} \\ = -\theta_a \frac{z}{1-\nu} E \alpha A_0 \omega_{m,n} \cos(\omega_{m,n}t) \times \left(\frac{\pi}{L}\right)^2 \sin \frac{m\pi x}{L} \sin \frac{n\pi y}{L} (m^2 + n^2) \end{aligned} \quad (\text{B.30})$$

Multiply the equation by  $\sin \frac{(2i+1)\pi z}{h}$  and integrate over  $z$ , and also dividing the equation by  $C_p$  gives an equation of motion for the  $\theta_i$

$$\dot{\theta}_i(t) \left(\frac{2}{h}\right)^{1/2} + D \theta_i(t) \left(\frac{2}{h}\right)^{1/2} \left(\frac{(2i+1)\pi}{h}\right)^2 = -\Gamma_{m,n} z_i \cos(\omega_{m,n}t) \sin \frac{m\pi x}{L} \sin \frac{n\pi y}{L} \quad (\text{B.31})$$

where the diffusion constant  $D$  is

$$D = \frac{K}{C_p} \quad (\text{B.32})$$

and the constant  $\Gamma_{m,n}$  is given by

$$\Gamma_{m,n} = \frac{(m^2 + n^2)\pi^2\theta_a E\alpha A_0\omega_{m,n}}{C_p(1-\nu)L^2} \quad (\text{B.33})$$

and  $z_i$  is given by

$$z_i = \frac{2}{h} \int_{-\frac{h}{2}}^{\frac{h}{2}} dz z \sin \frac{(2i+1)\pi z}{h} \quad (\text{B.34})$$

Equation B.31 has an oscillatory drive at frequency  $\omega_{m,n}$ , so we try an oscillatory solution and find it to be

$$\theta_i(t) = \text{Re} \left[ \left( \frac{h}{2} \right)^{1/2} \frac{-z_i \Gamma_{m,n} \sin \frac{\pi x}{L} \sin \frac{\pi y}{L} e^{i\omega_{m,n}t}}{i\omega_{m,n} + D \left( \frac{(2i+1)\pi}{h} \right)^2} \right] \quad (\text{B.35})$$

## B.2.6 Computing the mean loss rate during an oscillation

The energy loss per unit volume is again given by Eq. B.4 and copied here

$$\bar{\epsilon} = -\overline{\theta(t)\alpha\dot{\sigma}(t)} \quad (\text{B.36})$$

The product  $\alpha\dot{\sigma}(t)$  can be written as

$$\alpha\dot{\sigma}(t) = \frac{z}{1-\nu} E_Y \alpha A_0 \omega_{m,n} \cos \omega_{m,n}t \left( \frac{\pi}{L} \right)^2 \sin \frac{m\pi x}{L} \sin \frac{n\pi y}{L} (m^2 + n^2) \quad (\text{B.37})$$

$$= \frac{C_p}{\theta_a} z \Gamma_{m,n} \sin \frac{m\pi x}{L} \sin \frac{n\pi y}{L} \cos \omega_{m,n}t \quad (\text{B.38})$$

$$= \text{Re} [\chi_1 e^{i\omega_{m,n}t}] \quad (\text{B.39})$$

where

$$\chi_1 = \frac{C_p}{\theta_a} \Gamma_{m,n} z \sin \frac{m\pi x}{L} \sin \frac{n\pi y}{L} \quad (\text{B.40})$$

The temperature field  $\theta(\vec{x}, t)$  can be written as

$$\theta(t) = \sum_{i=0}^{\infty} \theta_i(t) \left(\frac{2}{h}\right)^{1/2} \sin(2i+1) \frac{\pi z}{h} \quad (\text{B.41})$$

$$= \theta_0(t) \left(\frac{2}{h}\right)^{1/2} \sin \frac{\pi z}{h} \quad (\text{B.42})$$

$$= \text{Re} \left[ \frac{-z_0 \Gamma_{m,n} \sin \frac{\pi x}{L} \sin \frac{\pi y}{L} \sin \frac{\pi z}{h} e^{i\omega_{m,n} t}}{i\omega_{m,n} + D \left(\frac{\pi}{h}\right)^2} \right] \quad (\text{B.43})$$

$$= \text{Re} [\chi_2 e^{i\omega_{m,n} t}] \quad (\text{B.44})$$

where  $\theta_i$  comes from Eq. B.35 and we define  $\chi_2$  as,

$$\chi_2 = -\frac{z_0 \Gamma_{m,n} \sin \frac{m\pi x}{L} \sin \frac{n\pi y}{L} \sin \frac{\pi z}{h}}{i\omega_{m,n} + D \left(\frac{\pi}{h}\right)^2} \quad (\text{B.45})$$

The decision to only keep the  $i = 0$  term is justified later.

Then the energy density loss rate becomes

$$\bar{\epsilon} = -\overline{\theta(t) \alpha \dot{\sigma}(t)} \quad (\text{B.46})$$

$$= -\overline{\text{Re} [\chi_2 e^{i\omega_{m,n} t}] \text{Re} [\chi_1 e^{i\omega_{m,n} t}]} \quad (\text{B.47})$$

$$= \frac{1}{2} \text{Re} [\chi_1^* \chi_2] \quad (\text{B.48})$$

$$= \frac{1}{2} \text{Re} \left[ \frac{C_p}{\theta_a} z \left( \Gamma_{m,n} \sin \frac{m\pi x}{L} \sin \frac{n\pi y}{L} \right)^2 z_0 \frac{-\sin \frac{\pi z}{h}}{i\omega_{m,n} + D \left(\frac{\pi}{h}\right)^2} \right] \quad (\text{B.49})$$

$$= \frac{1}{2} \text{Re} \left[ \frac{C_p}{\theta_a} z \left( \Gamma_{m,n} \sin \frac{m\pi x}{L} \sin \frac{n\pi y}{L} \right)^2 z_0 \frac{-\sin \frac{\pi z}{h} \left( -i\omega_{m,n} + D \left(\frac{\pi}{h}\right)^2 \right)}{\omega_{m,n}^2 + D^2 \left(\frac{\pi}{h}\right)^4} \right] \quad (\text{B.50})$$

$$= -\frac{1}{2} \frac{C_p}{\theta_a} z \left( \Gamma_{m,n} \sin \frac{m\pi x}{L} \sin \frac{n\pi y}{L} \right)^2 z_0 \frac{D \left(\frac{\pi}{h}\right)^2 \sin \frac{\pi z}{h}}{\omega_{m,n}^2 + D^2 \left(\frac{\pi}{h}\right)^4} \quad (\text{B.51})$$

If we plug in numerical values for silicon nitride given in Table B.2 we see that  $D(\pi/h)^2 \approx 6 \times 10^9 \gg \omega_{m,n} \sim 10^6 - 10^7$ . (This is the limit that allowed also justifies keeping only the  $\theta_0$  term.) In this

limit, Eq. B.51 simplifies to become

$$\bar{\epsilon} = -\frac{1}{2} \frac{C_p}{\theta_a} z \left( \Gamma_{m,n} \sin \frac{m\pi x}{L} \sin \frac{n\pi y}{L} \right)^2 z_0 \frac{\sin \frac{\pi z}{h}}{D \left( \frac{\pi}{h} \right)^2}$$

The energy loss density is integrated over the volume of the membrane to give the mean energy loss rate over a cycle

$$\bar{E} = \int_{-h/2}^{h/2} dz \int_0^L dx \int_0^L dy \bar{\epsilon} = -\frac{1}{2} \frac{C_p \Gamma_{m,n}^2 h^2 z_0}{\pi^2 \theta_a D} \int_0^L \sin^2 \frac{m\pi x}{L} dx \int_0^L \sin^2 \frac{n\pi y}{L} dy \int_{-h/2}^{h/2} z \sin \frac{\pi z}{h} dz \quad (\text{B.52})$$

where from the definition of  $z_i$  given in Eq. B.34 we calculate  $z_0$  as

$$\int_{-h/2}^{h/2} z \sin \frac{\pi z}{h} dz = \frac{z_0 h}{2} \quad (\text{B.53})$$

and the integrals

$$\int_0^L \sin^2 \frac{n\pi y}{L} dy = \int_0^L \sin^2 \frac{m\pi x}{L} dx = \frac{L}{2} \quad (\text{B.54})$$

Finally, we get that the mean energy loss rate over a cycle  $\bar{E}$  is

$$\bar{E} = -\frac{1}{2} \frac{C_p \Gamma_{m,n}^2 h^2 z_0}{\pi^2 \theta_a D} \frac{z_0 h}{2} \left( \frac{L}{2} \right)^2 \quad (\text{B.55})$$

### B.3 Calculation of $Q$

We now have all three factors needed to calculate  $Q$ : the resonant frequency  $\omega_{m,n}$ , the energy loss rate  $\bar{E}$ , and the oscillator's energy  $E$ .

$$Q = \frac{\omega_{m,n} \bar{E}}{E}$$

where  $\bar{E}$  is given by Eq. B.55 and  $E$  is given by Eq. B.2 and  $\omega_{m,n}$  is given by Eq. B.3. Substituting these into the equation for  $Q$  gives

$$Q = \frac{\pi}{L} \sqrt{\frac{\sigma_{\text{ext}}(m^2 + n^2)}{\rho}} \frac{16\pi^2\theta_a D}{C_p \Gamma_{m,n}^2 h^3 z_0^2 L^2} \frac{\pi^2 \sigma_{\text{ext}} h}{8} (m^2 + n^2) A^2 \quad (\text{B.56})$$

$$= \frac{\pi^5 \theta_a \sigma_{\text{ext}}^{3/2} (m^2 + n^2)^{3/2} A^2}{2\rho^{1/2} C_p z_0^2 h^2 L^3} D \frac{1}{\Gamma_{m,n}^2} \quad (\text{B.57})$$

$$= \frac{\pi^5 \theta_a \sigma_{\text{ext}}^{3/2} (m^2 + n^2)^{3/2} A^2}{2\rho^{1/2} C_p z_0^2 h^2 L^3} \frac{K}{C_p} \left( \frac{C_p (1 - \nu) L^2}{(m^2 + n^2) \pi^2 \theta_a E \alpha A_0 \omega_{m,n}} \right)^2 \quad (\text{B.58})$$

$$= \frac{\pi \sigma_{\text{ext}}^{3/2} L (1 - \nu)^2 K}{2\rho^{1/2} \theta_a z_0^2 h^2 (m^2 + n^2)^{1/2} E^2 \alpha^2} \frac{1}{\omega_{m,n}^2} \quad (\text{B.59})$$

$$= \frac{\rho^{1/2} \sigma_{\text{ext}}^{1/2} L^3 (1 - \nu)^2 K}{2\pi \theta_a z_0^2 h^2 (m^2 + n^2)^{3/2} E^2 \alpha^2} \quad (\text{B.60})$$

Now use the definition of  $z_0$  given in Eq. B.34 we can compute  $z_0$  as

$$z_0 = \frac{2}{h} \int_{-\frac{h}{2}}^{\frac{h}{2}} dz z \sin \frac{\pi z}{h} \quad (\text{B.61})$$

$$= \frac{4h}{\pi^2} \quad (\text{B.62})$$

Substitute  $z_0 = 4h/\pi^2$  into Eq. B.60 gives the final result:

$$\begin{aligned} Q_{\text{TED}} &= \frac{\rho^{1/2} \sigma_{\text{ext}}^{1/2} L^3 (1 - \nu)^2 K}{2\pi \theta_a h^2 (m^2 + n^2)^{3/2} E^2 \alpha^2} \frac{\pi^4}{16h^2} \\ &= \frac{\pi^3 \rho^{1/2} \sigma_{\text{ext}}^{1/2} L^3 (1 - \nu)^2 K}{32\theta_a h^4 (m^2 + n^2)^{3/2} E^2 \alpha^2} \end{aligned}$$

Substituting in the numerical values for our 1 mm square 50 nm-thick membrane given in Table B.2, a quality factor of

$$Q \approx 5 \times 10^{11}$$

## B.4 Discrepancy with other calculations of $Q_{\text{TED}}$

The prediction that the membranes used in this dissertation have a quality factor  $Q \sim 10^{11}$  is in disagreement with a published prediction given in Ref. [106] of  $Q \sim 10^8$ . The difference arises because Ref. [106] uses the final result from Norris and Photiadis Eqs. 4.16-4.19, which assumes the thin plates have no external stress. In the case of no external stress the energy of the thin plate is given by Norris and Photiadis Eq. 4.3, rather than Eq. B.2 which I use as the energy of a membrane under tension.

# Bibliography

- [1] P. Lebedew, *Annalen der Physik* (Leipzig), **311**, 433 (1901).
- [2] E. F. Nichols and G. F. Hull, *Physical Review* (Series I), **17**, 91 (1903).
- [3] E. F. Nichols and G. F. Hull, *Physical Review* (Series I), **17**, 26 (1903).
- [4] K. Børkje, A. Nunnenkamp, B. M. Zwickl, C. Yang, J. G. E. Harris, and S. M. Girvin, *Physical Review A*, **013818**, 1 (2010).
- [5] J. Kepler, *De Cometis Libelli Tres* (1619).
- [6] L. Euler, *Historie de l'Academie Royale de Berlin*, 121 (1746).
- [7] T. Young, *Philosophical Transactions of the Royal Society of London*, **94**, 1 (1804), ISSN 0261-0523.
- [8] J. C. Maxwell, *A Treatise on Electricity and Magnetism (Vol. 2)* (Dover, 1873).
- [9] A. Einstein, *Annalen der Physik* (Leipzig), **17**, 891 (1905).
- [10] A. Bartoli, *Nuovo Cimento*, **15**, 193 (1884).
- [11] J. C. Maxwell, *Philosophical Transactions of the Royal Society of London*, **170**, 231 (1879), ISSN 0261-0523.
- [12] O. Reynolds, *Philosophical Transactions of the Royal Society of London*, **170**, 727 (1879), ISSN 0261-0523.

- [13] W. Crookes, Philosophical Transactions of the Royal Society of London, **163**, 277 (1873), ISSN 0261-0523.
- [14] W. Crookes, Philosophical Transactions of the Royal Society of London, **164**, 501 (1874), ISSN 0261-0523.
- [15] W. Crookes, Philosophical Transactions of the Royal Society of London, **165**, 519 (1875), ISSN 0261-0523.
- [16] W. Crookes, Philosophical Transactions of the Royal Society of London, **166**, 325 (1876), ISSN 0261-0523.
- [17] W. Crookes, Philosophical Transactions of the Royal Society of London, **169**, 243 (1878), ISSN 0261-0523.
- [18] W. Crookes, Philosophical Transactions of the Royal Society of London, **170**, 87 (1879), ISSN 0261-0523.
- [19] E. F. Nichols and G. F. Hull, Physical Review (Series I), **13**, 307 (1901).
- [20] P. Lebedew, Astrophysical Journal, **31**, 385 (1910).
- [21] M. Planck, Annalen der Physik (Leipzig), **4**, 553 (1901).
- [22] A. Einstein, Annalen der Physik (Leipzig), **17**, 132 (1905).
- [23] N. Campbell, Proceedings of the Cambridge Philosophical Society, **15**, 310 (1909).
- [24] N. Campbell, Proceedings of the Cambridge Philosophical Society, **15**, 117 (1909).
- [25] M. N. Saha, The Astrophysical Journal, **50**, 220 (1919), ISSN 0004-637X.
- [26] A. H. Compton, The Physical Review - Second Series, **21**, 483 (1923).
- [27] R. Hanbury Brown and R. Q. Twiss, Nature, **178**, 1046 (1956).
- [28] A. Dorsel, J. McCullen, P. Meystre, E. Vignes, and H. Walther, Physical Review Letters, **51**, 1550 (1983), ISSN 0031-9007.

- [29] A. Ashkin, *Physical Review Letters*, **24**, 156 (1970), ISSN 0031-9007.
- [30] D. J. Griffiths, *Introduction to Quantum Mechanics*, 1st ed. (Prentice Hall, 1995) pp. 108–116.
- [31] W. Heisenberg, *The Physical Principles of the Quantum Theory* (Dover Publications, New York, 1930).
- [32] C. Caves, *Physical Review D*, **23**, 1693 (1981), ISSN 0556-2821.
- [33] E. D. Black, *American Journal of Physics*, **69**, 79 (2001), ISSN 00029505.
- [34] A. A. Clerk, M. Devoret, S. M. Girvin, F. Marquardt, and R. J. Schoelkopf, *Reviews of Modern Physics*, **82**, 1155 (2010), ISSN 0034-6861.
- [35] V. B. Braginsky and F. Y. Khalili, *Quantum Measurement*, edited by K. S. Thorne (Cambridge University Press, 1992).
- [36] J. D. Teufel, T. Donner, M. a. Castellanos-Beltran, J. W. Harlow, and K. W. Lehnert, *Nature nanotechnology*, **4**, 820 (2009), ISSN 1748-3395.
- [37] G. Anetsberger, O. Arcizet, Q. P. Unterreithmeier, R. Rivière, a. Schliesser, E. M. Weig, J. P. Kotthaus, and T. J. Kippenberg, *Nature Physics*, **5**, 909 (2009), ISSN 1745-2473.
- [38] G. Anetsberger, E. Gavartin, O. Arcizet, Q. Unterreithmeier, E. Weig, M. Gorodetsky, J. Kotthaus, and T. Kippenberg, *Physical Review A*, **82**, 1 (2010), ISSN 1050-2947.
- [39] J. D. Thompson, B. M. Zwickl, A. M. Jayich, F. Marquardt, S. M. Girvin, and J. G. E. Harris, *Nature*, **452**, 72 (2008), ISSN 1476-4687.
- [40] F. Marquardt, J. Chen, A. A. Clerk, and S. Girvin, *Physical Review Letters*, **99**, 1 (2007), ISSN 0031-9007.
- [41] F. Marquardt, A. A. Clerk, and S. M. Girvin, **2008**, 1 (2008), arXiv:arXiv:0803.1164v1 .
- [42] I. Wilson-Rae, N. Nooshi, W. Zwerger, and T. Kippenberg, *Physical Review Letters*, **99**, 1 (2007), ISSN 0031-9007.

- [43] S. Stenholm, *Reviews of Modern Physics*, **58**, 699 (1986), ISSN 0034-6861.
- [44] D. Leibfried, R. Blatt, C. Monroe, and D. Wineland, *Reviews of Modern Physics*, **75**, 281 (2003), ISSN 0034-6861.
- [45] K. Vahala, *Physical Review A*, **78**, 1 (2008), ISSN 1050-2947.
- [46] K. W. Murch, K. L. Moore, S. Gupta, and D. M. Stamper-Kurn, *Nature Physics*, **4**, 561 (2008), ISSN 1745-2473.
- [47] K. Jacobs, P. Tombesi, M. Collett, and D. Walls, *Physical Review A*, **49**, 1961 (1994), ISSN 1050-2947.
- [48] M. Pinard, C. Fabre, and A. Heidmann, *Physical Review A*, **51**, 2443 (1995), ISSN 1050-2947.
- [49] A. Heidmann, Y. Hadjar, and M. Pinard, *Applied Physics B: Lasers and Optics*, **64**, 173 (1997), ISSN 0946-2171.
- [50] A. Matsko and S. Vyatchanin, *Applied Physics B: Lasers and Optics*, **64**, 167 (1997), ISSN 0946-2171.
- [51] P. Verlot, a. Tavernarakis, T. Briant, P.-F. Cohadon, and a. Heidmann, *Physical Review Letters*, **102**, 1 (2009), ISSN 0031-9007.
- [52] R. Bondurant and J. Shapiro, *Physical Review D*, **30**, 2548 (1984), ISSN 0556-2821.
- [53] M. T. Jaekel and S. Reynaud, *Europhysics Letters (EPL)*, **13**, 301 (1990), ISSN 0295-5075.
- [54] A. Luis and L. Sánchez-Soto, *Physical Review A*, **45**, 8228 (1992), ISSN 1050-2947.
- [55] A. Luis and L. Sánchez-Soto, *Optics Communications*, **89**, 140 (1992), ISSN 00304018.
- [56] S. Mancini and P. Tombesi, *Physical Review A*, **49**, 4055 (1994), ISSN 1050-2947.
- [57] C. Fabre, M. Pinard, S. Bourzeix, A. Heidmann, E. Giacobino, and S. Reynaud, *Physical Review A*, **49**, 1337 (1994), ISSN 1050-2947.

- [58] A. Heidmann and S. Reynaud, *Physical Review A*, **50**, 4237 (1994), ISSN 1050-2947.
- [59] P. Meystre, E. M. Wright, J. D. McCullen, and E. Vignes, *Journal of the Optical Society of America B*, **2**, 1830 (1985), ISSN 0740-3224.
- [60] L. Hilico, J. M. Courty, C. Fabre, E. Giacobino, I. Abram, and J. L. Oudar, *Applied Physics B*, **55**, 202 (1992), ISSN 0721-7269.
- [61] A. Schliesser, P. Del’Haye, N. Nooshi, K. Vahala, and T. Kippenberg, *Physical Review Letters*, **97**, 1 (2006), ISSN 0031-9007.
- [62] Y.-S. Park and H. Wang, *Nature Physics*, **5**, 489 (2009), ISSN 1745-2473.
- [63] O. Arcizet, P.-F. Cohadon, T. Briant, M. Pinard, and A. Heidmann, *Nature*, **444**, 71 (2006), ISSN 1476-4687.
- [64] a. D. O’Connell, M. Hofheinz, M. Ansmann, R. C. Bialczak, M. Lenander, E. Lucero, M. Neeley, D. Sank, H. Wang, M. Weides, J. Wenner, J. M. Martinis, and a. N. Cleland, *Nature*, **464**, 697 (2010), ISSN 1476-4687.
- [65] E. Hecht, *Optics*, 4th ed. (Pearson, 2002).
- [66] G. Brooker, *Modern Classical Optics* (Oxford University Press, 2003).
- [67] A. Nunnenkamp, K. Børkje, J. G. E. Harris, and S. M. Girvin, *Physical Review A*, **82**, 021806 (2010), ISSN 1050-2947.
- [68] A. A. Clerk, F. Marquardt, and J. G. E. Harris, *Physical Review Letters*, **104**, 213606 (2010), ISSN 0031-9007.
- [69] J. C. Sankey, C. Yang, B. M. Zwickl, A. M. Jayich, and J. G. E. Harris, *Nature Physics*, **6**, 1 (2010), ISSN 1745-2473.
- [70] S. Bose, K. Jacobs, and P. Knight, *Physical Review A*, **56**, 4175 (1997), ISSN 1050-2947.
- [71] J. Zhang, K. Peng, and S. Braunstein, *Physical Review A*, **68**, 1 (2003), ISSN 1050-2947.

- [72] D. Vitali, S. Gigan, A. Ferreira, H. Böhm, P. Tombesi, a. Guerreiro, V. Vedral, a. Zeilinger, and M. Aspelmeyer, *Physical Review Letters*, **98**, 1 (2007), ISSN 0031-9007.
- [73] S. Mancini, V. Giovannetti, D. Vitali, and P. Tombesi, *Physical Review Letters*, **88**, 3 (2002), ISSN 0031-9007.
- [74] M. Pinard, a. Dantan, D. Vitali, O. Arcizet, T. Briant, and a. Heidmann, *Europhysics Letters (EPL)*, **72**, 747 (2005), ISSN 0295-5075.
- [75] M. Hartmann and M. Plenio, *Physical Review Letters*, **101**, 1 (2008), ISSN 0031-9007.
- [76] S. Mancini, V. I. Man'ko, and P. Tombesi, *Physical Review A*, **55**, 3042 (1997), ISSN 1050-2947.
- [77] W. Marshall, C. Simon, R. Penrose, and D. Bouwmeester, *Physical Review Letters*, **91**, 1 (2003), ISSN 0031-9007.
- [78] A. Bassi, E. Ippoliti, and S. Adler, *Physical Review Letters*, **94**, 28 (2005), ISSN 0031-9007.
- [79] D. Kleckner, I. Pikovski, E. Jeffrey, L. Ament, E. Eliel, J. van den Brink, and D. Bouwmeester, *New Journal of Physics*, **10**, 095020 (2008), ISSN 1367-2630.
- [80] S. Gröblacher, J. B. Hertzberg, M. R. Vanner, G. D. Cole, S. Gigan, K. C. Schwab, and M. Aspelmeyer, *Nature Physics*, **5**, 485 (2009), ISSN 1745-2473.
- [81] T. Rocheleau, T. Ndukum, C. Macklin, J. B. Hertzberg, A. A. Clerk, and K. C. Schwab, *Nature*, **463**, 72 (2010), ISSN 1476-4687.
- [82] S. Riviere, S. Deleglise, S. Weis, E. Gavartin, O. Arcizet, A. Schliesser, and T. J. Kippenberg, , arXiv:1011.0290v1 [quant (2010), arXiv:arXiv:1011.0290v1 .
- [83] V. B. Braginsky, A. B. Manukin, and M. Y. Tikhonov, *Soviet Physics Journal of Experimental and Theoretical Physics*, **31**, 829 (1970).
- [84] V. B. Braginsky and A. B. Manukin, *Measurement of Weak Forces in Physics Experiments*, edited by D. H. Douglas (University of Chicago Press, 1977).

- [85] S. Mancini, D. Vitali, and P. Tombesi, *Physical Review Letters*, **80**, 688 (1998), ISSN 0031-9007.
- [86] P. Cohadon, A. Heidmann, and M. Pinard, *Physical Review Letters*, **83**, 3174 (1999), ISSN 0031-9007.
- [87] D. Kleckner and D. Bouwmeester, *Nature*, **444**, 75 (2006), ISSN 1476-4687.
- [88] T. Li, S. Kheifets, and M. G. Raizen, *Nature Physics*, **7**, 1 (2011), ISSN 1745-2473.
- [89] B. Sheard, M. Gray, C. Mow-Lowry, D. McClelland, and S. Whitcomb, *Physical Review A*, **69**, 051801 (2004), ISSN 1050-2947.
- [90] C. H. Metzger and K. Karrai, *Nature*, **432**, 1002 (2004), ISSN 1476-4687.
- [91] J. G. E. Harris, B. M. Zwickl, and A. M. Jayich, *The Review of scientific instruments*, **78**, 013107 (2007), ISSN 0034-6748.
- [92] S. Gigan, H. R. Böhm, M. Paternostro, F. Blaser, G. Langer, J. B. Hertzberg, K. C. Schwab, D. Bäuerle, M. Aspelmeyer, and A. Zeilinger, *Nature*, **444**, 67 (2006), ISSN 1476-4687.
- [93] T. Corbitt, Y. Chen, E. Innerhofer, H. Müller-Ebhardt, D. Ottaway, H. Rehbein, D. Sigg, S. Whitcomb, C. Wipf, and N. Mavalvala, *Physical Review Letters*, **98**, 11 (2007), ISSN 0031-9007.
- [94] M. Bhattacharya and P. Meystre, *Physical Review Letters*, **99**, 073601 (2007), ISSN 0031-9007.
- [95] F. Elste, S. M. Girvin, and A. A. Clerk, *Physical Review Letters*, **102**, 1 (2009), ISSN 0031-9007.
- [96] S. Barnett, J. Jeffers, A. Gatti, and R. Loudon, *Physical Review A*, **57**, 2134 (1998), ISSN 1050-2947.

- [97] A. M. Jayich, J. C. Sankey, B. M. Zwickl, C. Yang, J. D. Thompson, S. M. Girvin, A. A. Clerk, F. Marquardt, and J. G. E. Harris, *New Journal of Physics*, **10**, 095008 (2008), ISSN 1367-2630.
- [98] O. Kilic, S. Kim, W. Suh, Y.-A. Peter, A. S. Sudbø, M. F. Yanik, S. Fan, and O. Solgaard, *Optics letters*, **29**, 2782 (2004).
- [99] C. W. Gardiner and M. J. Collett, *Physical Review A*, **31**, 3761 (1985).
- [100] Norcada Inc. 4465 - 99 Street Edmonton, AB T6E 5B6 Canada <http://www.norcada.com>, .
- [101] B. M. Zwickl, W. E. Shanks, A. M. Jayich, C. Yang, A. C. Bleszynski Jayich, J. D. Thompson, and J. G. E. Harris, *Applied Physics Letters*, **92**, 103125 (2008), ISSN 00036951.
- [102] C. Zener, *Physical Review*, **52**, 230 (1937), ISSN 0031-899X.
- [103] C. Zener, "Internal Friction in Solids II. General Theory of Thermoelastic Internal Friction," (1938).
- [104] R. Lifshitz and M. Roukes, *Physical Review B*, **61**, 5600 (2000), ISSN 0163-1829.
- [105] A. N. Norris and D. M. Photiadis, *The Quarterly Journal of Mechanics and Applied Mathematics*, **58**, 143 (2005), ISSN 0033-5614.
- [106] D. Wilson, C. Regal, S. Papp, and H. Kimble, *Physical Review Letters*, **103**, 3 (2009), ISSN 0031-9007.
- [107] H. Kogelnik and T. Li, *Applied Optics*, **5**, 1550 (1966), ISSN 0003-6935.